

Final Report

U.S. DOD-Navy Contract N0014-99-1-0958

Seven-Segment Organic Polymer Based Light-Emitting Devices on Plastic Substrates

Period: 7/15/1999 – 7/14/2001

End date: 10/13/2001

Amount: \$538,199

PI: Jerzy Kanicki
Organic & Molecular Electronics Research Group
Solid-State Electronics Laboratory
Department of Electrical Engineering & Computer Science
The University of Michigan, Ann Arbor, MI
Tel. 734-936-0964
Fax: 734-615-2843
e-mail: Kanicki@eecs.umich.edu
[http:// www.eecs.umich.edu/omelab](http://www.eecs.umich.edu/omelab)

DISTRIBUTION STATEMENT A
Approved for Public Release
Distribution Unlimited

20030930 114

EXECUTIVE SUMMARY

In this project we studied the properties of the flexible plastic substrate with transparent conducting electrode (TCE), which are important for organic light-emitting devices (OLEDs). Specifically, we evaluated the TCE surface properties, electrical resistivity, surface roughness, electrode patterning, optical transmission, and the substrate water vapor/oxygen transmission. The sheet resistance of $12\sim13\ \Omega/\square$, optical transmission greater than 80% over visible range, surface roughness of $1.4\sim2.2\ \text{nm RMS}$ over $50\times50\ \mu\text{m}^2$ have been obtained for the plastic substrates. These properties are adequate for OLED applications based on USDC specifications. Finally, a combination of hydrogenated amorphous silicon nitride and silicon oxide layers deposited on one side of the substrate at low-temperature reduces the water vapor and oxygen transmission rates to less than $10^{-5}\ \text{g/cm}^2\text{-day-atm}$ and about $10^{-7}\ \text{cc/cm}^2\text{-day-atm}$, respectively.

We have also developed technology for high-performance bi-layer organic polymer light emitting-devices (OPLEDs) on plastic substrates. The device consists of a hole transporting and an light-emissive conjugated polymer layers. The opto-electronic properties of the PLEDs described in this report are acceptable for flat panel display applications.

To investigate the PLEDs opto-electronic characteristics, an integrating sphere-based measurement set up was developed, in which a photo-diode or charge coupled device was used as a light output detector.

Finally, to produce the active-matrix organic polymer light-emitting display (AM-PLED) on plastic substrate we have developed low temperature amorphous silicon thin-film transistors (a-Si:H TFTs) active-matrix arrays (AM) that are suitable for AM-PLEDs. Experimental results shown that continuous pixel electrode excitation can be achieved with developed circuits. Also the pixel electrode circuits use a current driver to automatically adjust their current level for threshold voltage shifts of both the PLEDs and the drive a-Si:H TFTs. A high output current level and a good output-input current linearity have been demonstrated with these circuits.

Accomplishments are summarized below according to the research tasks.

Task 1: Design, fabrication and characterization of the OLEDs:

- Identified and characterized the most suitable ITO-coated flexible plastic substrate for organic polymer light-emitting devices (OLEDs).
- Developed appropriate a low temperature coating methods to improve water vapor and oxygen impermeability of the plastic substrates.
- Identified and characterized organic polymers that are suitable for multi-layer OLEDs.
- Constructed multi-layer OLED energy band diagrams based on organic polymers electrochemical and optical spectra.
- Optimized the double-layer OLED structure on plastic substrates.
- Developed the hydrogenated amorphous silicon (a-Si:H) thin-film transistors (TFTs) based active-matrix (AM) arrays for AM-PLEDs.

Task 2: Lifetime evaluation of the OLEDs:

- Studied OLED degradation mechanisms.
- Developed suitable packaging method for OLEDs on plastic substrates.
- Identified the best adhesive for the OLEDs packaging.
- Designed device lifetime testing cell.
- Evaluated lifetime of unpackaged OLED on plastic substrates.

Promised but not accomplished items are given below according to the research tasks.

Task 2: Lifetime evaluation of the OLEDs:

- Did not optimize the OLED packaging method.
- Did not evaluate lifetime of the packaged OLED on plastic substrates.
- Did not study the influence of water vapor, oxygen, and temperature on lifetime of the packaged OLED on plastic substrates.

These tasks were not accomplished because the length of the project was too short. More time and financial support were needed to finish this project.

Accomplishments

Task 1

Organic light-emitting devices (OLEDs) are now being considered as the next generation flat panel displays (FPDs) for such applications as smart identification cards, screens of mobile units, and vehicular displays. This is because they have several advantages such as low operating voltage, low power consumption, self-emission, fast response time, large viewing angle, high luminous efficiency, ultra-thin structure, and light-weight [1, 2]. However, so far, most displays have been built on rigid glass or silicon substrates, even though a low-cost, low-temperature processing of the OLEDs renders them as one of the most promising candidates for display implementation on the flexible plastic substrate. Also, the plastic substrate has several distinct advantages, such as ruggedness, robustness, ultra-lightness, conformability, and impact resistance over the glass substrate that is mainly used in FPDs today [3, 4]. Furthermore, its flexibility becomes a very attractive feature as the OLED technology matures [5-8]. However, high transparency, good surface roughness, low gas permeability, and high transparent electrode conductivity of the plastic substrate are required for commercial applications.

Mahon et al. [9] have reported several important properties of the plastic substrate coated with transparent conducting electrode, which are required for OLED applications. It should have transparency greater than 85% with less than 0.5% haze over visible range, surface roughness less than 2.0 nm RMS, gas permeability of less than 10^{-6} g/cm²-day-atm and 10^{-7} cc/cm²-day-atm for water vapor and oxygen, respectively, and sheet resistance of less than 50 Ω/\square , preferably about 10 Ω/\square . The plastic substrate should also be stable under heat, humidity and UV-light. The substrate hardness should be > 6H and the cost should be < 60 US\$/m². Especially, for OLEDs whose operating stability is very sensitive to water vapor and oxygen, low permeability of water vapor and oxygen through the substrate is a critical requirement [10, 11].

In this report, first we describe the characteristics of the flexible plastic substrates that are suitable for OLEDs.

1. Structure and characterization of the plastic substrates

Figure 1(a) and (b) shows the schematic structure and transmission electron microscope (TEM) cross-section of the dry-etchable plastic substrate; the wet-etchable substrate has only one barrier layer between bottom ITO and the hard coat layers as shown in Figure 1(c). The multi-layer composition for both substrates is very similar. The transparent conducting electrode (TCE-ITO) deposited over the plastic substrate can be etched either by a laser-based method (dry-etchable) [12, 13] or by a wet chemical process (wet-etchable) [14], respectively. To improve TCE conductivity without significantly affecting the optical transmission through the substrate, a semitransparent thin metal multi-layer (for example, Au/Ag/Au or Ag/Au/Ag) is added between indium tin transparency oxide (ITO) and metal oxide (ITO or SnO₂) layers. It is well known that a

very thin silver or silver containing palladium layer between transparent conducting oxide layers allows a very high electric conductivity, a good mechanical durability, and a high transparency in the visible range due to the anti-reflection effect [15]. We have also observed similar effect for our multi-layer TCE structure, which is described in the next section. To enhance the substrate thermal stability, optical characteristics, and gas blocking property, a multi-layer structure was used on both sides of a high-glass transition temperature (T_g) and low-birefringence base film (polydicyclo-pentadiene – “transphan”). The acrylic and low temperature amorphous silicon oxide (a-SiO_x) can be used as hard coat and oxygen /

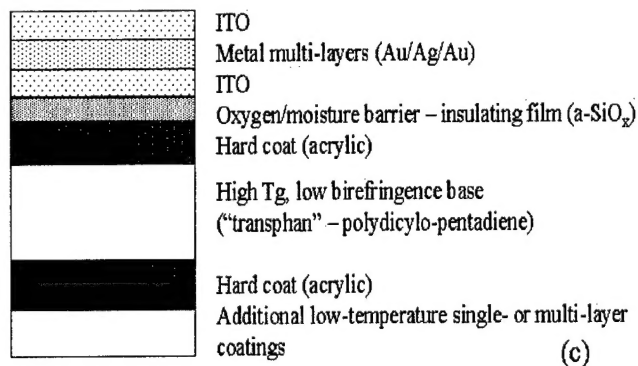
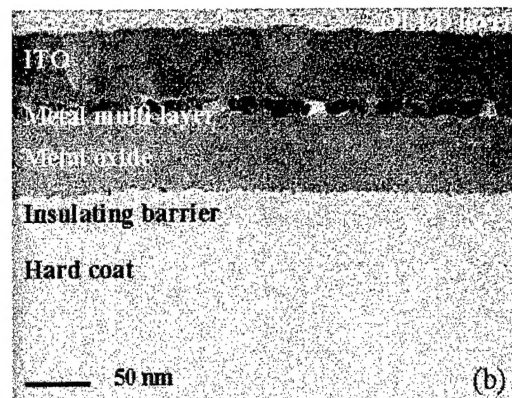
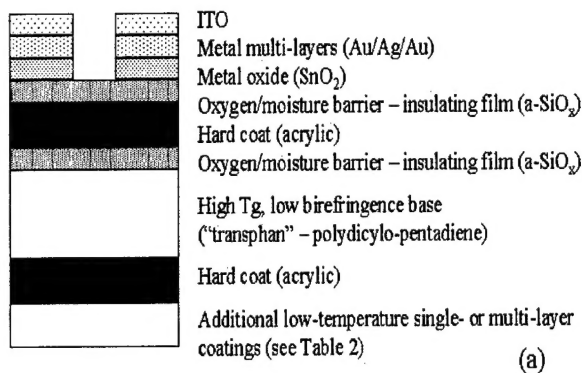


Figure 1. Schematic structure of the multi-layer dry- and wet-etchable flexible plastic substrate (a),(c) [12-14] and the transmission electron microscope (TEM) image of dry-etchable plastic substrate cross-section (b) are shown.

.moisture barrier, respectively [12-14]. To further reduce the gas transmission through the substrate, we deposited additional layers on one side of the plastic substrate, which are indicated as additional low-temperature coating layers in Figure 1 (a) and Figure 1 (c). Their impact on substrate properties will be discussed in later section.

ITO Film Composition

Table 1 shows the chemical compositions of the ITO film deposited over both dry-etchable [12, 13] and wet-etchable [14] plastic substrates, which were determined by

Table 1. Chemical composition of the dry- and wet-etchable ITO plastic substrates are summarized.

	as-received	As-received	15 sec argon sputter	30 sec argon sputter
Dry-Etchable	[O]	0.605	0.548	0.541
	[In]	0.36	0.408	0.422
	[Sn]	0.035	0.044	0.037
	[O]/(1.5[In]+2[Sn])	0.99	0.78	0.765
	[Sn]/[In]	0.097	0.108	0.088
Wet-Etchable	[O]	0.644	0.55	0.557
	[In]	0.319	0.406	0.406
	[Sn]	0.036	0.044	0.037
	[O]/(1.5[In]+2[Sn])	1.17	0.789	0.815
	[Sn]/[In]	0.113	0.108	0.091

X-ray photoelectron spectroscopy (XPS) using Mg K α radiation ($h\nu = 1253.6$ eV) under a high vacuum (10^{-9} Torr). The film composition was measured for as-received substrate and after argon sputtering of the ITO surface for 15 and 30 sec. To determine the ITO film stoichiometry, the oxygen amount was related to indium and tin and the value of [O]/(1.5[In]+2[Sn]) was calculated. The ratio of [Sn]/[In] is also included in Table 1. Since argon sputtering removes the outermost surface of ITO, Table 1 shows that the surface is oxygen (0.99 and 1.17) and tin (0.097 and 0.113) rich in comparison with the region just below the surface for both dry-etchable and wet-etchable plastic substrates. Overall, the wet-etchable plastic substrate shows higher oxygen and tin ratios in comparison with the dry-etchable plastic substrate. We also observed carbon core signal in XPS for both substrates (not shown here), which represents the common carbon contamination of the ITO surface as reported in the literature [16]. Therefore, surface treatment such as oxygen plasma or UV-ozone, needs to be performed before deposition of the organic layer, especially from aqueous solution. This type of surface treatment will

remove the contaminations and render the ITO surface hydrophilic [17, 18]. At the same time, the surface treatments will increase the work function of ITO and improve the OLED opto-electronic performances [19].

Electrical and Optical Properties

The equally spaced (0.159 cm) linear four-point probes [20] were used to measure the sheet resistance of TCE on the plastic substrate. To reduce any measurement error,

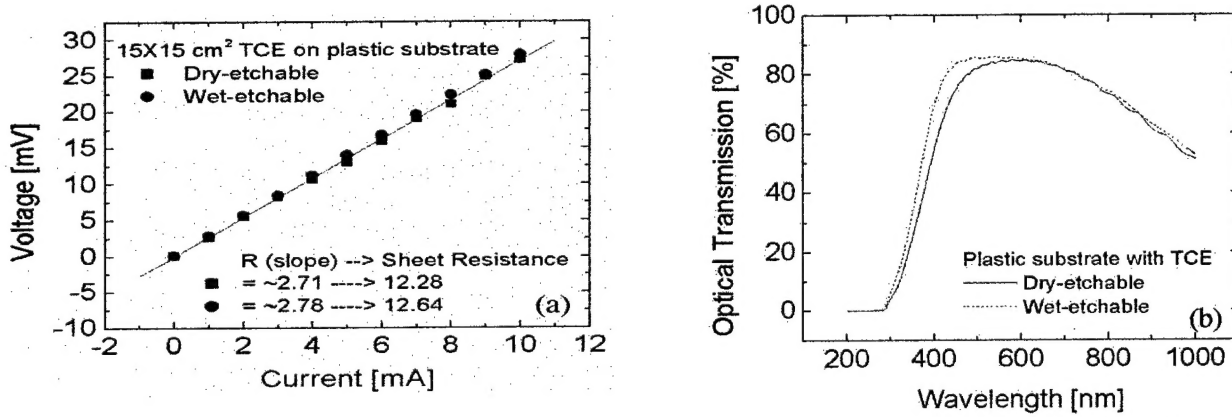


Figure 2. Electrical conductivity (a) and optical transmission (b) of the dry-etchable and wet-etchable plastic substrates with TCE are shown.

15×15 cm² electrode-coated substrate was used. In this method, current of 1 to 10 mA range was applied between two outer probes and the voltage drop across two inner probes was measured. The sheet resistance (R_s) was calculated by using the following equation with the slope extracted from the measured current-voltage characteristics as shown in Figure 2(a), since the electrode thickness ($\sim 1000 \text{ \AA} < 0.1S$) is small and the sample boundaries ($15 \text{ cm} > 40S$) are large compared to the probe spacing ($S = 0.159 \text{ cm}$) [21]. When the thickness (d) of conductive thin film is considered, the resistivity (ρ) can also be calculated.

$$R_s = 4.5324 \frac{V}{I} \quad (\Omega/\square) \quad (1)$$

$$\rho = R_s \times d \quad (\Omega\text{-cm}) \quad (2)$$

Due to the unique structure of TCE layer, a sheet resistance of about 12~13 Ω/\square has been obtained without any significant reduction of optical transmission through the substrate. Figure 2 (b) shows the plastic substrate optical transmission spectrum measured with Cary UV-vis-NIR-Spectrophotometer, where air was used as a reference. The optical transmission greater than 80 % over 450 to 750 nm ranges has been obtained, with maximum 85 and 86% for dry-etchable and wet-etchable plastic substrates, respectively. Better optical transmission of our plastic substrate compensate for slightly higher sheet resistance in comparison with the results (2 Ω/\square and average 70% optical transmission) [15] reported for similar multi-layer TCE deposited on the glass substrate.

Surface Roughness

Since OLED has the typical structure of thin organic active layers (1000-2000 Å) deposited on anode followed by cathode deposition, the surface roughness of anode is critical for OLED opto-electronic performances. If the surface is not smooth enough, non-

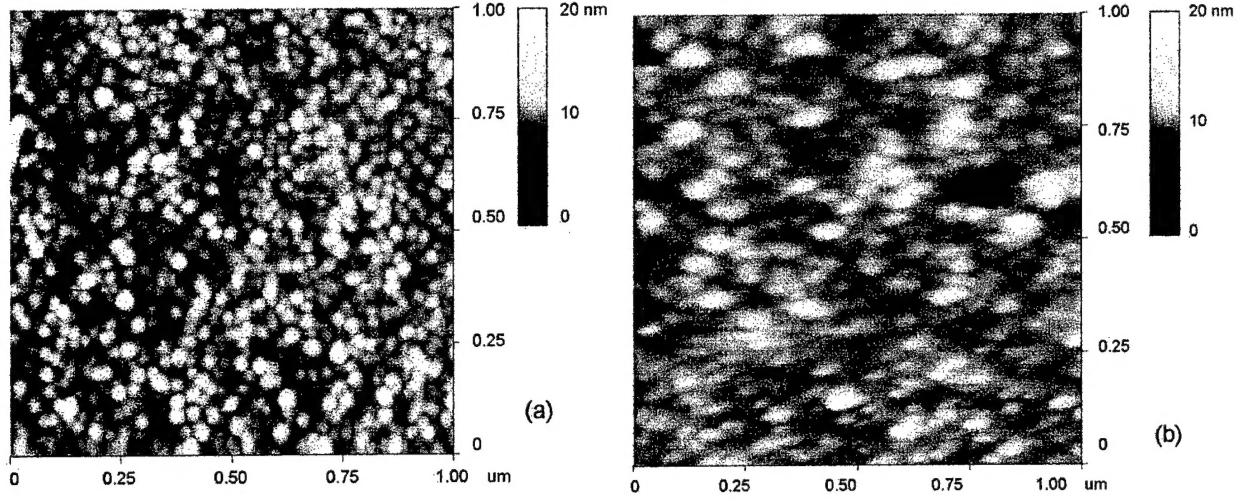


Figure 3. The atomic force microscope (AFM) images of TCE surface over $1 \times 1 \mu\text{m}^2$ area of (a) dry-etchable and (b) wet-etchable plastic substrates are shown.

uniform electric field distribution inside the device can trigger the localized degradation [16]. We used the contact-mode DI Multimode Atomic Force Microscope (AFM) to investigate the surface roughness of the TCE on the plastic substrate, where 0.58 N/m^2 silicon nitride cantilever was used at 1.0 Hz scan rate. All the measured values were expressed as the root-mean-square values characterized by the following equation:

$$X_{RMS} = \sqrt{\frac{\sum (X_i - X_{ave})^2}{N}} \quad (3)$$

where X_i , X_{ave} , and N are measured values, average of the measured values, and total number of measurement for a specific area, respectively.

Figure 3 shows the AFM images measured for $1 \times 1 \mu\text{m}^2$ TCE area for both dry- and wet-etchable plastic substrates. From this figure, we obtained 1.1 and 1.0 nm RMS values for ITO on dry- and wet-etchable plastic substrates, respectively. We also measured the surface roughness over $50 \times 50 \mu\text{m}^2$ and obtained 2.2 and 1.4 nm RMS value for dry- and wet-etchable plastic substrates, respectively. The measured RMS values are comparable to the surface roughness (less than 2 nm) required for the plastic substrate to be used for OLEDs.

TCE Patterning: dry and wet etching methods

Wet chemical [22] and reactive ion etching [23] combined with photolithography, and laser-based direct-write dry etching [24] methods have been used to pattern ITO on

glass substrates. Since no wet chemical processes are needed for the laser-based dry etching method, this method was also applied to pattern ITO on plastic substrates [25]. Initially, the laser-based method was used for our devices to pattern the TCE on dry-etchable plastic substrates [12, 13]. More recently, the wet etching capability of the TCE on wet-etchable plastic substrates was also developed [14] and was used in this study.

Dry Etching: The TCE layer on the dry-etchable plastic substrate was patterned by direct-write digital laser ablation [12, 13]. Figure 4 (a) shows a micrograph of 25 μm lines patterned by using this technique. As mentioned earlier, no masks and no wet

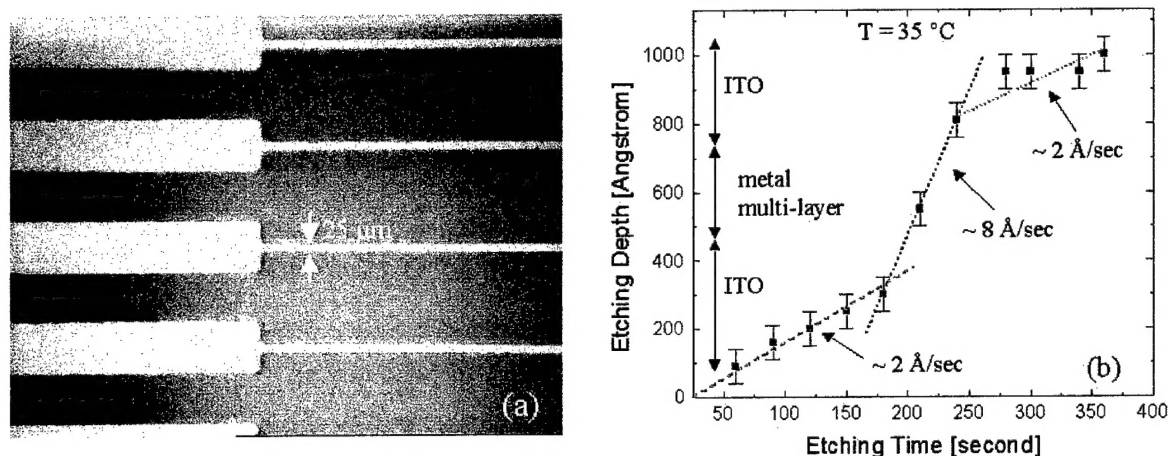


Figure 4. Micrograph of 25 μm lines patterned on the dry-etchable plastic substrate by the digital-laser ablation technique (a) and etching depth versus etching time characteristics of TCE on the wet-etchable plastic substrate (b) are shown.

chemical processes are needed since the patterns are directly transferred from digital image file via a raster image processor (RIP). During the patterning process, the plastic substrate is located in an internal drum with vacuum holding capability and scanned with the laser beam using a spinning mirror. The pattern is created by modulation of the laser light according to the digital data signal received from the RIP.

Wet Etching: Since the TCE on the wet-etchable plastic substrate consists of ITO, metal multi-layer, and metal oxide layer, a specific etching solution [14] has been used to etch the multi-layer electrode, which is a 5:1 mixture of 3% H_2SO_4 and 0.01% FeCl_3 . The wet-etching was performed in the ultrasonic bath at 35 $^{\circ}\text{C}$. The evolution of the film thickness with etching time is shown in Figure 4 (b), which was measured by using Dektak 8000 profilometer. It is noted that there are three different etching rates, which can be associated with ITO, metal multi-layer (Au/Ag/Au), and ITO. The ITO and Au/Ag/Au layer were etched at 2 and 8 $\text{\AA}/\text{sec}$, respectively.

Water Vapor and Oxygen Transmission Analysis

Since organic materials used in OLED applications are sensitive to water vapor and oxygen, it is critical to protect the active organic layers from contacting water vapor and oxygen for better device operating stability and longer display lifetime [10]. Therefore, the plastic substrate must also have a very good gas blocking property for OLED applications. The water vapor and oxygen transmission rates (TR_{WV} and TR_O) through our dry-etchable plastic substrate were analyzed by using American Society for Testing and Material (ASTM) methodology [26, 27].

Figure 5 shows the experimental setup used to measure water vapor and oxygen transmission rates (TR_{WV} and TR_O) through the plastic substrate. TR_{WV} is the time rate of water vapor flow normal to the substrate surface per unit area under steady-state conditions, which were measured using a pulsed infrared sensor under the partial pressure 49 mmHg of 100% relative humidity (RH) water vapor and the substrate temperature of

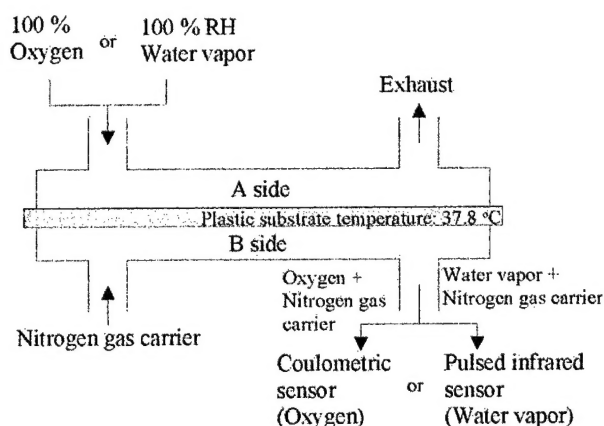


Figure 5. Experimental setup used for TR_{WV} and TR_O of the plastic substrate is shown. The pulsed infrared and Coulometric sensors are used to detect the amount of water vapor and oxygen diffusing from A side to B side through the substrate, respectively.

37.8 °C. "A side" of the chamber was maintained at 100% RH during analysis and "B side" of the chamber was about 0% RH, before, during and after analysis, respectively. When water vapor diffusing through the substrate to "B side" is carried into the infrared sensor, the sensor measures the fraction of infrared energy absorbed by the water vapor and produces an electrical signal, whose amplitude is proportional to the water vapor concentration. The amplitude of electrical signal measured for the plastic substrate is then

compared to the signal produced from the calibration film of known transmission rate [27]. TR_O is the quantity of oxygen gas passing through a unit area of the substrate under the conditions of test, which was measured using a Coulometric sensor at the substrate temperature of 37.8 °C [26]. The partial pressure of oxygen was measured during the analysis. "A side" of the chamber was maintained at 90% RH during analysis and "B side" of the chamber was about 0% RH, before, during and after analysis, respectively. Since the Coulometric sensor is insensitive to water vapor, it measures only the amount of oxygen flowing into the detector and produces the corresponding electrical current. As shown in Figure 5, the nitrogen carrier transports water vapor or oxygen molecule diffusing through the substrate into the infrared or Coulometric sensor, respectively. From the described experimental setup, the transmission rate (TR) values for the plastic substrate can be obtained using the following procedure. First, the change of TR versus gas exposure time is measured. Figure 6 shows an example of the measured TR_{WV} and

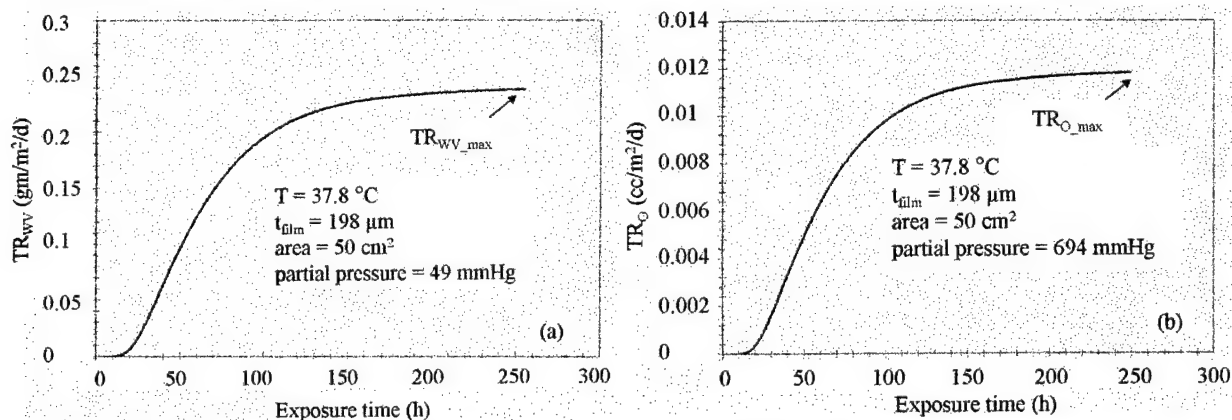


Figure 6. Examples of TR_{WV} (a) and TR_O (b) characteristics versus gas exposure time for the dry-etchable plastic substrate are shown. Experimental conditions are also included in graphs. TR saturate as gas exposure time increases and these saturated values represent the maximum transmission rates (TR_{max}), which are used to calculate TR_{WV} and TR_O of the plastic substrates.

TR_O characteristics versus gas exposure time for the plastic substrate. The TR saturate as gas exposure time increases and these saturated values represent the maximum transmission rates (TR_{max}). Using TR_{max} , TR values can be calculated as follows:

$$TR = TR_{max} \times P_{gas} \quad (4)$$

where P_{gas} is the partial pressure in atm unit of water vapor or oxygen. From the above graphs, TR_{max} values are 0.241 g/m²-day and 0.0119 cc/m²-day for water vapor and

oxygen, and the partial pressure values for water vapor and oxygen measurements are 49 and 694 mmHg; thus, TR_{WV} and TR_O of 3.74×10^{-4} g/cm²-day-atm and 1.30×10^{-6} cc/cm²-day-atm are obtained, respectively. By using this methodology, we analyzed the gas transmission rates for the plastic substrates coated with additional low-temperature layers, which will be discussed in the next subsection.

To further reduce the water vapor and oxygen transmission through the substrate, additional several types of low-temperature layers have been deposited on the substrate and their characteristics have also been analyzed. Although the substrate has a multi-layer structure to enhance the gas blocking properties as shown in Figure 1, $10^{-4} \sim 10^{-6}$ g/cm²-day-atm and $10^{-5} \sim 10^{-7}$ cc/cm²-day-atm for TR_{WV} and TR_O were obtained for the plastic substrate with no additional coating layers. An improvement of gas blocking properties by one to three orders of magnitude for water vapor and oxygen is still needed for the plastic substrate to satisfy the requirements for OLED applications (TR_{WV} and TR_O of $< 10^{-6}$ g/cm²-day-atm and $< 10^{-7}$ cc/cm²-day-atm, respectively) [28, 29]. To further reduce the TR_{WV} and TR_O through the plastic substrates, several types of low-temperature layers have been deposited on the plastic substrates. Polypropylene glycol (PPG, ~ 8.9 μ m) was spin-coated and cured at low temperature (Sample A). Chromium (~ 400 Å) and aluminum (~ 2000 Å) layers were consecutively deposited by DC-cathode-sputtering method under the high vacuum ($\sim 10^{-6}$ mbar) (Sample B). We also deposited the hydrogenated amorphous silicon nitride (a-SiN_x:H, ~ 2500 Å) (Sample C) and amorphous silicon oxide (a-SiO_x:H, ~ 2500 Å) (Sample D) by a low-temperature (120 °C) plasma-enhanced chemical vapor deposition (LT-PECVD) method. We also consecutively deposited a-SiN_x:H (~ 1500 Å) and a-SiO_x:H (~ 1500 Å) on the plastic substrate by LT-PECVD method (Sample E). The measured TR_{WV} and TR_O for the plastic substrates with several additional coatings are summarized in Table 2. For sample A, the PPG layer does not help to block the gas transmission through the substrate although a very thick layer was deposited. The bi-layer of chromium and aluminum (sample B), the a-SiN_x:H layer (sample D) and the combination of a-SiN_x:H and a-SiO_x:H layers (sample E) showed a very good water vapor blocking property. For these samples, a decrease of TR_{WV} by more than one order of magnitude has been achieved in comparison with the initial substrate measured. TR_{WV} values are much lower than the detection limit of the measurement setup, which is 1.55×10^{-5} g/cm²-day-atm. Therefore, to accurately analyze the water vapor transmission properties of the plastic substrates, a new method, such as calcium test [29], should be used. The TR_O is also reduced by one order of magnitude for samples B, C, and D. Especially, for the sample E, a very good TR_O (2.53×10^{-7} cc/cm²-day-atm) has been achieved in comparison with the initial substrate. From our result, we can conclude that a-SiN_x:H and a-SiO_x:H layers consecutively deposited on one side of the substrate will reduce the water vapor and oxygen transmission rates to the acceptable levels for OLED applications.

<i>Sample</i>	TR_{WV} (g/cm ² -day-atm)	TR_O (cc/cm ² -day-atm)
E	$< 1.55 \times 10^{-5}$ *	2.53×10^{-7}

D	$<1.55 \times 10^{-5} *$	1.30×10^{-6}
C	3.74×10^{-5}	3.86×10^{-6}
B	$<1.55 \times 10^{-5} *$	3.94×10^{-6}
A	5.06×10^{-4}	2.13×10^{-5}
Substrate 4	1.17×10^{-4}	2.27×10^{-5}
Substrate 3	3.66×10^{-4}	1.56×10^{-5}
[†] Substrate 2	$(1.2 \sim 9.4) \times 10^{-6}$	$(1.09 \sim 1.15) \times 10^{-5}$
[†] Substrate 1	$(1.2 \sim 2) \times 10^{-6}$	$<5 \times 10^{-7}$
[†] Substrate ii	$(7.42 \sim 7.51) \times 10^{-5}$	$(3.87 \sim 3.89) \times 10^{-5}$
[†] Substrate i	$(0.49 \sim 1.02) \times 10^{-5}$	$(0.71 \sim 0.8) \times 10^{-5}$

Table 2 Transmission rates of the water vapor and oxygen (TR_{wv} and TR_O) through the dry-etchable plastic substrate coated with several additional low-temperature layers are summarized. TR_{wv} and TR_O for the unetched (Substrate i) and etched (Substrate ii) wet-etchable plastic substrate are also included. Substrate1: unetched dry-etchable substrate; Substrate2: laser etched dry-etchable substrate; Substrate3: pITO/substrate; Substrate4: bITO/substrate; Sample A: pITO/ substrate/PPG; Sample B: bITO/substrate/Cr/Al; Sample C: pITO/substrate/a-SiN_x:H; Sample D: pITO/substrate/a-SiO_x:H; Sample E: pITO/substrate/a-SiN_x:H/a-SiO_x:H; where pITO and bITO are patterned and blank ITO, respectively. (*: measurement setup detection limit; †: different measurement conditions are used – TR_O : 90% RH, 100% O₂, 0% RH, 100% N₂, 1 atm, 23 °C; TR_{wv} : 100% RH, 0% RH, 1 atm, 23 °C).

The overall properties of the flexible plastic substrate used in this study are given in Table 3. In summary, the sheet resistance of about 12~13 Ω/\square , optical transmission of greater than 80% over visible range, surface roughness of 1.4~2.2 nm RMS over 50×50 μm^2 have been obtained for the TCE coated on the plastic substrate. We also investigated the patterning capability of the electrode by using laser-based dry etching and wet chemical etching methods. The gas blocking properties of the plastic substrate were analyzed by using ASTM methodology. By additionally depositing a combination of hydrogenated amorphous silicon nitride and silicon oxide layers, the water vapor and oxygen transmission rates were reduced to less than 10^{-5} g/cm²-day-atm and about 10^{-7} cc/cm²-day-atm, respectively. In addition to the result discussed in this report, other important aspects of plastic substrates are also included in Table 3. Based on our experimental results, we can conclude that the flexible plastic substrates studied during this project have properties acceptable for OLED applications.

Item	Description	Requirements [9]
R_s	12~13 Ω/\square	< 50 Ω/\square
		preferably < 10 Ω/\square
Optical transmission	> 80 % with < 1% haze over visible range	> 85 % with < 0.5 % haze over visible range
Surface roughness	1.0~1.1 nm (RMS) over $1 \times 1 \mu\text{m}^2$	< 2.0 nm RMS
	1.4~2.2 nm (RMS) over $50 \times 50 \mu\text{m}^2$	
Patterning capability	Dry-etchable: layer-based method Wet-etchable: chemical process \rightarrow 3% H_2SO_4 :0.01% FeCl_3 (5:1)	$\text{HCl}:\text{HNO}_3:\text{HF}:\text{H}_2\text{O}$ (5:1:1:3) ITO etching, no attack on substrate
Chemical resistance	γ -Butyrolacetone, NMP, MEK, IPA, 10% NaOH, acetone, IPA, PR, PR stripper, detergent	acetone, methanol, IPA, NMP, TEC, standard PR, PR stripper, H_2O_2 , NaOH, NH_4F
Heat resistance	Up to 145°C with 170°C glass transition temperature	No change of physical and optical properties at 200°C for one hour
Environmental stability	1000 hours @ 90°C	100 hours @ 50°C, 90% RH 250 hours @ 100°C and -25°C
Thickness	100-188 μm	100 ~ 1100 μm
TR_0^*	1.56×10^{-5} cc/cm ² -day-atm	< 10^{-7} cc/cm ² -day-atm

	$\leq 1.5 \pm 1 \times 10^{-7}$ cc/cm ² -day-atm	
	(with a-SiN _x :H and a-SiO _x :H coating)	
	3.66×10^{-4} g/cm ² -day-atm	
TR _{wv} *	$< 10^{-5}$ g/cm ² -day-atm (below detection limit)	$< 10^{-6}$ g/cm ² -day-atm
	(with a-SiN _x :H and a-SiO _x :H coating)	

Table 3 Properties of the flexible plastic substrate are summarized.

2. Identification and characterization of organic polymers

In this project, two types of emissive and hole transport polymers have been used. The light emissive layer (LEL) polymers are a random co-polymer of poly (9,9'-dioctyl fluorene-2,7-diyl) and poly (benzothiadiazole 2,5-diyl) (co-POF-BTD) and an alternating co-polymer of poly (9,9'-dihexyl fluorine-2,7-diyl) and poly (benzothiadiazole 2,5-diyl) (co-PHF-BTD). The hole transport layer (HTL) polymers are a random co-polymer of poly (9,9'-dioctyl fluorene-2,7-diyl) and poly (diphenyl-p-tolyl-amine-4,4'-diyl) (co-POF-DPTA) and poly (9-hexyl carbazole-3,6-diyl) (PC6). The co-POF-BTD, co-POF-DPTA, co-PHF-BTD and PC6 were synthesized in our laboratory under a nitrogen atmosphere using standard Schlenk line techniques. The chemical structures of all polymers used in this work are shown in Figure 7. For the emissive polymers, co-POF-BTD and co-PHF-BTD, poly (benzothiadiazole) group (A-group) was added to poly (fluorene) group (B-group) to increase the polymer electron affinity, hence to improve the electron injection into the OLEDs. The A-group is playing the role of electron-withdrawing group in the conjugated polymers. In our co-polymers, the ratios of A-group to B-group were 10:1 and 1:1 for POF-BTD and PHF-BTD, respectively. The absorbance, photoluminescence, and electroluminescence (EL) spectral of emissive polymers are shown in Figure 8. The absorbance and PL spectra were obtained for single layer thin film deposited on quartz substrates. The EL spectra were measured for ITO/HTL/LEL/Al structure. The peak values of absorbance, PL, and EL of co-POF-BTD/co-PHF-BTD are 360/459 nm, 530/570 nm, and 547/570 nm, respectively. From the Figure 8, poly (fluorene) based LEL polymers clearly show the Stokes shift between absorbance and PL/EL spectra.

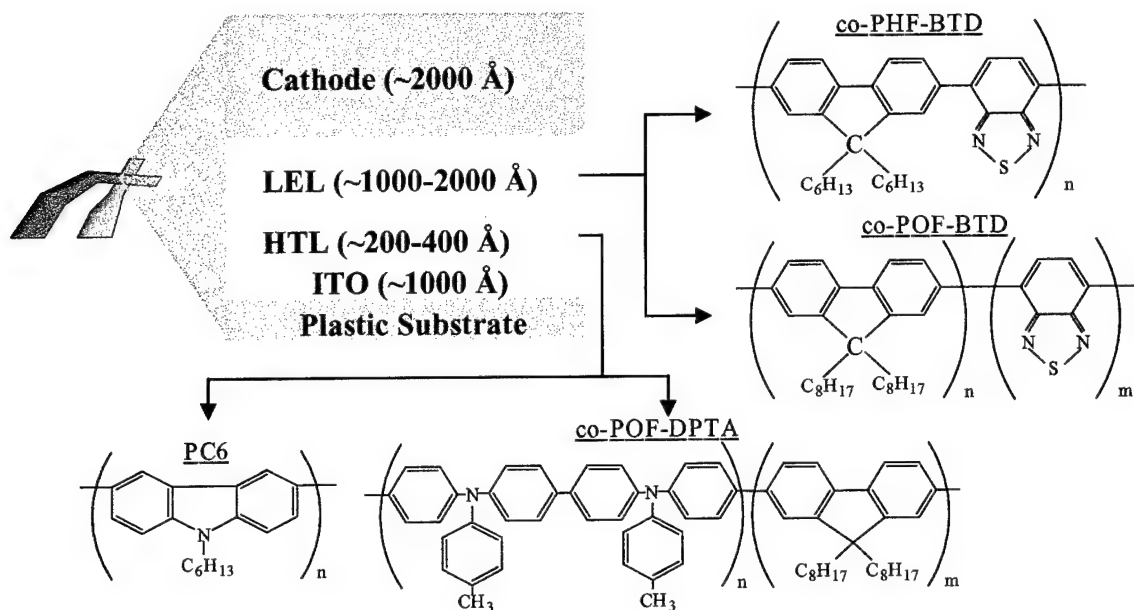


Figure 7. The OPLED structure (HTL: hole transport layer, LEL: light emissive layer) used in this work is shown. The chemical structures of emissive and hole transport polymers are also given.

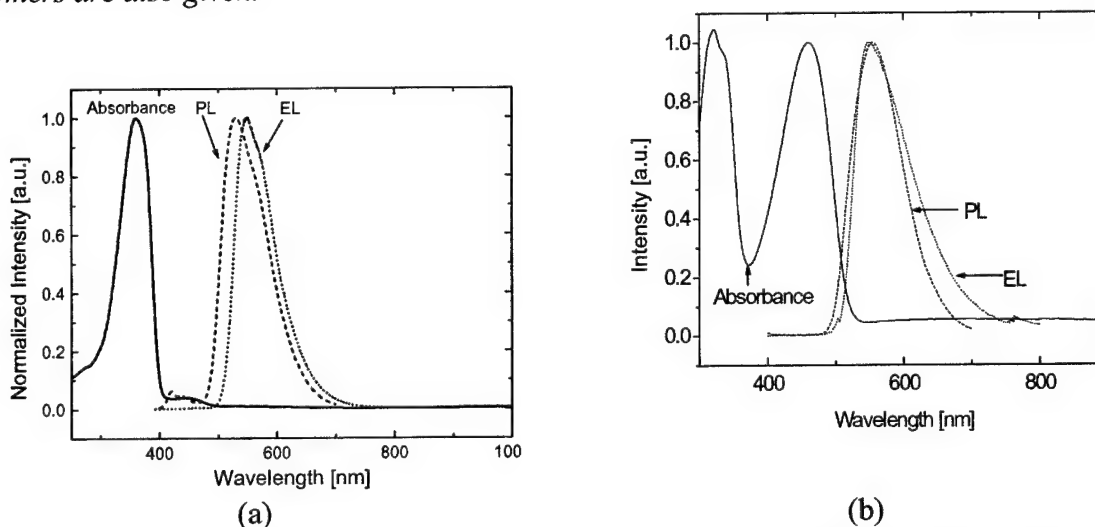


Figure 8. Absorbance, photoluminescence (PL), and electroluminescence (EL) spectra of emissive polymers are shown: (a) co-POF-BTD and (b) co-PHF-BTD.

3. Device optimization and energy band diagram construction of the OPLEDs

In this project, double-layer organic polymer light-emitting devices (OPLEDs) have been studied, which consist of the ITO, HTL, LEL, and cathode metal as shown in Figure 7. The HTL and LEL layers have been consecutively spin-coated on the UV-ozone treated ITO layer under the clean room environment. Cathode metals have been deposited by e-beam or thermal evaporations. Aluminum (Al), calcium (Ca), and erbium (Er) have been used [30-32]. Thickness of each layer of HTL and poly (fluorene)-based LEL polymers is also included in Figure 7.

A combination of the cyclic voltammetry (CV) and absorption spectrum was used to extract transport (E_T) and optical (E_G) band gap values of all our polymers, leading to construction of the OPLEDs energy band diagram shown in Figure 9 [33, 34]. The E_T was

extracted from the difference between oxidation (ionization potential) and reduction (electron affinity) edges clearly defined in the CV spectra. These values are equivalent to the highest occupied molecular orbital (HOMO) and the lowest unoccupied molecular orbital (LUMO) of the organic polymers, respectively. The E_G was extracted from optical absorption spectra of organic polymers. The values of E_G and E_T are very different, and the physical origin of this is under present investigation.

As indicated in Figure 9, when Er or Ca is used in place of Al, the electron injection energy barrier between LEL LUMO and metal cathode work function is reduced by 0.9 or 1.3 eV, respectively. This barrier height reduction allows a better electron injection at lower applied voltage; that is, a same current level can be achieved at lower applied voltage. As shown in Figure 9(a), PC6 gives an intermediate HOMO level between LEL HOMO and ITO work function, leading to a better hole injection from ITO without loss of an effective hole blocking at the HTL/LEL interface. On the other hand, POF-DPTA has a higher HOMO level than ITO work function and LEL HOMO level as shown in Figure 9(b). In general, we can say that HTL enhanced the electro-optical performances of the OLEDs in comparison with the LEL-only single layer devices. This observation is in agreement with the observations made by other laboratories.

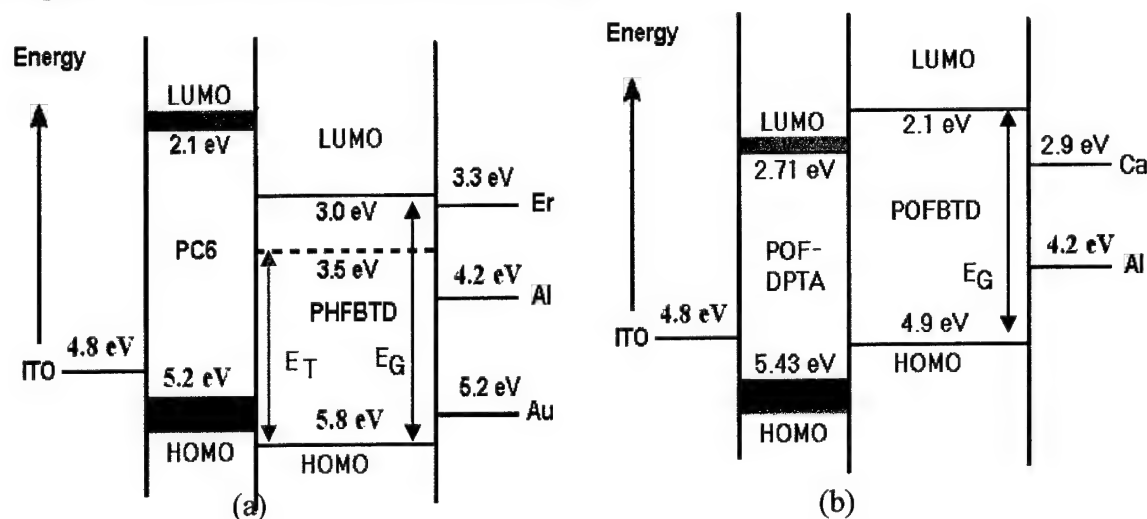


Figure 9. Energy band diagrams of the OLEDs used in this work are shown. (Dotted and solid LUMO levels are calculated by using E_T and E_G , respectively, with respect to HOMO level extracted from CV spectra).

We also inserted hole injection layer (HIL) between ITO and HTL to improve OLEDs opto-electronic performances. For this device structure, PEDOT/PSS, PC6, and Dow Chemical red/green light emissive polymers were used for, HIL, HTL, and LEL, respectively. The material characteristics of PEDOT/PSS and Dow Chemical red/green polymers have been published elsewhere [35, 36]. Energy band diagrams for OLEDs with this multi-layer structure have been reported elsewhere [36].

4. Electrical and optical properties of the OLEDs

We have fabricated the double-layer OLEDs based on poly (fluorene) using aluminum, calcium, and erbium as cathod metals. The band diagram for this structure is shown in Figure 9. Figure 10 shows the current density-voltage (J-V) characteristics for double-layer OLEDs based on PC6/co-PHF-BTD and POF-DPTA/co-POF-BTD with Al, Er, and Ca cathodes. The J-V characteristics have shifted to lower voltages and the OLEDs voltage for the same current density level, has been reduced when Er and Ca were used as cathodes. These metals have a lower work function than Al as shown in Figure 10. The electroluminescence (EL) spectra for different current densities are also included. The electrical and optical performances for all fabricated double-layer OLEDs are summarized in Table 4. From this table, we can conclude that low work function metals allow to achieve an increased maximum power efficiency (about 2 times increase has been measured), while the maximum quantum and emission efficiencies are about the same. Therefore, by lowering the injection barrier height for electrons, electron current increases at the same applied voltage, thus the device total current increases. However, since the light emission is strongly related to the balance between holes and electrons in the device, the increased electron current seems not to have a major effect on OLED external quantum and emission efficiencies, only on power efficiency by reducing the consumed electrical power for a given optical output power.

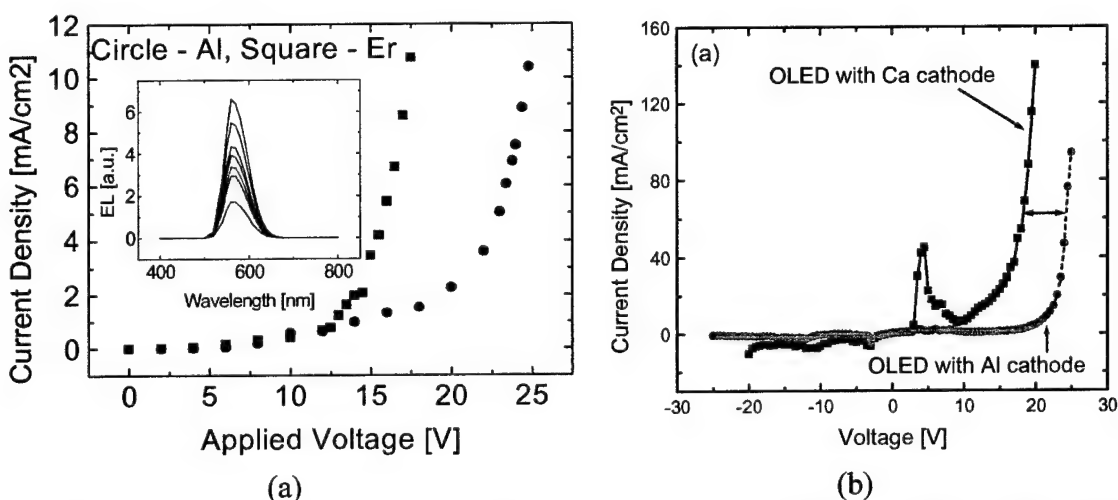


Figure 10. An example of electrical and optical performance of the OLEDs is shown. J-V characteristics for devices with Al and Er cathodes are shown. EL spectra are also included.

Anode	ITO			
HTL	PC6		co-POF-DPTA	
EL	co-PHF-BTD		co-POF-BTD	
Cathode	Al	Er/Au	Al	Ca/Al
EL peak (nm)	570	590	570	547
EQE _{max} (%)	1.2	1.3	14.8	16.7
EE _{max} (cd/A)	1.8	1.7	56.2	66.1
PE _{max} (lm/W)	0.23	0.36	8.97	17.2
J _{max} (mA/cm ²)	13.6	14	0.64	20

Table 4. Electro-optical data for fabricated OLEDs (EQE_{max} : maximum external quantum efficiency, EE_{max} : maximum emission efficiency, PE_{max} : maximum power efficiency, and J_{max} : current density where maximum efficiencies are obtained) [30-32].

We also investigated the effect of the HIL/HTL bi-layer structure and different cathode metalization such as electron-beam and thermal evaporations, on red OLED performances. Figure 11 shows that better device performances are obtained for the devices with HIL/HTL bi-layer, in comparison with HIL only devices. The staircase-like HOMO level increase has reduced effective hole injection energy barrier between anode and LEL. This reduction enhanced the device efficiencies. In addition to the device structure, the device performances are also affected by cathode metallization methods. We have demonstrated that thermal evaporation of aluminum gave less damage and metal

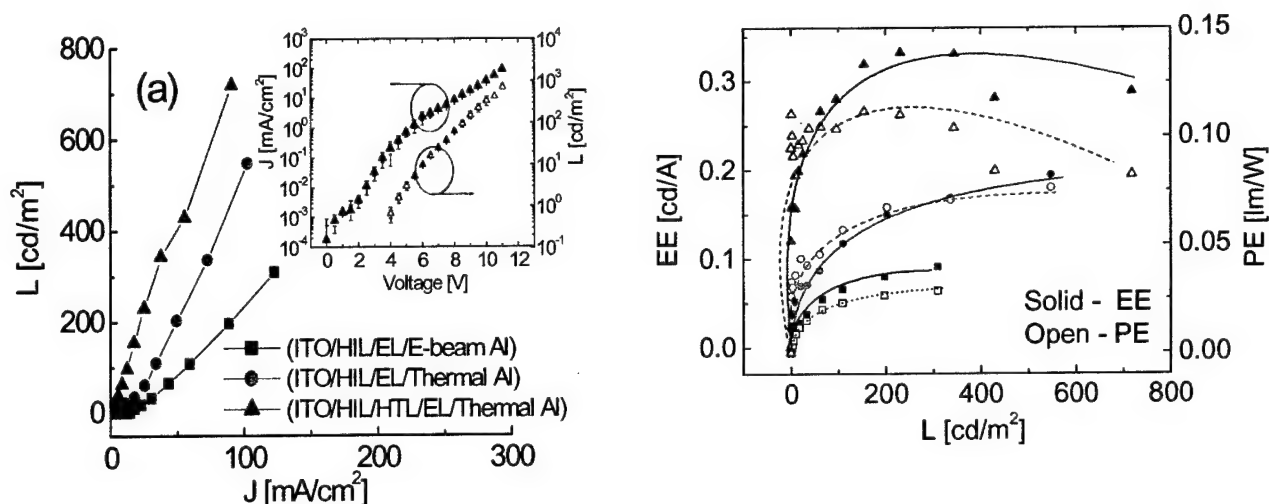


Figure 11. J-L and EE/PE-L characteristics of the red OLEDs on plastic substrates. The effects of HIL/HTL bi-layer and electron-bema/thermal metalization on device performances are shown.

migration between LEL and cathode in comparison with the electron-beam evaporation method. Thus OLEDs made with thermally evaporated cathode showed the best device performances [36].

5. Development of the hydrogenated amorphous silicon thin-film transistor active-matrix arrays for AM-OLEDs

As organic polymer device technology has matured, there are tremendous interests in OLEDs based plastic flat panel displays. During this project we initiated the development of the hydrogenated amorphous silicon thin-film transistor (a-Si:H TFT) active-matrix arrays for AM-OLEDs on plastic substrates.

We have developed two types of pixel electrode circuits – three [37] and four [38, 39, 40] a-Si:H TFT configurations, where voltage and current signals are used as data

signals, respectively. For both cases, appropriate control signals and circuit configurations are included, which automatically compensate for the long-term-operation threshold voltage shifts of the OPLEDs and a-Si:H TFTs.

Our 3- a-Si:H TFT pixel electrode circuit has five components: C_{ST} is storage capacitor, T1 is switching TFT, T2 is active resistor (AR), T3 is constant current driver TFT, and OPLED is organic polymer light-emitting diode. The pixel is selected through switching transistor while the scan voltage (V_{SCAN}) is "high". The driver TFT is used to provide constant current to OPLED. The active resistor compensates the current drifts by driver a-Si:H TFT (T3) and OPLED characteristics shifts. The operation conditions of our pixel electrode circuit were visualized with load-line analysis, Figure 12. The I_D - V_{DS} curves shown in Figure 12(b) are measured a-Si:H TFT driver characteristics. The load-lines with ($V_{AR} + V_{OP-LED}$) and without (V_{OP-LED}) active resistor are calculated using HSPICE. The crossing point between I_D - V_{DS} and load-lines represent output current (I_{OUT}) of the pixel circuit. Our pixel electrode circuit operates in linear regime for the V_{DATA} larger than 5 V. Since the active resistor shares a high-voltage drop (V_{DD}) with the driving TFT and OLED, any reduction in I_{OUT} will be reflected by voltage increase at the node A ($V_A = V_{DD} - V_{AR}$ where V_{AR} is the voltage drop across active resistor), Figure 12 (b). As V_A increases, V_{DS} of T3 increases, resulting in I_{OUT} increase, Figure 12 (b). This represents partial compensation for initial I_{OUT} decrease.

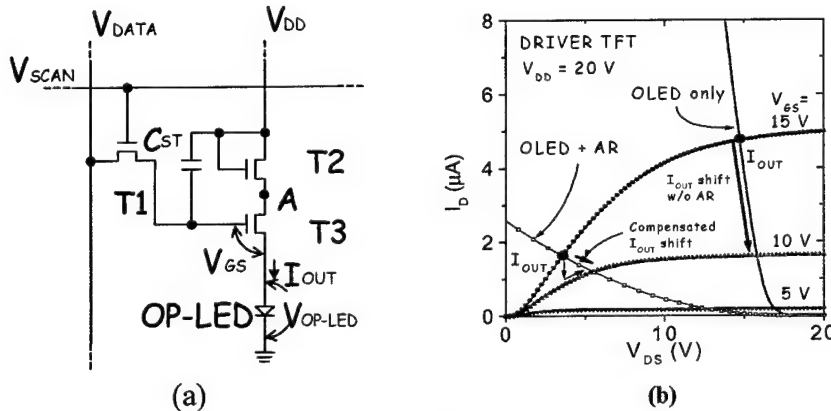


Figure 12. (a) Schematics of 3-a-Si:H TFT pixel electrode circuit for AM-OLED, and the (b) load-lines of 3- a-Si:H TFT pixel electrode circuit for $V_{DD}=20V$ are shown. The open symbol and solid line represent the load-line with ($V_{AR}+V_{OP-LED}$) and without (V_{OP-LED}) active resistor.

Figure 13 shows the schematic of 4-a-Si:H TFT pixel electrode circuits [38-41]. T1 and T2 serve as switches to adjust OPLED output current (I_{out}) to input data current (I_{data}) level when a pixel electrode is selected ($V_{select1}$ is high, $V_{select2}$ is low). T4 is another switching TFT that is turned on only when the pixel electrode is deselected ($V_{select1}$ is low, $V_{select2}$ is high). A common source line (V_{dd}) is used to supply I_{out} current when the pixel electrode is deselected. T3 operates as driving TFT connected to OPLED and C_{ST} is a storage capacitor. In our circuit, the threshold voltage shift of OPLEDs is compensated by making the driving TFT (T3) operate in saturation regime. The simulation results also

have shown that our pixel circuit well compensates the TFT threshold voltage shift [41]. To fabricate the active-matrix arrays, first, chromium (Cr) gate electrode was defined on corning 1737 glass substrates. After n^+ a-Si:H / a-Si:H / a-SiNx:H layer was deposited by PECVD, the active island is defined by reactive ion etching (RIE). Then, gate via was formed by wet-etching and molybdenum (Mo) source and drain electrodes are defined. To provide a flat ITO surface for organic polymer layer deposition, a BCB planarization layer was inserted before ITO pixel electrode is deposited. The thickness of each layer is 2000 Å for Cr, 3000 Å for a-SiNx:H, 1000 Å for a-Si:H, 300 Å for n^+ a-Si:H, 2000 Å for Mo, 3000 Å for BCB, and 1000 Å for ITO. The size (W/L) of each transistor is 15/6, 55/6, 58/6, and 70/6 for T1, T2, T3, and T4, respectively.

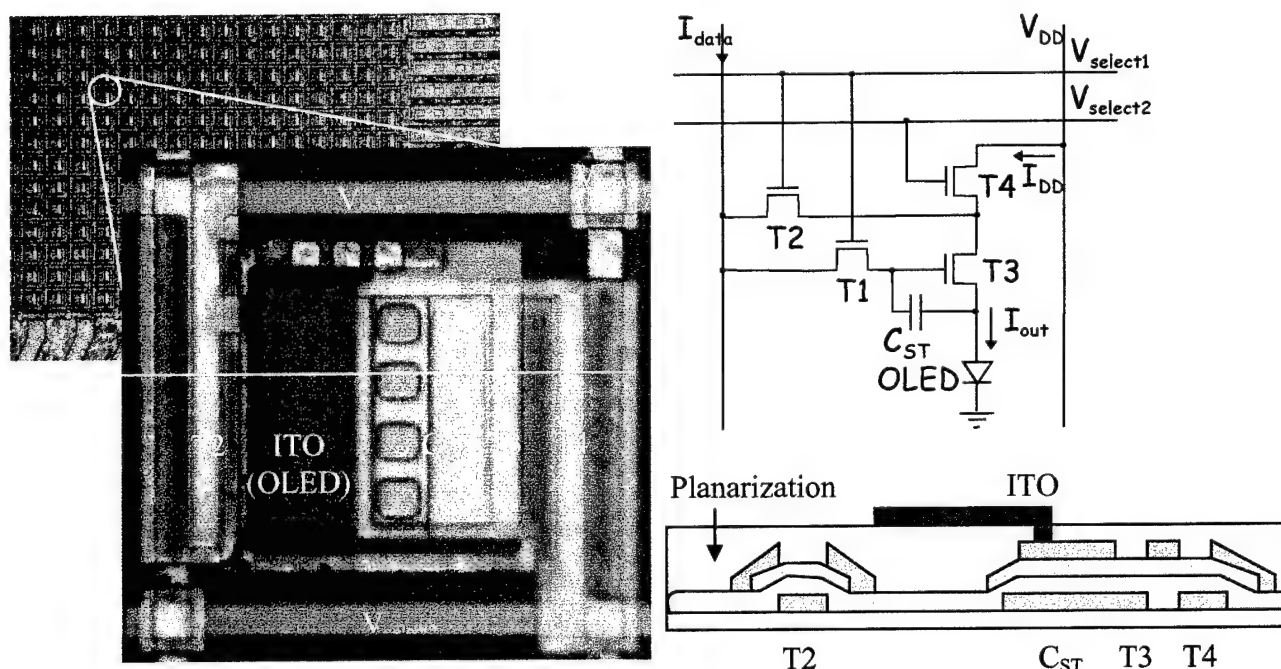


Figure 13. Schematics and top view of fabricated of 4-a-Si:H TFT pixel electrode circuit for AM-OLED.

Accomplishments

Task 2

1. *Degradation mechanism study*

Today, the limited lifetime of the OLEDs on flexible plastic substrates is a critical barrier for commercial applications. The lifetime of the devices is defined as the time when the light output falls to 50% of the initial brightness at the same driving current level. This parametric device failure can be explained by several possible mechanisms, such as dark spots formation, polymer photo-oxidation, polymer/cathode interface degradation, and ITO surface degradation.

a) Dark spots formation and delamination at polymer/cathode interface: [42-45]

Non-emission areas, so called “dark spots”, are observed during OLED operation. It is well known that this phenomenon is related to water vapor and oxygen penetration into the polymer/cathode interface through the pinholes formed during the cathode metal evaporation. If the penetrated gas accumulates around specific pinholes at the interface, the polymer can be delaminated from the cathode. Then, no light emission is observed in the delaminated area since the current flow through the interface will be interrupted. Once dark spots are formed, generally, the size increases with the device operation time. Thus, the light-emitting area will be reduced, resulting in the device brightness reduction at the same current level.

b) Polymer photo-oxidation (bleaching):

Photo-oxidation of the polymer happens when the polymer is exposed to UV or short wavelength lights under ambient conditions, which can result in interruption of the conjugation of organic polymer by converting the vinyl-bond into the carbonyl bond. The formed carbonyl bond can act as quenching sites for light emission, or the conjugation interruption can hamper the carrier transport and recombination. Both can cause the decrease of polymer photoluminescence efficiency [46]. Oxygen permeation into the polymer layer is the major source for photo-oxidation of the polymer [47].

c) ITO instability:

ITO surface usually needs additional treatment, such as oxygen plasma or UV-ozone curing, to increase oxygen content at the surface. High oxygen content at the ITO surface is considered favorable for hole injection into the organic HTL layer since it is well known that the ITO work function increases as the oxygen content increases. However, the gradual decrease of oxygen at the ITO surface has been observed during heating or even storing. The release of oxygen from ITO surface is considered to be a source of polymer degradation (oxidation that can be accelerated by OLED light emission).

2. *Development of packaging method*

We have developed a suitable packaging method, named as an indirect packaging, as shown in Figure 14. The same type of plastic film as the bottom substrates is used for the top cover plate. After the OPLEDs are fabricated on the plastic substrates, UV-curable adhesive is applied around the device area. Then, the top plastic cover is placed and appropriate amount of force is applied on it to remove any possible void between the top plastic plate and glue lines. Finally, the adhesive is cured using 5000-EC Ultraviolet light source with 365 nm wavelength and 103 mW/cm² intensity. During the UV-curing process, the OPLED area is shielded with a metal cover to avoid any exposure of device area to UV-light. The curing time has been optimized during this work. In our case, 17-sec was sufficient to complete the curing process without any softening of plastic films. However, the glue-based indirect packaging method still has water vapor or oxygen permeation path through the side glue walls. Since the UV-curing adhesive used in this work is based on the epoxy bonding, which has the water vapor permeability of $10^{-8} - 10^{-10}$ g/cm-sec-atm, the amount of possible water vapor diffusion through the glue cannot be ignored in comparison with the plastic substrates (measured water vapor permeability of about $10^{-10} - 10^{-12}$ g/cm-sec-atm).

To address this issue, we developed a direct packaging method based on organic/inorganic multi-layer coating right on the fabricated devices, which are under present investigation. We expect this method can further reduce the water vapor or oxygen permeation into the device area. The results of this investigation will be reported in the near future.

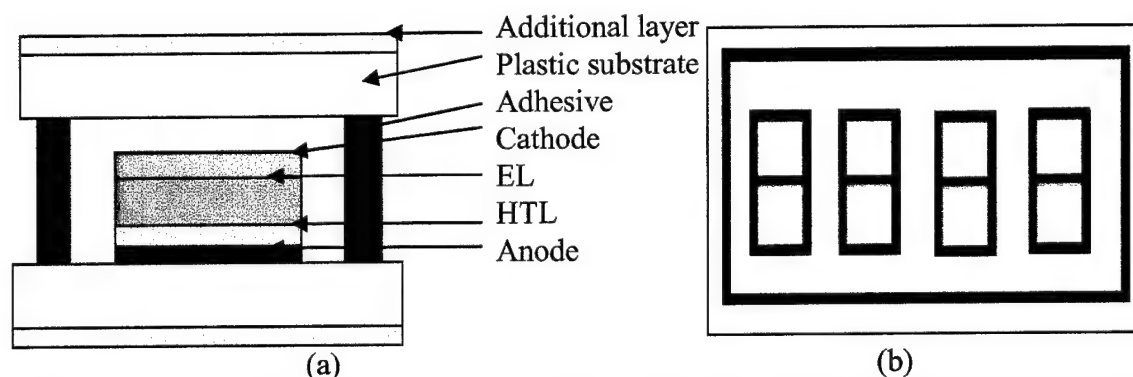


Figure 14. Schematic diagrams of the indirect OPLEDs packaging method used in this work. (a) Cross-section and (b) Top-view are shown.

3. Identification of the best glue

We used Light Weld 489 high flex UV adhesive, specially developed for this project. This UV-curable adhesive has a thermal expansion coefficient of 16.6×10^{-6} in/°C and a modulus of elasticity of 475 psi. Since the adhesive is dispensed through an appropriate syringe, the tip size has been optimized to obtain the appropriate glue width with a desirable adhesion. The best tip size for our case has an outer-diameter of 0.5 mm, which produces the glue lines with about 3mm width. We also tested the adhesion strength of this adhesive after two plastic substrates were attached to each other. Before the two films were separated, the forced edges of the films were broken without any damage on

the bonded area. This test indirectly shows that this type of glue has acceptable adhesion properties to our plastic substrates with desirable bonding strength.

4. Design of device lifetime testing cell

We have designed an OPLED lifetime testing cell that can allow controlling the temperature and gas flows, such as oxygen, nitrogen, and water vapor, as shown in Figure 15. The temperature can be changed from 20 to 80°C by circulating hot liquid. A vacuum pump and a barometer are connected to the cell to control the cell pressure and atmosphere. Additional thermocouple, humidity and/or oxygen sensor are implemented for more accurate measurements. With this testing cell, we can test the OPLEDs lifetime performance under different ambient condition: pure oxygen, pure nitrogen, high humidity, different gas mixtures, etc. at different temperatures.

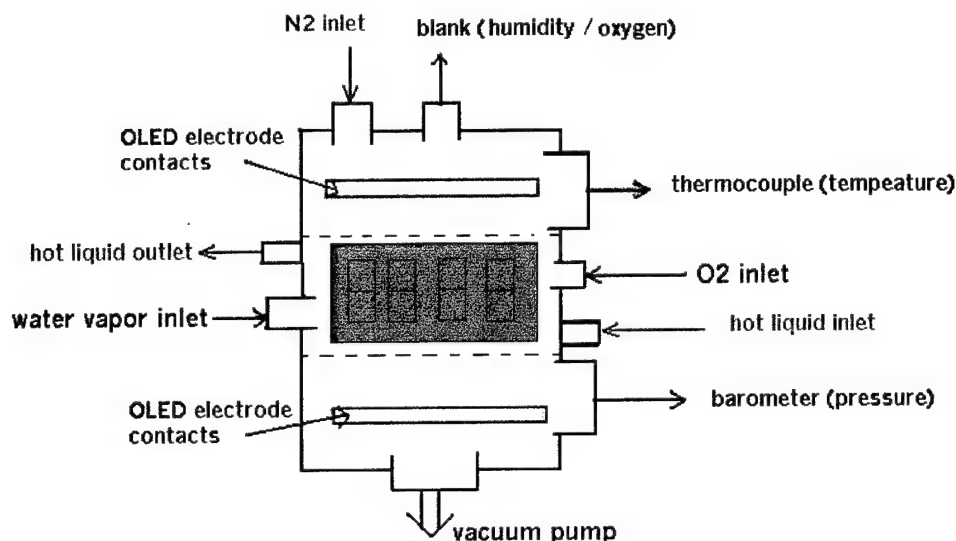


Figure 15. Schematic of the OPLED testing cell developed during this study.

5. Lifetime evaluation of unpackaged OPLEDs on plastic substrates

We have studied OPLEDs operating lifetime related to the initial brightness levels and the type of device driving signals. It is well known that alternative current (ac) driving can improve the device operation stability in Alq based OLEDs since the negative bias component can remove the accumulated or trapped charge in the devices [47]. We also found that by refreshing our OPLEDs with an appropriate negative bias during the continuous direct current (dc) operation, the device operation lifetime can be increased. Using this ac-like driving method, we also established the relationship between the device lifetime and the initial brightness for our unpackaged devices, which can be expressed as a first-order exponentially decaying function:

$$t_{50\%_drop} = A + B \times e^{\frac{-L_{initial}}{C}},$$

where A, B, and C are fitting constants and the operating lifetime ($t_{50\% \text{-drop}}$) is defined as the time corresponding to 50% loss of the initial device brightness (L_{initial}). Figure 16 shows an example of measured lifetime result for red OPLEDs on flexible plastic substrate without any packaging.

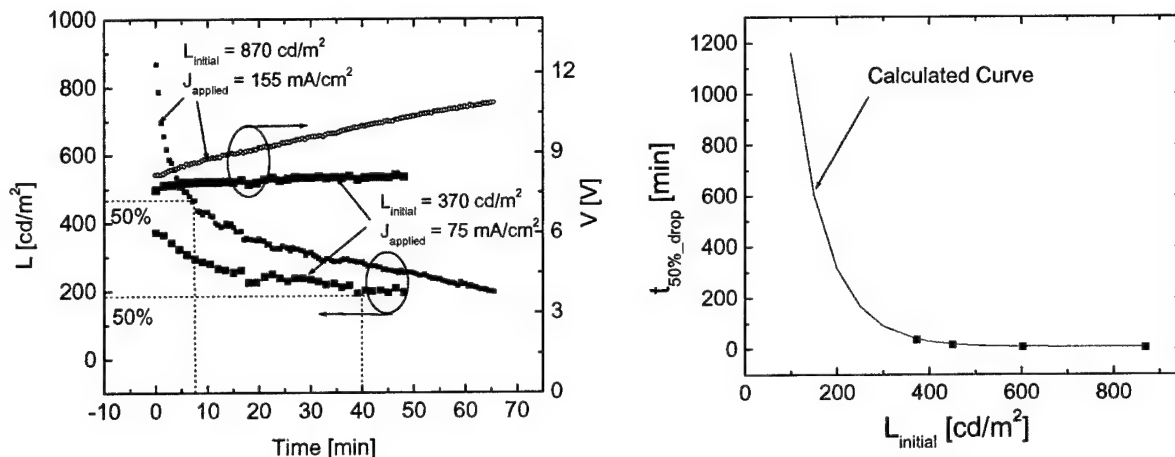


Figure 16. Examples of the OPLED brightness evaluation with the time for initial brightness level of 870 and 370 cd/m^2 are shown (a). The relationship between device lifetime ($t_{50\% \text{ drop}}$) and initial brightness (L_{initial}) of our unpackaged red OPLEDs is shown (b). The calculated curve is also included in this figure. All data were obtained at room temperature under the ambient conditions.

From this data we can conclude that as expected the PLED lifetime decreases with the increasing device brightness. In order to fabricate very bright stable devices it is critical to develop adequate PLED direct packaging methods.

U.S. Patents:

Patents, filed applications and disclosures under this contract include:

None.

Publications:

Publications written under this contract include (see attachment):

1. Y. He and J. Kanicki, "High Efficiency Organic Polymer Light-Emitting Heterostructure Devices on Flexible Plastic Substrates", *Proceedings of Euro Display '99*, 143 (1999).
2. Y. He, S. Gong, R. Hattori, and J. Kanicki, "Organic Light Emitting Devices on the Plastic Substrates", *Proceedings of SPIE 3669*, 330 (1999).
3. Y. He, R. Hattori, and J. Kanicki, "The Light Output Measurements of the Organic Light-Emitting Device", *Review of Scientific Instruments* **71**, 2104 (2000).
4. Y. He and J. Kanicki, "High-efficiency Organic Polymer Light-Emitting Heterostructure Devices on Flexible Plastic Substrates", *Appl. Phys. Lett.* **76**, 661 (2000).
5. Y. Hong, Z. Hong, M.D. Curtis, and J. Kanicki, "Organic Light Emitting Devices on Plastic Flexible Substrates: New Cathode and Light Emissive Materials", *Conference Record of the 20th International Display Research Conference*, 183 (2000).
6. Y. He, R. Hattori, and J. Kanicki, "Current-Source a-Si:H Thin-Film Transistor Circuit for Active-Matrix Organic Light-Emitting Displays", *IEEE Elec. Dev. Lett.* **21**, 590 (2000).
7. Y. He and J. Kanicki, "Polyfluorene Light Emitting Devices on Flexible Plastic Substrates", *Proceedings of SPIE 4105*, 143 (2001).
8. Y. Hong, Z. Hong, and J. Kanicki "Materials and Device Structures for High-Performance OLEDs", *Proceedings of SPIE 4105*, 356 (2001).
9. Y. He, R. Hattori, and J. Kanicki, "Four-Thin Film Transistor Pixel Electrode Circuits for Active-Matrix Organic Light-Emitting Displays", *Jpn. J. Appl. Phys.* **40**, 1199 (2001).
10. Y. Hong and J. Kanicki, "Organic Polymer Light-Emitting Devices on Flexible Plastic Substrates for AM-OLED", *Proc. of Asia Display / IDW'01*, p. 1443-1446 (2001).
11. J. Kanicki, J.-H. Kim, J.Y. Nahm, Y. He and R. Hattori, "Amorphous Silicon Thin-Film Transistors Based Active-Matrix Organic Light-Emitting Displays," *Proc. of Asia Display / IDW '01*, p. 315-318 (2001).
12. J. Kanicki, Y. Hong, S.-J. Lee and Z. He, "Organic Polymer Light-Emitting Devices (OLEDs) on Plastic Substrates for Active-Matrix Organic Polymer Light-Emitting Displays (AM-OLEDs), *Extended Abstracts of The 1st Int. Conf.*

on the Science and Technology of Emissive Displays and Lighting," p. 119-122 (2001).

13. Y. Hong, Z. He, S. Lee, and J. Kanicki, "Air-stable Organic Polymer Red Light-Emitting Devices on Flexible Plastic Substrates", *Proceedings of SPIE* **4464**, 329-335 (2002).
14. Y. Hong, Z. He, N.S. Lennhoff, D. Banach, G.C. Bazan, and J. Kanicki, "Transparent Flexible Plastic Substrate for Organic Light-Emitting Devices," *J. Electronics Materials* (submitted, 2002)

Presentations:

Presentations given at conferences under this contract include:

1. Euro Display '99, "High Efficiency Organic Polymer Light-Emitting Hetero-structure Devices on Flexible Plastic Substrates," Y. He and J. Kanicki.
2. SPIE's 44th Annual Meeting, The International Symposium on Optical Science and Technology, "Organic Light Emitting Devices on the Plastic Substrates," Y. He and J. Kanicki.
3. SPIE's 45th Annual Meeting, The International Symposium on Optical Science and Technology (7/30/00 – 8/4/00, San Diego, CA), "Polyfluorene Light Emitting Devices on Flexible Plastic Substrates," Y. He and J. Kanicki.
4. SPIE's 45th Annual Meeting, The International Symposium on Optical Science and Technology (7/30/00 – 8/4/00, San Diego, CA), "Materials and Device Structures for High-Performance OLEDs," Y. Hong, Z. Hong, and J. Kanicki.
5. The 20th International Display Research Conference (9/25/00 – 9/28/00, Palm Beach, FA), "Organic Light Emitting Devices on Plastic Flexible Substrates: New Cathode and Light Emissive Materials," Y. Hong, Z. Hong, M.D. Curtis, and J. Kanicki
6. The 6th International Conference on the Science and Technology of Display Phosphors (11/06/00 – 11/08/00, San Diego, CA), "Organic Polymer Light-emitting Devices and Displays on Plastic Flexible Substrates," J. Kanicki, Y. He, Y. Hong, Z. He, Z. Hong, and A. Badano.
7. SPIE's 46th Annual Meeting, The International Symposium on Optical Science and Technology (7/29/01 – 8/3/01, San Diego, CA), "Air-stable Organic Polymer Red Light-Emitting Devices on Flexible Plastic Substrates," Y. Hong, Z. He, S. Lee, and J. Kanicki
8. SPIE's 46th Annual Meeting, The International Symposium on Optical Science and Technology (7/29/01 – 8/3/01, San Diego, CA), "High Performance Organic Polymer Light-Emitting Devices (OPLEDs) with Two-stacked Double Layers on Flexible Plastic Substrates," Y. Hong and J. Kanicki
9. 3rd International Conference on Electroluminescence of Molecular materials and Related Phenomena (09/05/01 – 09/08/01, Los Angeles, CA), "Optimization of Organic Polymer Red Light-Emitting Devices on Flexible Plastic Substrates," Y. Hong, S. Lee, and J. Kanicki

10. Asia Display 2001 (10/16/01 – 10/19/01, Nagoya, Japan), “Organic Polymer Light-Emitting Devices on Flexible Plastic Substrates for AM-OPLED,” Y. Hong and J. Kanicki
11. 2001 International Conference on the Science and Technology of Emissive Displays and Lighting (11/12/01 – 11/14/01, San Diego, CA), “Organic Polymer Light Emitting Devices on Plastic Substrates,” J. Kanicki, Y. Hong, Z. He, S. Lee, and A. Badano.

REFERENCES

1. G.E. Jabbour, S.E. Shaheen, M.M. Morrell, B. Kippelen, N.R. Armstrong, and N. Peyghambarian, *Opt. Photonics News* 10, 24 (1999).
2. J.W. Allen, *J. Lumin.* 60/61, 912 (1994).
3. N.D. Young, R.M. Bunn, R.W. Wilks, D.J. McCulloch, S.C. Deane, M.J. Edwards, G. Harkin, and A.D. ^{Pearson}, *J. SID* 5/3, 275 (1997).
4. M.J. Lee and C.P. Judge, *Solid State Electron.* 44, 1431 (2000).
5. Y. He and J. Kanicki, *Appl. Phys. Lett.* 76, 661 (1998).
6. Y. Hong, Z. He, S. Lee, and J. Kanicki, *Proceedings of The International Society for Optical Engineering* 4464, 329 (2002).
7. J. Zhao, S. Xie, S. Han, Z. Yang, L. Ye, and T. Yang, *Phys. Status Solidi A* 184, 233 (2001).
8. M.S. Weaver, S.Y. Mao, J.K. Mahon, L.A. Michalski, T. Ngo, K. Rajan, M.A. Rothman, J.A. Silvernail, J.J. Brown, W.E. Bennett, C. Bonham, P.E. Burrows, G.L. Graff, M.E. Gross, M. Hall, P.M. Martin, and E. Mast, *Proceedings of 44th Annual Technical Conference – Society of Vacuum Coaters*, 155 (2001).
9. J.K. Mahon, J.J. Brown, T.X. Zhou, P.E. Burrows, and S.R. Forrest, *Proceedings of 42nd Annual Technical Conference – Society of Vacuum Coaters*, 456 (1999).
10. P.E. Burrows, G.L. Graff, M.E. Gross, P.M. Martin, M. Hall, E. Mast, C. Bonham, W. Bennett, L. Michalski, M. Weaver, J.J. Brown, D. Fogarty, and L.S. Sapochak, *Proceedings of The International Society for Optical Engineering* 4105, 75 (2000).
11. A. Berntsen, Y. Croonen, C. Liedenbaum, H. Schoo, R-J, Visser, J. Vleggaar, and P. van de Weijer, *Opt. Mater.* 9, 125 (1998).
12. H.C. Choi, Y.Z. Chu, L.S. Heath, and W.K. Smyth, US Patent 6,379,509.

13. P.Y.Z. Chu, H.C. Choi, L.S. Heath, C.S. Ko, J. Mack, P. Nagarka, J. Richard, W. Smyth, and J. Wang, *Society for Information Display International Symposium, Digest of Technical Papers* 29, 1099 (1998)
14. N.S. Lennhoff and J. Ram, US Patent Publication 20020182386.
15. Y. Aoshima, M. Miyazaki, K. Sato, Y. kao, S. Takaki, and K. Adachi, *Jpn. J. Appl. Phys.* 40, 4166 (2001).
16. M.G. Mason, L.S. Hung, C.W. Tang, S.T. Lee, K.W. Wong, and M. Wang, *J. Appl. Phys.* 86, 1688 (1999).
17. C.C. Wu, C.I. Wu, J.C. Sturm, and A. Kahn, *Appl. Phys. Lett.* 70, 1348 (1997).
18. T. Osada, Th. Kugler, P. Broms, and W.R. Salaneck, *Synth. Met.* 96, 77 (1998).
19. J.S. Kim, M. Granstrom, R.H. Friend, N. Johansson, W.R. Salaneck, R. Kaik, W.J. Feast, and F. Cacialli, *J. Appl. Phys.* 84, 6859 (1998).
20. W.R. Runyan, *Semiconductor Measurements and Instrumentation*, (New York: McGraw-Hill, 1975).
21. M.A. Logan, *J. Bell System Tech.* 46, 2277 (1967).
22. J-H. Lan and J. Kanicki, *J. Electron. Mater.* 25, 1806 (1996).
23. W. Cunningham, K. Mathieson, F.A. McEwan, A. Blue, R. McGeachy, J.A. McLeod, C. Morris-Ellis, V. O'Shea, K.M. Smith, A. Litke, and M. Rahman, *J. Phys. D Appl. Phys.* 34, 2804 (2001).
24. H. Hosono, M. Kurita, and H. Kawazoe, *Jpn. J. Appl. Phys.* 37, L1119 (1998).
25. H-Y Tsai, H. Yang, C-T Pan, and M-C Chou, *Proceedings of The International Society for Optical Engineering* 4230, 156 (2000).

26. Standard Test Method for Oxygen Gas Transmission Rate Through Plastic Film and Sheeting Using a Coulometric Sensor, ASTM, West Conshohocked, PA, 1995, D3985-95.
27. Standard Test Method for Water Vapor Transmission Rate Through Plastic Film and Sheeting Using a Modulated Infrared Sensor, ASTM, West Conshohocked, PA, 1995, F1249-90.
28. P.E. Burrows, G.L. Graff, M.E. Gross, P.M. Martin, M.K. Shi, M. Hall, E. Mast, C. Bonham, W. Bennett, and M.B. Sullivan, *Displays* 22, 65 (2001).
29. G. Nisato, P.C.P. Bouten, P.J. Slikkerveer, W.D. Bennett, G.L. Graff, N. Rutherford, and L. Wiese, *Proceedings of Asia Display/IDW '01*, 1435 (2001).
30. Y. He and J. Kanicki, *Appl. Phys. Lett.*, 76, 661 (2000).
31. Y. He and J. Kanicki, *Proc. of SPIE*, 4105, 143 (2001).
32. Y. Hong, Z. Hong, M.D. Curtis and J. Kanicki, "OLED Based Display for Automotive Applications," *Asia Display '98*, 1095 (1998).
33. Y. He, S. Gong, R. Hattori, and J. Kanicki, "OLED Based Display for Automotive Applications", *Asia Display '98*, 1095 (1998).
34. Y. Hong, Z. Hong, and J. Kanicki, "Materials and Device Structures for High Performance Poly OLEDs on Flexible Plastic Substrates", *Proceedings of SPIE* **4105** 356 (2001).
35. M. Bernius, M. Inbasekaran, E. Woo, W. Wu, and L. Wujkowski, *Proceedings of SPIE* **3797**, 129 (1999).
36. Y. Hong and J. Kanicki, *Conference Record of the IDRC 2001* (in press).
37. J-H. Kim and J. Kanicki, *Proceedings of SPIE* **4319**, 306 (2001).
38. Y. He, R. Hattori, and J. Kanicki, *IEEE Elec. Dev. Lett.* **21**, 590 (2000).

39. Y. He, R. Hattori, and J. Kanicki, *IEEE Trans. Elec. Dev.* **48**, 1322 (2001).
40. Y. He, R. Hattori, and J. Kanicki, *Jpn. J. Appl. Phys.* **40**, 1199 (2001).
41. J. Kanicki, J.-H. Kim, J.Y. Nahm and R. Hattori, "Amorphous Silicon Thin-Film Transistors Based Active-Matrix Organic Light-Emitting Displays" *Proc. of Asia Display / IDW '01*, p. 315-318 (2001).
42. J.R. Sheats and D.B. Roitman, *Synthetic Metals* **95** 79 (1995).
43. A. Berntsen, Y. Crooner, C. Liedenbaum, H. Schoo, R.J. Visser, J. Vleggaee, and P. van de Weijer, *Optical materials* **9** 125 (1998).
44. J. Mc Elvain, H. Antoniadis, M.R. Hueschen, J.N. Miller, D.M. Roitman, J.R. Sheats, and R.L. Moon, *J. Appl. Phys.* **80** 6002 (1996).
45. Y. He, J.K. Politis, H. Cheng, M.D. Curtis and J. Kanicki, *IEEE Trans. Elec. Dev.*, **44** 1282 (1997).
46. G. Gustafsson, Y.Cao, G.M.Treacy, F.Klaavetter, N.Colaneri and A.J.Heeger, *Nature* **357** 477(1992).
47. S.A. Van Slyke, C.H. Chen, and C.W. Tang, *Appl. Phys. Lett* **69**, 2160 (1996).

EuroDisplay '99

The 19th International
Display Research Conference

Proceedings

September 6-9, 1999
Berlin, Germany

General Chair
Ernst Lüder, Stuttgart University, Germany

organized by
ITG/VDE, SID, EUREL

VDE VERLAG GMBH • Berlin • Offenbach

High-Efficiency Organic Polymer Light-Emitting Heterostructure Devices on Flexible Plastic Substrates

Yi He and Jerzy Kanicki

Center for Integrated Microsystems, Department of Electrical Engineering and Computer Science
The University of Michigan, Ann Arbor, MI 48109, USA.

Abstract

We report a high-efficiency organic polymer light-emitting heterostructure device (OLED) fabricated on the thin, flexible plastic substrate. The device consists of a hole transporting (amine-fluorene) and an emissive (benzothiadiazole-fluorene) conjugated polymer layers. The heterostructure device shows a green light emission peaked at ~ 570 nm, a high luminance ($> 2,000$ to $13,000$ cd/m^2), a good emission efficiency (~ 56 to 66 cd/A), a high luminance (8.96 to 18.3 lm/W) and external quantum efficiencies (~ 14.8 to 16.2%). This OLED on plastic substrate has the highest external quantum efficiencies ever reported in the open literature.

1 Introduction

There is a long sought desire to use flexible plastic substrates in many flat panel applications because of their distinct advantages over glass substrates. Unlike glass, the plastic is usually more robust, compact, lighter and cost effective. The use of the plastic substrates will also enable new product concepts such as curved displays, smart cards, and all plastic electronic devices. While it is a very promising new technology, the plastic substrate, however, is limited by its low processing temperature, heat induced shrinkage, oxygen and moisture permeability, birefringence, chemical resistance, solvent durability, low transparency, and large surface roughness. The low thermal durability of the plastic substrate prevents, for example, a high temperature ($\geq 200^\circ\text{C}$) post-deposition annealing of the transparent conducting oxide (TCO), which is typically used in the organic light-emitting device (OLED) as transparent electrode. As a result, the TCO usually has a low transparency, a low conductivity, and a poor adhesion in comparison with its counterpart on the glass substrate.

In this paper we describe the opto-electrical characteristics of a high-efficiency bi-layer organic polymer light-emitting device with Al (and Ca) cathode fabricated on the ITO coated thin, flexible plastic substrate.

2 Experimental

The bi-layer OLED structure, shown in Fig. 1, consists of a hole transporting (HTL, ~ 170 Å) and an emissive (EL, ~ 2000 Å) conducting polymer layers

sequentially deposited on the plastic substrate by the spin-coating technique. The chemical structures, the absorption and photoluminescence spectra of these two polymers are published elsewhere [1]. The schematic energy band diagram of this structure and the cross-section of the flexible plastic substrate are shown in Fig. 1. The lowest unoccupied molecular

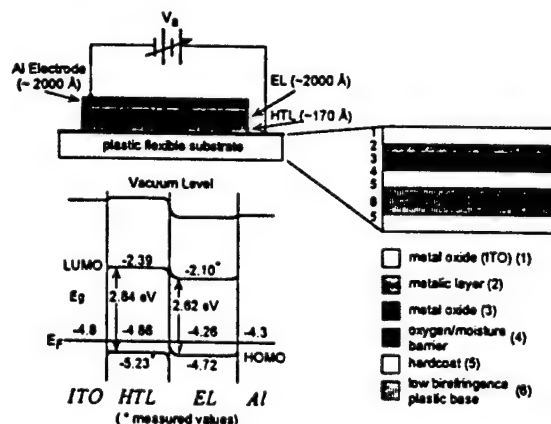


Fig. 1 The OLED bi-layer structure, the schematic energy band diagram in equilibrium, and the cross-section of the plastic substrate.

orbit (LUMO) and the highest occupied molecular orbit (HOMO) levels for both polymers are derived from their cyclic voltammograms and absorption spectra [2]. Fig. 2 shows an example of the hole-transporting (HTL) polymer cyclic voltammogram. In this specific case, the HOMO energy level of HTL is equal to $-4.8 - \Delta E$ (assuming that the energy level of Fc/Fc^+ is -4.8V [3]), where the energy difference, $\Delta E = e[(P1+P2)/2 - (F1+F2)/2]$. Knowing the polymer optical bandgap (E_g), the LUMO energy level can then be calculated (Fig. 1). Similarly, the LUMO and

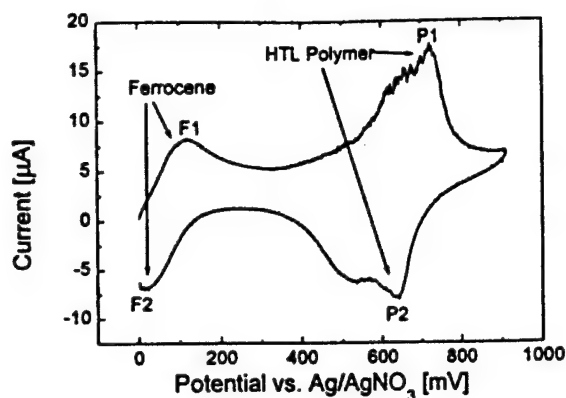


Fig. 2 Cyclic voltammogram of the hole-transporting polymer.

HOMO levels of the EL polymer can be derived using the same method. The optical bandgaps of both polymers were determined from the onset of the absorption peak that corresponds to the π - π^* transitions of π -electron states. The Fermi level positions ($E_F = E_A + \text{HOMO}$) for both polymers were derived from their conductivity activation energies calculated from the Arrhenius plots (Fig. 3) [$\sigma = \sigma_0 \exp(-E_A/kT)$].

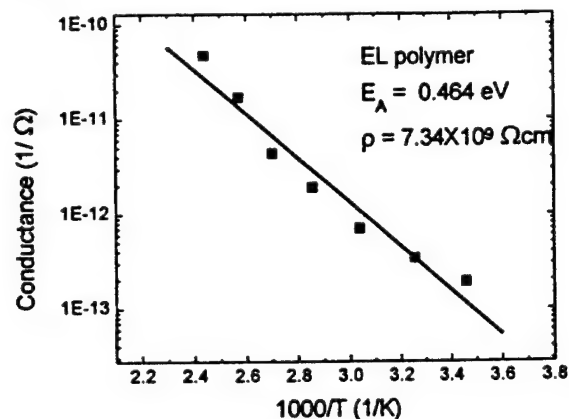


Fig. 3 The variation of the dark conductivity of the electroluminescence polymer with the temperature.

The substrate was repeatedly cleaned in the ultrasonic baths of de-ionized water and isopropanol before use. After the pre-deposition cleaning, the substrate was exposed to UV-ozone atmosphere before the spin coating of the polymer layers. Aluminum (or Ca) top cathode electrode was evaporated in a vacuum chamber at the base pressure $\sim 10^{-6}$ torr through a shadow mask. The electroluminescence (EL) of the OLEDs was measured with a CCD spectral analyzer through optical fibers. The CCD spectral analyzer has been calibrated with a Labsphere USS-600 Uniform Source System (incorporating a calibrated lamp and a motorized variable attenuator). This calibration allows us to obtain the luminance wavelength distribution of the measured light-emitting object [4]. The angular

distribution of the Lambertian emission was assumed to correct the measured OLED luminance (cd/m^2) [5].

3 Results and Discussion

3.1 Plastic substrate

The ITO coated flexible plastic substrate $\sim 0.2\text{mm}$ thick has a sheet resistance of $\sim 25.7 \Omega/\square$, and the transmittance higher than 80% in the photon energy range from 470 to 750nm (Fig. 4). The maximum transmittance is $\sim 84.5\%$. The root-mean-square (RMS) of the ITO surface roughness, deduced from the atomic force microscopy (AFM) image, is $\sim 2.85 \text{ nm}$ over an area of $\sim 30 \times 30 \mu\text{m}^2$ (Fig. 4). This value is better than the values obtained for the annealed ($\sim 3.76 \text{ nm}$ over $\sim 5 \times 5 \mu\text{m}^2$) and un-annealed ($\sim 3.57 \text{ nm}$ over $\sim 5 \times 5 \mu\text{m}^2$) ITO surfaces on the glass substrates.

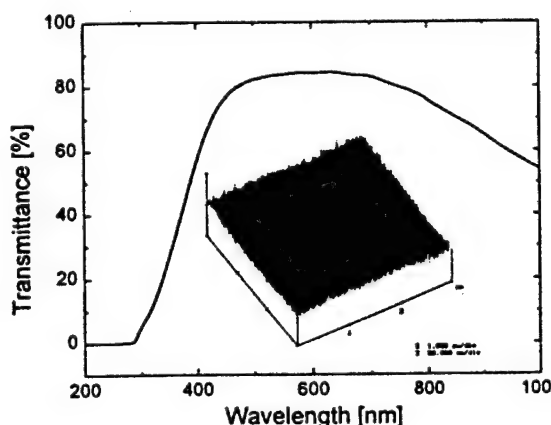


Fig. 4 The transmittance spectrum and the atomic force microscope image (inset) of the ITO coated plastic substrate.

A major disadvantage of the plastic substrate is its relatively high penetration level of the moisture (water) and oxygen. The presence of the moisture and oxygen is considered to be one of the major factors affecting the OLED electrical stability [5]. To fabricate OLED with a long lifetime, the diffusion of the oxygen and moisture through the substrate need to be minimised.

We have analysed the oxygen transmission rate through the plastic substrate at the room temperature with 50% relative humidity. The 100% dry nitrogen was introduced to both sides of the flat plastic at a flow rate of 10 cc/min. At equilibrium, the flow of nitrogen of the test gas side was switched to a flow of 100% oxygen. Then, the oxygen transfer of the flat film from the test gas side into the carrier gas side was measured with a coulometric detector until the equilibrium transmission rate is reached. Measurements of

several plastic samples indicate an oxygen permeability ranging from 0.0491 to 0.0510 cc/m²·day·atm. These values suggest that the oxygen penetration through the substrate is at the acceptable level.

3.2 OLED optical properties

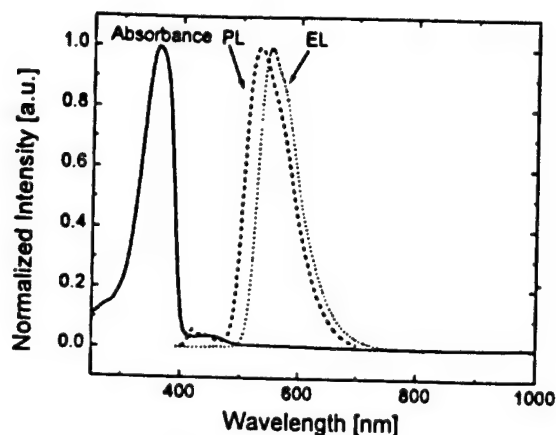


Fig. 5 The absorbance, photoluminescence, and electroluminescence spectra of the OLED structure.

Fig. 5 shows the normalised absorbance, photoluminescence, and electroluminescence spectra of the OLED structure. The EL and PL spectra are Stokes shifted with respect to the absorption spectrum. Also the PL and EL spectra are very similar, suggesting that the same emitting species are involved in both cases. We can speculate that under forward applied bias, the electrons and holes are injected (or transported) into the polymer LUMO and HOMO bands. These carriers, through electron-phonon lattice coupling, will relax to negatively and positively charged polarons that can move toward each other under the influence of the applied electrical field. Eventually they can recombine on a certain segment of polymer chain to form the singlet excitons. Through the resonance interactions, these singlet excitons can also form the excimers, which can emit light Stokes shifted with respect to the absorption spectrum. This description of the light-emitting mechanism is in good agreement with our experimental data. Fig. 6 illustrates the OLED luminance distribution spectra at different applied current densities. The integration of these curves over the wavelength (the area under the luminance distribution peak) yields the actual luminance of the OLED at different applied current densities. Fig. 7 shows the typical variation of the brightness with the applied current density. A near-linear relationship obtained between the luminance and the applied current density, with a gradual saturation at the current densities higher than 5 mA/cm² (lumi-

nance above 1200 cd/m²), can be described by the following equation:

$$L \cong AJ + BJ^2 \quad (2)$$

where L is the luminance (cd/m²), J is the applied current density (mA/cm²) and A (354±28) and B (-14±3) are constants. At the low and high current injection limits this equation can be approximated by $L \propto J$ and $L \propto J^2$, respectively. In this case (Al cathode), this equation suggests that the light-emission will saturate at ~2300 cd/m² with a current density of ~12.6 mA/cm². This saturation is due to the heat influence on light-emission that is usually observed at high current injection levels. The saturation value is much larger in the case of Ca cathode.

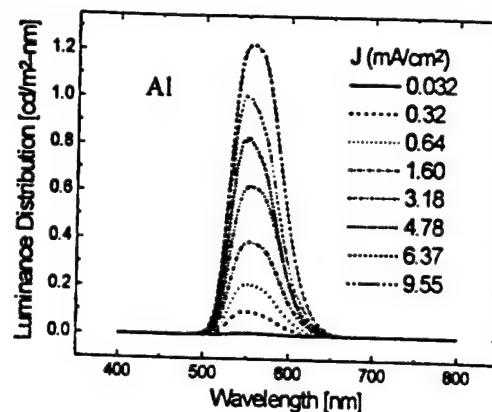


Fig. 6 The OLED luminance distribution spectra at different applied current densities.

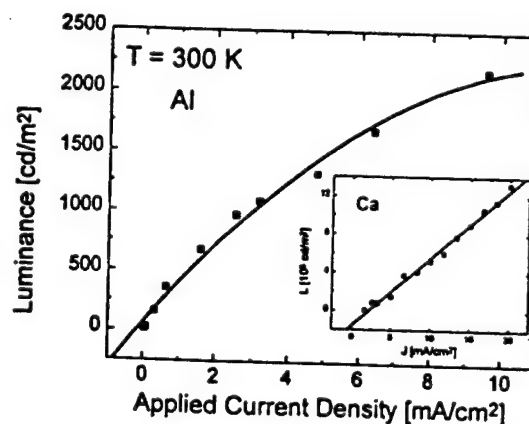


Fig. 7 The evolution of the OLED brightness as a function of the applied current density. The solid line represents the fit of eq. (2) to the experimental data. The inset shows the results obtained for OLED with Ca cathode.

Fig. 8 illustrates the spectral distribution of the OLED photon emission at different applied current densities. We define the OLED external quantum efficiency = number of photons emitted / electron supplied by the external circuit (applied current density).

The integration of the areas under the photon density distribution curves provides the number of photons emitted. Fig. 9 illustrates the evolution of the OLED emission efficiency and external quantum efficiency as functions of the applied current density. We can conclude from this figure that the OLED emission efficiency increases rapidly at first then drops down gradually and starts slowly to flat out at about 4.78 mA/cm² (27.7 cd/A) with the increasing applied current density (or luminance). The evolution of device external quantum efficiency also follows the same trend with the applied current density. The maximum emission efficiency, luminous efficiency, and external quantum efficiency for our OLED with Al cathode are 56.2 cd/A, 9.0 lm/W, and 14.8%, respectively. As shown in Figs. 7 and 9 insets, the OLED with Ca cathode exhibit brightness of ~13,000 cd/m², luminance efficiency of 18.3 lm/W and external quantum efficiency of ~16.2%. To our best knowledge, these values represent the highest optical performances ever reported in the open literature for the OLEDs fabricated on plastic substrate.

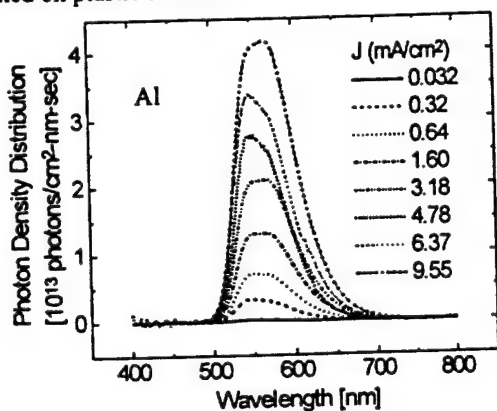


Fig. 8 The OLED photon density distribution induced by different applied current densities.

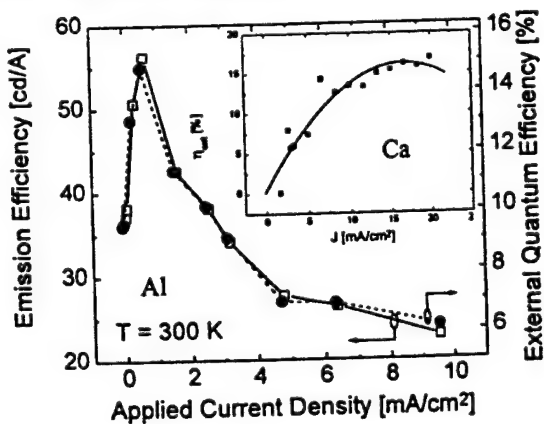


Fig. 9 The OLED emission efficiency and external quantum efficiency as functions of the applied current density. The inset shows the results obtained for the OLED with Ca cathode.

4 Conclusions

In conclusion, a high-performance heterostructure OLED has been fabricated on plastic flexible substrate. For this device the OLED peak efficiency and maximum external quantum efficiency, which are calculated from its luminance and photon emission distribution spectra, are the highest ever reported in the open literature. These values are acceptable for flat panel display and other applications.

5 Acknowledgement

We would like to thank Dr. R. Hattori, Dr. S. Gong and Mr. Y. Hong for their technical assistance during this project. All devices have been fabricated at Electronics Manufacturing Laboratory of the University of Michigan. The organic polymers used in this study have been provided by the Dow Chemical Company (Midland, MI). The plastic film conductor was provided by Polaroid Corporation. This research project was supported by the Center for Display Technology and Manufacturing at the University of Michigan, Ann Arbor, and the DARPA-ONR.

6 Literature

- [1] He, Y., Gong, S., Hattori, R., Kanicki, J., Appl. Phys. Lett., 74, 2265 (1999).
- [2] He, Y., Gong, S., Hattori, R., Kanicki, J., Proc. Of Asia Display'98, 1095 (1998).
- [3] Sheats, J., Antoniadis, H., Hueschen, M., Leonard, W., Miller, J., Moon, R., Roitman, D., Stocking, A., Science, 273, 884 (1996).
- [4] He, Y., Hattori, R., Kanicki, J., unpublished.
- [5] Greenham, Friend, R., Bradley, D., Adv. Mater., 6, 491 (1994).
- [6] Berntsen, A., Croonen, Y., Liedenbaum, C., Schoo, H., Visser, R-J., Vleggaar, J., Weijer, P., Optical Materials, 9, 125 (1998).

PROCEEDINGS OF SPIE REPRINT



SPIE—The International Society for Optical Engineering

Reprinted from

Smart Structures and Materials 1999

Electroactive Polymer Actuators and Devices

1-2 March 1999
Newport Beach, California



Volume 3669

©1999 by the Society of Photo-Optical Instrumentation Engineers
Box 10, Bellingham, Washington 98227 USA. Telephone 360/676-3290.

Organic polymer light-emitting devices on the plastic substrates

Yi He ^a, Shaoqin Gong ^b, and Jerzy Kanicki ^c

^aApplied Physics Program, University of Michigan, Ann Arbor, MI 48109

^bDept. of Materials Science & Engineering, University of Michigan, Ann Arbor, MI 48109

^cDept. of Electrical Engineering & Computer Science, University of Michigan, Ann Arbor, MI 48109

ABSTRACT

In this paper, we describe a high-performance organic polymer light-emitting device (OLED) fabricated on the ITO coated plastic substrates. The device, using air-stable Al as the cathode, has a bi-layer structure consisting of a hole transporting (amine-fluorene) and an emissive (benzothiadiazole-fluorene) conjugated polymer layers prepared by the spin-coating technique. Device shows a green light emission (~ 570 nm), and has a good brightness (> 400 cd/m²), acceptable emission efficiency (> 6.4 cd/A), and high external quantum efficiency (> 1.8 %).

Keywords: Organic light-emitting devices, plastic substrate, transparent conducting oxide, luminance, quantum efficiency

1. INTRODUCTION

The first demonstration of the electroluminescence from the conjugated polymer thin films in 1990¹ has ignited a worldwide attention of the polymeric light-emitting diodes (OLEDs). The inherent thin-film structure of the OLED makes it a particularly attractive candidate for the flat panel display (FPD) applications,² which is now dominated by liquid-crystal displays (LCDs). Since 1990, the performance of the single layer polymer based OLEDs has been improved dramatically. Both red and green emission devices with the external quantum efficiency higher than $\sim 1\%$ and luminous efficiency greater than ~ 2 lumen/watt have been reported,^{3,4} while the blue emission devices with the external quantum efficiency as high as 3% have also been presented.⁵ All these devices have been fabricated on the glass substrates.

On the other hand, the flexible plastic substrate has a distinct advantage over the glass substrate in display applications. Unlike glass, the plastic is usually more robust and compact, has lighter weight and is more cost effective. This is especially true for new portable display products, such as cellular phones, mobile phones, personal digital assistants, and laptop computers.⁶ The use of the plastic substrates will also enable new product concepts such as curved or flexible displays and all plastic electronic device.^{7,8} While it is a very promising new technology, the plastic substrate, however, is limited by its low processing temperature, heat induced shrinkage, gas permeability, birefringence, chemical resistance, water and solvent durability, transparency, etc. The low thermal durability of the plastic substrate prevents, for example, high temperature ($\geq 200^\circ\text{C}$) post-deposition annealing of the transparent conducting oxide (TCO), which is typically used in the organic light-emitting device as the transparent electrode. As a result, the TCO on the plastic substrate usually has a low transparency, a low conductivity and a poor TCO/organic layer adhesion in comparison with its counterpart on the glass substrate. This is one of the reasons why the OLED's performance on the plastic substrates usually is worse in comparison with the OLED fabricated on the glass substrate (e.g. the highest external quantum efficiency ever reported for the OLEDs on the plastic substrate is $\sim 1\%$ —about 4 times lower than the highest value reported for the OLEDs on the glass substrate.). Another disadvantage of the plastic substrate is its relatively high penetration level of the moisture and oxygen. The presence of the moisture and oxygen is considered to be one of the major factors affecting the OLED electrical stability.⁹ Various inorganic or organic materials are being deposited on the plastic substrate to reduce the moisture and oxygen diffusion. The compatibility of the plastic substrate with the various solvents used during the polymer spin-coating is another important issue to be considered for its application in the OLEDs.

In this paper we describe the fabrication and characteristics of a high performance bi-layer organic polymer light-emitting device (OLED) fabricated on the ITO coated plastic substrates. Compared with the highest external quantum efficiency value previously reported⁷ for OLEDs on the plastic substrate, the value for our device is nearly doubled.

* Correspondence: Email: heyi@engin.umich.edu; Telephone: 734 936 0972; Fax: 734 936 0347. All the authors belong to the Center for Integrated Microsystems at the University of Michigan, Ann Arbor.

2. EXPERIMENTAL

The plastic substrate used in this study was 1-mm thick polycarbonate. The substrate was repeatedly cleaned in the ultrasonic baths of de-ionized water and isopropanol before use. A layer of amorphous silicon nitride (a-SiNx:H) (~ 2000 Å) was then deposited on the plastic substrate in a plasma-enhanced chemical vapor deposition (PECVD) system. The a-SiNx:H layer serves as the moisture and oxygen barrier as well as the protection layer of the plastic substrate. After the deposition of a-SiNx:H layer, the substrate was transferred to a vacuum sputtering system (base pressure $< 10^{-7}$ mbar), where a layer of Indium Tin Oxide (ITO) (~ 1600 Å) was sputtered at the room temperature. This ITO layer was used as the transparent electrode of the OLED. The as-deposited ITO layer usually has a transparency higher than 80% throughout the visible range (400–800 nm) and a sheet resistance less than $100 \Omega/\square$. The ITO covered plastic substrate was cleaned again in the ultrasonic bath of isopropanol and exposed to the UV-ozone atmosphere for 15 minutes. Then, the hole transporting polymer (HTL, ~ 170 Å) and the emissive polymer (EL, ~ 2000 Å) layers were sequentially deposited on the plastic substrate by the spin-coating technique. Aluminum, which was thermally evaporated in a vacuum chamber at the base pressure $\sim 10^{-6}$ torr through a shadow mask, was used as the top cathode electrode. Although devices using air-stable cathode materials generally suffer high operating voltage and low efficiencies, Al offers significant advantages in the display applications over the reactive, air-unstable, low work function materials usually employed as the cathode electrodes in OLEDs to achieve a high electron injection level. Despite the efforts such as using another stable protection cover layer on the top of the cathode electrode or encapsulating the device in the inert gas atmosphere to minimize its oxidation pace, the low work function electrode may still act as a fast diffusing species, which could potentially affect the device stability.¹¹ The high work function materials, however, could be potentially beneficial to the development of the process integration and packaging steps needed for the display applications.

The electroluminescence (EL) of the OLEDs was measured by a CCD spectral analyzer through optical fibers. The CCD spectral analyzer has been calibrated by a Labsphere USS-600 Uniform Source System equipped with a calibration lamp and a motorized variable attenuator. During the EL measurement, the OLED and the optical fiber were placed at the different sides of a convex lens. Both the distance between the lens and the OLED and the distance between the lens and the optical fiber are 2 times the focal length of the lens. The actual luminance (cd/m^2) and radiant power of the OLEDs were corrected by assuming the angular distribution of the Lambertian emission.¹⁰ No corrections were made for the absorption of the lens and plastic substrate, refraction/reflection at the polymer-plastic-air interfaces, or other effects that could decrease the light emission intensity from the OLEDs. The current-voltage characteristics of the OLEDs were measured in a vacuumed metal box with shielded cables connecting the voltage source, current meter and the probes inside the measurement box. The absorption and the photoluminescence (PL) spectra were collected by a CARY UV-Visible spectrophotometer and a Shimadzu 4121, respectively. Films about 100nm and 1–2 μm thick have been used for absorption and PL measurements, respectively.

3. RESULTS AND DISCUSSIONS

Figure 1(a), (b) illustrate the absorbance, PL and EL spectra of the polymer A (amine-fluorene) and B (benzothiadiazole-fluorene), respectively. The inset figures show the chemical structures of both polymers. The benzothiadiazole has been added to the emissive polymer structure to provide the electron transport property, thus trying to balance the hole and electron injection into the emissive layer. The EL spectra were obtained from the Al/polymer/ITO/glass structure. The EL emission of the polymer B (~ 1400 Å) clearly shows a peak located at around 545 nm, which is consistent with its PL counterpart. The PL peak is Stokes shifted from the absorption peak corresponding to the π - π^* transitions. The photo excitation of an electron from the highest occupied molecular orbit (HOMO) to the lowest unoccupied molecular orbit (LUMO) generates a singlet excitation that ultimately will be responsible for the formation of excimers, which will emit light at a longer wavelength (the Stokes shift). The magnitude of the Stokes shift between the maximum (zero-phonon transition) of the excitation and emission spectra measures the extent of relaxation in the excited states. No electroluminescence has been observed from the Al/polymer A (~ 200 Å)/ITO/glass structure at a current density up to 7.0 mA/mm^2 . The absence of EL in the hole-transporting polymer is probably due to the low electron mobility and the existence of an excessive hole concentration in such a material. As a result, the lifetime of the injected electrons (minority carriers) from Al electrode is greatly reduced. Therefore, similarly to what happens in a p-type crystalline silicon, the majority of the injected holes from ITO contact will reach the Al electrode through band conduction without encountering a large density of electrons needed for the electron-hole recombination. In addition, most of the singlet excitons will be localized very close to the Al cathode electrode, where the non-radiative decay processes will more likely occur. The existence of the defect centers and other quenching sites near the Al/polymer interface will further enhance the non-radiative decay processes. As a result, only a very

small portion of the injected electrons/holes can successfully contribute to electroluminescence (electron-hole recombination rate is very low) and a very high current density might be needed to produce a visible EL emission in this structure.

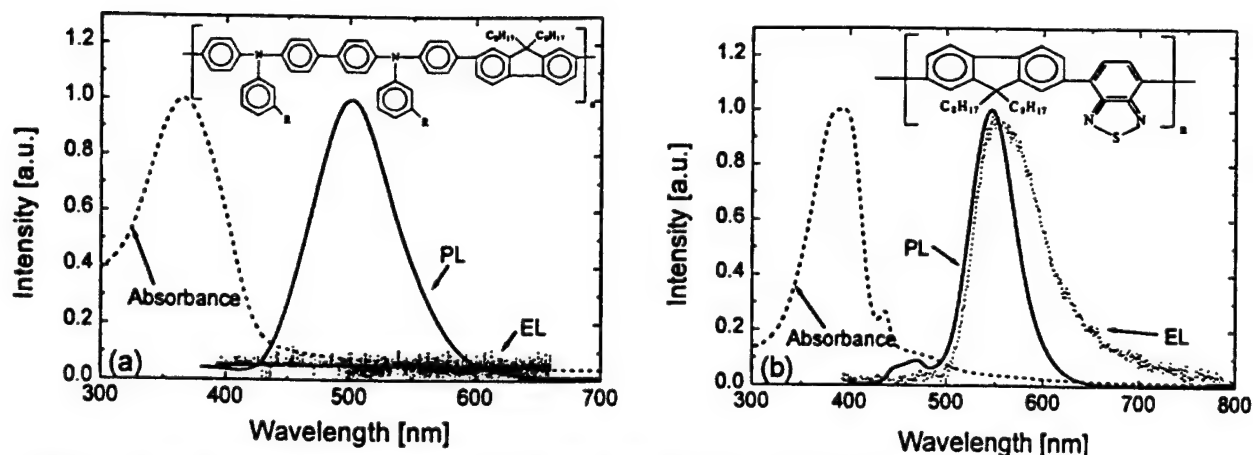


Figure 1. The absorbance, photoluminescence and electroluminescence spectra of (a) amine-fluorene (hole transport polymer) and (b) benzothiadiazole-fluorene (emissive homopolymer) thin films. The chemical structures of both polymers are shown in the insets.

Fig. 2(a) shows the bi-layer OLED structure. The schematic energy band diagram, Fig. 2(b), illustrates the relative positions of the Fermi levels of both electrodes, LUMO and HOMO for both polymers, and the vacuum level in the equilibrium state. The optical bandgap of both polymers was determined from the onset of the absorption peak that corresponds to the π - π^* transitions for π -electron states. The Fermi levels of both polymers were derived from their activation energy values, which were determined from the Arrhenius plots of the dark conductivity versus the inverse of the temperature. The band bending at the HTL/EL interface forms two small energy barriers for the holes in the HTL and the electrons in the EL, respectively. These barriers are responsible for the accumulation of local charge density for both carriers at the HTL/EL interface, providing an enhanced electron-hole recombination process. Because the energy barrier for the holes in HTL is much lower than the energy barrier for the electrons in EL, it is expected that the probability for the holes tunneling through the hole barrier into the EL layer is much larger than the probability for the electrons tunneling through the electron barrier into the HTL layer. Therefore, it is very likely that the electron-hole recombination is taking place in the EL layer and the resulting EL spectrum would be similar to the EL spectrum of the polymer B single layer device (Fig. 1(b)). Consequently, the quality (cleanness, roughness, etc) of the HTL/EL interface is critical for the overall device performance. It is also the major source for the device performance variations.

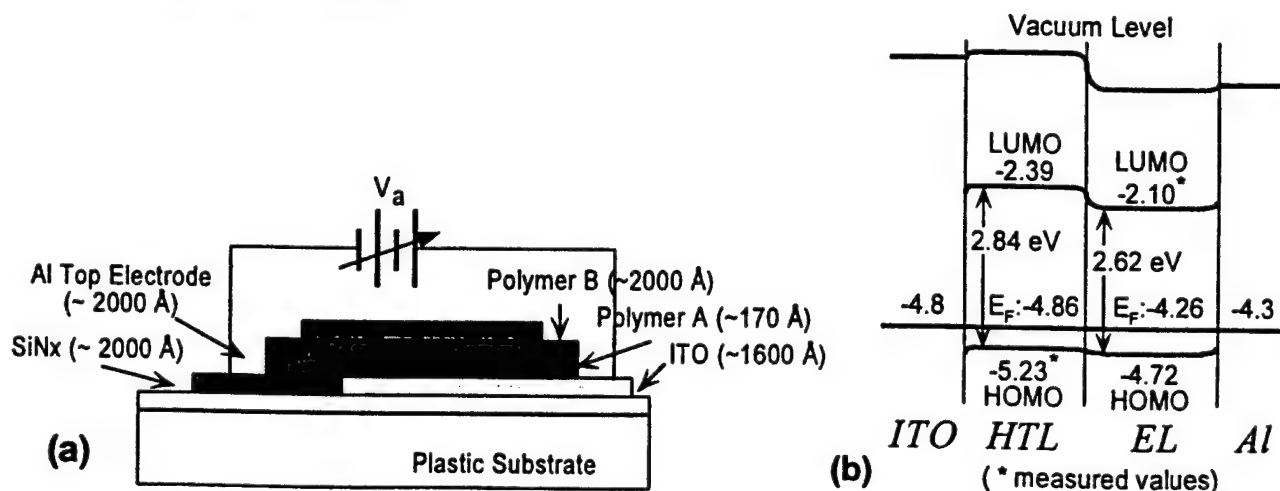


Figure 2. (a) The OLED bi-layer structure. (b) Equilibrium schematic energy band diagram for the OLED. All values shown are relative to the vacuum level.

The typical DC current-voltage (I-V) characteristic and electroluminescence spectrum (inset) of the OLEDs fabricated on the plastic substrate are illustrated in Fig. 3. The electroluminescence spectrum clearly shows a peak located at around 570 nm, with a shoulder peak located at around 545 nm. The full-width-at-half-maximum (FWHM) of this peak is about 80 nm. The I-V curve indicates a diode-like behavior, with a threshold voltage at about 20 V. The ON/OFF current rectification ratio is about 2×10^2 at ± 25 V.

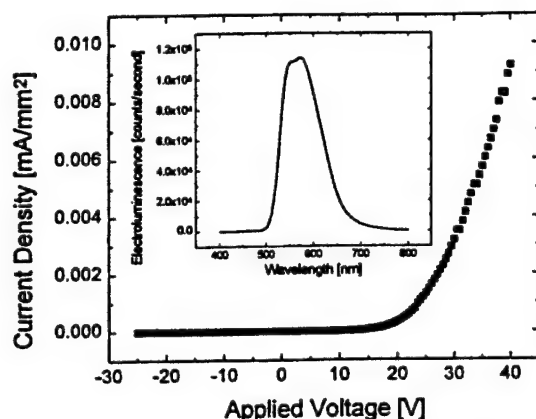


Figure 3. The current-voltage characteristics of the bi-layer OLED fabricated on the plastic substrate. The inset shows the OLED electroluminescence spectrum collected by the CCD system.

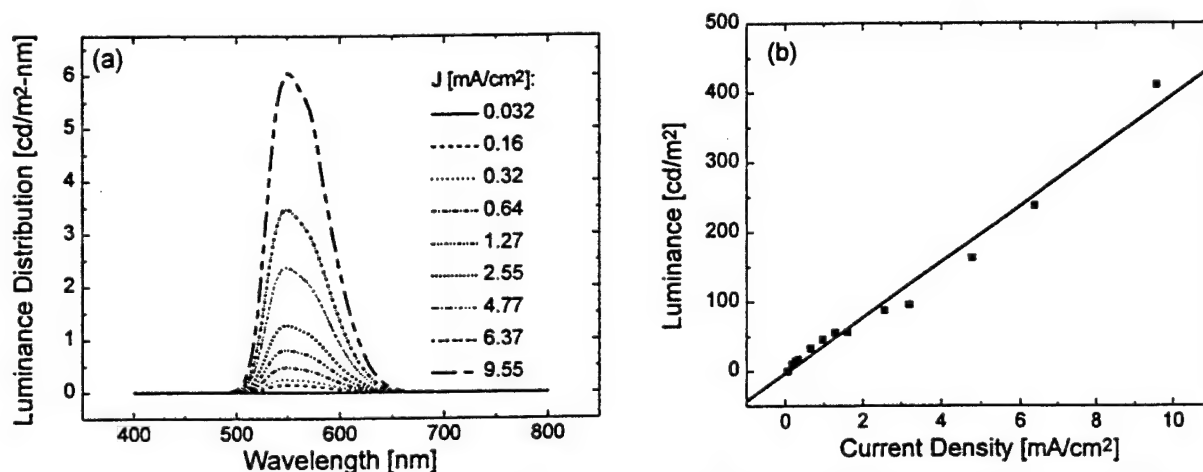


Figure 4. (a) Spectral distribution of the OLED luminance obtained at the different operating current densities. (b) The evolution of the brightness versus the operating current density is shown.

Under the forward bias conditions, i.e., ITO was positively biased with respect to Al, the light emission occurred when the applied voltage was greater than ~ 14 V. No light emission has been observed when the reversed bias was applied, i.e., Al was positively biased with respect to ITO. The reverse resistance of the device is large. According to Ohm's law, a fixed voltage divided by a large resistance yields a very small current (e.g., 8.6×10^{-4} mA/cm² at -25 V in Fig. 3). In this case the current level is insufficient to cause the OLED to light. In fact, OLED will not produce visible light until a certain current density level (around 0.03 mA/cm² in our case) is reached. Under the forward bias, electrons and holes are injected into the LUMO and HOMO bands of the polymers from the cathode and anode, respectively. The electrons and holes are relaxed to negatively and positively charged polarons or bipolarons through electron-phonon lattice coupling. Most of the doubly-charged bipolarons can dissociate into singly-charged polarons at room temperature because of the increase in configurational entropy of this process.¹² Due to the preferred direction of bond alternation of the conjugated polymers, these polarons, which are weakly coupled with the chain geometry, are driven by the externally applied electrical field and quickly move toward each other. The recombination of the oppositely charged polarons on a segment of the polymer chain forms the singlet excitons. When an excited state (singlet excitons) collides with a non-excited one, a dimer is formed in which the excitation delocalization will take place over both components. This exciton interaction (resonance), combined with the charge transfer,

will be responsible for the formation of the excimers, which will emit light Stokes shifted with respect to the absorption spectrum. For the best performance the injection and transport of the holes/electrons into the polymer bulk from the anode/cathode must be balanced.

The electroluminescence of the OLED induced by the different operating current densities has also been studied. Fig. 4(a) shows the OLED spectral distribution of the luminance at the different current densities. The shapes of all the EL spectra are almost identical to each other with a minor exception at lower current densities, where the vibration modes appear to have larger contribution to the EL spectrum at off-peak wavelength. The brightness versus current density plot, Fig. 4(b), indicates a nearly linear relationship between the luminance (obtained through integration of the area under the luminance distribution peak at different current densities) and current density.

To calculate the OLED external quantum efficiency (defined by the number of photons emitted by the device in the forward direction per electron supplied by the external circuit), it is necessary to know the wavelength distribution of the photon emission, which can only be obtained from a known electroluminescence radiance distribution. Fig. 5(a) illustrates the photon density distribution of the OLED at different applied current densities. For our OLEDs, the external quantum efficiency is calculated by dividing the output photon density by the applied current density. The emission efficiency of the OLED (Fig. 5(b)) increases rapidly at first then gradually drops down and finally fluctuates around 3.5 cd/A with the increasing current density. The evolution of the device external quantum efficiency also follows the same trend with the applied current density. The peak emission efficiency, 6.41 cd/A, appears at about 10.2 cd/m² of luminance (0.159 mA/cm²). The maximum external quantum efficiency, calculated using the method described above from the photon density distribution curve (Fig. 5(a)), is ~1.8%, which also appears at about 0.159 mA/cm². To our best knowledge, these values represent the highest plastic substrate-based OLED optical performance ever reported in the literature.

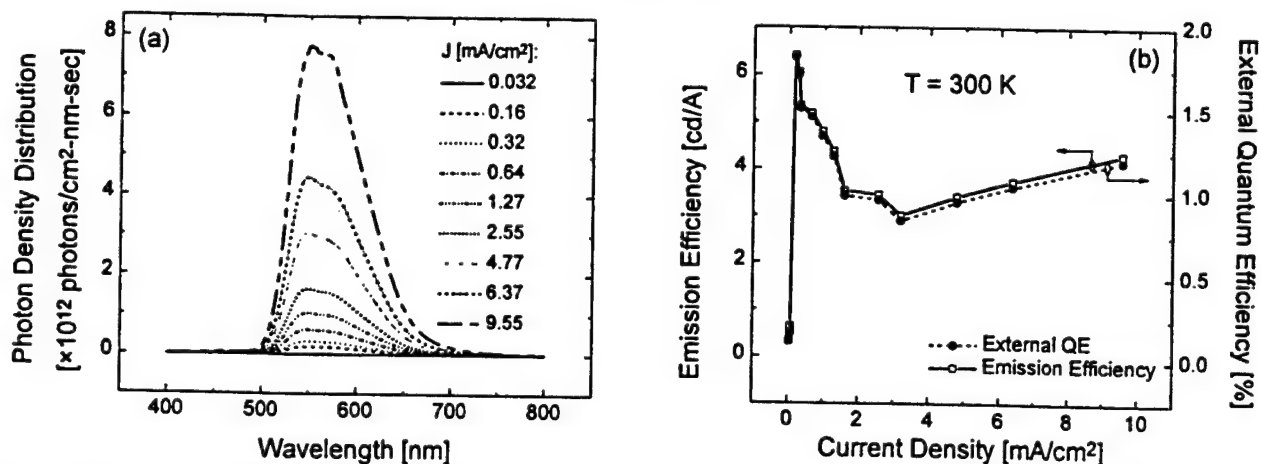


Figure 5. (a) Photon density distribution of the OLED induced by different operating current densities. (b) The current density dependence of the emission efficiency (open square) and the external quantum efficiency (solid circle).

4. CONCLUSIONS

We have demonstrated a high performance bi-layer organic polymer based light-emitting device on the plastic (polycarbonate) substrate using air-stable Al as the cathode material. A-SiNx:H was used as the moisture/oxygen blocking layer as well as the substrate-protecting layer. Both the OLED luminance efficiency and the external quantum efficiency have been greatly improved in this structure. Good brightness (> 400 cd/m²), acceptable emission efficiency (> 6.4 cd/A), and high external quantum efficiency (~ 1.8 %) have been achieved for this device.

ACKNOWLEDGEMENT

This research was supported by the Center for Display Technology and Manufacturing at the University of Michigan. The organic polymers used in this study were provided by the Dow Chemical Company.

REFERENCES

1. J.H. Burroughes, D.D.C. Bradley, A.R. Brown, R.N. Marks, K. Mackay, R.H. Friend, P.L. Burn and A.B. Holmes, "Light-emitting diodes based on conjugated polymers", *Nature*, **347**, pp. 539-541, 1990.
2. *IEEE Trans. On Electron Devices*, **44**, Special Issue on "Small Molecule and Polymer Organic Devices", ed. A. Dodabalapur, August 1997.
3. G. Yu, H. Nishino, A.J. Heeger, T.-A. Chen, R.D. Rieke, "Enhanced electroluminescence from semiconducting polymer blends", *Synth. Met.*, **72**, pp. 249-252, 1995.
4. F. Cacialli, R.H. Friend, N. Haylett, R. Daik, W.J. Feast, D.A. dos Santos, and J.L. Bredas, "Efficient green light-emitting diodes from a phenylated derivative of poly(p-phenylene-vinylene)", *Appl. Phys. Lett.*, **69**, 3794-3796, 1996.
5. Y. Yang, Q. Pei, and A.J. Heeger, "Efficient blue polymer light-emitting diodes from a series of soluble poly(paraphenylene)s", *J. Appl. Phys.*, **79**, 934-939, 1996.
6. N.D. Young, R.M. Bunn, R.W. Wilks, D.J. McCulloch, S.C. Deane, M.J. Edwards, G. Harkin, A.D. Pearson, "Thin-film-transistor- and diode-addressed AMLCDs on polymer substrates", *Journal of the SID* **5/3**, pp. 275-281, 1997.
7. G. Gustafsson, Y. Cao, G.M. Treacy, F. Klavetter, N. Colaneri and A.J. Heeger, "Flexible light-emitting diodes made from soluble conducting polymers", *Nature*, **357**, pp. 477-479, 1992.
8. A. Stein, A. Liss, S. Fields, "High-temperature acrylic plastic substrates: thermal, chemical, and mechanical properties", *SID 97 Digest*, pp. 817-820, 1997.
9. A. Berntsen, Y. Croonen, C. Liedenbaum, H. Schoo, R.-J. Visser, J. Vleggaar, P. Weijer, "Stability of polymer LEDs", *Optical Materials*, **9**, pp. 125-133, 1998.
10. N.C. Greenham, R.H. Friend, and D.D.C. Bradley, "Angular dependence of the emission from a conjugated polymer light-emitting diode: implications for efficiency calculations", *Adv. Mater.*, **6**, pp. 491-493, 1994.
11. L.S. Huang, C.W. Tang, and M.G. Mason, "Enhanced electron injection in organic electroluminescence devices using an Al/LiF electrode", *Appl. Phys. Lett.*, **70**, pp. 152-154, 1997.
12. R.H. Friend, "Conjugated polymer semiconductor devices: characterization of charged and neutral excitations", *Synth. Met.*, **51**, pp. 357-371, 1992.

Light output measurements of the organic light-emitting devices

Yi He,^{a)} Reiji Hattori, and Jerzy Kanicki

*Solid-State Electronics Laboratory, Department of Electrical Engineering and Computer Science,
The University of Michigan, Ann Arbor, Michigan 48109*

(Received 13 December 1999; accepted for publication 20 January 2000)

In this article we describe a novel light output measurements method of the organic light-emitting devices (OLEDs). This method not only provides the electroluminescence (EL) spectral response of the OLEDs, but also gives the spectral distribution of the radiant power (W), luminance (cd/m^2), luminous flux (lm), and photon emission of the measured light-emitting object. Also an accurate calculation method of the OLED EL external quantum efficiency is proposed. © 2000 American Institute of Physics. [S0034-6748(00)02905-1]

I. INTRODUCTION

Silicon photodiode (or silicon photodiode arrays) and charge-coupled device (CCD) arrays are the most widely used photosensitive detectors for the photoluminescence (PL) and electroluminescence (EL) measurements of the organic light-emitting devices (OLEDs). They feature high sensitivity, stable quantum efficiency over a certain wavelength range, and near-linear response with the incident light power. Both devices are able to simultaneously collect the photosignals over a range of wavelengths. For the OLED brightness (luminance) measurement, in which the EL spectral distribution is not important, the best choice seems to be the calibrated photodiode method. For the external quantum efficiency measurement, a calibrated photodiode could also be used. To determine the absolute PL external quantum efficiency, Greenham *et al.* developed a method using an integrating sphere and a calibrated photodiode.¹ However, another work² from the same group using a CCD spectrometer provides several advantages including better accuracy and reliability. To determine the EL external quantum efficiency, most of the research groups still use a calibrated photodiode method. Based on this method, the EL external quantum efficiency can be defined using the following steps: first, the total optical output power Q (measured in watts) is measured using the photodiode; second, the total number of photons emitted is calculated from $Q/\text{photon energy}$; third, the operating current is measured and the total number of electrons is calculated from operating current/ e ; finally, the external quantum efficiency is calculated from number of photons/number of electrons. The problem associated with this method is the value of the photon energy used in this calculation. In general, the EL spectrum of the OLED is too broad to be treated as a monochromatic light source, and an average photon energy value has to be used during this calculation. The use of a single photon energy value during this calculation to represent a broad light emission distribution is intrinsically not accurate. Therefore, a systematic error is introduced during this calculation. Moreover, the photon energy value is very difficult to choose when the emission

spectrum shows multiple peaks or irregular shape. The systematic error further increases when the EL spectrum changes with the external electrical field.³ Under this circumstance, the photon energy value has to be recalculated for every single applied voltage. This is not practical for a routine determination of the OLED EL external quantum efficiencies.

In this article we describe a new method to accurately calculate the OLED EL external quantum efficiency using charge-coupled device arrays. A detailed description of the calibration method of the CCD is also provided. Using this method, the wavelength distribution of the OLED radiant power, luminance, and photons emitted can be obtained.

II. EXPERIMENT

The CCD spectral analyzer (Instrument S. A.) used in this study consists of a CCD detector, an imaging spectrograph, and an optical fiber. The CCD detector has a 2000×800 pixel array and each pixel size is $15 \times 15 \mu\text{m}^2$. The optical fiber bundle contains 37 fibers (diameter $200 \mu\text{m}/\text{fiber}$) with an optical response ranging from 200 to $800 \mu\text{m}$. The CCD chip is cooled with the liquid nitrogen during the measurements. The calibration system used in this work is a Labsphere USS-600V Uniform Source System. This system consists of two integrating spheres separated by a motorized, mechanically variable attenuator. A calibration lamp (tungsten halogen) with a known spectral radiance was mounted at the center of the bottom satellite sphere (3 in.). A calibrated luminance meter (photodiode) and an exit port were mounted on the top sphere (6 in.). A baffle was used in the top sphere to prevent light reaching the exit port and the luminance meter directly from the bottom satellite sphere. The experimental setup described above is shown in Fig. 1.

III. RESULTS AND DISCUSSIONS

The calibration of a CCD system consists of two steps: first, the CCD response curve is calibrated according to the known spectral radiance of the standard lamp; second, the luminance and photon density distribution of the light-emitting object are derived from the calibrated CCD response curve.

^{a)}Applied Physics Program.

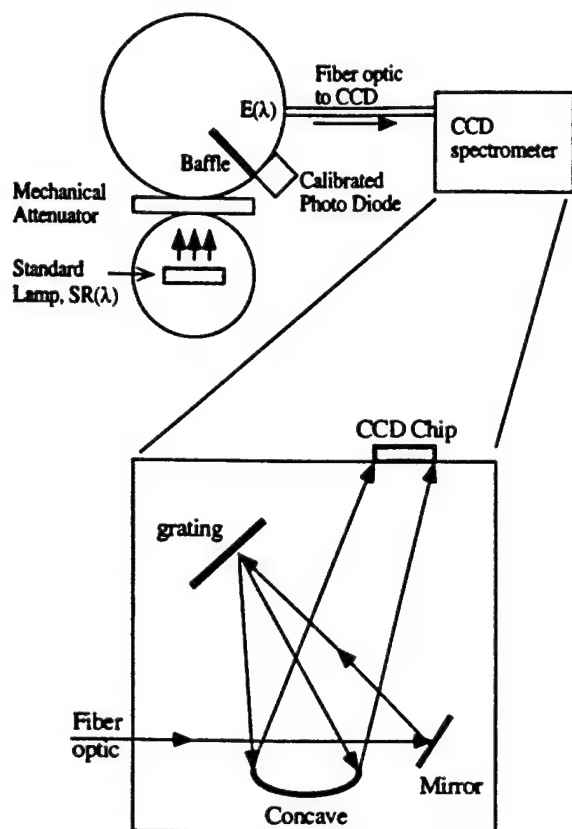


FIG. 1. This diagram illustrates the experimental configuration of the spheres and CCD system used in this calibration. The light path and inside configuration of the CCD spectrometer are also shown.

In the normal conditions, the calibration lamp in the satellite integrating sphere emits a stable spectral radiance which does not change with time. The emitted light passes through the mechanical attenuator and is diffused by the wall of the top sphere. Since the mechanical attenuator is a linear optical element which evenly changes the intensity of the incident light over the wavelengths, the light emission observed at the exit port of the top sphere should always exhibit a same spectrum shape as emitted by the calibration lamp of the bottom sphere. The intensity of the light at the exit port can be changed by varying the attenuator opening. The relationship between the spectral radiance at the exit port and the known spectral radiance of the calibration lamp can then be described by the following equation:

$$E(\lambda) = A \cdot SR(\lambda), \quad (1)$$

where λ is the wavelength, $E(\lambda)$ is the spectral radiance at the exit port of the sphere, $SR(\lambda)$ is the known spectral radiance curve of the calibration lamp, and $A (\leq 1)$ represents the attenuation factor. Due to the nonlinear responses of the optical elements (e.g., the grating) in the CCD system at different wavelengths, the spectral response of the CCD system usually does not match the shape of $E(\lambda)$. Therefore, to correctly analyze the spectral distribution curve measured by the CCD system, a correction curve, $corr(\lambda)$, is needed:

$$Sp(\lambda) \cdot corr(\lambda) = E(\lambda) = A \cdot SR(\lambda), \quad (2)$$

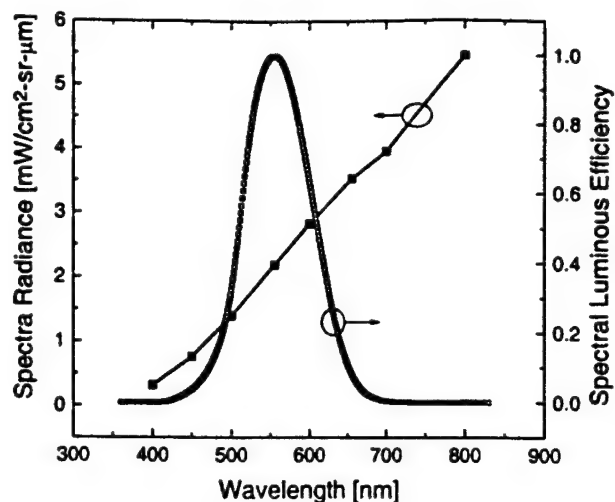


FIG. 2. The spectral radiance of the tungsten calibration lamp in the normal conditions and the normalized CIE photopic spectral luminous efficiency curve of a standard observer.

where $Sp(\lambda)$ represents the spectral response curve of the CCD. The CCD correction curve, $corr(\lambda)$, is usually a function of the wavelength and independent of different attenuator openings.

To calculate $corr(\lambda)$ the radiometric quantity [$= A \cdot SR(\lambda)$, $\text{mW/cm}^2 \text{sr} \mu\text{m}$] of the light emission at the exit port must be known. However, the luminance meter of the top sphere only outputs a photometric quantity (cd/m^2) that is already weighted according to the response of the human eyes. According to photometry theory, the actual photometric quantity obtained from the radiometric emission follows a conversion formula:⁴

$$\begin{aligned} \text{Photometric quantity} &= 683(\text{lm/W}) \int E(\lambda) V(\lambda) d\lambda \\ &= A \cdot 683(\text{lm/W}) \int SR(\lambda) V(\lambda) d\lambda. \end{aligned} \quad (3)$$

where $V(\lambda)$ represents the CIE photopic spectral luminous efficiency curve for "standard" light adapted eyes.⁵ Therefore, the attenuator factor A can be calculated from photometric quantity / [$683(\text{lm/W}) \int SR(\lambda) V(\lambda) d\lambda$]. Figure 2 shows the spectral radiance of the calibration lamp and the CIE photopic spectral luminous efficiency curve. Note that only part (400–800 nm) of the original spectral radiance of the calibration lamp was considered during the calculation because the photometric contributions are very small for the wavelength regions below 400 and above 800 nm. For a specific example, the luminance meter reads 4.98 foot-lamberts (17.06 cd/m^2), the integration [$\int SR(\lambda) V(\lambda) d\lambda$] gives $0.242 \text{ mW/cm}^2 \text{sr}$, therefore the attenuation factor $A \approx 0.0103$.

Using Eq. (2), the CCD correction curve $corr(\lambda)$ could be obtained for a specific attenuator opening from the CCD spectral response curve. For the above attenuator setting (luminance of 4.98 foot-lamberts), Fig. 3(a) shows the CCD spectral response curve. The attenuation factor is a function of attenuator setting. However, as discussed previously, the CCD correction curve should remain unchanged for different

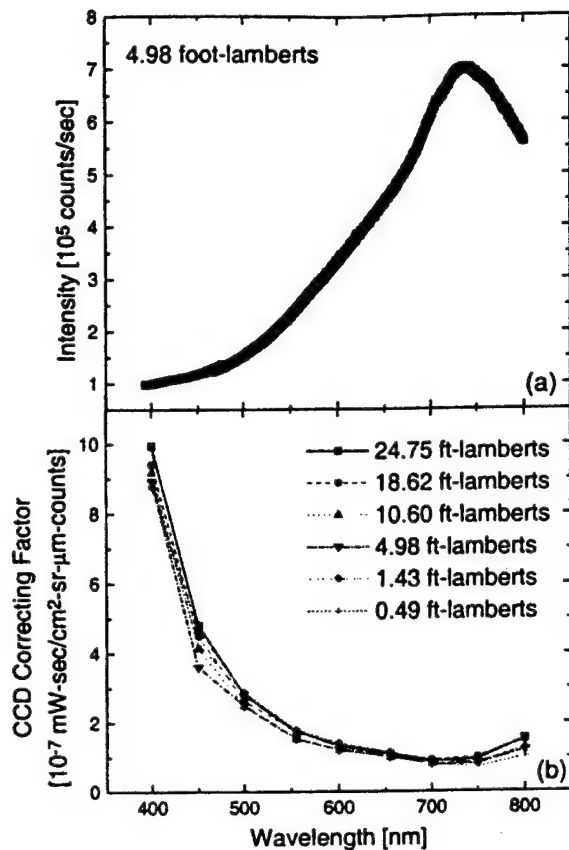


FIG. 3. (a) The CCD spectral response curve for a 4.98 foot-lamberts (17.06 cd/m^2) luminance reading. (b) The CCD correction curves for different attenuator settings.

attenuator settings. This is demonstrated in Fig. 3(b) where several CCD correction curves with different attenuator settings are plotted together. All these CCD correction curves are virtually the same, supporting the arguments made previously.

The actual CCD correction curve is an average of the several CCD correction curves obtained at different attenuator settings. Using this correction curve, the CCD spectral response curve of any visible-range light-emitting object can be converted to its corresponding radiometric spectrum. For the OLEDs, researchers are usually more interested in the brightness (luminance) of the devices than their radiometric spectrum. According to Eq. (2), Eq. (3) can be rewritten as follows:

$$\begin{aligned} \text{Photometric quantity} &= 683(\text{lm/W}) \int S_p(\lambda) \text{corr}(\lambda) V(\lambda) d\lambda \\ &= \int S_p(\lambda) L(\lambda) d\lambda, \end{aligned} \quad (4)$$

where $L(\lambda) = 683(\text{lm/W}) \text{corr}(\lambda) V(\lambda)$. $L(\lambda)$ is the conversion function from the CCD spectral response of the light-emitting object to its luminance distribution. Figure 4 shows the CCD luminance calibration curve, $L(\lambda)$. The product of this curve and the CCD spectral response is the luminance distribution of the measured light-emitting object. Because of the influence of the CIE photopic curve $V(\lambda)$, i.e., the human eye sensitivity, the luminance distribution curve usually peaks at around 555 nm—the same peak location that is

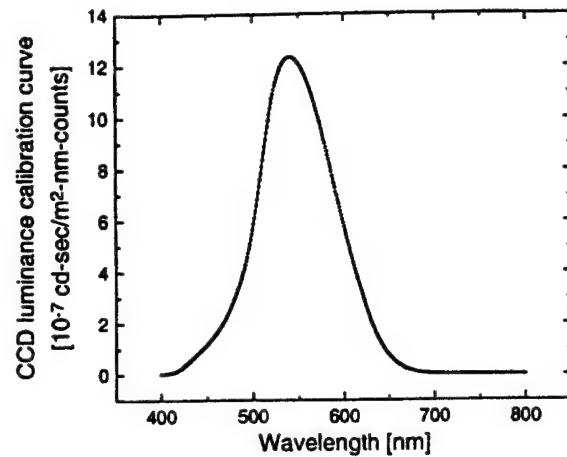


FIG. 4. The CCD luminance calibration curve.

observed in $V(\lambda)$. The actual emission peak location, which should be defined as the most probable emission wavelength, can only be obtained from its photon distribution curve.

Figure 5 illustrates an example of the CCD (previously calibrated with the calibrated light source) EL response curve and the luminance distribution curve of a bilayer OLED.⁶ In this case the OLED, operated at a current density of 0.324 mA/cm^2 , has a green light emission. The total luminance (area under the luminance distribution curve in Fig. 5) of this OLED is $\sim 40.83 \text{ cd/m}^2$.

The external quantum efficiency of the OLED represents the number of externally emitted photons per electron produced by the external circuit. In this case the density of the produced electrons is represented by the current density applied to OLED. The photon density, on the other hand, can be calculated from the OLED EL spectrum.

From the spectral radiance [a product of $\text{corr}(\lambda)$ and the CCD response curve] of the OLED, its photon density distribution over the wavelength can be obtained:

$$ph(\lambda) = \frac{\pi S_p(\lambda) \text{corr}(\lambda)}{h\nu} = \frac{\pi S_p(\lambda) \text{corr}(\lambda) \lambda}{hc}, \quad (5)$$

where h is the Planck's constant, c is the velocity of the light.

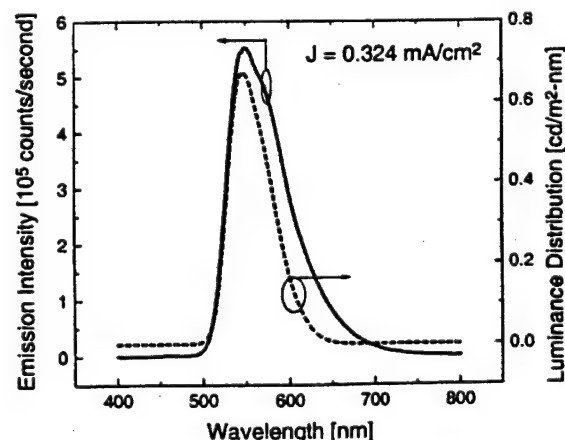


FIG. 5. The CCD spectral response of the OLED operated to 0.324 mA/cm^2 , and the corresponding luminance distribution curve.

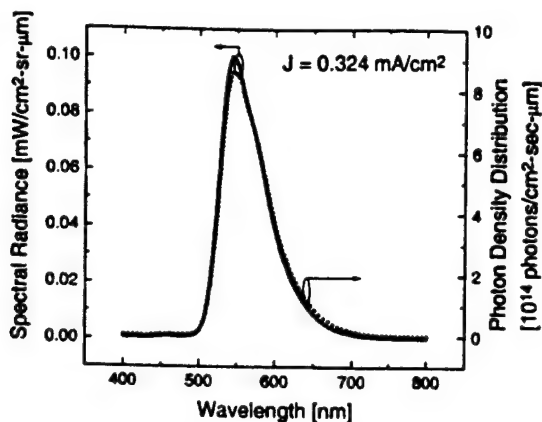


FIG. 6. The spectral radiance of the OLED operated at 0.324 mA/cm^2 , and the corresponding photon density distribution curve.

and $ph(\lambda)$ is the photon density distribution. Factor π is an integration factor induced by assuming Lambertian emission.^{7,8}

Figure 6 illustrates the spectral radiance obtained for a bilayer OLED and its photon density distribution.⁶ According to the photon density distribution, the external quantum efficiency can then be derived from the following equation:

$$\eta_e = \frac{\int ph(\lambda) d\lambda}{J/e} \quad (6)$$

where J is the current density applied to the OLED. For the example given above, J is 0.324 mA/cm^2 , the integration of Fig. 6 yields $6.76 \times 10^{13} \text{ photons/cm}^2 \text{ s}$, therefore the external quantum efficiency calculated using this method is 3.3%. For this specific case the OLED brightness was 40.83 cd/m^2 .

ACKNOWLEDGMENTS

The authors would like to thank Professor Stephen Rand for valuable discussions. The financial support of this research is provided by the Center for Display Technology and Manufacturing at the University of Michigan, and DARPA-ONR grant (N0014-99-1-0958).

¹N. C. Greenham, I. D. W. Samuel, G. R. Hayes, R. T. Phillips, Y. A. R. R. Kessener, S. C. Moratti, A. B. Holmes, and R. H. Friend, *Chem. Phys. Lett.* **241**, 89 (1995).

²J. C. de Mello, H. Felix Wittmann, and R. H. Friend, *Adv. Mater.* **9**, 230 (1997).

³M. Berggren, O. Inganäs, G. Gustafsson, J. Rasmussen, M. R. Andersson, T. Hjertberg, and O. Wennerström, *Nature (London)* **372**, 444 (1994).

⁴T. N. Cornsweat, *Visual Perception* (Academic, New York, 1970).

⁵L. Levi, *CRC Handbook of Tables of Functions for Applied Optics* (Chemical Rubber, Cleveland, OH, 1974).

⁶Y. He, S. Gong, R. Hattori, and J. Kanicki, *Appl. Phys. Lett.* **74**, 2265 (1999).

⁷N. C. Greenham, R. H. Friend, and D. D. C. Bradley, *Adv. Mater.* **6**, 491 (1994).

⁸G. Gu, D. Z. Garbuzov, P. E. Burrows, S. Venkatesh, and S. R. Forest, *Opt. Lett.* **22**, 396 (1997).

High-efficiency organic polymer light-emitting heterostructure devices on flexible plastic substrates

Yi He^{a)} and Jerzy Kanicki^{b)}

Center for Integrated MicroSystems, Department of Electrical Engineering and Computer Science,
University of Michigan, Ann Arbor, Michigan 48109-2122

(Received 8 July 1999; accepted for publication 8 December 1999)

In this letter, we describe a high-efficiency organic polymer light-emitting heterostructure device with aluminum cathode fabricated on a thin, flexible plastic substrate. The device consists of a hole transporting (amine-fluorene) and an emissive (benzothiadiazole-fluorene) conjugated organic polymer layers. The best heterostructure device has a green light emission and a maximum luminance higher than 2000 cd/m². Device shows a maximum emission of ~56.2 cd/A and, accordingly, a maximum luminous and external quantum efficiency of ~9.0 lm/W and ~15%, respectively. This organic light-emitting diode performance is acceptable for flat panel display applications. © 2000 American Institute of Physics. [S0003-6951(00)01206-7]

Flexible plastic substrate has a distinct advantage over glass substrate in many applications. Unlike glass, the plastic is usually more robust and compact, has lighter weight, and is more cost effective. The use of the plastic substrates will also enable new product concepts such as curved displays, smart cards, and all plastic electronics. Because of these advantages, in the last decade, plastic substrates have been used in supertwisted nematic liquid-crystal displays (STN-LCDs),¹ active-matrix liquid-crystal displays (AMLCDs),² and organic light-emitting devices (OLEDs).^{3,4} While it is a very promising new technology, the plastic substrate, however, is limited by its low processing temperature, high heat-induced shrinkage, high gas permeability, low chemical resistance, average water and solvent durability, and average transparency. The low thermal durability of the plastic substrate prevents, for example, the high temperature ($\geq 200^\circ\text{C}$) postdeposition thermal annealing of the transparent conducting oxide (TCO), which is typically used in the organic light-emitting device as the transparent electrode. As a result, the TCO on the plastic substrate usually has a lower transparency, a lower conductivity, and a poorer adhesion in comparison with its counterpart on the glass substrate. Another disadvantage of the plastic substrate is its relatively high permeability of the moisture and oxygen that can affect the OLED electrical stability.⁵

In this letter we describe the optoelectrical characteristics of a high-efficiency, bilayer organic polymer light-emitting device with aluminum cathode fabricated on the ITO coated thin, flexible plastic substrate.

The bilayer OLED structure, shown in Fig. 1, consists of a hole transporting [(HTL), ~170 Å] and an emissive [EL, ~2000 Å] conducting polymer layers sequentially deposited on the plastic substrate by the spin-coating technique. The polymer absorption and photoluminescence spectra have been published elsewhere.⁶ The schematic energy band diagram of the OLED structure and the cross-section of the flexible plastic substrate are shown in Fig. 1. The lowest

unoccupied molecular orbit (LUMO) and the highest occupied molecular orbit (HOMO) levels for both polymers are derived from their cyclic voltammograms and absorption spectra.⁷ The polymer optical band gaps were determined from the onset of the absorption peak that corresponds to the $\pi-\pi^*$ transitions of π electrons. The polymer Fermi level positions ($E_F = E_A + \text{HOMO}$) were derived from their dark conductivity (σ) activation energies (E_A) calculated from the Arrhenius plots [$\sigma = \sigma_0 \exp(-E_A/kT)$]. The properties of the plastic substrate were reported elsewhere.⁸ Aluminum top cathode electrode was evaporated in a vacuum chamber at the base pressure $\sim 10^{-6}$ Torr through a shadow mask. The OLED electroluminescence (EL) spectra were measured with a charge-coupled device (CCD) spectral analyzer through optical fibers. The CCD spectral analyzer has been calibrated with a Labsphere USS-600 Uniform Source System incorporating a calibrated lamp and a motorized variable attenuator.⁹ The OLED current-voltage characteristics were measured in a vacuumed metal box.

Figure 2 illustrates a typical OLED dc current-voltage ($I-V$) characteristic and electroluminescence spectrum (inset). The electroluminescence spectrum clearly shows a peak located at ~570 nm, with a shoulder peak at ~545 nm; the full width at half maximum (FWHM) of this peak is about 80 nm. The $I-V$ curve displays a diode-like behavior, with an ON/OFF current ratio of about 6.7×10^4 at ± 25 V. Through the $I-V$ characteristic modeling, we have established that this characteristic cannot be simply described by either one of the following models previously suggested in the literature: space charge limited current (SCLC); trapped charge limited current (TCL); thermionic emission combined with the diode series resistance R_s ; or simple Fowler-Nordheim tunneling. This result implies that none of the above mechanisms is solely dominant in our OLED.

We found that the forward bias current-voltage characteristic can be simply described by the following equations based on the equivalent circuit shown in Fig. 1:

$$V_A = V' + V'' \quad \text{with } R_s \approx 0 \quad (1)$$

^{a)}Applied Physics Program.

^{b)}Electronic mail: Kanicki@eecs.umich.edu

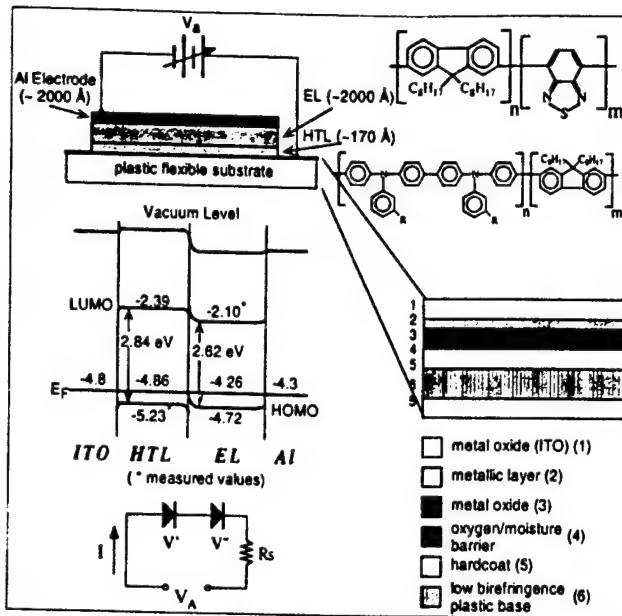


FIG. 1. The OLED bilayer structure, the polymers chemical structures, the schematic energy band diagram of the OLED in equilibrium, the cross-section of the plastic substrate, and the equivalent circuit of the OLED are shown. The EL and HTL polymers are benzothiadiazole-fluorene and amine-fluorene copolymer, respectively. The "*" represents measured values.

$$\text{and } V' = V'_0 \ln \left(\frac{I}{I'_0} + 1 \right), \quad V'' = V''_0 \ln \left(\frac{I}{I''_0} + 1 \right), \quad (2)$$

where $V'_0 (= S'kT/q)$ and $V''_0 (= S''kT/q)$ are the fitting parameters; S' and S'' are the slopes of the I - V characteristics; k is Boltzmann constant, T ($= 300$ K) is the temperature, q is the charge of electron, and I'_0 and I''_0 are constants. The V' and V'' represent the voltage drops across the two junctions connected in series, and R_s is the equivalent device series resistance. The best fit (solid line in Fig. 2) to the experimental data has been obtained for the following fitting parameters: $I'_0 \approx 4.07 \times 10^{-9}$ mA/cm², $I''_0 \approx 2.27 \times 10^{-2}$ mA/cm², $V'_0 \approx 0.44$, and $V''_0 \approx 3.35$.

The above equations describe the deep gap state (defects)-assisted multistep tunneling process¹⁰ that can take place across both junctions; and the V'_0 and V''_0 parameters represent the number of steps (involving a series of closely spaced deep gap defects) that carrier must travel through a

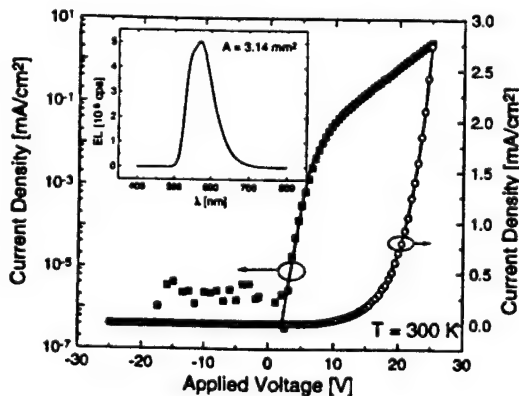


FIG. 2. The experimental (■, ○) and simulated (—) current-voltage characteristics of the bilayer OLED are given. The inset shows the electroluminescence spectrum of the OLED collected by the CCD system.

given junction. These defects can be associated with the impurities and/or carbon or nitrogen point defects. In our case we assume that the HTL/EL junction is behaving like a $p^+ - p^-$ heterojunction, while the EL/Al junction is acting as a typical metal-semiconductor junction. Also the ITO/HTL (p^+ -like) junction is assumed to be ohmic-like in our OLEDs, and therefore this contact will not provide any significant contribution to the I - V characteristic. Hence, at a constant electrical field the OLED carrier current is mainly limited by both junctions (e.g., multistep carrier tunneling/hopping through the HTL/EL junction and electron injection followed by the multistep tunneling/hopping through the EL/Al junction), rather than by the carrier transport through the polymer bulk; although the influence of the deep gap states-assisted bulk carrier transport can also be important in the OLED. In agreement with our experimental data the OLED injected current level (and the OLED brightness) is indeed higher if the low work function metals are used.⁷

In the forward bias conditions, i.e., ITO is positively biased with respect to Al, the light emission occurred when the applied voltage is greater than ~ 6 V. No light emission is observed when the reversed bias is applied to the OLED structure, i.e., Al is positively biased with respect to ITO. In this case, the reverse resistance of the OLED is large. According to the Ohm's law, a reverse voltage divided by a large device resistance yields a very small reverse current (e.g., 4.1×10^{-4} mA/cm² at -25 V in Fig. 2) that is insufficient to cause the light emission. A certain current density level (around 0.01 mA/cm² in our case) is needed to produce the visible light. The electrons and holes that are injected, and transported through the junctions by multisteps process under the forward bias, into the polymer LUMO and HOMO bands are relaxed to negatively and positively charged polarons through electron-phonon lattice coupling. These polarons will move toward each other under the influence of the applied electrical field and they will recombine on a certain segment of polymer chain to form the singlet excitons. Through the resonance interactions, these singlet excitons can form the excimers, which will emit light Stokes shifted with respect to the absorption spectrum.¹¹ The proposed mechanism of the light generation is in agreement with our experimental data.^{6,7}

Figure 3 shows a typical variation of the OLED brightness (or luminance, L in cd/m²) with the applied current density (the inset shows the OLED spectral distribution of luminance obtained at the different applied current densities). The integration of the OLED spectral distribution of luminance over the wavelength yields the luminance of the OLED. A near-linear relationship obtained between the luminance and the applied current density (J in mA/cm²), with a gradual saturation at $J \geq 5$ mA/cm², can be described by the following equation:

$$L \cong AJ + BJ^2, \quad (3)$$

where A (354 ± 28) and B (-14 ± 3) are constants. At the low current injection this equation can be approximated by: $L \propto J$; and at the high current injection the light-emission saturates at a certain level (in our case at ~ 2300 cd/m² for

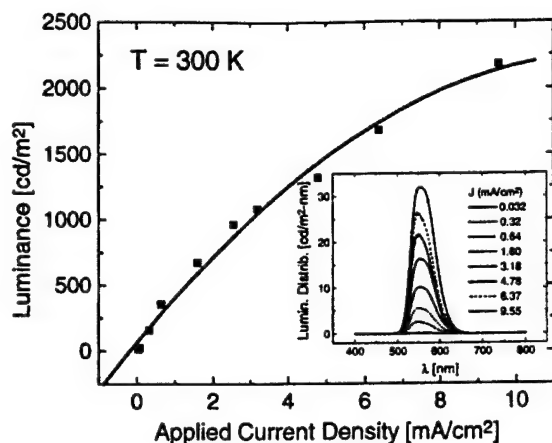


FIG. 3. The evolution of the OLED brightness as a function of the operating current density is shown. The solid line represents the fit of the experimental data to Eq. (3). The inset shows the OLED luminance distribution spectra for different applied current densities.

$J \approx 12.6 \text{ mA/cm}^2$). The saturation in this curve is due to the OLED heating that is usually observed at the high current injection levels.¹²

The evolution of the OLED external quantum efficiency (= number of the photons emitted/electron supplied by the external circuit, e.g., applied current density) at different applied current densities is shown in Fig. 4 (the inset illustrates the photon density distribution spectra at the different applied current densities). The integration of the areas under the photon density distribution provides the number of photons emitted per unit area. We can conclude from this figure that the OLED emission efficiency increases rapidly at first then drops down gradually and starts slowly to flat out at about 4.78 mA/cm^2 (27.7 cd/A) with the increasing applied

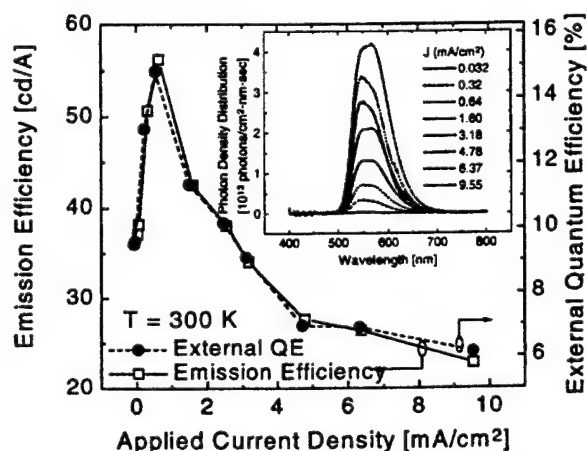


FIG. 4. The evolution of the OLED emission efficiency (□) and external quantum efficiency (●) as a function of the applied current density are shown. The inset shows the OLED photon density distribution spectra for different applied current densities.

current density (or luminance). The evolution of device external quantum efficiency also follows the same trend with the applied current density, and the maximum emission efficiency, luminous, and external quantum efficiencies for our OLED are $\sim 56.2 \text{ cd/A}$, $\sim 8.96 \text{ lm/W}$, and $\sim 14.8\%$, respectively. This excellent OLED performance could be obtained through the development of the following technologies for this device: minimum ITO surface roughness [root-mean-square (rms) $\sim 2.85 \text{ nm}$ measured over $\sim 30 \times 30 \mu\text{m}^2$]; thin flexible substrate ($\sim 0.2 \text{ mm}$); adequate refractive index matching between polymer (~ 1.72) and substrate; good control of the polymer morphology (aggregated species) during spin coating through the optimization of the solvent concentration of the polymer solution and the spin speed; and adequate electron transport within the EL polymer through the introduction of benzothiadiazole group (electron-withdrawing group), e.g., EL polymer is used for both the electron transport and light emission. The reduction of the external quantum efficiency at the higher current density is due to the light-induced defects creation (bond breaking) and/or device internal field modification leading to reduction of the density of the excimer states.

We would like to thank Dr. R. Hattori and Dr. S. Gong for their technical assistance during this project. All devices have been fabricated at the University of Michigan Electronics Manufacturing Laboratory. The organic polymers used in this study have been provided by the Dow Chemical Company (Midland, MI). The plastic film conductor was provided by Polaroid Corporation. This research project was financially supported by the Applied Physics Program and the Center for Display Technology and Manufacturing at the University of Michigan, Ann Arbor, and DARPA-ONR grant (N0014-99-1-0958).

¹ F. Matsumoto, T. Nagata, T. Miyabori, H. Tanaka, and S. Tsushima, SID 93 Digest, 1993, p. 965.

² N. D. Young, R. M. Bunn, R. W. Wilks, D. J. McCulloch, S. C. Deane, M. J. Edwards, G. Harkin, A. D. Pearson, J. Soc. Inf. Disp. 5/3, 275 (1997).

³ G. Gustafsson, Y. Cao, G. M. Treacy, F. Klavetter, N. Colaneri, and A. J. Heeger, Nature (London) 357, 477 (1992).

⁴ G. Gustafsson, G. M. Treacy, Y. Cao, F. Klavetter, N. Colaneri, and A. J. Heeger, Synth. Met. 55-57, 4123 (1993).

⁵ A. Bernsten, Y. Croonen, C. Liedtbaum, H. Schoo, R.-J. Visser, J. Vlegaar, and P. Weijer, Opt. Mater. 9, 125 (1998).

⁶ Y. He, S. Gong, R. Hattori, and J. Kanicki, Appl. Phys. Lett. 74, 2265 (1999).

⁷ Y. He and J. Kanicki, Proceedings of Euro Display'99, 1999, p. 143.

⁸ P. Y. Z. Chu, H. C. Choi, L. S. Health, C. S. Ko, J. Mack, P. Nagarkar, J. Richard, W. Smyth, and T. Wang, SID 98 Digest, 1998, p. 1099.

⁹ Y. He, R. Hattori, and J. Kanicki (unpublished).

¹⁰ J. Kanicki, Handbook of Conducting Polymers, edited by T. A. Skotheim (Dekker, New York, 1986), p. 543.

¹¹ Practical Fluorescence, edited by G. G. Guilbault (Dekker, New York, 1990).

¹² P. W. M. Blom and M. J. M. De Jong, Philips J. Res. 51, 479 (1998).



SOCIETY FOR INFORMATION DISPLAY

**CONFERENCE RECORD OF THE
20TH
INTERNATIONAL DISPLAY
RESEARCH CONFERENCE**

**SEPTEMBER 25-28, 2000
PALM BEACH, FLORIDA, USA**

**Featuring
Invited Symposia
on
MicroDisplays, Technologies for Electronic Paper,
OLEDs, and Substrates and Electronics
for Flexible Displays**

**Sponsored by
The Society for Information Display**

**In cooperation with
The IEEE Electron Devices Society**

**Available from:
Society for Information Display
31 East Julian Street, San Jose, CA 95112**

Organic Light Emitting Devices on Plastic Flexible Substrates: New Cathode and Light Emissive Materials

Yongtaek Hong^a, Zhiyong Hong^b, M. David Curtis^b, and Jerzy Kanicki^a

^aSolid State Electronics Laboratory, Dept. of Electrical Engineering and Computer Science, University of Michigan, Ann Arbor, MI 48109

^bDept. of Chemistry, Macromolecular Science and Engineering, University of Michigan, Ann Arbor, MI 48109

Abstract

The polymer-based double-layer light-emitting devices on plastic flexible substrates have been fabricated and characterized. A homo-polymer of poly (9,9'-dihexyl fluorine-2,7-diyl) (PHF) and its derivative, an alternating co-polymer of poly (9,9'-dihexyl flourene-2, 7-diyl) and poly (benzothiadiazole 2, 5-diyl) (PHF-BTD) were used as emissive materials. And a homo-polymer of poly (9-hexyl carzole-3, 6-diyl) (PC6) was used as a hole transport layer in this work. Both aluminum (Al) and erbium (Er) metals were used as cathode materials in our devices.

Introduction

The organic light emitting devices (OLEDs) have recently gained considerable attention in mobile communication and automotive area, since their introduction in 1990¹. So far, poly (p-phenylene vinylene) (PPV) and its derivatives have been studied by most research and development laboratories due to their excellent electrical and optical performances.^{1,2,3} In this paper, the properties of the OLEDs based on PHF and PHF-BTD will be described.

Experimental

Figure 1 shows the device structure and schematic of the measurement configurations used in this study. The ITO covered plastic substrates having the sheet resistance of less than 10 ohms/square and the transmission greater than 80 % over the visible photon energy range were used. The substrates were treated in the UV-ozone just after they were cleaned in the ultrasonic bath of isopropanol. Hole transport layer (HTL) and light emissive layers (LEL) were sequentially spin coated and cured in the vacuum oven. Then, erbium-gold double layer was electron-beam (E-beam) evaporated without interruption through shadow masks under a high vacuum condition ($\sim 10^{-6}$ Torr). The area of evaporated contact is about 2 mm².

The PHF, PHF-BTD and PC6 were

synthesized in the Chemistry department. The details of the synthesis will be reported elsewhere.

The electrical and optical measurements were performed in the air. The J-V characteristics of devices were measured with a programmable voltage source and a current meter. The OLED electroluminescence (EL) was measured with a CCD spectrum system calibrated with a Labsphere USS-600 Uniform Sources System having a light source and a programmable attenuator.⁴ The schematic of the measurement setup is shown in Figure 1.

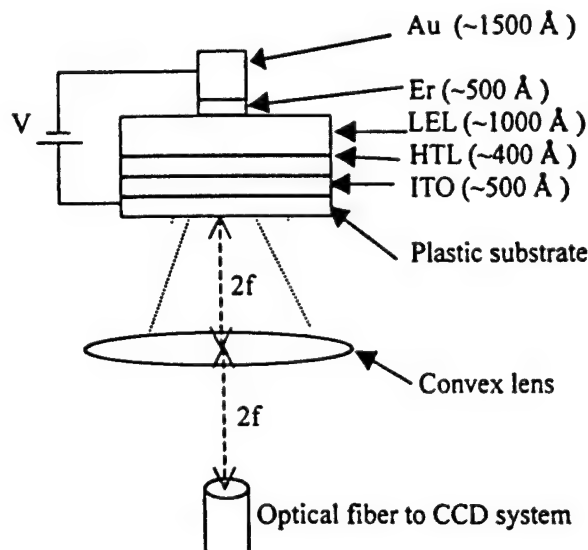


Figure 1. Device structure and measurement setup used in this work.

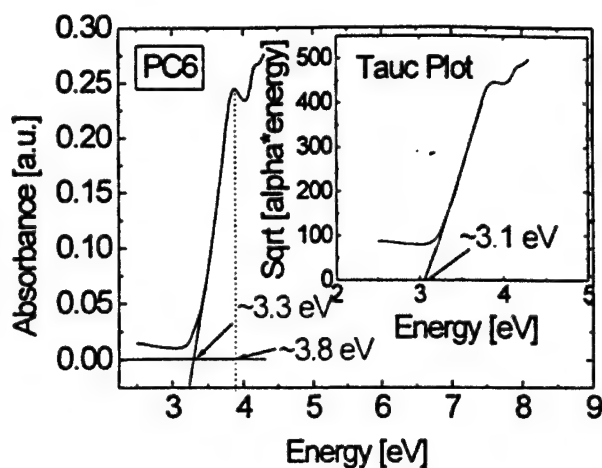
Results and Discussions

Figure 2(a) shows the absorption spectra and the Tauc plot⁵ of PHF, PHF-BTD and PC6. The optical band gap (E_G) values have been determined by the following methods; (a) absorption edge extrapolation, (b) from absorption peak location, and (c) Tauc plots. The electronic transport gap (E_T) values have been obtained from cyclic voltammetry (CV) spectra shown in Figure 2(b) by assuming a scale factor relating F_c/F_{c+} to vacuum of ~ 4.8 eV^{4,6}. The band gap values are summarized in the Table

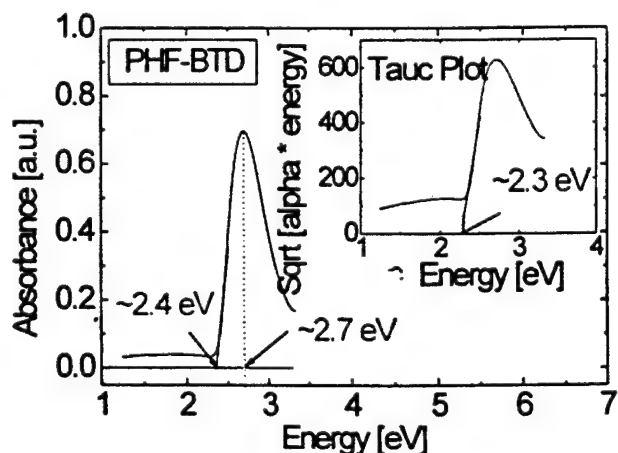
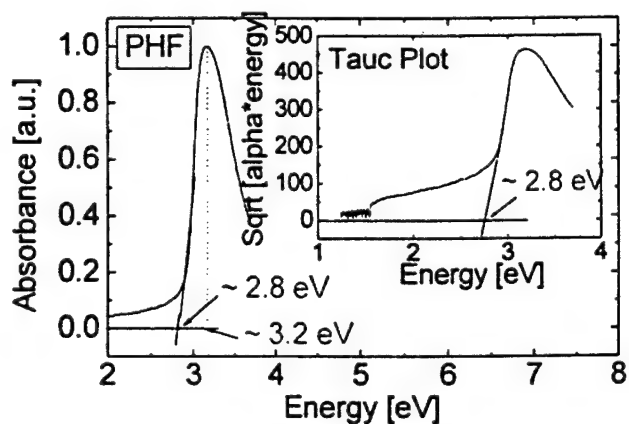
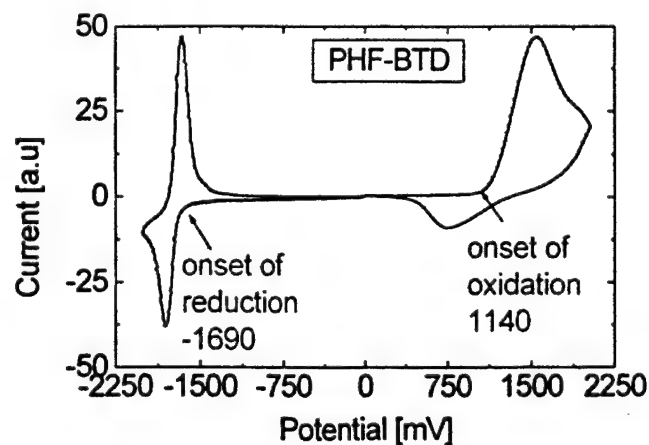
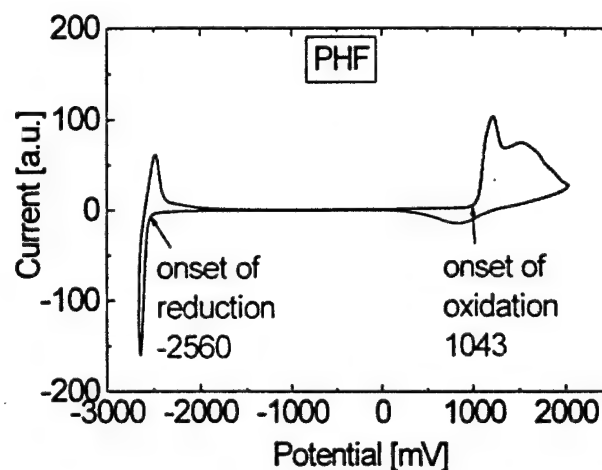
1. From these values, we concluded that the Tauc method is the best method to determine the optical band gap of the organic materials. Also there is a large difference between the optical bandgap and electronic transport gap values as shown in the Table 1. The origin of this difference is under present investigation.

Table 1. Band gap energies of the PHF, PHF-BTD, and PC6 (unit: eV)

Methods	PHF	PHF-BTD	PC6
Absorption peak	3.2	2.7	3.8
Absorption edge	2.8 (± 0.1)	2.4 (± 0.1)	3.3 (± 0.1)
Tauc plot (E_G)	2.8 (± 0.1)	2.3 (± 0.1)	3.1 (± 0.1)
CV spectra (E_T)	3.5	2.7	N/A
$E_T - E_G$	0.7	0.4	N/A



(a)



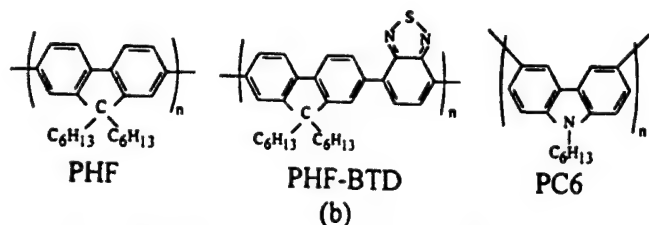
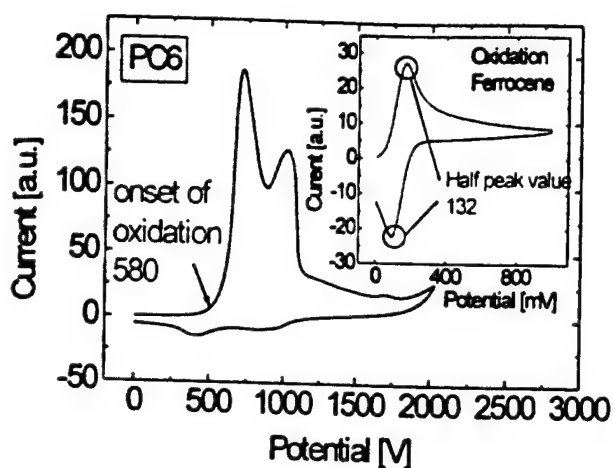


Figure 2 (a) Absorption spectra and Tauc plots of the PHF, PHF-BTD, and PC6 (b) The cyclic voltammetry spectra and chemical structures of the PHF, PHF-BTD, and PC6. (Onset values are linearly extrapolated)

Figure 3 shows the schematic diagram of energy levels for bi-layer OLEDs. The energy levels of aluminum, erbium, and gold are also shown. The solid lines in this figure represent the HOMO and LUMO levels extracted from the CV spectra by using the following equations. The dotted lines represent the LUMO levels obtained from a combination of E_G and HOMO level determined from the CV spectra.

$$\text{HOMO} = (V_{ox} - V_{1/2}) + 4.8 \text{ [eV]},$$

$$\text{LUMO} = (V_{red} - V_{1/2}) + 4.8 \text{ [eV]},$$

where V_{ox} , V_{red} , and $V_{1/2}$ are onset values of oxidation and reduction of polymers and averaged half peak value of ferrocene level, respectively.

The band gap value of the PHF-BTD and the electron injection barrier are reduced in comparison with the PHF as shown in Figure 3. The benzothiadiazole group (A-group), which is the electron-withdrawing group, was added to fluorine-based polymer (B-group) to enhance the electron injection. In our co-polymer, the ratio of A-group to B-group is about 1:1.

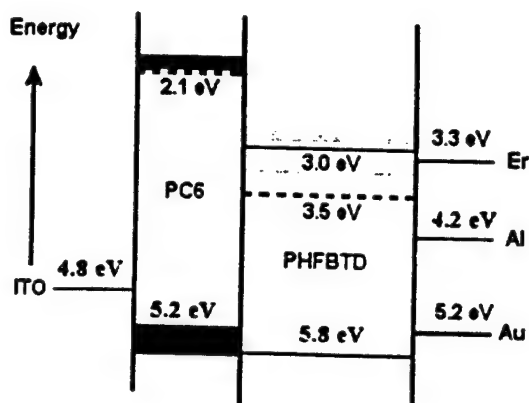
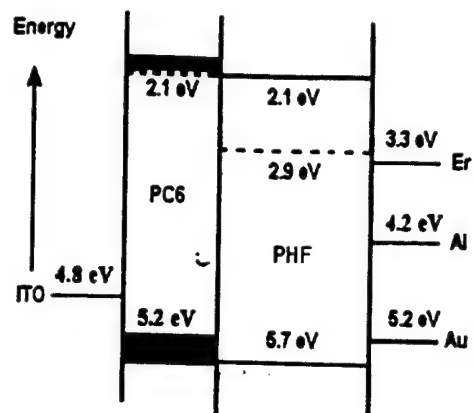


Figure 3 The energy band diagram of the fabricated bi-layer OLEDs. All values are determined within ± 0.1 eV.

The current density versus applied voltage characteristics (J-V) are shown in Figure 4. It is clearly shown in this figure that the J-V curves of the PHF-BTD OLEDs with Er have shifted by about 10 V to lower voltages in comparison with the aluminum cathode. The decrease of electron injection barrier is responsible for this shift. A shift is also observed when PHF is replaced by PHF-BTD. In this case, the barrier for electron injection is further reduced. In addition, it can also be noted from the Figure 4 that the HTL has an effect on the J-V characteristics. The curves of the double-layer OLEDs have shifted by 5-6 V in comparison with the single-layer devices. The reduction of the hole injection barrier at the anode interface is responsible for this threshold voltage shift. In summary, the introduction of the A-group in PHF-BTD and HTL in the OLEDs with Er contact have shifted the J-V characteristics by about 20 V in comparison with the PHF single layer OLEDs.

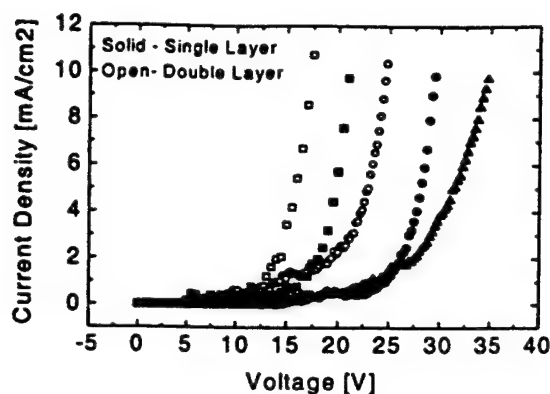
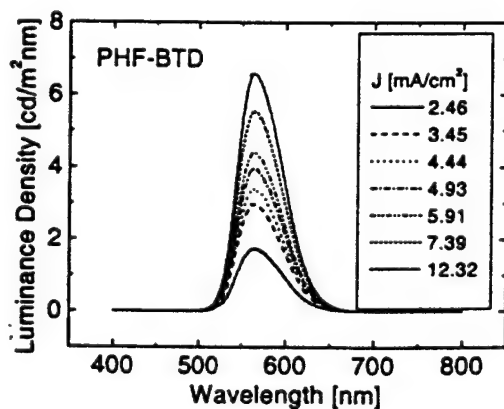
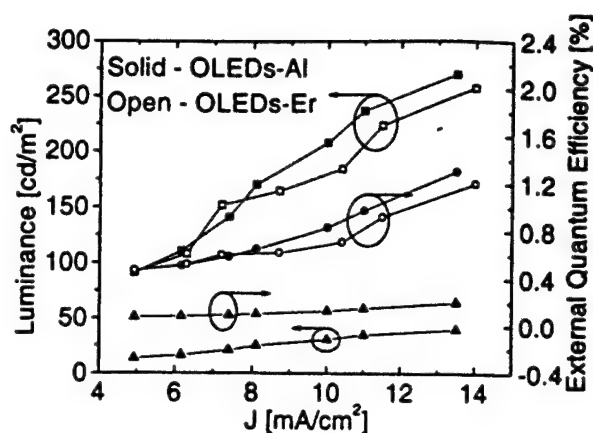


Figure 4. J-V characteristics of the fabricated OLEDs (○, ● - Al-PHF-BTD, □, ■ - Er-PHF-BTD, ▲ - Al-PHF)

In Figure 5(a) the luminance density spectra of double-layer OLEDs for various current levels are shown. From these curves, the luminance values versus current density can be obtained. For the external quantum efficiency, the number of collected photons can be also calculated from photon density curves which are similar to the luminance density curves.⁴ We found the EL peak/FWHM are 540/100 nm and 570/80 nm for PHF and PHF-BTD, respectively. In Figure 5(b), luminance of ~250 cd/m^2 , maximum external quantum efficiency of ~1.3 %, maximum power efficiency of ~0.35 lm/W and maximum emission efficiency of ~2 cd/A were obtained at relatively low current levels for both cathode metals. From this figure, about 7 to 8 times enhancement of optical performance can easily be observed between double- and single-layer devices. This is due to the reduction of the barrier for hole injection and better balance between electron and hole injections.



(a)



(b)

Figure 5 (a) EL spectra for various current density levels (b) Luminance and external quantum efficiency versus operating current density. (○, ■ - double-layer PHF-BTD, ▲ - single-layer PHF-BTD)

Conclusions

We have fabricated the bi-layer OLEDs based on poly (fluorene) using erbium as a cathode metal. A shift of the J-V characteristics by about 20 V, luminance of ~250 cd/m^2 , maximum external quantum efficiency of ~1.3 %, maximum power efficiency of ~0.35 lm/W and maximum emission efficiency of ~2 cd/A have been obtained at relatively low operating voltage for our double layer OLEDs.

Acknowledgement

This research was supported by ONR-DARPA grant (N0014-99-1-09850)

References

1. J.H. Burroughes, D.D.C. Bradley, A.R. Brown, R.N. Marks, K. Mackay, R.H. Friend, P.L. Burn, and A.B. Holmes, *Nature*, **347**, pp.539-541, 1990.
2. J. Morgado, R.H. Friend, F. Cacialli, B.S. Chuah, S.C. Moratti, and A.B. Holmes, *J. Appl. Phys.* **86**, pp.6392-6395, 1999.
3. C. Zhang, D. Braun, and A.J. Heeger, *J. Appl. Phys.*, **73**, pp.5177-5180, 1993.
4. Y. He, R. Hattori, and J. Kanicki, *Rev. Sci. Instr.*, **71**, pp. 2104-2107, 2000.
5. J. Tauc, R. Grigorovici, and A. Vancu, *Phys. Stat. Sol.* **15**, pp.627-637, 1966.
6. S. Janietz, D.D.C. Bradley, M. Grell, C. Giebeler, M. Inbasekaran, and E.P. Woo, *Appl. Phys. Lett.*, **73**, pp.2453-2455, 1998

Current-Source a-Si:H Thin-Film Transistor Circuit for Active-Matrix Organic Light-Emitting Displays

Yi He, *Member, IEEE*, Reiji Hattori, and Jerzy Kanicki, *Senior Member, IEEE*

Abstract—In this letter, we describe a four thin-film-transistor (TFT) circuit based on hydrogenated amorphous silicon (a-Si:H) technology. This circuit can provide a constant output current level and can be automatically adjusted for TFT threshold voltage variations. The experimental results indicated that, for TFT threshold voltage shift as large as ~ 3 V, the output current variations can be less than 1 and 5% for high (≥ 0.5 μ A) and low (≤ 0.1 μ A) current levels, respectively. This circuit can potentially be used for the active-matrix organic light-emitting displays (AM-OLEDs).

Index Terms—Amorphous semiconductors, light-emitting diodes, light-emitting diode displays, thin-film transistors.

RECENT enhancements of the organic light-emitting devices (OLEDs) luminous efficiency [1], brightness [2], and lifetime [3] have made possible to extend this technology to the active-matrix organic light-emitting displays (AM-OLEDs). Over the last several years, one-TFT [4], two-TFT [6], [7], and four-TFT [5] based circuits have been proposed for AM-OLEDs. Today, it is accepted that continuous excitation during the whole frame period is needed for high-performance AM-OLEDs. This requirement cannot be fulfilled by one-TFT pixel circuit (i.e., one TFT per pixel). The continuous excitation can only be achieved by either the two-TFT or four-TFT pixel circuits. Up to now most of the devices for AM-OLEDs have been based on polycrystalline silicon technology [5]–[7]. Among them, the four-TFT circuit can not only provide a continuous excitation to the OLED during the frame period, but can also partially compensate for the TFTs' threshold voltage instabilities induced by process variation and circuit aging [5].

In this work, we proposed a current-source four-TFT pixel circuit based on amorphous silicon (a-Si:H) technology. This circuit can provide a continuous current flow even after the pixel select line signal is turned off. In addition, in this circuit the TFTs threshold voltage variations can be fully compensated,

and consequently a constant current flow can be provided at all times. The proposed circuit can be used for the AM-OLEDs.

Fig. 1(a) and (b) illustrates the equivalent circuit and the top view of the current-source four-TFT pixel circuit. In this circuit, the OLED is represented by a TFT (T5) in combination with a diode capacitance (C_{diode}) in parallel. The T5 and C_{diode} sizes were optimized to ensure that under the forward bias condition the current flow in T5- C_{diode} combination is similar to the one expected for the OLED's. The fabrication process of this four- a-Si:H TFT circuit is comparable to the standard process steps developed for a conventional inverted-staggered back-channel-etch a-Si:H TFT. First, a 1000-Å thick chromium layer was deposited on Corning 1737 glass by sputtering method and patterned to form the TFT gate electrodes and the storage capacitor (C_s) bottom electrode. A-SiNx:H (3000 Å), intrinsic a-Si:H (2000 Å), and n^+ a-Si:H (500 Å) layers were then deposited by the plasma-enhanced chemical vapor deposition (PECVD) technique. After the patterning of the active area (a-Si:H island), 2000 Å thick molybdenum was deposited by sputtering method and patterned to form the TFT source-drain electrodes and storage capacitor top electrode. The interconnects between different TFTs were formed at the same time. The TFT back channel is reactive-ion etched (RIE) using the dry etching process. Then, a-SiNx:H (3000 Å) was deposited on the top to passivate the circuit.

The electrical properties of the circuit were measured using the probe station. The data (constant current, I_{data}) and source line (constant voltage, $V_{DD} = 9$ V) signals were provided by a HP 4156A semiconductor analyzer. The select line signal (pulsed voltage, V_{select}) was provided by a Keithley 237 source-measure unit with an ON voltage = 25 V, OFF voltage = 0 V, and a duty cycle of 10% (ON time: 100 ms, period: 1000 ms). The output current (I_{out}) of this circuit was measured by the HP semiconductor analyzer after the input data current (I_{data}) and source line voltage (V_{DD}) were turned off, i.e., after the pixel circuit is deselected. This will allow to verify the pixel circuit ability to provide a continuous excitation. The sampling of the output current (I_{out}) was triggered by the falling edge of the select pulse voltage signal to ensure that the data is collected after the circuit is turned off. The TFT threshold voltage was deduced from the drain current-gate voltage ($I_{DS} - V_{GS}$) characteristics.

Fig. 1(a) shows the equivalent four-TFT circuit. This circuit has four external terminals: V_{select} , I_{data} , V_{DD} , and ground. The V_{select} , I_{data} , and V_{DD} signals are provided externally, while the OLED cathode is ground terminal. Fig. 1(c) shows an example of the operational waveform that can be used for these signals. The operation of this circuit can be described as follows.

Manuscript received May 1, 2000. This work was supported in part by the Applied Physics Program, the Center for Display Technology and Manufacturing at the University of Michigan, and the DARPA-ONR Project. The review of this letter was arranged by Editor T.-J. King.

R. Hattori was with the Solid-State Electronics Laboratory, Department of Electrical Engineering and Computer Science, University of Michigan, Ann Arbor, MI 48109 USA. He is now with the Department of Electronic Device Engineering, Graduate School of Information Science and Electrical Engineering, Kyushu University, Fukuoka 812-8581, Japan.

Y. He was with the Solid-State Electronics Laboratory, Department of Electrical Engineering and Computer Science, University of Michigan, Ann Arbor, MI, 48109 USA. He is now with the Applied Physics Program, University of Michigan, Ann Arbor, MI 48109 USA (e-mail: yi.he@amd.com).

J. Kanicki was with the Solid-State Electronics Laboratory, Department of Electrical Engineering and Computer Science, University of Michigan, Ann Arbor, MI 48109 USA. He is now with Advanced Micro Devices, Sunnyvale, CA 94088-3453 USA (e-mail: kanicki@eecs.umich.edu).

Publisher Item Identifier S 0741-3106(00)10809-2.

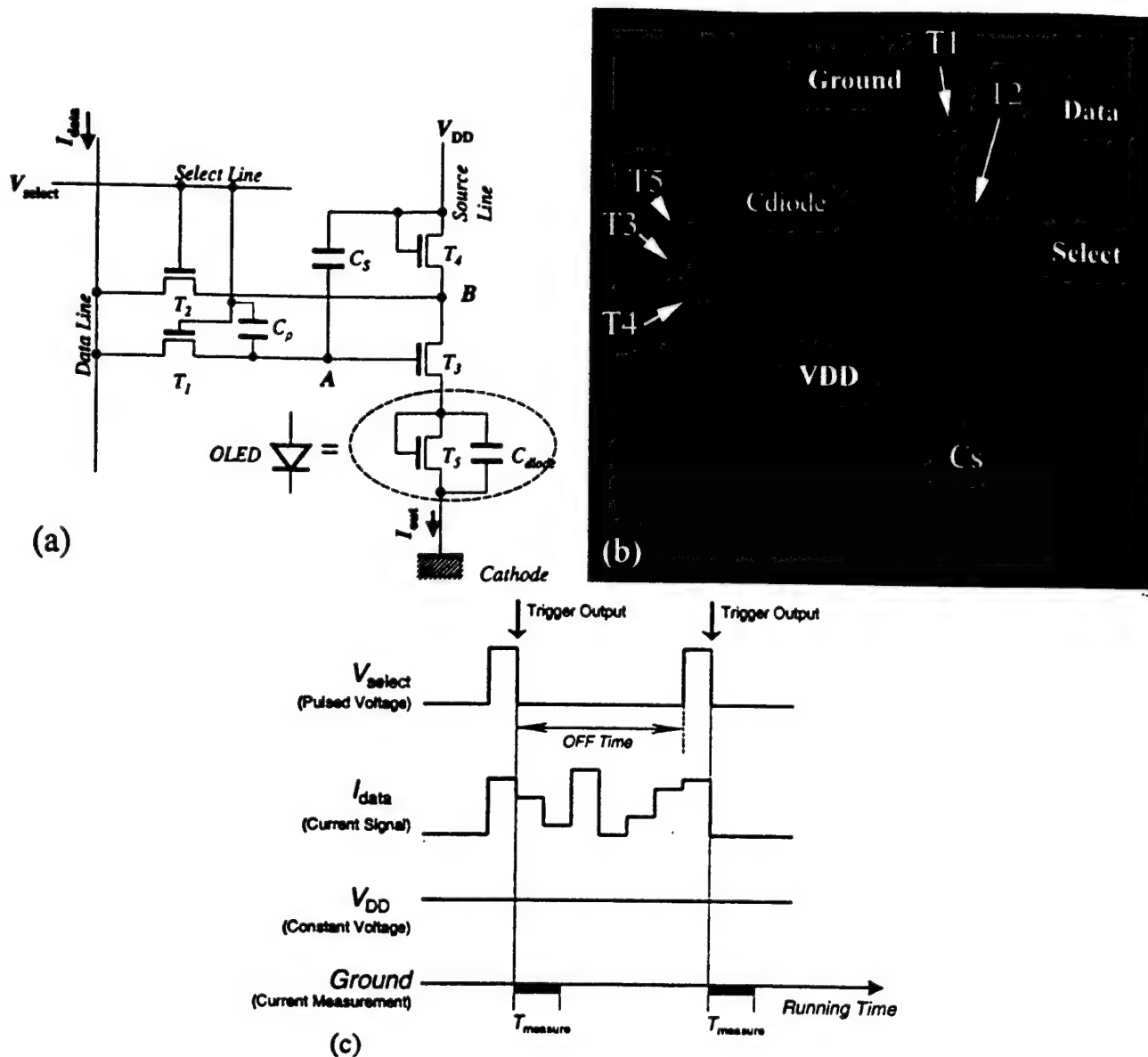


Fig. 1. (a) Equivalent circuit of the constant current-source, 4-TFT pixel circuit and (b) the top view of the circuit are shown. (c) An example of the operation waveforms that can be used for the external terminals is shown. The select line signal is a pulsed voltage with 10% duty cycle (ON time 100 ms, period 1000 ms). The data line signal is current signal that can be adjusted. The source line signal is a constant voltage source. The output current is measured on the OLED ground pad after the select line voltage signal is set low. The measurement time ($T_{measure}$) is typically 2 to 3 ms.

When the select line (V_{select}) signal is high, both T1 and T2 are turned ON. The data line signal (I_{data}) then passes through T1 and T2 and sets both the drain and gate voltages of T3. Consequently, the potentials at nodes A and B will allow the data current (I_{data}) to pass through T3. The T3 is working in the deep saturation region, e.g., $V_{DS} > V_{GS} - V_{th}$ (threshold voltage). The V_{DD} is chosen to be lower than the T3 drain voltage (to ensure that no current can flow through T4 from V_{DD}). Therefore, in this case the current flowing through T3 is equal to I_{data} . This current then will turn on the T5 (e.g., representing OLED) and will reach the ground pad. This is ON state.

When the pixel circuit is deselected and the select line signal is low, both the T1 and T2 are OFF. The T3 gate voltage, however, is maintained high by the charges stored in the storage capacitor C_s during ON state. The drain voltage of T3 will drop very quickly to lower values and consequently T4 will turn on

to maintain the same level of the output current (I_{out}). This time the current will flow from the V_{DD} to T3 via T4. If the T3 gate voltage is high and the T3 is in the saturation region, it is expected that $I_{out} = I_{data}$. This is OFF state.

In automatic adjustment, if the drive TFT (T3) threshold voltage changes and if this change is not larger than the amplitude of V_{select} during the circuit operation, T3 gate voltage needs to be changed accordingly to ensure the same output current level. This is achieved through automatic adjustment by the current signal (I_{data}) during the ON state. Therefore, the gate voltage of T3 is always adjusted to maintain the data current (I_{data}) level at about the same value, regardless of the threshold voltage value. Hence, the local V_{th} variation of the drive TFT will not affect the output current (I_{out}) level. The threshold voltage shift of other TFTs in this circuit will not have a major impact on the output current level,

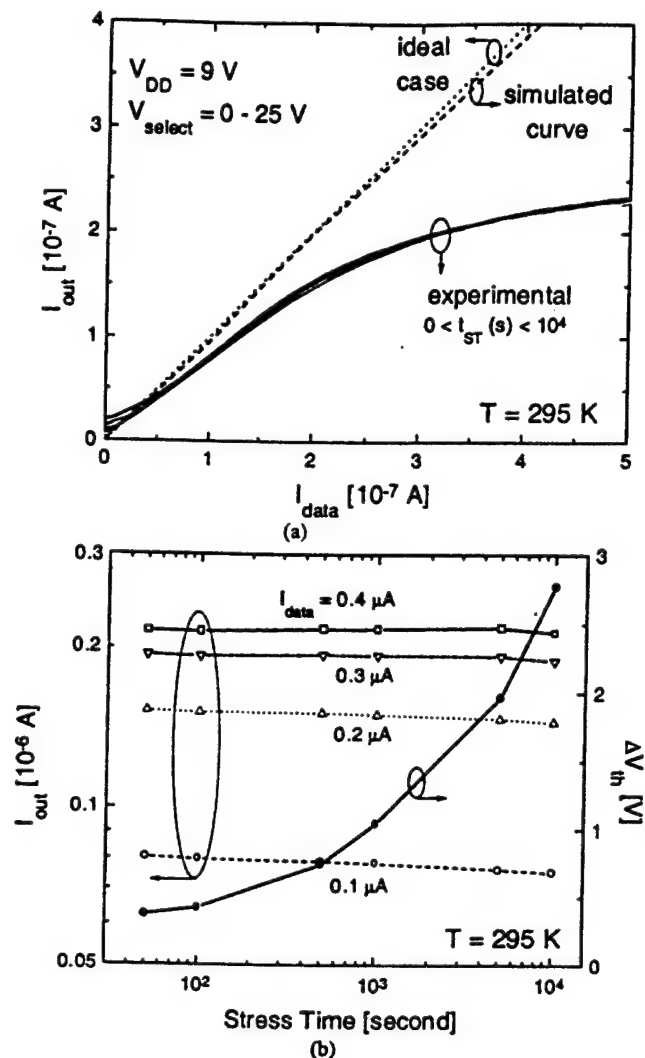


Fig. 2. (a) Output current versus data current characteristics of the four-a-Si:H TFT circuit are shown. The dotted line indicates the ideal characteristic. The dashed line represents simulated curve when a separate line in the circuit shown in Fig. 1(a) is used to control V_{dd} . (b) Output current variations as a function of the BTS time at different input data currents are shown. The t_{ST} represents the BTS time. Also shown in the figure is the drive-TFT (T3) threshold voltage shift (ΔV_{th}) with BTS time. ΔV_{th} = final threshold voltage after BTS (V_{th}^f)-initial threshold voltage (V_{th}^i).

because they are not used to control the current output in this circuit.

The above arguments also hold if the OLED current-voltage (I - V) characteristic shifts with time, which can happen after a long-term OLED operation. Consequently, the circuit can provide a constant current flow even if local variations of the diode characteristics exist.

The experimental results obtained for this circuit are shown in Fig. 2(a). The data indicate that indeed the output current is flowing even after the input data current is turned OFF, and the pixel electrode is deselected. Thus a continuous excitation can be achieved in this circuit.

To study the influence of the T3 threshold voltage (V_{th}) variation on the circuit performance, we have conducted the bias-temperature stress (BTS) of the drive TFT (T3). After BTS of 20 V on the gate electrode at 295K for about 10^4 s, the output

current levels remain essentially unchanged, as shown in Figs. 2 (a) and (b). During the BTS, the V_{th} shifted from 6.4 to 9.2 V (e.g. $\Delta V_{th} = 9.2 - 6.4 \text{ V} = 2.8 \text{ V}$), Fig. 2(b). At the same time, the output current changed only by $\sim 1\%$ at high input current ($\geq 0.5 \mu\text{A}$) and by $\sim 5\%$ at low input current ($\leq 0.1 \mu\text{A}$). These results indicate that this circuit is able to compensate for the TFT V_{th} variation to ensure a stable, constant output current level. This will allow to achieve both a good control of the display gray levels and a uniform luminance distribution over the whole AM-OLEDs.

In the ideal case $I_{out} = I_{data}$, as shown in Fig. 2(a). However, our experimental data shows that I_{out} is lower than the ideal value, and the deviation becomes larger at higher I_{data} . The curve starts to saturate at $\sim 0.4 \mu\text{A}$, resulting in a small I_{out} . This behavior is due to the shift of T3 operation point from the saturation to linear region. In this case during the OFF-state, V_{dd} is not high enough to keep T3 in the saturation region of operation. So I_{out} cannot reach the ideal level as it is during the ON-state. A higher V_{dd} is needed to enhance the output current level, but at the same time this will introduce some deviations at low current levels. This deviation can be avoided when a separate line is provided to control T4 gate voltages [8]. Furthermore, the OLED emulating configuration T5- C_{diode} has a parabolic current-voltage characteristic, while the current-voltage curve of real OLED shows an exponential behavior. Consequently, when this circuit is combined with the OLED and a separate T4 gate line, a much higher V_{dd} voltage can be selected to achieve a much higher output current level ($\geq 5 \mu\text{A}$) with an acceptable deviation ($< 0.1\%$) at low current levels [Fig. 2(a)].

In conclusion, we have developed a constant current-source pixel electrode circuit based on four a-Si:H TFTs. We have shown that this circuit can provide a stable current output independent of TFT threshold voltage shift. This circuit can potentially be used for the AM-OLEDs.

ACKNOWLEDGMENT

The authors would like to thank T. Tsukamizu, R. Tsuchiya, and Dr. S. Martin for the technical assistance.

REFERENCES

- [1] L. S. Hung, C. W. Tang, and M. G. Mason, "Enhanced electron injection in organic electroluminescence devices using an Al/LiF electrode," *Appl. Phys. Lett.*, vol. 70, pp. 152-154, 1997.
- [2] F. G. Celii and S. J. Jacobs, "High-efficiency organic LEDs," in *Proc. IDRC*, 1997, p. 314.
- [3] C. W. Tang, "Organic luminescent materials and devices," *Inf. Display*, vol. 12-10, pp. 16-19, 1996.
- [4] C. Wu *et al.*, "Integration of organic LED's and amorphous Si TFT's onto unbreakable metal foil substrates," in *IEDM Tech. Dig.*, 1996, pp. 957-959.
- [5] R. Dawson *et al.*, "The impact of the transient response of organic light emitting diodes on the design of active matrix OLED displays," in *IEDM Tech. Dig.*, 1998, pp. 875-878.
- [6] T. Shimoda *et al.*, "High resolution light emitting polymer display driven by low temperature polysilicon thin film transistor with integrated driver," in *Proc. Asia Display'98*, pp. 217-220.
- [7] M. Stewart *et al.*, "Polysilicon VGA active matrix OLED display—Technology and performance," in *IEDM Tech. Dig.*, 1998, pp. 871-874.
- [8] Y. He, R. Hattori, and J. Kanicki, Improved A-Si:H TFT circuits for active-matrix organic light emitting displays, submitted for publication.

PROCEEDINGS OF SPIE REPRINT



SPIE—The International Society for Optical Engineering

Reprinted from

Organic Light-Emitting Materials and Devices IV

**31 July–2 August 2000
San Diego, USA**



Volume 4105

Polyfluorene Light Emitting Devices on Flexible Plastic Substrates

Yi He ^{a, b} and Jerzy Kanicki ^{*b}

^aApplied Physics Program, University of Michigan, Ann Arbor, MI 48109

^bSolid State Electronics Laboratory, Department of Electrical Engineering & Computer Science, University of Michigan, Ann Arbor, MI 48109

ABSTRACT

Organic light-emitting devices (OLEDs), made of polymer bi-layer thin films, on the thin flexible plastic substrates have been fabricated and studied. The ITO and Ca/Al electrodes have been used as anode and cathode, respectively, in this structure. Both polymers--the hole-transporting and electron-transporting / light emissive co-polymers--used in this study demonstrated a very good thermal and photo-oxidative stabilities. The hole transporting co-polymer (amine-fluorene) thin film is amorphous, while the light emissive / electron-transporting co-polymer (benzothiadiazole-fluorene) thin film is partially crystalline. The photoluminescence (PL) and electroluminescence (EL) emission peaks are both located around 550 nm. The plastic substrate coated with ITO used in this study is less than 0.2 mm thick and highly flexible. It has a sheet resistance in the range of about 10 to 20 Ω/\square , and the transmittance higher than 80% in the photon energy ranging from 470 to 750 nm; the maximum transmittance is ~84.5%. The root-mean-square (RMS) of the ITO surface roughness is ~1.70 nm. The oxygen and water vapor transmission rate through the flexible plastic substrate was about 14.2×10^{-6} cc/cm²·day·atm and 1.14×10^{-4} gm/cm²·day·atm, respectively. For the OLEDs fabricated on the thin flexible plastic substrates, the typical turn-on voltage is less than 6 V, and maximum brightness is higher than 13,000 cd/m². The maximum emission efficiency, luminous efficiency, and external quantum efficiency for our OLEDs are 66.2 cd/A, 18.3 lm/W, and 16.2%, respectively.

Keywords: Organic light-emitting devices, flexible plastic substrate, permeability, luminance, quantum efficiency

1. INTRODUCTION

Since 1990¹, the opto-electric performance of the single layer polymer based OLEDs has been improved dramatically. Both red and green emission devices with the external quantum efficiency higher than ~1 % and luminous efficiency greater than ~2 lumen/watt have been reported^{1, 2}, while the blue emission devices with the external quantum efficiency as high as 3 % have also been demonstrated³. All these devices have been fabricated on the glass substrates.

On the other hand, unlike glass, the flexible plastic substrate has a distinct advantages (more robust and compact, lighter weight and cost effective) that can be very attractive for certain display applications. This is especially true for new portable display products, such as cellular phones, mobile phones, personal digital assistants, and laptop computers⁴. The use of the flexible plastic substrates will also enable new product concepts such as curved or flexible displays and all plastic electronic devices^{5, 6}. While it is a very promising new technology, its low processing temperature, large heat induced shrinkage, high gas permeability, low chemical resistance, water and solvent durability, and somewhat low transparency, however, limit the plastic substrate application. In general, the OLED's performance on the plastic substrates is worse in comparison with the OLED fabricated on the glass substrate (e.g. the highest external quantum efficiency ever reported for the OLEDs on the plastic substrate is ~1 %⁵—about 4 times lower than the highest value reported for the OLEDs on the glass substrate.). As mentioned above another major disadvantage of the plastic substrate is its relatively high penetration level of the moisture and oxygen. Their presence is considered to be one of the major factors affecting the OLED electrical stability⁷. Various inorganic or organic materials are being deposited on the plastic substrate to reduce the moisture and oxygen diffusion. The compatibility of the plastic substrate with the various solvents used during the polymer spin-coating is another important issue to be considered for its application in the OLEDs.

In this paper we describe the fabrication and opto-electrical characteristics of a high-efficiency bi-layer organic polymer light-emitting device (OLED) with Ca cathode fabricated on the ITO coated thin, flexible plastic substrate. Compared with

* Correspondence: kanicki@eecs.umich.edu; WWW: <http://www.eecs.umich.edu/~fpdum>; Telephone: 734 936 0964; Fax: 734 936 0347

the highest external quantum efficiency value previously reported⁵ for OLEDs on the plastic substrate, the value for our device is significantly improved.

2. EXPERIMENTAL

Figure 1 illustrates the compound structure and chemical formula of the two polymers used in this study. Polymer A, random co-polymer poly(9,9'-dioctyl fluorene-2,7-diyl)-co-poly(diphenyl-p-tolyl-amine-4,4'-diyl), is used as the hole transport polymer. Polymer B, random co-polymer poly(9,9'-dioctyl fluorene-2,7-diyl)-co-poly(benzothiadiazole 2,5-diyl) is used as the light emissive polymer. Both polymers used in this study were provided by Dow Chemical Corp. (Midland, MI). The bi-layer OLED heterostructure, shown in Figure 2, consists of a hole transporting (HTL, ~170 Å) and an emissive (EL, ~2000 Å) polymer layers sequentially deposited on the flexible plastic substrate by the spin-coating technique. The substrate was repeatedly cleaned in the ultrasonic baths of de-ionized water and isopropanol before its use. After the pre-deposition cleaning, the substrate was exposed to UV-ozone atmosphere before the spin coating of the polymer layers. Calcium cathode electrode (~1000 Å) was evaporated in a vacuum chamber at the base pressure ~ 10^{-6} torr through a shadow mask. On the top of the calcium cathode electrode, a layer of aluminum (~1000 Å) was evaporated in the same vacuum chamber to protect the calcium electrode from oxidation. The electroluminescence (EL) of the OLEDs was measured with a CCD spectral analyzer through optical fibers. The CCD spectral analyzer was calibrated with a Labsphere USS-600 Uniform Source System (incorporating a calibrated lamp and a motorized variable attenuator)⁸. This calibration allows us to obtain the luminance wavelength distribution of the measured light-emitting object. During the EL measurement, the OLED and the optical fiber were placed at the different sides of a convex lens. Both the distance between the lens and the OLED and the distance between the lens and the optical fiber are 2 times the focal length of the lens. The angular distribution of the Lambertian emission was assumed to correct the measured OLED luminance (cd/m^2)⁹.

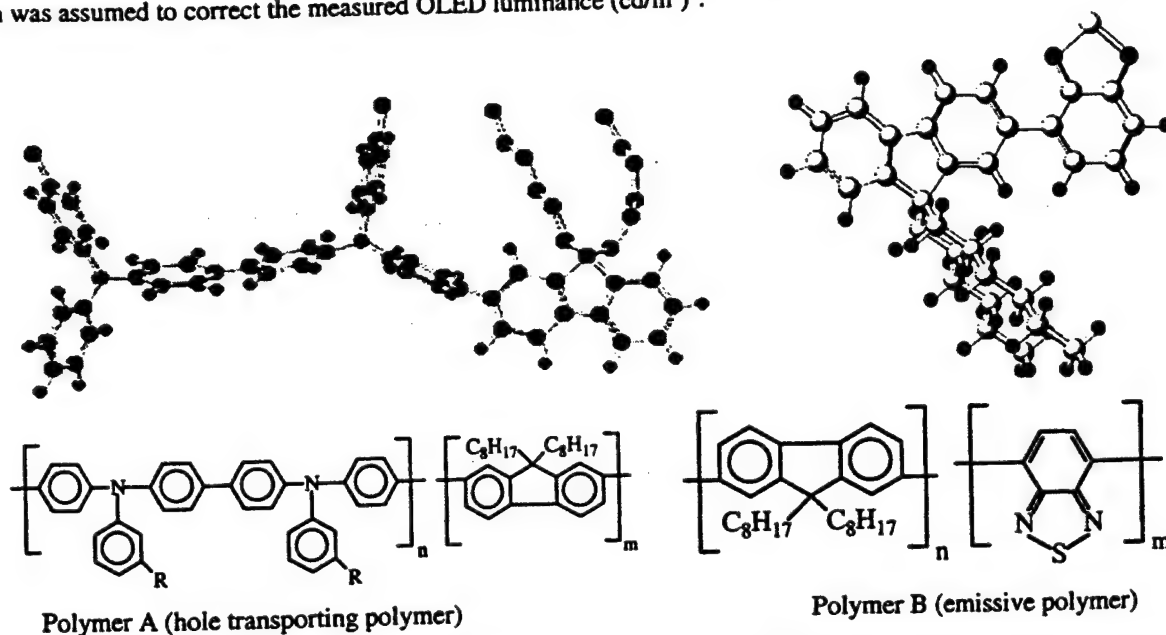


Figure 1. The chemical structures of amine-fluorene (polymer A) and benzothiadiazole benzothiadiazole-fluorene (polymer B) used in this study.

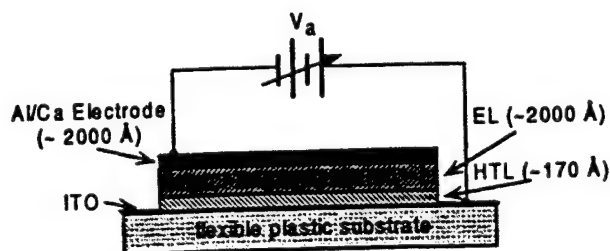


Figure 2. The device structure of the organic light-emitting heterostructure device on flexible plastic substrate.

No corrections were made for the absorption of the lens and plastic substrate, refraction/reflection at the polymer-plastic-air interfaces, or other effects that could decrease the light emission intensity from the OLEDs. The current-voltage characteristics of the OLEDs were measured in a vacuumed metal box with shielded cables connecting the voltage source, current meter and the probes inside the measurement box.

3. RESULTS AND DISCUSSION

3.1 Flexible Plastic Substrate

Polaroid Corp. provided the flexible plastic substrate used in this study¹⁰. It has a multi-layer structure, as illustrated in Figure 3, to minimize the oxygen and moisture penetration rate through the substrate and to maximize the ITO conductivity. The thickness of the ITO layer is ~470 nm and the thickness of the remaining plastic base is ~140 μm . The refractive indexes of the top ITO layer and plastic base are 2.1 and 1.51, respectively. The O:In:Sn atomic ratio of the ITO film, as determined by XPS, is 0.54:0.42:0.04, respectively.

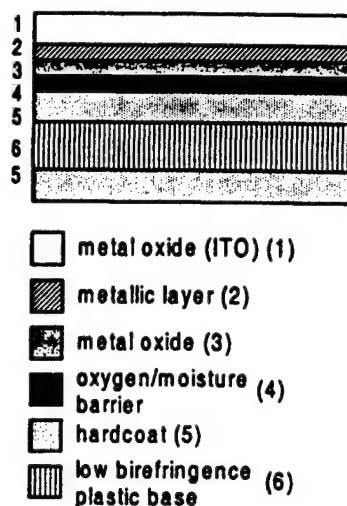


Figure 3. The multi-layer structure of the flexible plastic substrate used in this study.

Electrical Conductivity

Due to the low resistivity of the ITO layer, contact resistance between the probe and the ITO layer cannot be ignored in the ITO conductivity measurements. Therefore, the van der Pauw (four-point-probe) method was used¹¹. In this work, the four-point-sharp-tip method was used to measure the ITO conductivity of the flexible plastic substrate, as shown in Figure 4. For this method, four evenly spaced sharp tips were aligned in a straight line. The distance between two adjacent tips was 62.5 mil (~1.59 mm). The current was applied on the two outer tips and the voltage drop was measured on the inner two tips.

To calculate the ITO film sheet resistance (Ω/\square), equation (1) was used¹¹. For this equation to be valid, the sample size needs to be much greater than the probe spacing and the film thickness needs to be much smaller than the probe spacing, i.e., $D \gg s \gg t$, where D , s , t are the dimension of the sample, probe spacing, and ITO film thickness, respectively.

$$R = \frac{\ln 2}{\pi} \frac{V}{I} \approx 4.532 \frac{V}{I} \quad (1)$$

Figure 5 illustrates the obtained results for 6"×6" sample. The sheet resistance, calculated using equation (1), is ~12.18 Ω/\square .

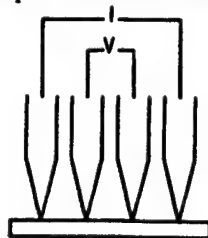


Figure 4. The four-point-sharp-tip measurement method used to determine the ITO conductivity.

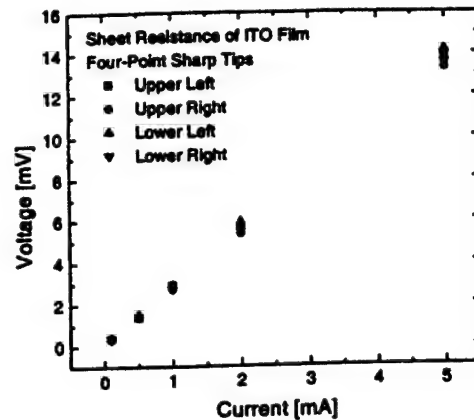


Figure 5. ITO sheet resistance.

Surface Roughness

The surface roughness of the ITO film was measured using Atomic Force Microscope (AFM) in the contact mode. The root-mean-square (RMS) value for the $0.5 \times 0.5 \mu\text{m}$ sample size is about 1.70 nm (Figure 6). This RMS value is comparable with the RMS value obtained for thermally-annealed ITO film deposited on the glass substrate.

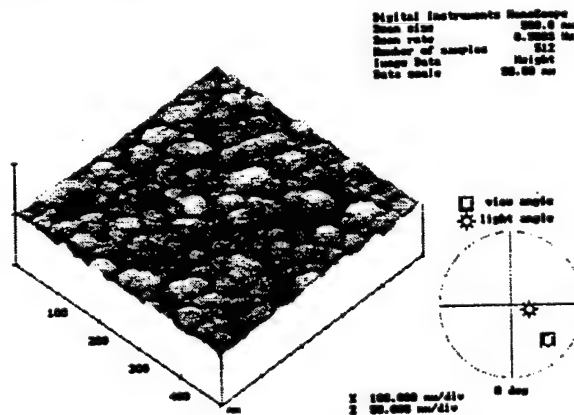


Figure 6. AFM images of the ITO film deposited on flexible plastic substrate.

Optical Transmittance

Figure 7 shows the transmittance spectrum of the ITO coated flexible plastic substrate measured against the air. The optical transmittance is higher than 80% from ~440 to ~760 nm, with the peak transmittance of ~84.5% at around 630 nm. The optical transmittance is ~83.7% at around 550 nm, where the peak of the OLED electroluminescence is located. Figure 7 also indicates that electroluminescence peak is located in the region of maximum transmittance of the substrate.

The optical bandgap (E_g) for the direct bandgap allowed transition¹² of the ITO deposited on plastic substrate can be associated with the film absorption coefficient (α) by equation (2):

$$\alpha = (h\nu - E_g)^2 \quad (2)$$

where $h\nu$ is the photon energy. Figure 8 shows the square of absorption coefficient versus photon energy for the ITO film deposited on the flexible plastic substrate. By extrapolating the straight portion of the α^2 curve to the $h\nu$ axis, the energy

gap of ~ 3.56 eV can be obtained. Because there is no direct evidence for whether ITO film is direct or indirect bandgap semiconductor, it is convenient to define an optical energy (E_g^{opt}) for a given α , for example, $\alpha=6 \times 10^4 \text{ cm}^{-1}$. A plot of α in logarithm scale versus $h\nu$ is also shown in Figure 8. The optical energy value obtained by this definition is ~ 3.26 eV.

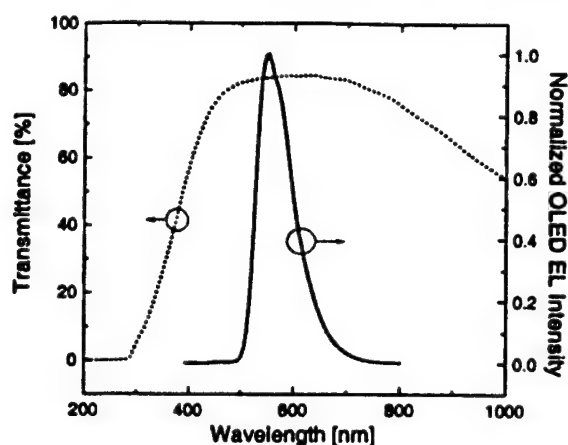


Figure 7. Transmittance spectrum of the flexible plastic substrate. The OLED EL peak is located in the maximum transmittance region of the substrate.

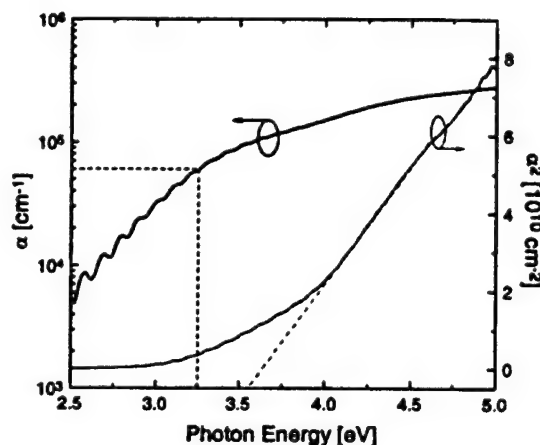


Figure 8. Plots of α^2 and α as a function of photon energy for the ITO film deposited on flexible plastic substrate.

X-ray diffraction

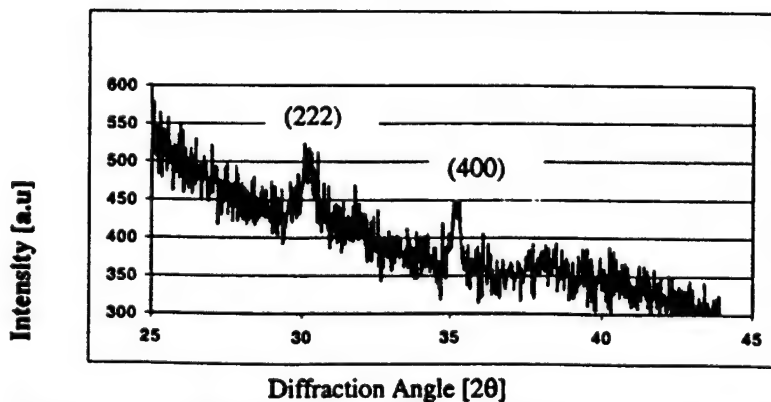


Figure 9. X-ray diffraction of the ITO film deposited on flexible plastic substrate.

The X-ray was performed by using rotating anode Rigaku X-ray facility (Cu K α radiation). The (222) and (400) peaks can be identified in the Figure 9. From the XRD pattern we can see that the ITO film does not show any very strong well-defined peaks, indicating that the ITO structure is mostly amorphous.

Oxygen and Water Permeability

A major disadvantage of the plastic substrate is its relatively high penetration level of the moisture (water) and oxygen. The presence of the moisture and oxygen is considered to be one of the major factors affecting the OLED electrical stability⁹. To fabricate OLED with a long lifetime, the diffusion of the oxygen and moisture through the substrate need to be minimized.

We have analyzed the oxygen transmission rate through the plastic substrate at 37.8 C with 90% relative humidity. The 100% dry nitrogen was introduced to both sides of the flat plastic at a flow rate of 10 cc/min. At equilibrium, the flow of nitrogen of the test gas side was switched to a flow of 100% oxygen. Then, the oxygen transfer of the flat film from the test gas side into the carrier gas side was measured with a coulometric detector until the equilibrium transmission rate is reached. Measurements of several plastic samples indicate oxygen transmission rate ranging from 14.2×10^{-6} to 22.7×10^{-6} cc/cm²·day·atm.

The water vapor permeability through the flat thin film from the test side into the carrier gas side until the equilibrium transmission rate is reached was monitored at 37.8 C using an infrared detector method. The water vapor transmission rate was about 1.14×10^{-4} gm/cm²·day·atm.

These values indicating that the plastic substrate used in this study is a good oxygen and water vapor barrier. Proper film coatings can further reduce these values below detectable limit of the measurement system. These results will be reported in a separate publication.

3.2 OLED Electrical and Optical Properties

The materials' properties of the polymers used in this study were reported elsewhere¹³. The typical DC current-voltage (I-V) characteristic of the OLEDs fabricated on the plastic substrate is illustrated in Figure 10.

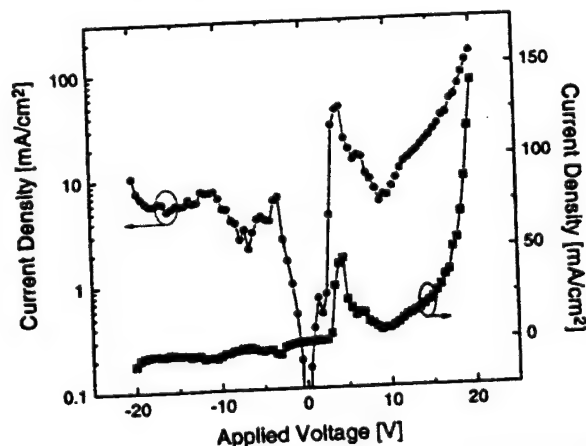


Figure 10. DC current-voltage characteristic of the OLED with Ca cathode fabricated on the flexible plastic substrate.

The I-V curve indicates a diode-like behavior, with a threshold voltage at about 15 V. The I-V characteristic shows a "bump" starting at -2 V and peaking at -4 V. Visible light emission occurred at voltage corresponding to the peak of the I-V characteristic.

Figure 11 shows the normalized absorbance, photoluminescence (PL), and electroluminescence (EL) spectra of the OLED structure. The emission spectra clearly show a peak located at around 545 nm, with a shoulder peak located at around 570 nm. The full-width-at-half-maximum (FWHM) of this peak is about 80 nm. The EL and PL spectra are Stokes shifted with respect to the absorption spectrum. Also the PL and EL spectra are very similar, suggesting that the same emitting species have been involved in both cases. We can speculate that under forward applied bias, the electrons and holes are injected (or

transported) into the polymer LUMO and HOMO bands. These carriers, through electron-phonon lattice coupling, will relax to negatively and positively charged polarons that can move toward each other under the influence of the applied electrical field. Eventually they can recombine on a certain segment of polymer chain to form the singlet excitons. Through the resonance interactions, these singlet excitons can also form the excimers or exciplexes, which can emit light Stokes shifted with respect to the absorption spectrum. This description of the light-emitting mechanism is in good agreement with our experimental data.

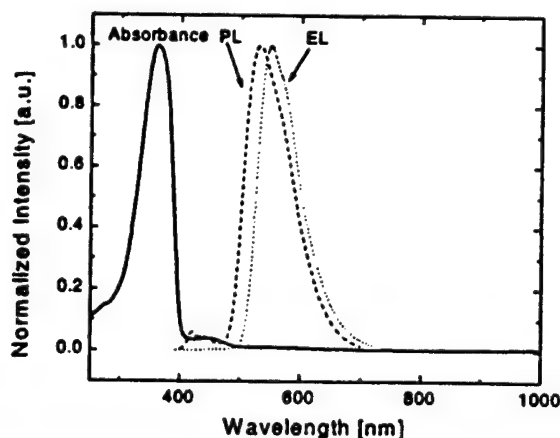


Figure 11. The absorbance, photoluminescence, and electroluminescence of the OLED heterostructure.

The electroluminescence of the OLED induced by the different operating current densities has been studied. Figure 12(a) shows the OLED spectral distribution of the luminance at the different current densities. The shapes of all the EL spectra are almost identical to each other with a minor exception at lower current densities, where the vibration modes appear to have larger contribution to the EL spectrum at off-peak wavelength. The brightness versus current density plot, Figure 12(b), indicates a nearly linear relationship between the luminance (obtained through integration of the area under the luminance distribution peak at different current densities) and current density. The maximum device brightness achieved is $\sim 13,000$ cd/m^2 .

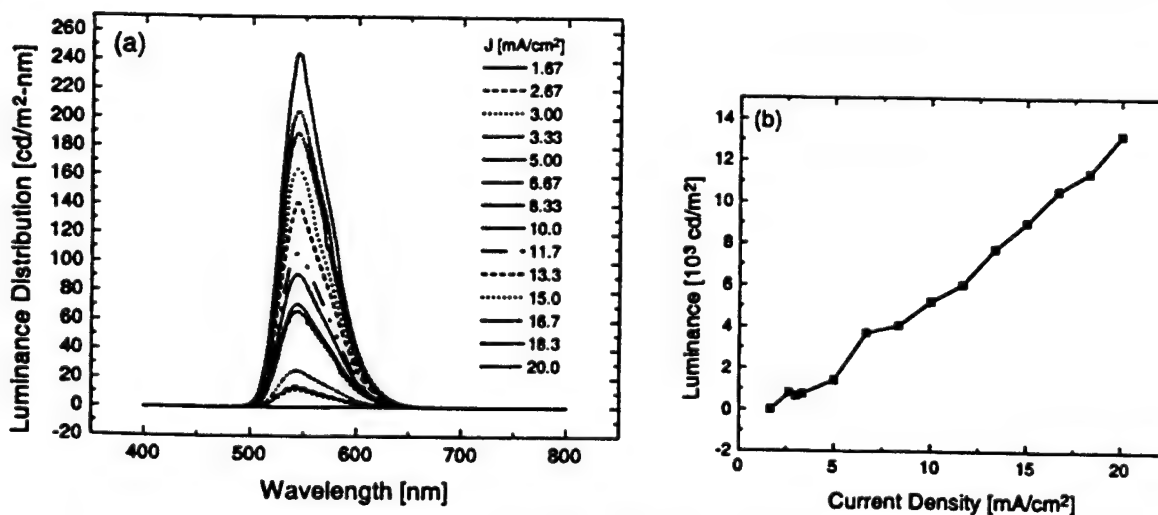


Figure 12 (a) Spectral distribution of the OLED luminance obtained at the different operating current densities. (b) The evolution of the brightness versus the operating current density is shown.

To calculate the OLED external quantum efficiency (defined by the number of photons emitted by the device in the forward direction per electron supplied by the external circuit), it is necessary to know the wavelength distribution of the photon emission, which can only be obtained from a known electroluminescence radiance distribution. Figure 13(a) illustrates the photon density distribution of the OLED at different applied current densities. For our OLEDs, the external quantum

efficiency is calculated by dividing the output photon density by the applied current density. The device external quantum efficiency of the OLED (Figure 13 (b)) increases near monotonically with the increasing current density. The maximum external quantum efficiency, calculated using the method described above from the photon density distribution curve (Figure 13 (a)), is $\sim 16.2\%$ which appears at about 20 mA/cm^2 .

Figure 14 shows the evolution of the OLED emission efficiency and power efficiency as functions of the device brightness. It is clear from this figure that the emission efficiency increases near monotonically with the device brightness but slowly saturates at high OLED brightness. However, the device power efficiency decreases rapidly and monotonically when the device brightness is high. The maximum emission and power efficiencies we obtained are $\sim 66.2 \text{ cd/A}$ and 18.3 lm/W , respectively.

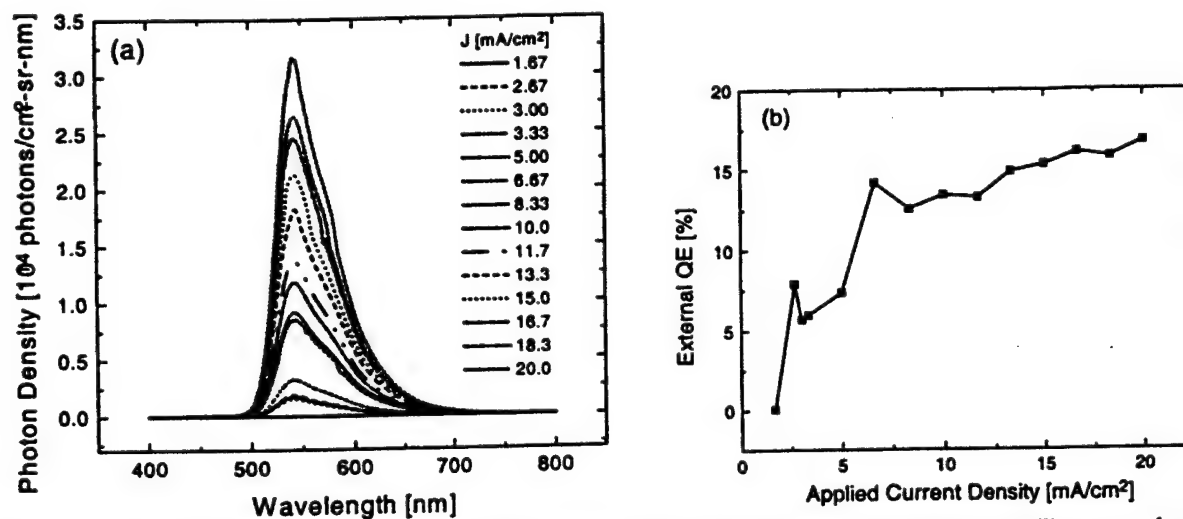


Figure 13. (a) Photon density distribution of the OLED induced by different operating current densities. (b) The current density dependence of the device external quantum efficiency.

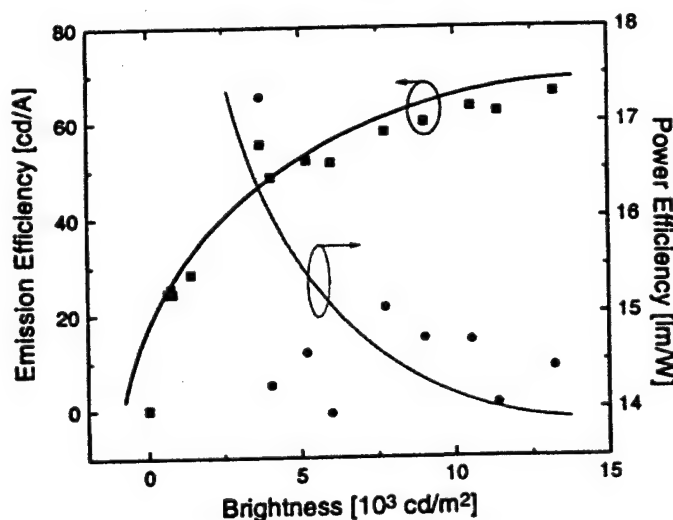


Figure 14. The evolution of the OLED emission efficiency and power efficiency as functions of device brightness.

4. CONCLUSIONS

We have demonstrated a high performance organic polymer based light-emitting heterostructure device fabricated on the flexible plastic substrate using calcium as the cathode material. Both the OLED luminance efficiency and external quantum

efficiency have been greatly improved in this structure in comparison with the published data in the open literature. Good brightness ($> 13,000 \text{ cd/m}^2$), high emission efficiency ($> 66.2 \text{ cd/A}$) and external quantum efficiency ($\sim 16.2 \%$), and acceptable power efficiency ($\sim 18.3 \text{ lm/W}$) have been achieved for our devices.

ACKNOWLEDGEMENT

This research project was supported by the Center for Display Technology and Manufacturing at the University of Michigan, and DARPA-ONR grant (N0014-99-1-0958). We also would like to thank Zhiqi He for her assistance with this paper preparation and for some of experimental data.

REFERENCES

- 1 G. Yu, H. Nishino, A.J. Heeger, T.-A. Chen, R.D. Rieke, "Enhanced electroluminescence from semiconducting polymer blends", *Synth. Met.*, **72**, pp. 249-252, 1995.
- 2 F. Cacialli, R.H. Friend, N. Haylett, R. Daik, W.J. Feast, D.A. dos Santos, and J.L. Bredas, "Efficient green light-emitting diodes from a phenylated derivative of poly(p-phenylene-vinylene)", *Appl. Phys. Lett.*, **69**, 3794-3796, 1996.
- 3 Y. Yang, Q. Pei, and A.J. Heeger, "Efficient blue polymer light-emitting diodes from a series of soluble poly(paraphenylene)s", *J. Appl. Phys.*, **79**, 934-939, 1996.
- 4 N.D. Young, R.M. Bunn, R.W. Wilks, D.J. McCulloch, S.C. Deane, M.J. Edwards, G. Harkin, A.D. Pearson, "Thin-film-transistor- and diode-addressed AMLCDs on polymer substrates", *Journal of the SID* **5/3**, pp. 275-281, 1997.
- 5 G. Gustafsson, Y. Cao, G.M. Treacy, F. Klavetter, N. Colaneri and A.J. Heeger, "Flexible light-emitting diodes made from soluble conducting polymers", *Nature*, **357**, pp. 477-479, 1992.
- 6 A. Stein, A. Liss, S. Fields, "High-temperature acrylic plastic substrates: thermal, chemical, and mechanical properties", *SID 97 Digest*, pp. 817-820, 1997.
- 7 A. Bernsten, Y. Croonen, C. Liedenbaum, H. Schoo, R.-J. Visser, J. Vleggaar, P. Weijer, "Stability of polymer LEDs", *Optical Materials*, **9**, pp. 125-133, 1998.
- 8 Y. He, R. Hattori, and J. Kanicki, "Light output measurements of the organic light-emitting devices", *Review of Scientific Instruments*, **71**, pp. 2104-2107, 2000.
- 9 N.C. Greenham, R.H. Friend, and D.D.C. Bradley, "Angular dependence of the emission from a conjugated polymer light-emitting diode: implications for efficiency calculations", *Adv. Mater.*, **6**, pp. 491-493, 1994.
- 10 P. Y. Z. Chu, H. C. Choi, L. S. Heath, C. S. Ko, J. Mack, P. Nagarkar, J. Richard, W. Smyth, T. Wang, "A New Conductor Structure for Plastic LCD Applications Utilizing 'All Dry' Digital Laser Patterning", *SID 98 Digest*, 1099 (1998).
- 11 R. L. Elsenbaumer and L. W. Shacklette, *Handbook of Conducting Polymers*, (Edited by T. A. Skotheim), Marcel Dekker, Inc., 1986.
- 12 J.-H. Lan, J. Kanicki, A. Catalano, J. Keane, W. den Boer, T. Gu, "Patterning of Transparent Conducting Oxide Thin Film by Wet Etching for a-Si:H TFT-LCDs", *Journal of Electronic Materials*, **25**, pp. 1806-1817, 1996.
- 13 Y. He and J. Kanicki, "High-efficiency organic polymer light-emitting heterostructure devices on flexible plastic substrates", *Applied Physics Letters*, **76**, pp. 661-663, 2000.

PROCEEDINGS OF SPIE REPRINT



SPIE—The International Society for Optical Engineering

Reprinted from

Organic Light-Emitting Materials and Devices IV

**31 July–2 August 2000
San Diego, USA**



Volume 4105

Materials and Device Structures for High Performance Poly OLEDs on Flexible Plastic Substrates

Yongtaek Hong, Zhiyong Hong, and Jerzy Kanicki

Solid State Electronics Laboratory, Department of Electrical Engineering and Computer Science,
University of Michigan, Ann Arbor, MI 48109

ABSTRACT

Organic polymer light-emitting devices (Poly OLEDs) with the bi-layer thin film structures have been fabricated on both glass and flexible plastic substrates. The structural, optical, and electrical properties of each organic polymer layer have been optimized for the Poly OLED optimum electrical performances. The spin coating technique was used to fabricate our devices. An alternating co-polymer of poly (9, 9'-dihexyl fluorene-2, 7-diyl) and poly (benzothiadiazole 2, 5-diyl) (PHF-BTD), and poly (9-hexyl carbazole-3, 6-diyl) (PC6) have been used as light emitting and hole transporting polymer, respectively. The combination of the optical and cyclic voltammetry (CV) analysis has been used to develop the band diagram for our Poly OLEDs. For our polymers, the oxidation / reduction processes are well defined and clearly observed in the CV spectra. This allows a direct comparison of the polymers band gaps determined by both the optical and electrical methods. The photoluminescence and electroluminescence emission peaks are both located around 570 nm, and maximum brightness up to 2000 cd/m² was obtained. Turn-on voltages of ~16 and ~20 V, acceptable emission efficiencies of ~5.5 and ~4.2 cd/A, good power efficiencies of ~0.9 and 0.6 lm/W, and acceptable external quantum efficiencies of 1.8 and 1.6 % have been obtained for OLEDs fabricated on both glass and plastic substrates, respectively.

Keywords: Organic light-emitting devices, plastic substrate, cyclic voltammetry, luminance, quantum efficiency

1. INTRODUCTION

Since the first development of the organic polymer light emitting devices (Poly OLEDs) based on conjugated polymers in 1990¹, only recently the Poly OLEDs have gained considerable attention for such applications as mobile communication and automotive displays. The thin films can easily be fabricated by a spin coating technique, which renders polymers a low cost and uniform process over the large substrates. So far, research and development of the Poly OLEDs have mostly been concentrated on poly (phenylenevinylene) (PPV) and its derivatives due to excellent device performances.^{1, 2, 3, 4, 5} Our group reported the comparable electrical and optical performances for Poly OLEDs based on poly (fluorene) polymer.⁶ The poly (fluorene) based polymers were also used to fabricate blue light-emitting devices.^{7, 8} In our light emitting polymer, poly (benzothiadiazole) group (A-group) was added to poly (fluorene) (B-group) to increase the polymer electron affinity, hence to improve the electron injection into the Poly OLED. The benzothiadiazole group is playing role of electron-withdrawing group in the conjugated polymers. In our co-polymer the ratio of A-group to B-group was about 1:1. In this paper, we report on performance of the bi-layer Poly OLEDs fabricated on both glass and flexible plastic substrates from these new light emissive and hole transporting materials.

2. EXPERIMENT

Corning 1737 glass substrates 1.1mm thick were used in this study. The glass substrates were cleaned in acetone and isopropanol solutions before sputtering of the indium tin oxide (ITO) (~ 900 Å) in a vacuum chamber (base pressure < 10⁻⁷ mbar) at room temperature. The Polaroid plastic substrates coated with ITO were used in this work. The ITO layer was used as a transparent anode electrode in Poly OLEDs. The ITO layer for both substrates has a transparency higher than 80% over the visible range (400 – 800 nm). The sheet resistance was ~ 50 ohm/□ and ~ 10 ohm/□ for glass and plastic substrates, respectively. The ITO covered substrates were cleaned in the ultrasonic bath of isopropanol and exposed to UV-ozone for 15 minutes before polymer spin coating. First, a hole-transporting layer (HTL, 300–400 Å) was spin coated from the solution in chloroform. Then, an emissive layer (EL, ~1000 Å) was spin-coated from the solution in benzene. Solvents used for the EL and HTL material were carefully chosen according to the polymer solubility in several solvents. In the double layer structure

used in this work, the HTL was not dissolved by benzene during the device fabrication. As a cathode electrode, aluminum was evaporated through shadow masks in an electron-beam (E-Beam) evaporation system under a high vacuum ($\sim 10^{-7}$ torr).

The absorption and photoluminescence (PL) spectra were measured with a CARY UV-Visible spectrophotometer and FluoroMax-2, respectively. Films of comparable thickness used in Poly OLEDs were prepared on the quartz substrates for these measurements. The cyclic voltammetry (CV) data were recorded by a home made three-electrode electrochemical controlled by a computer. The electroluminescence (EL) was measured in the air by a CCD spectrum system with optical fibers, which has been calibrated by a Labsphere USS-600 Uniform Source System with a light source and a programmable attenuator. The initial light emission data were collected through a convex lens located at two times focal length from Poly OLEDs and optical fibers as shown in figure 1. The luminance and light output power were derived from measured data by assuming the angular distribution of the Lambertian emission⁹. The effect of the substrates and interfaces between different layers were not included in this calculation. The current-voltage characteristics were also measured in the air with a programmable voltage source and a current meter.

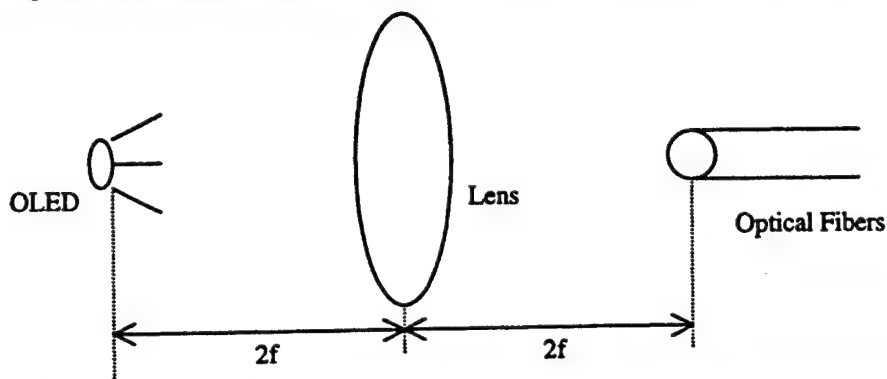


Figure 1. Schematic representation of the EL measurement system. A convex lens was used to collect light. The effect of lens was also included in the calibration method.¹⁰

3. RESULTS AND DISCUSSION

3.1. Materials Properties

Figure 2 shows the absorption, photo-luminescence (PL), and electroluminescence (EL) spectra of PHF-BTD and PC6,

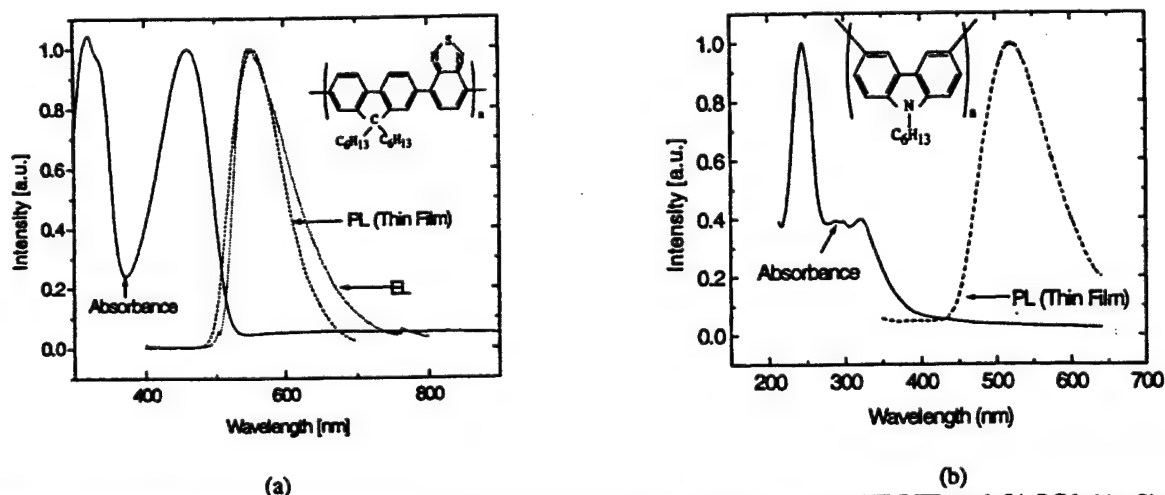


Figure 2. The absorption, photoluminescence, and electroluminescence spectra of (a) PHF-BTD and (b) PC6 thin films. (Inset figure shows the chemical structures for both polymers).

respectively. The chemical structures for both polymers are shown in the inset of Figure 2. To increase the electron affinity of the emissive polymer, the benzothiadiazole has been added to the poly (fluorene). The number and weight average molecular weights of PHF-BTD, were $M_n=15000$, $M_w=25000$, respectively. For PC6, $M_n=21000$ and $M_w=100000$ have been obtained. Both polymers also showed a good thermal stability. The 5% weight-loss, which was measured in the nitrogen environment, was observed at 447 and 506 °C for PHF-BTD and PC6, respectively, by using the thermal gravity analysis (TGA). The EL spectrum measured for the ITO/PHF-BTD/Al single-layer structure showed a peak located at 570 nm. No EL was observed from the ITO/PC6/Al single-layer structure. The PL spectra showed a Stokes-shifted peak from the absorption peak for both polymers. The PL peak values are located at 570 and 520 nm for PHF-BTD and PC6, respectively. The EL and PL peak values of the emissive polymer used in this study are red shifted in comparison with the values obtained for our previous emissive co-polymer (~ 545 nm).¹¹ The origin of the PL emission for both EL and HTL is under present investigation. It can be speculated that PL emission for both polymers can be associated with the excimer emission due to poly (fluorene) aggregation.¹²

To determine the optical band gap and the position of the lowest unoccupied molecular orbital (LUMO) and highest occupied molecular orbital (HOMO) for both polymers, the cyclic voltammetry (CV) analysis, combined with the absorption spectra, was used. The CV analysis is a dynamic electrochemical method employed to study reduction and oxidation (redox) properties of the materials.¹³ The cyclic voltammograms of PHF-BTD and PC6 are shown in Figure 3. The potentials have been measured versus the

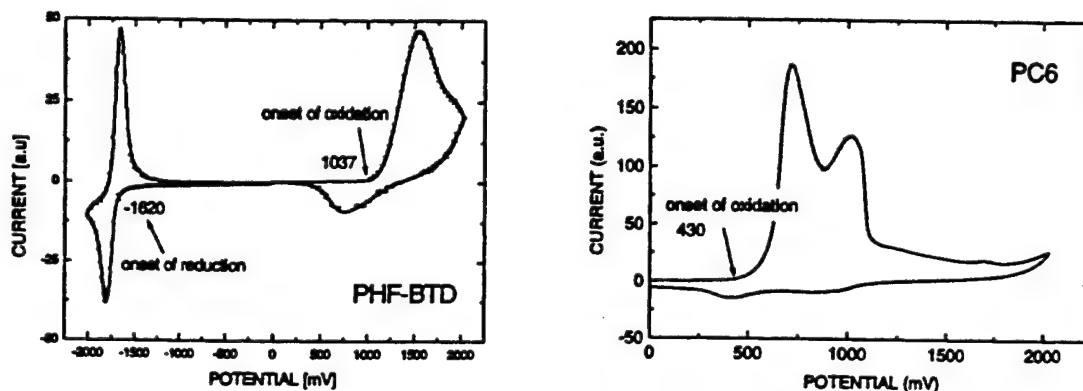


Figure 3. The cyclic voltammograms measured for PHF-BTD and PC6. The potentials were measured versus the Fc/Fc⁺ couple.

Ferrocene / Ferrocenium (Fc/Fc⁺) couple. The onsets of redox are well defined for PHF-BTD (-1.62V for reduction and 1.04V for oxidation process) while only the onset of oxidation is observed for PC6 (0.04V). It should be noticed that the

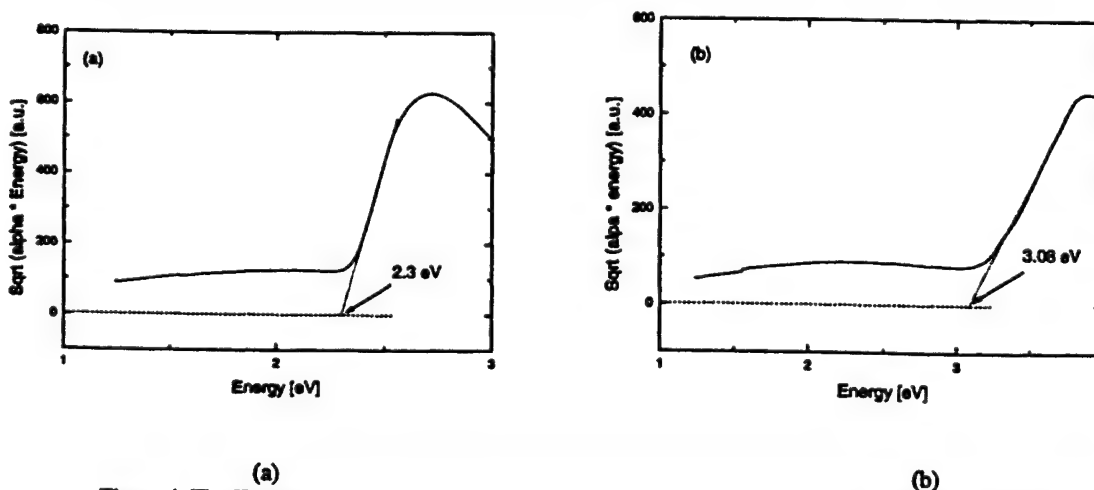


Figure 4. The Tauc plots and extrapolated optical band gap energy values for (a) PHF-BTD and (b) PC6.

PHF-BTD film can be both reversibly oxidized and reduced, which allows determination of both ionization potential and electron affinity for the same sample. Therefore, these onset potentials were used to derive the LUMO and HOMO levels for each polymer by assuming a scale factor relating Fc/Fc^+ to vacuum of ~ 4.8 eV^{8,10}. The schematic diagram of energy levels for each polymer is shown in Figure 5. The HOMO and LUMO energy levels of PHF-BTD, which are represented by solid lines, are located at 5.8 and 3.2 eV below the vacuum level, respectively. For PC6, only HOMO level can be obtained from the CV spectrum, which is located at 5.2 eV below the vacuum level and represented as a solid line. It should be noted that this value would increase to 5.5 eV if the peak value of 714 mV is used instead of the onset potential in Figure 3. In our case, we have used onset reduction/oxidation potentials in all calculations of the HOMO and LUMO levels. In agreement with the previously published data⁸, we think that onset potentials are associated more closely with the reduction/oxidation processes than the peak potentials. The dotted lines in the Figure 5 indicate the LUMO energy levels derived from the optical band gap values determined from polymer absorption spectra. They were estimated from the Tauc plots¹⁴ shown in Figure 4:

$$\sqrt{\alpha\hbar\omega} \propto (\hbar\omega - E_g) \quad (1)$$

This equation shows that optical band gap can be extrapolated when the square root of the product of absorption coefficient and photon energy is plotted versus photon energy. The optical band gap of 2.3 and 3.1 eV were obtained for PHF-BTD and PC6, respectively. From these values, the dotted LUMO energy levels shown in Figure 5 were derived against the HOMO energy levels (3.5 and 2.1 eV below the vacuum level for PHF-BTD and PC6, respectively). The origin responsible for 0.3eV

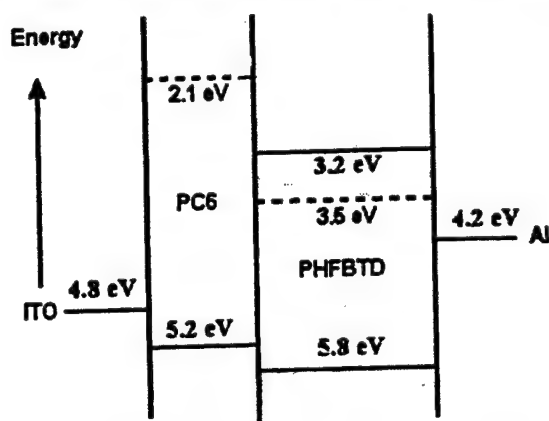


Figure 5. Schematic diagram of energy levels for PHF-BTD and PC6. All energy levels are shown with reference to vacuum level. The dotted lines represent LUMO energy levels deduced using optical band gap values. The solid lines represent LUMO energy levels deduced from Fig. 3.

difference between optical (deduced from optical spectrum) and electrical (deduced from CV spectrum) band gap obtained for EL polymer is not known at this time. The band gap energy values for PHF-BTD and PC6 are summarized in Table 1, where the peak and absorption edge values extracted from absorption spectra are also given.

Table 1. Band gap energy of PHF-BTD and PC6. Tauc gap, absorption peak, absorption edge, and CV gap represent the band gap energy extracted from Tauc plots, peak location in absorption spectra, photon energy values at which the absorption start to increase very rapidly, and LUMO – HOMO difference in CV spectrum, respectively.

	Unit: eV			
	Tauc gap	Absorption peak	Absorption edge	CV gap
PHF-BTD	2.3	2.7	2.4	2.7
PC6	3.1	3.9	3.3	Not available

3.2. Poly OLEDs Opto-Electronic Characteristics

The current density versus applied voltage characteristics (J-V) and EL spectra are shown in Figure 6 for bi-layer Poly OLEDs fabricated on glass and flexible plastic substrates. The peak of EL spectrum was clearly observed at around 570 nm for both cases. The full width half maximum (FWHM) of this peak is about 90 nm. The threshold voltages deduced from J-V curves are ~ 16 and ~ 20 V for Poly OLED fabricated on glass and plastic substrates, respectively. The initial light

emission was observed at voltage of ~ 12 V for both cases. This voltage value is somewhat high at this time. A further reduction can be achieved by doing the followings: replacement of Al by Ca or Er^{15} cathode metal (e.g. lower work function metal is used), EL thickness optimization, and HTL thickness and chemical structure optimization. The studies related to the above topics will be published elsewhere. The purpose of this work is to use Al cathode in the Poly OLEDs. At higher current density (greater than about 10 mA/cm^2), the devices failed to operate, only giving maximum luminance (up to 2000 cd/m^2) during short time and lower external quantum efficiency. Figure 7(a) shows the emission efficiency and power efficiency versus luminance, which were obtained over the operating current level without device failure. The emission efficiency of 5.5 and 4.2 cd/A and power efficiency of 0.9 and 0.6 lm/W were obtained over the luminance range of $100\text{--}200 \text{ cd/m}^2$ for bi-layer devices on glass and flexible plastic substrates, respectively. The luminance and the external quantum efficiency versus current density are shown in the Figure 7(b), where the data are plotted for device operating current density region. Luminance over 100 cd/m^2 , which represents the acceptable value for certain flat panel display applications, can be easily obtained with our devices. The quantum efficiency of 1.8 and $\sim 1.6\%$ were obtained for Poly OLEDs fabricated on glass and flexible plastic substrates, respectively.

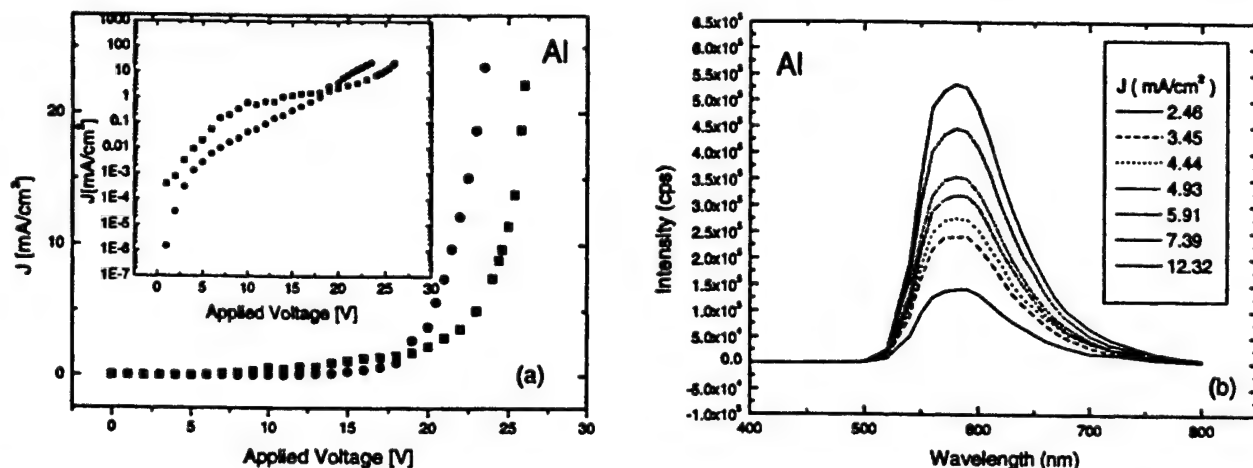


Figure 6. The J-V characteristics (a) and EL spectrum (b) of the bi-layer Poly OLEDs fabricated on glass (circle) and flexible plastic (square) substrates.

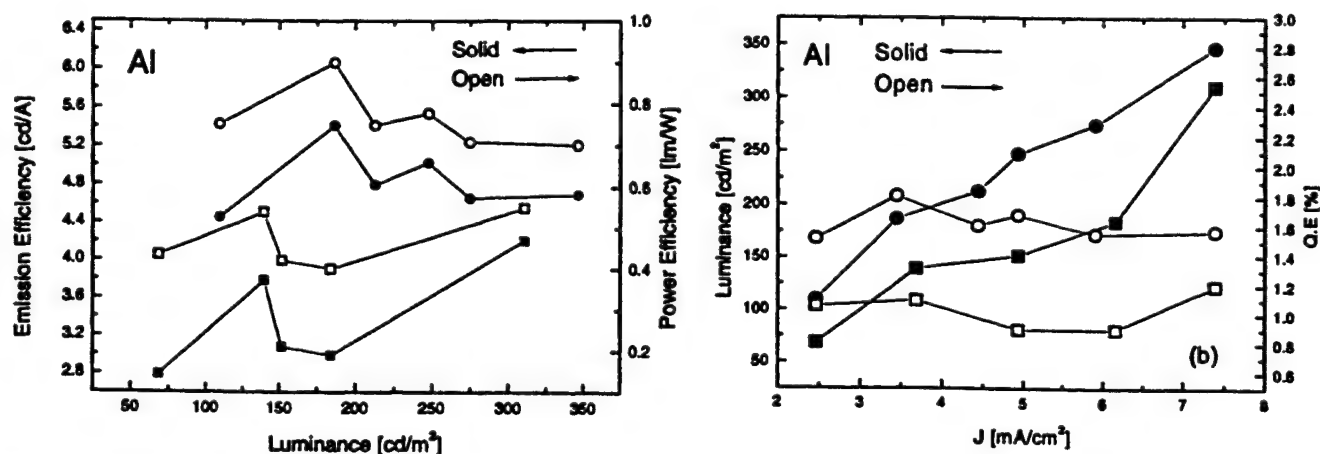


Figure 6. Emission efficiency and power efficiency versus luminance (a) and luminance and external quantum efficiency versus current density (b) for bi-layer devices fabricated on glass (circle) and flexible plastic (square) substrates.

4. CONCLUSIONS

We have studied the structural, optical, and electrical properties of the organic polymers that can be used to fabricate a high performance organic polymer light-emitting devices on both glass and flexible plastic substrates using air-stable aluminum as the cathode metal. Maximum brightness ($\sim 2000 \text{ cd/m}^2$), good emission efficiency (~ 5.5 and $\sim 4.2 \text{ cd/A}$), good power efficiency (~ 0.9 and $\sim 0.6 \text{ lm/W}$) and acceptable external quantum efficiency (~ 1.8 and $\sim 1.6 \%$) have been achieved for our devices on glass and flexible plastic substrates.

ACNOWLEDGEMENT

This research was supported by ONR - DARPA grant (N0014-99-1-0985).

REFERENCES

1. J.H. Burroughes, D.D.C. Bradley, A.R. Brown, R.N. Marks, K. Mackay, R.H. Friend, P.L. Burn, and A.B. Holmes, *Nature*, **347**, pp.539-541, 1990.
2. N.C. Greenham, S.C. Moratti, D.D.C. Bradley, R.H. Friend, and A.B. Holmes, *Nature*, **365**, pp.628-630, 1993.
3. J. Morgado, R.H. Friend, F. Cacialli, B.S. Chuah, S.C. Moratti, and A.B. Holmes, *J. Appl. Phys.* **86**, pp.6392-6395, 1999.
4. C. Zhang, D. Braun, and A.J. Heeger, *J. Appl. Phys.*, **73**, pp.5177-5180, 1993.
5. S. Roman, M. Berggren, O. Inganäs, *Appl. Phys. Lett.*, **75**, pp.3557-3559, 1999.
6. Y. He and J. Kanicki, *Appl. Phys. Lett.* **76**, pp.661-663, 2000.
7. W.L. Yu, Y. Cao, J. Pei, W. Huang, A.J. Heeger, *Appl. Phys. Lett.*, **75**, pp.3270-3272, 1999.
8. S. Janietz, D.D.C. Bradley, M. Grell, C. Giebeler, M. Inbasekaran, and E.P. Woo, *Appl. Phys. Lett.*, **73**, pp.2453-2455, 1998.
9. N.C. Greenham, R.H. Friend, and D.D.C. Bradley, *Adv. Mater.*, **6**, pp.491-493, 1994.
10. Y. He, R. Hattori, and J. Kanicki, *Rev. Sci. Instr.*, **71**, pp. 2104-2107, 2000.
11. Y. He, S. Gong, R. Hattori, and J. Kanicki, *Asia Display '98*, pp.1095-1098, 1998.
12. Y. He and J. Kanicki, *Appl. Phys. Lett.* **76**, pp.661-663, 2000.
13. A.J. Bard and L.R. Faulkner, *Electrochemical Methods Fundamentals and Applications*, John Wiley & Sons, 1980.
14. J. Tauc, R. Grigorovici, and A. Vancu, *Phys. Stat. Sol.* **15**, pp.627-637, 1966.
15. Y. Hong, Z. Hong, D. Curtis, and J. Kanicki, *Proceedings of IDRC*, 2000 (in press).

Four-Thin Film Transistor Pixel Electrode Circuits for Active-Matrix Organic Light-Emitting Displays

Yi HE*, Reiji HATTORI† and Jerzy KANICKI‡

Solid-State Electronics Laboratory, Department of Electrical Engineering and Computer Science, The University of Michigan, Ann Arbor, MI 48109, USA

(Received June 2, 2000; accepted for publication November 13, 2000)

Constant-current, four-thin-film-transistor (TFT) pixel electrode circuits, based on hydrogenated amorphous silicon (a-Si:H) TFT technology for active-matrix organic light-emitting displays (AM-OLEDs), have been designed, fabricated, and characterized. Experimental results indicate that continuous pixel electrode excitation can be achieved with these circuits. The pixel electrode circuits use a current driver to automatically adjust their current level for threshold voltage shifts of both the organic light-emitting devices and the drive TFT. Consequently, these pixel electrode circuits have excellent electrical reliability even when a large threshold voltage shift is present. A high output current level and a good output-input current linearity have been demonstrated with these circuits.

KEYWORDS: thin-film-transistor, active-matrix, amorphous silicon, organic light-emitting devices, circuit, luminance, quantum efficiency

1. Introduction

The rapid development of organic light-emitting devices (OLEDs) has made possible their application to high-resolution large-area flat panel displays. Such high-resolution displays require thin-film-transistor (TFT) based active-matrix (AM) driving schemes to reduce their power dissipation. Over the past few years, much effort has been made to develop AM driving techniques for organic light-emitting displays.^{1–4)} Pixel electrode driving schemes based on one-TFT,¹⁾ two-TFT,^{2,3)} and four-TFT⁴⁾ circuits have been proposed. Today, it is well established that the one-TFT pixel electrode configuration¹⁾ cannot be used for AM-OLED because continuous excitation during the entire frame period cannot be achieved with this type of pixel circuit. Continuous pixel electrode excitation can be achieved by a two-TFT configuration.^{2,3)} However, in this type of pixel electrode circuit, non-negligible threshold voltage (V_{th}) variation of the drive TFT, due to TFT process variation or long-term operation, can occur and cause output current level variation over the display panel. As a result, the light emission intensity of OLED and AM-OLED brightness can change accordingly, which may not be acceptable for certain applications. The previously proposed four-TFT pixel configuration,⁴⁾ although partially compensating for V_{th} variation, uses four control lines and its driving scheme is too complicated for practical use. It should also be noted that so far, the proposed four-TFT pixel electrode circuit has been based on polysilicon TFT technology,^{2–4)} which may not be a cost-effective production technology in comparison with the well-established amorphous silicon (a-Si) TFT technology developed for AM-liquid crystal displays (AM-LCDs).

In this paper, we describe the current-source four-TFT pixel electrode circuits based on amorphous silicon TFT technology. The developed circuits are extensively characterized for different sets of circuit parameters. We clearly demon-

strate, for the first time, that this type of pixel electrode circuit can provide continuous current flow even after the select line signal is turned off. In addition, current flow can be fully adjusted for the current-voltage characteristic variation of the TFTs and OLEDs. Consequently, these pixel circuits are able to maintain a constant level of current flow and have high electrical reliability. Also, these pixel electrode circuits have only two control lines and, as a result, their driving schemes are simple. Finally, two improved circuits are proposed to further enhance pixel circuit electrical performance. Pixel electrode circuit simulations and experimental results indicate that the proposed circuits are acceptable for AM-OLEDs.

2. Pixel Electrode Circuit Schematic and Operation

Figure 1(a) shows the schematic of the equivalent constant current four-TFT pixel electrode circuit. T1 and T2 are the switching transistors. T3 is the drive TFT while T4 serves as a one-direction diode that only allows current flow from V_{DD} (common source) line to the OLED. This circuit has four external terminals: V_{select} , I_{data} , V_{DD} , and ground. The select line voltage signal, V_{select} , and the source line voltage signal, V_{DD} , are pulsed and constant voltage signals, respectively. The data line signal, I_{data} , is an adjustable current signal to be provided by an external current driver. All signals (V_{select} , I_{data} , and V_{DD}) are provided externally, and the ground terminal is the cathode (metal electron injecting electrode) of the OLED. Figure 1(b) shows an example of the operational waveforms that can be used for different signals. The operation of this circuit is described as follows:

ON state: When the select line (V_{select}) signal is high (H), both T1 and T2 are turned ON. The data line signal (I_{data}) then passes through T1 and T2 and sets both the drain and gate voltages of T3. Consequently, the potentials at nodes A and B will allow the data current (I_{data}) to pass through T3. T3 is working in the saturation region, e.g., $V_{DS} > V_{GS} - V_{th}$ (threshold voltage). V_{DD} must be chosen to be lower than the T3 drain voltage (V_D) during the ON state to ensure that no current flows through T4 from V_{DD} . Therefore, in this case, the current flowing through T3 is equal to I_{data} . This current,

*Present address: One AMD Place, P.O. Box 3453, MS 177, Sunnyvale, CA 94088-3453, USA.

†Present address: Department of Electronic Device Engineering, Graduate School of Information Science and Electrical Engineering, Kyushu University, Hakozaki 6-10-1, Higashi-ku, Fukuoka 812-8581, Japan.

‡Corresponding author: kanicki@eecs.umich.edu

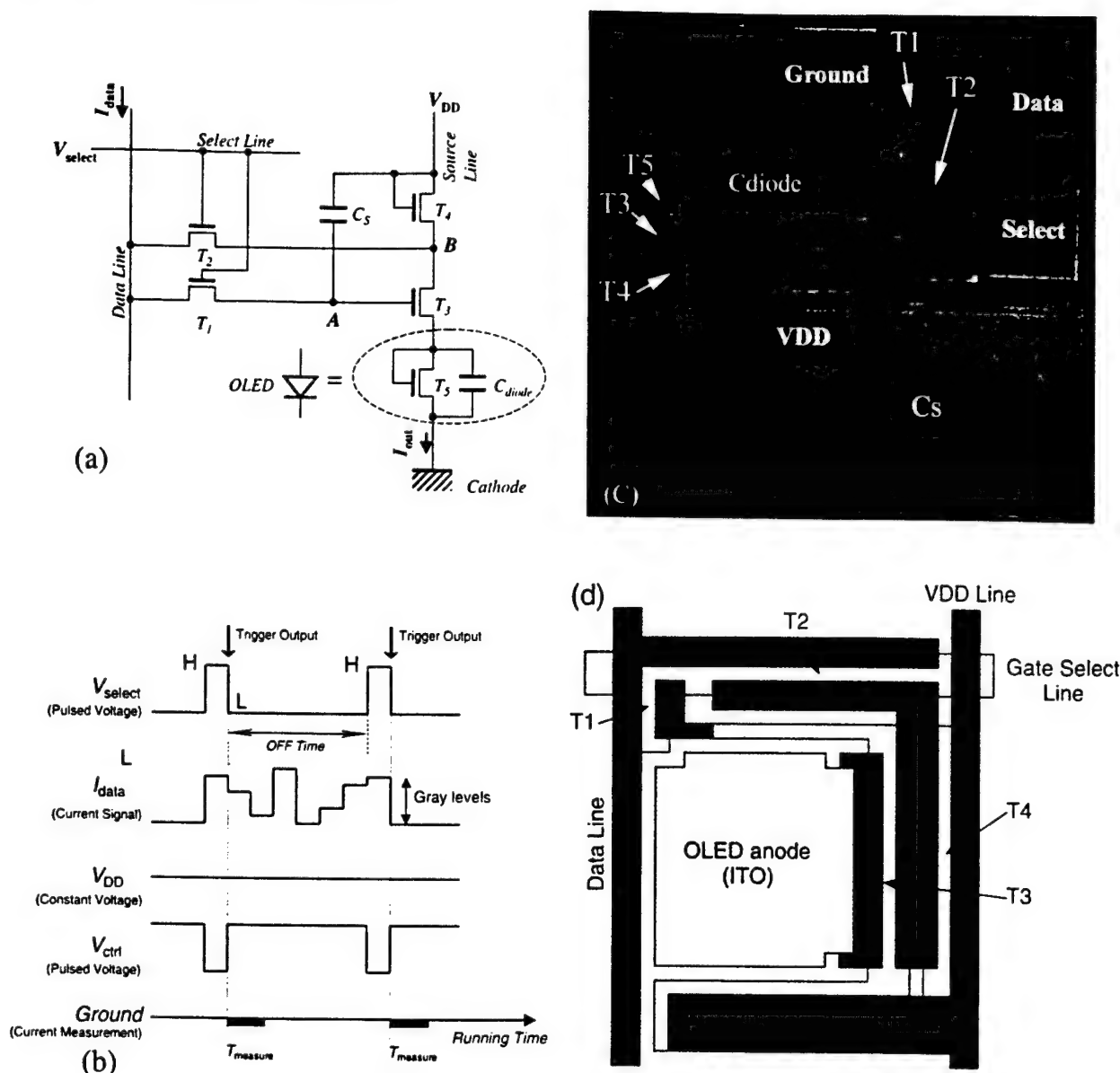


Fig. 1. (a) Schematic representation of the four-TFT pixel electrode circuit. (b) Example of the operation waveforms that can be used for different external terminals. (c) Top view of the four-TFT pixel electrode circuit fabricated in our laboratory. (d) Schematic top view of the four-TFT pixel electrode circuit. C_s represents the storage capacitor. T1, T2, ..., T5 represent TFT1, TFT2, ..., TFT5, respectively.

applied to the OLED anode (ITO electrode), will turn on the OLED and reach the ground pad (OLED cathode). The OLED light emission brightness will depend on the applied current level that can be modulated, as shown in Fig. 1(b).

OFF state: When the pixel electrode circuit is de-selected and the select line signal is low (L), both T1 and T2 are OFF. The T3 gate voltage (V_G), however, should be maintained high by charges stored in the storage capacitor (C_s) during pixel electrode ON state. During OFF state, the T3 drain voltage will drop to a lower value and T4 will be turned on to maintain the same output current level. This time, the current will flow from V_{DD} to T3 via T4. If the T3 gate voltage is maintained and T3 is operated in the saturation region, the output current level

would be equal to I_{data} . Therefore, the current flowing through OLED is expected to be maintained constant.

Automatic adjustment: If the drive TFT (T3) threshold voltage changes and if this change is not larger than the amplitude of V_{select} during pixel electrode circuit operation, V_G of T3 must be changed accordingly to ensure the same output current level. This is achieved through automatic adjustment of the current signal (I_{data}) during the ON state. Therefore, the gate voltage of T3 is always adjusted to maintain the data current (I_{data}) level at about the same level, regardless of the TFT threshold voltage value. Hence, the local V_{th} variation of the drive TFT will not affect the output current (I_{out}) level. The threshold voltage shifts of other TFTs will not have a major impact on the output current level, because they are not

involved in controlling the current output in this pixel electrode circuit.

These above arguments also hold if the OLED current-voltage characteristic shifts with time, which usually happens after long-term OLED operation. Consequently, this pixel electrode circuit can provide constant current flow even if local variations of the OLED characteristics occur.

The gray level of this pixel electrode circuit is controlled by adjusting the data current level [Fig. 1(b)]. As discussed above, the output current is expected to be the same as the data current in both ON and OFF states. Therefore, the output current level is directly controlled by the data current from the data line. Since OLED brightness is usually proportional to the current density passing through it,⁵⁾ different output currents will generate different OLED brightness levels that can be used to control the display gray levels.

3. Experimental

To verify pixel electrode circuit functionality, we have designed and built this circuit based on a-Si:H TFT technology. The four-TFT pixel circuit fabricated during this study is shown in Fig. 1(c). In this figure, the OLED structure is represented by a combination of TFT (T5) and a parallel capacitance (C_{diode}) [Fig. 1(a)]. The geometrical sizes of T5 and C_{diode} have been optimized to ensure that under forward bias condition, the current flow through the T5- C_{diode} combination is similar to that expected in the fabricated OLED. Indeed, T5, whose gate electrode is connected to its drain electrode, shows a rectifying characteristic.⁶⁾ The channel length for all TFTs is $6\ \mu\text{m}$.

The pixel electrode circuit was fabricated on a Corning 1737 $6'' \times 6''$ square glass substrate using a conventional inverted-staggered back-channel-etch process.⁷⁾ First, a 1000-Å-thick chromium layer was deposited on Corning 1737 glass by the sputtering method and patterned to form the gate electrodes of all five TFTs and the bottom electrode of the storage capacitor (C_s). A-SiN_x:H (3000 Å), intrinsic a-Si:H (2000 Å), and n^+ a-Si:H (500 Å) layers were then deposited sequentially by the plasma-enhanced chemical vapor deposition (PECVD) technique. After the patterning of the active area (a-Si:H island) for all TFTs and the gate via opening for T3, T4, and T5, 2000-Å-thick molybdenum was deposited by the sputtering method and patterned to form the source-drain electrodes of all five TFTs and the top electrode of the storage capacitor. The interconnects (for example, T1 source to T3 gate, etc.) between different TFTs were formed at the same time. The TFT back channel was reactive-ion etched (RIE) using the dry etching process. Then, a-SiN_x:H (3000 Å) was deposited on top to passivate the pixel circuit. The via in the passivation layer was opened afterwards. Finally, the ITO electrode was sputtered, annealed and etched. When OLED is incorporated into this pixel electrode circuit, the T5 and C_{diode} structure can be omitted, the OLED structure will be fabricated on top of the ITO electrode, and light will be emitted down through the ITO layer. Figure 1(d) illustrates the schematic representation of the fabricated pixel electrode circuit.

The electrical properties of the pixel circuit were evaluated using a probe station. Data (constant current, I_{data}) and source line (constant voltage, $V_{\text{DD}} = 9\text{ V}$) signals were supplied

by HP 4156A semiconductor analyzer. The select line signal (pulsed voltage, V_{select}) was supplied by a Keithley 237 source-measure unit with an ON voltage = 25 V, an OFF voltage = 0 V, and a duty cycle of 10% (ON time: 100 ms, period: 1000 ms). The output current (I_{out}) of this circuit was measured by the HP semiconductor analyzer after input data current (I_{data}) and source line voltage (V_{DD}) were turned off, i.e., after the pixel electrode circuit was de-selected. This will enable verification of the pixel electrode circuit's ability to provide continuous excitation. The sampling of the output current was triggered by the falling edge of the select pulse voltage signal to ensure that data were collected after the pixel circuit was turned off. The typical sampling time for each data point was found to be $\sim 2\text{--}3\text{ ms}$ using the HP 4156A semiconductor analyzer. Therefore, all measurements were performed in the OFF state, e.g., when the V_{select} signal was low. The experimental noise was below 10 pA.

4. Experimental Results and Discussions

4.1 $I_{\text{out}}\text{--}I_{\text{data}}$ characteristics

During the ON state, The output current (I_{out}) measured at the ground pad (OLED cathode) approximately equals the data current (I_{data}) provided by the current source from the data line. However, as discussed previously, continuous pixel excitation is necessary for an AM-OLED driving circuit. To verify the circuit's ability to continuously supply the pixel electrode current, the output current in the OFF state was investigated.

Figure 2(a) illustrates the output current in the OFF state versus data current characteristics of the four-TFT pixel circuit at different V_{DD} voltages for a storage capacitor of $\sim 6.61\text{ pF}$. All the characteristics were measured after V_{select} was switched off from 25 to 0 V and the pixel electrode circuit was de-selected. It is clear that continuous pixel electrode excitation was achieved in this pixel circuit. For all V_{DD} voltages, the output current level increases monotonically with the data current, indicating that the output current level is solely controlled by the data current for given V_{DD} voltage and storage capacitor values. This characteristic will enable the control of AM-OLED gray scale solely by the data current. In addition, a higher output current level can be achieved with higher V_{DD} values. Note that when V_{DD} was high, the output current was not zero even if the input data current was zero. This is due to the fact that even when I_{data} is zero, the T4 source voltage [point B in Fig. 1(a)] is not zero. Since I_{data} is zero, the voltage at point A will be equal to the voltage at point B. This will keep T3 slightly ON to allow a small amount of current to pass through. When V_{DD} voltage is higher, the voltage at point A will also be higher, leading to an even larger output current.

In Fig. 2(b), the output current characteristics in the OFF state for different C_s are plotted together at a given V_{DD} voltage (9 V). These experimental results verified that a larger output current level could be achieved for a larger size of the storage capacitor. The I_{out} values for $I_{\text{data}} = 0.2\ \mu\text{A}$ in the OFF state are listed in Table I. From this table, we can conclude that the output current (I_{out}) decreases with respect to the input data current (I_{data}) when the pixel circuit is switched from ON to OFF state. The data listed in this table were measured using the follow-

Table 1. Output current and storage capacitor values deduced from Fig. 2(b). The ΔV values were calculated using eq. (8).

Circuit no.	Storage capacitor (pF)	$I_{out} (ON)^*$ (μA)	$I_{out} (OFF)$ (μA)	$\Delta I_{out} (\mu A)$	$\Delta V (V)$
1	0.052	0.20	0.03	0.17	0.85
2	0.41	0.20	0.04	0.16	0.71
3	0.83	0.20	0.07	0.13	0.55
4	1.65	0.20	0.09	0.11	0.44
5	3.31	0.20	0.12	0.08	0.32
6	6.61	0.20	0.15	0.05	0.17

* $I_{out}(ON) = I_{data}$; $\Delta I_{out} = I_{out}(ON) - I_{out}(OFF)$.

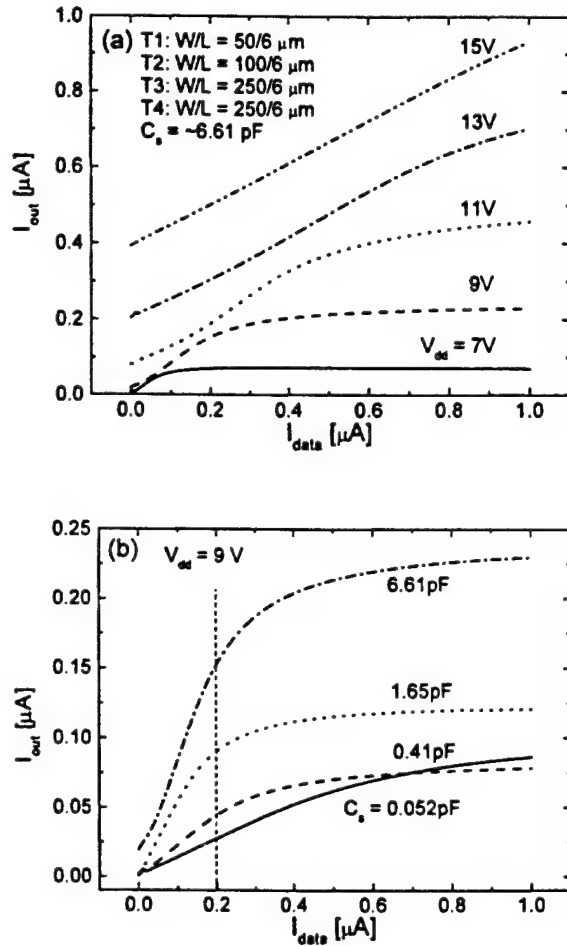


Fig. 2. (a) Output current versus data current characteristics of the four-TFT pixel electrode circuits at different V_{DD} voltages for a storage capacitor size of ~ 6.61 pF. (b) Output currents at $V_{DD} = 9$ V for different C_s . All curves were measured during OFF state of the pixel electrode circuit.

ing parameters: $V_{select} = 25$ V \rightarrow 0 V, $V_{DD} = 9$ V, and $I_{data} = 0.2$ μ A. Also, the TFTs have the following W/L ratios: T1 $W/L = 50/6$ μ m, T2 $W/L = 100/6$ μ m, T3 $W/L = 250/6$ μ m, T4 $W/L = 250/6$ μ m, and T5 (OLED-emulating TFT) $W/L = 200/6$ μ m. The output current level decrease observed for higher I_{data} values is mainly due to the gate voltage decrease induced by the parasitic capacitor.

In general, the TFT parasitic capacitor (C_p) is due to the overlap between TFT source/drain and gate electrodes, as

shown schematically in Figs. 3(a) and 3(b). It should be noted that all TFTs shown in Fig. 1(a) have their own parasitic capacitors. Among them, the T1 parasitic capacitor (C_{p1}) will cause a T3 gate potential drop when V_{select} is switched from 25 to 0 V. Figure 3(c) illustrates the equivalent pixel circuit at node A shown in Fig. 1(a). When V_{select} is 25 V, node A (T3 gate) is charged up to the data line voltage (V_{data}) by I_{data} . This voltage value is determined by the present current source voltage. Thus, the charge stored at node A is

$$Q = C_{p1}(V_{data} - V_{select(ON)}) + C_{gd}(V_{data} - V_d) + C_{gb}(V_{data} - V_{a-Si})C_{gs}(V_{data} - V_s) + C_s(V_{data} - V_{dd}), \quad (1)$$

where C_{p1} is the T1 parasitic capacitor; and C_{gd} and C_{gs} are the T3 gate-to-drain and gate-to-source capacitors, respectively. If the source/gate and the drain/gate overlaps of T3 are identical, $C_{gd} = C_{gs} = C_{p3}$, where C_{p3} represents the T3 parasitic capacitance. C_{gb} is the capacitance associated with the gate over the field region,⁸⁾ and is equal to the gate oxide capacitor ($C_{gb} = C_{ox}$). V_d and V_s are the T3 drain and source voltages. V_{a-Si} is the equivalent T3 field region potential. Then, the above equation can be simplified as

$$Q = C_{p1}(V_{data} - V_{select(ON)}) + C_{p3}(2V_{data} - V_d - V_s) + C_{ox}(V_{data} - V_{a-Si}) + C_s(V_{data} - V_{dd}). \quad (2)$$

When V_{select} is switched to 0 V, the charge stored at node A is

$$Q' = C_{p1}V' + C_{p3}(2V' - V_d - V_s) + C'_{gb}(V' - V_{a-Si}) + C_s(V' - V_{dd}), \quad (3)$$

where V' represents the potential at node A after V_{select} is switched from 25 to 0 V. After this switching step, if T3 still operates in the saturation region, C'_{gb} would remain the same (C_{ox}). Assuming that the T3 field region (V_{a-Si}) and the T3 drain and source (the potential applied to OLED) potential changes are negligible after each switching, eq. (3) can be rewritten as

$$Q' = C_{p1}V' + C_{p3}(2V' - V_d - V_s) + C'_{ox}(V' - V_{a-Si}) + C_s(V' - V_{dd}). \quad (4)$$

Q' would be equal to Q if there were no charge leakage from node A back to the data line through T1 in the OFF state. Therefore, by substituting of eq. (4) into eq. (2) and replacing ($V_{data} - V'$) by ΔV , we obtain

$$\Delta V = \frac{C_{p1}\Delta V_{select}}{C_{p1} + 2C_{p3} + C_{ox} + C_s}. \quad (5)$$

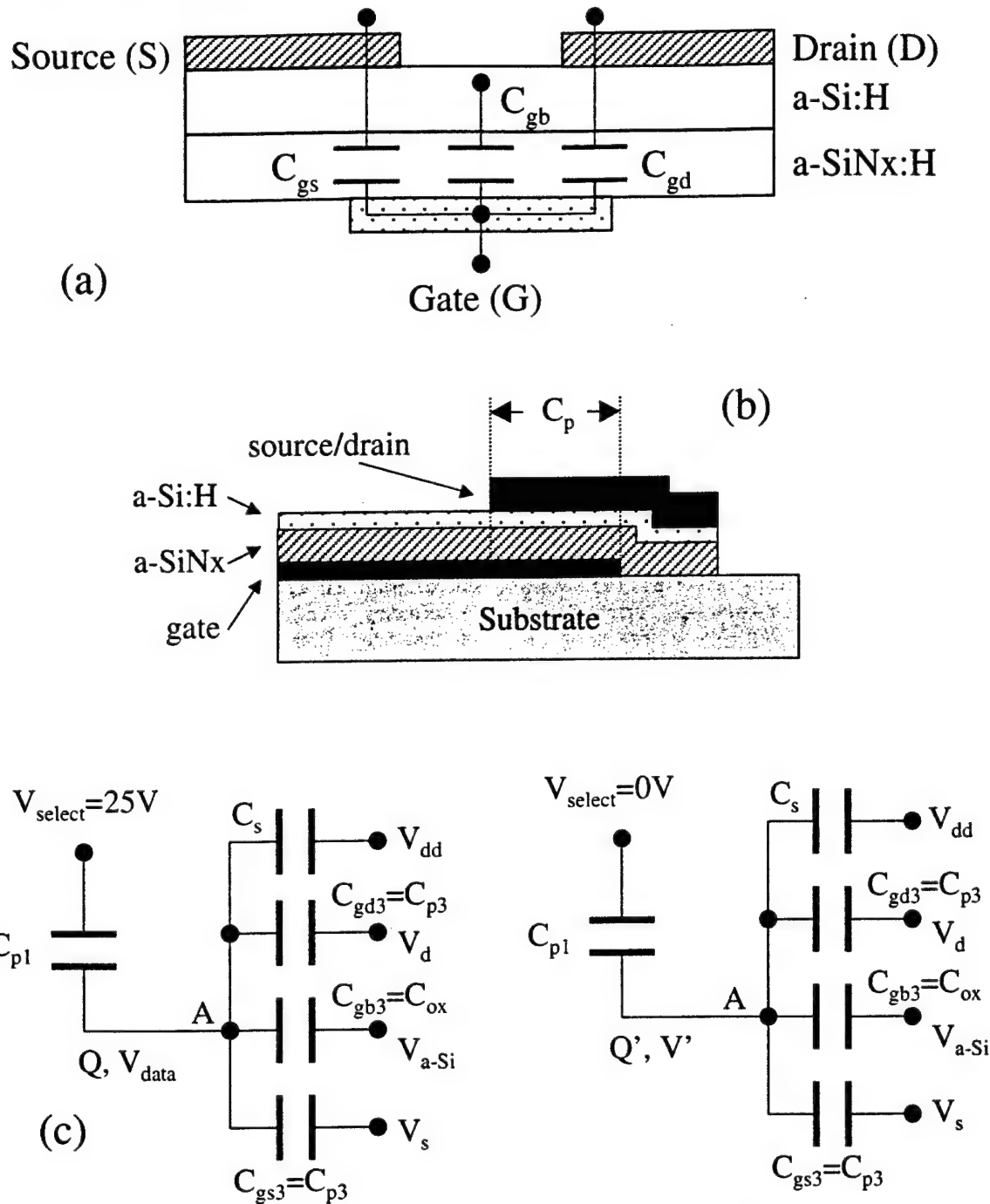


Fig. 3. (a) Schematic representation of TFT. (b) Cross-sectional view of the TFT near source/drain-gate electrodes; C_p represents the TFT parasitic capacitor. (c) The equivalent circuit at node A of Fig. 1(a).

The inverse of eq. (5) gives

$$\frac{1}{\Delta V} = \frac{C_{p1} + 2C_{p3} + C_{ox} + C_s}{C_{p1} \Delta V_{select}} = \frac{1}{C_{p1} \Delta V_{select}} C_s + \frac{C_{p1} + 2C_{p3} + C_{ox}}{C_{p1} \Delta V_{select}}. \quad (6)$$

The second term on the right-hand side of eq. (6) is a constant for fixed V_{select} and pixel electrode circuit parameters. Therefore, the relationship between $1/\Delta V$ and the storage capacitor should be linear. In order to use eq. (6) to analyze the data given in Table I, the gate voltages responsible for the out-

put current drops must be derived. Assuming that T3 (drive TFT) is in the saturation region before and after pixel electrode circuit switching, the T3 output current should follow the equation

$$I_{ds} = \frac{1}{2} \mu C_{ox} \frac{W}{L} (V_{gs} - V_{th})^2, \quad (7a)$$

where I_{ds} is the drain-to-source current; μ is the field-effect mobility; W and L are the channel width and length, respectively; and V_{gs} and V_{th} are the gate-to-source and threshold voltages, respectively. Rewriting the above equation to show

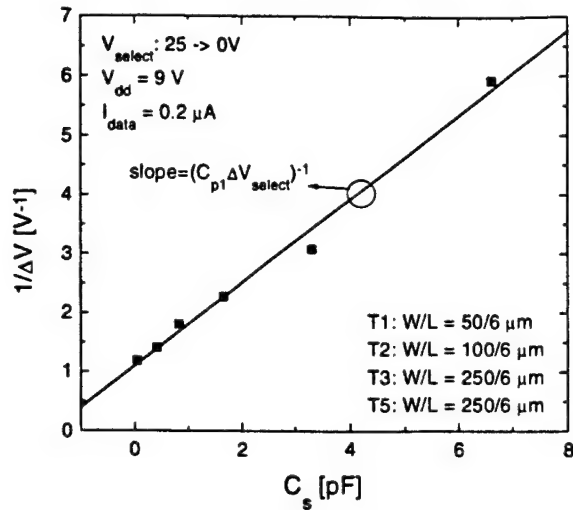


Fig. 4. Calculated ΔV as a function of the storage capacitor (—). The calculated ΔV values (■) from experimental data are also shown.

V_{gs} in the left term, we obtain

$$V_{gs} = V_{th} + \sqrt{\frac{2L}{\mu C_{ox} W}} I_{ds}. \quad (7b)$$

Because data collection takes only ~ 2 – 3 ms after pixel circuit switching, it is expected that no significant threshold voltage shift of T3 will take place. Therefore, in general, the gate voltage variation should obey the following equation:

$$\Delta V = V_{gs} - V'_{gs} = \left(\frac{2L}{\mu C_{ox} W} \right)^{1/2} (\sqrt{I_{on}} - \sqrt{I_{off}}), \quad (8)$$

where V'_{gs} is the T3 gate-to-source voltage after the pixel circuit switching step. $I_{on} = I_{out}(ON)$, $I_{off} = I_{out}(OFF)$, $\mu \approx 0.26 \text{ cm}^2/\text{V}\cdot\text{s}$, $C_{ox} \approx 2.07 \times 10^{-8} \text{ F/cm}^2$, $L = 6 \mu\text{m}$, $W = 250 \mu\text{m}$ for the data listed in Table I.

Figure 4 shows the variation of the inverse of the gate voltage (ΔV), derived from eq. (8) based on the data given in Table I, as a function of the storage capacitor. It is clear from this figure that the inverse of the gate voltage decreases linearly with the size of the storage capacitor, as suggested by eq. (6). According to eq. (6), the slope $[(0.71 \pm 0.04) \times 10^{12} \text{ F}^{-1}\cdot\text{V}^{-1}]$ of the straight fit line should be equal to $1/C_{p1} \Delta V_{select}$. Thus, from this slope, we can calculate the T1 parasitic capacitor value as

$$C_{p1} = \frac{1}{0.71 \times 10^{12} \Delta V_{select}} \approx 56.3 \text{ fF}, \quad (9)$$

where $\Delta V_{select} = 25 \text{ V}$. If we take into consideration film thickness variation, dielectric constant uncertainty, and misalignment associated with the photo-process during TFT fabrication, the parasitic capacitance value ($= \epsilon_r \epsilon_0 W L_{overlap}/t$, $\epsilon_r \approx 7$, $t \approx 3000 \text{ \AA}$), calculated directly from the design parameters, for T1 ($W/L = 50/6 \mu\text{m}$, $L_{overlap} = 2 \mu\text{m}$) is $\sim 20.7 \pm 20 \text{ fF}$. This value is comparable in magnitude to the parasitic capacitance derived from Fig. 4. Therefore, the above analyses provide a good justification for the origin of the T3 gate voltage reduction associated with the T1 parasitic capacitor. The observed deviation between theoretical and measured results may also be due to the following:

a) Some of the assumptions made during the derivation

of eq. (6) may not hold during pixel circuit operation. For example, during the derivation of eq. (5), it is assumed that the T3 source potential (the potential applied to OLED) remains at the same level after pixel circuit switching step. This assumption cannot be 100% correct because the current (I_{out}) flowing through OLED changes. The current change is a direct result of the OLED bias change. Therefore, the T3 source potential cannot remain at the same level if an output current change is observed. In many cases, such a potential change could be very small, particularly in the high-current regions where a slight voltage change induces a large current fluctuation. In the case of $I_{out} = 0.2 \mu\text{A}$, however, this potential change may not be sufficiently small to be neglected.

b) Other output current reduction mechanisms may be involved. For example, the charge leaks through T1 to the data line, or the T3 (drive TFT) operation point moves from saturation to the linear region after the pixel electrode circuit switching step.

In both cases, the output current level will be further reduced, resulting in a larger calculated C_{p1} value using eq. (6).

According to eq. (6), the Y-axis intercept (1.10 ± 0.12) of the fitted straight line in Fig. 4 corresponds to $(C_{p1} + 2C_{p3} + C_{ox})/(C_{p1} \Delta V_{select})$. Therefore, the C_{p1} value can be also derived from the intercept value if other parameters are known. This calculated C_{p1} value is $\sim 19.5 \text{ fF}$, in excellent agreement with the parasitic capacitance value (20.7 fF) calculated above directly from the TFT design parameters.

From the above analysis, it is clear that a certain size of storage capacitor is needed for the four-TFT pixel electrode circuit. In general, a larger C_s is preferred to minimize the reduction of the output current after pixel electrode circuit switching. Also, the V_{DD} voltage must be carefully selected to reduce the output current deviation observed at low data currents.

4.2 Impact of TFT W/L ratios

Figure 5(a) illustrates the influence of the T1 W/L ratio on the output current characteristics in the OFF state. Experimentally, we have observed that a larger output current level can be reached for a larger T1 W/L ratio. However, at the same time, when the T1 W/L ratio was too large, the output current could not reach zero even if the input data current was set to zero. The pixel electrode circuit output current characteristics showed little dependence on the T2 W/L ratio.

Figure 5(b) shows the influence of the T3 (drive TFT) W/L ratio on the output current characteristics in the OFF state. It is clear that for a larger T3 W/L ratio, a higher output current level can be achieved. However, when the T3 W/L ratio was too large, the output current could not reach zero even if the input data current was zero. Figure 5(c) illustrates the transient characteristic of the output current for the four-TFT pixel circuit. The V_{DD} voltage and the input data current were 13 V and $0.2 \mu\text{A}$, respectively. From this figure, it is clear that the output current slightly decreased after the pixel electrode circuit was switched OFF, but the output current level remained unchanged for at least 1 second after the select line signal was turned off, indicating a negligible pixel electrode circuit leakage current.

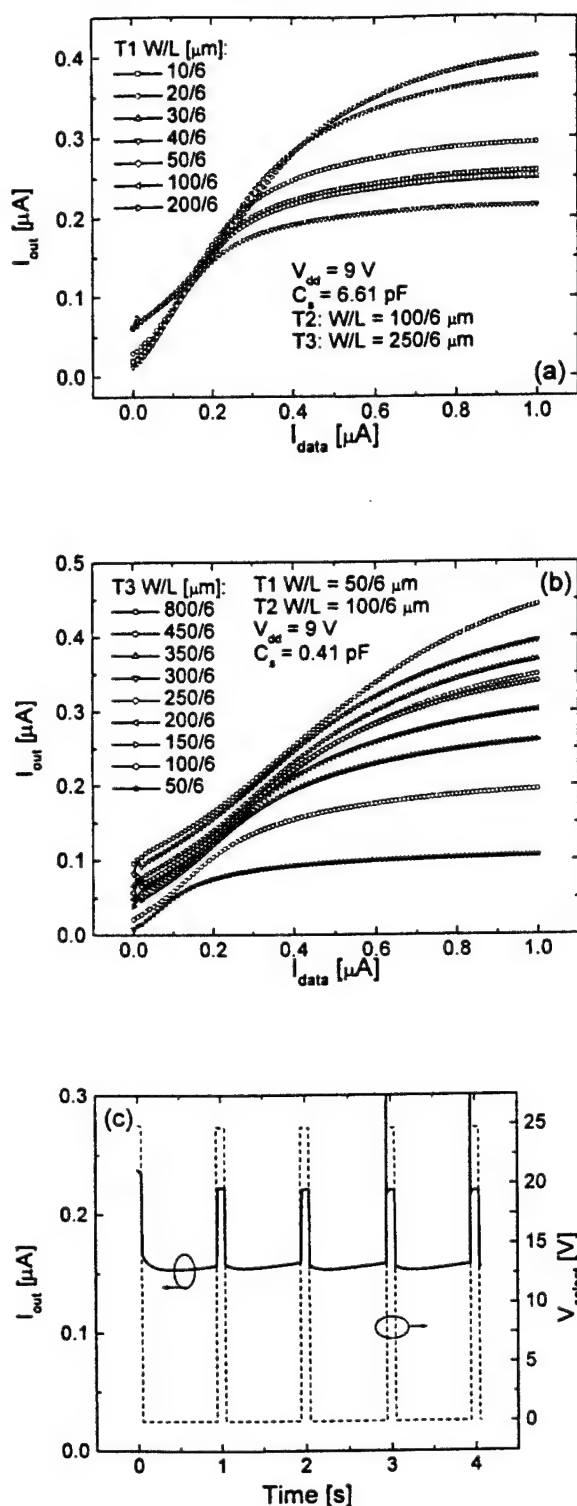


Fig. 5. Influences of (a) T1 W/L ratio and (b) T3 W/L ratio on the output current characteristics of the four-TFT pixel electrode circuit. (c) The transient response of the four-TFT pixel electrode circuit.

Based on our experimental results and pixel electrode circuit analyses, the best set of pixel electrode circuit parameters is listed in Table II for the pixel circuit described above. Further improvement of this pixel circuit will require further process refinement and video-rate test current signals.

Table II. Best pixel electrode circuit parameters to be used for the a-Si:H four-TFT pixel electrode circuit described in this paper.

T1 W/L (μm)	T2 W/L (μm)	T3 W/L (μm)	C_s (pF)	V_{DD} (V)
50/6	200/6	250/6	6.61	9

4.3 Pixel electrode circuit electrical reliability

One basic function of the AM-OLED pixel electrode circuit is to consistently provide a *constant* current for the OLED during the frame period. The experimental results showed that this is indeed the case for the four-TFT pixel circuit and the output current level can simply be adjusted by supplying different data current values. This should allow good control of the AM-OLED gray levels.

However, serious circuit electrical instability may occur due to the drive TFT threshold voltage shift, particularly for the two-TFT circuit.⁶⁾ This drive TFT threshold voltage shift can cause a large AM-OLED brightness variation. To study the electrical reliability of this pixel electrode circuit, we have conducted a series of DC bias-temperature-stress (BTS) on the drive TFT (T3) to accelerate the aging process of the pixel electrode circuit. The threshold voltage shift of other TFTs presented in this circuit will not have a major impact on the output current level, because they are not used to control the pixel electrode current output. During BTS, a bias stress voltage of +20 V was applied to the T3 gate at room temperature. The best pixel electrode circuit parameters given in Table II were used for pixel circuit electrical reliability evaluation.

Figure 6(a) illustrates the variation of pixel electrode circuit output current characteristics as a function of BTS time. It is clear from this figure that the output current level remained essentially unchanged during BTS up to 10^4 s. Figure 6(b) shows the T3 threshold voltage evolution as a function of BTS time. For a BTS time of 10,000 s, the threshold voltage was shifted by ~ 2.77 V from its initial value. Figure 6(b) also illustrates that the output current changed by only $\sim 1\%$ at high input current (≥ 0.5 μA) and by $\sim 5\%$ at low input current (≥ 0.1 μA). These results clearly show that this pixel electrode circuit is capable of compensating for the T3 V_{th} variation to ensure a stable, constant pixel output current level. This will allow both good control of the display gray levels and uniform luminance distribution over the entire AM-OLEDs.

5. Improved Four-TFT Pixel Electrode Circuits

In an ideal case, the pixel electrode output current level in the OFF state should be equal to the input data current, as indicated by the ideal line in Fig. 6(a). However, experimental results showed that the output current levels were substantially lower than the ideal case, particularly at high input current levels [Fig. 6(a)]. This deviation from the ideal case may be associated with (a) gate voltage reduction induced by the parasitic capacitor, C_{p1} , as discussed in detail above. The consequence of the gate voltage decrease is the decrease of the T3 output current level. This effect is large at low input current levels, where both V_{gs} and V_{ds} are small; (b) after the pixel electrode circuit is de-selected, the magnitude of the T3 drain voltage will decrease. This voltage drop could produce $V_{ds} < V_{gs} - V_{th}$. As a result, the T3 operating point will shift

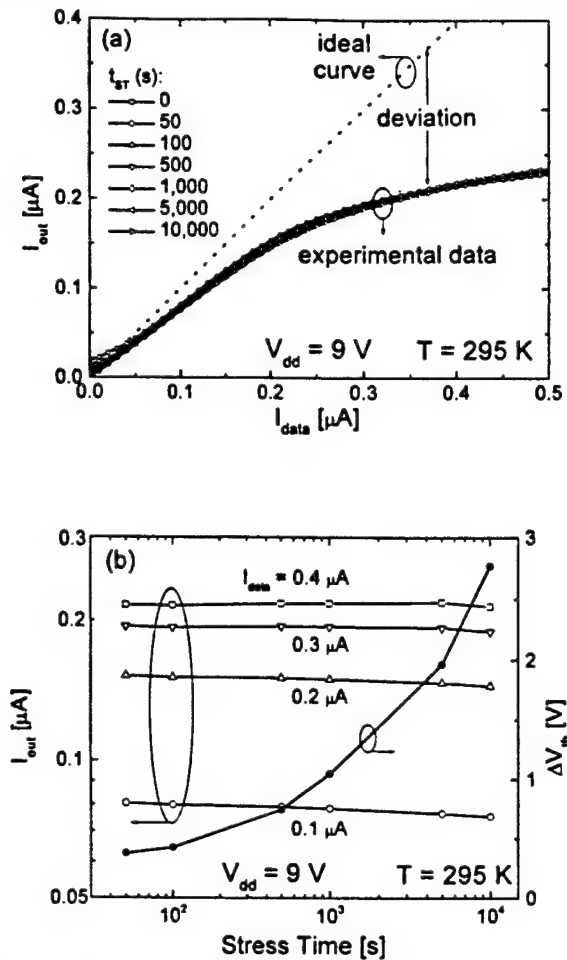


Fig. 6. (a) Impact of BTS on the four-TFT pixel electrode circuit characteristics. (b) BTS time dependence of the threshold voltage and the output current at several data currents. $\Delta V_{th} = V_{th}^f - V_{th}^i$, where V_{th}^f and V_{th}^i are the TFT final and initial threshold voltages, respectively.

from the saturation region to the linear region, and the output current (I_{out}) will decrease with respect to I_{data} . This effect will be dominant at high input current levels, where both V_{gs} and V_{ds} of T3 in the ON state are large in comparison with V_{DD} .

The output current deviation can be reduced by increasing the external source line voltage (V_{DD}). A higher V_{DD} will result in larger output current levels (see Fig. 2). However, at the same time, an incorrect output current level can be induced at low input currents, where the T3 drain voltage could be lower than V_{DD} . As a result, current [$I_D(T4)$] will flow from V_{DD} to T3 via T4 and the total output current $I_{out} = I_{data} + I_D(T4) > I_{data}$. This situation can be seen in both Figs. 2 and 5. For the circuit to work reasonably well at both low and high data current levels, a compromise V_{DD} voltage must be reached. In the case of our four-TFT pixel electrode circuit, $V_{DD} = 9$ V seemed to be the best choice (Table II).

However, even at $V_{DD} = 9$ V, a large deviation and non-linearity between the output and input currents still exist, and the output current tends to saturate at high currents [Fig. 6(a)]. Therefore, this pixel circuit might not be able to provide a sufficiently large current density if a high OLED brightness is required. To achieve a high output current and a good output-

input current linearity, the four-TFT pixel electrode circuit was slightly modified [Fig. 7(a), the top view of this circuit is shown in Fig. 7(d)]. By connecting an extra voltage control line (V_{ctrl}) to the T4 gate electrode, the V_{DD} voltage can now be set at 25 V or higher. During the ON-time, the V_{ctrl} signal is low and T4 is turned off. The data line signal (I_{data}) then passes through T1 and T2 and sets both the drain and gate voltages of T3. Consequently, the potentials at nodes A and B will allow the data current (I_{data}) to pass through T3. T3 is working in the saturation region, e.g., $V_{DS} > V_{GS} - V_{th}$ (threshold voltage). Because T4 is off, no current can flow through it from V_{DD} . Hence, the current flowing through T3 is equal to I_{data} . This current then will turn on T5 (e.g., OLED) and reach the ground. During the OFF time, the V_{ctrl} signal is high to turn on T4, allowing for the current to flow from V_{DD} to T3 via T4. Since V_{DD} now represents a high potential power source, the potential at point B will increase after the pixel circuit is switched from ON to OFF state. The T3 gate voltage is maintained at the previous level by charges stored in the storage capacitor C_s . Therefore, V_{DS} of T3 remains higher than $V_{GS} - V_{th}$ and the TFT remains in the saturation region. Consequently, the pixel output current (I_{out}) is maintained at the same level as that in the ON state. Thus, $I_{out} = I_{data}$.

A closer inspection of this pixel electrode circuit reveals that the signal of the V_{ctrl} terminal is exactly the inverse of the select line signal (V_{select}). Therefore, a two-TFT based inverter can be added to this pixel electrode circuit to replace the V_{ctrl} terminal. This approach, illustrated in Fig. 7(b), will reduce the number of pixel electrode terminals but will increase pixel electrode circuit complexity. However, the two-TFT based inverter does not have to be included in every pixel electrode circuit. Instead, it can be fabricated at the edge of the display panel or included in the driving display circuit to reduce pixel electrode circuit complexity. To achieve the voltage inversion, the geometrical dimensions of T6 and T7 need to be optimized, so that $W_7 L_6 / L_7 W_6 \gg 1$ (W_6 , W_7 , L_6 and L_7 represent the channel widths and lengths of T6 and T7, respectively). In the ON state, V_{select} will turn on T1, T2, and T7. T6 is always on because its drain and gate electrodes are connected. Since both T6 and T7 are on, the current flows from V_{DD} to ground through T6 and T7. In equilibrium, T6 and T7 will function as two resistors linked in series, and the gate voltage of T4 at node C will be determined by these two resistor and V_{DD} values. Since the resistance of TFT in the ON state is proportional to its W/L ratio, the T4 gate voltage will be $\sim V_{DD} \times W_6 L_7 / L_6 W_7 \ll V_{DD}$. This voltage can be adjusted to a value smaller than the threshold voltage of T4 by choosing the appropriate W_6 , W_7 , L_6 and L_7 values. Then T4 will be off and, therefore, no current will flow through T4, as in the case of the V_{ctrl} -line approach. In the OFF state, T1, T2, and T7 will be turned off. The gate voltage of T4 at node C will be set high by V_{DD} through T6. This circuit condition will allow the current to flow from V_{DD} to T3 through T4. Similar to the case of the V_{ctrl} -line approach, V_{DS} of T3 will remain higher than $V_{GS} - V_{th}$, and T3 will still operate in the saturation region. As a result, the pixel electrode output current level will remain constant.

To support the above analysis, circuit simulation was performed using Cadence. The pixel circuit simulation parameters used in this work are summarized in Table III. Note that for the pixel circuit simulation, all the TFT parasitic capac-

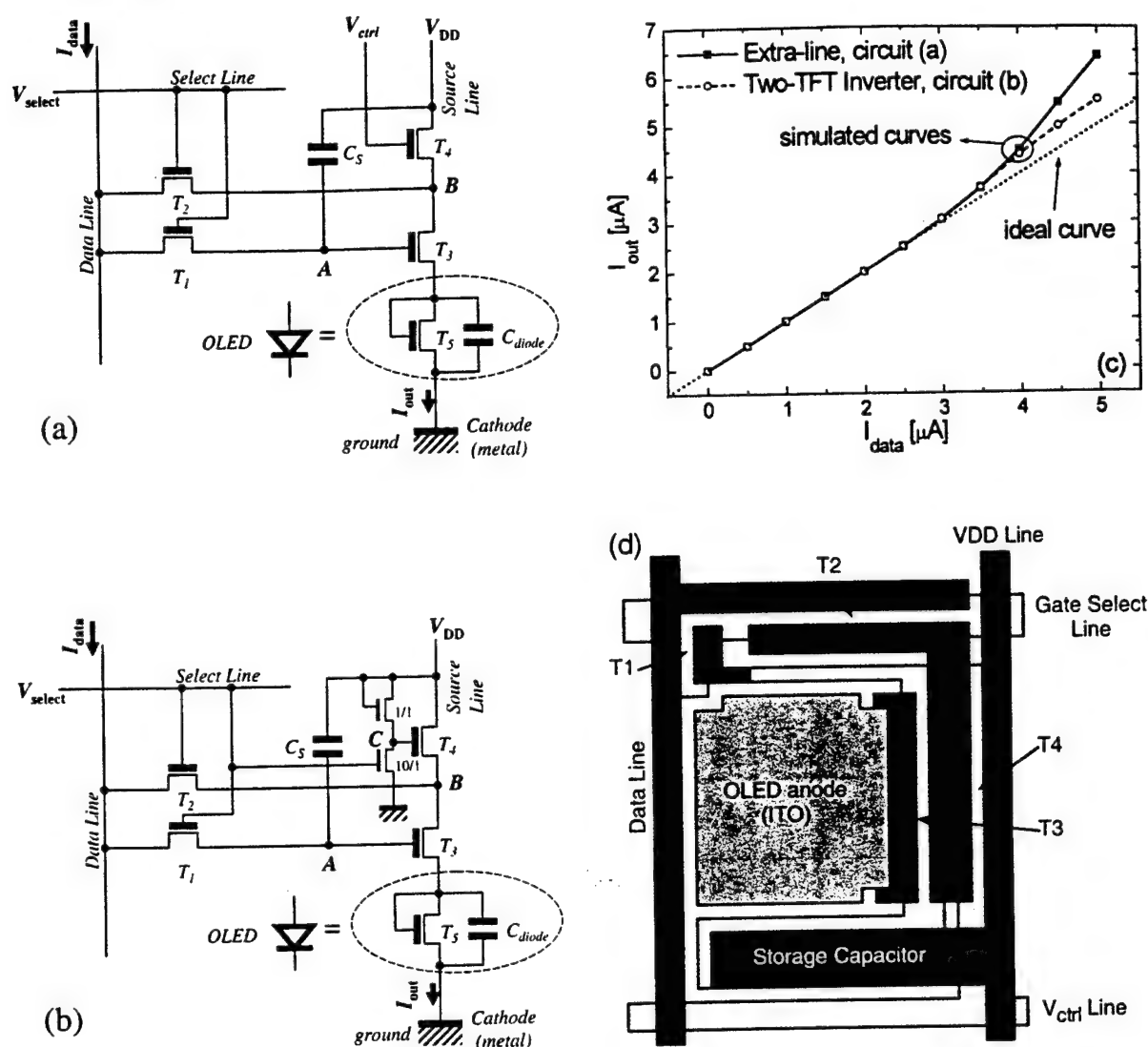


Fig. 7. (a) Constant current-source, four-TFT pixel electrode circuit using an extra voltage terminal (V_{ctrl}). (b) Constant current-source pixel electrode circuit using a two-TFT based inverter. (c) Pixel electrode circuit simulation results for the two pixel electrode circuits given in (a) and (b). (d) Top view of the four-TFT pixel electrode circuit using an extra voltage terminal (V_{ctrl}). TFTs labeled 1/1 and 10/1 are T_6 and T_7 , respectively. The label represents their W/L ratio in units of μm .

Table III. Summary of the simulation parameters used for calculation of Fig. 7(c).

W_1/L_1	W_2/L_2	W_3/L_3	W_4/L_4	W_5/L_5	W_6/L_6	W_7/L_7	
50/6 μ	100/6 μ m	250/6 μ m	250/6 μ m	200/6 μ m	1/6 μ m	10/6 μ m	
V_{DD}	V_{select}	V_{ctrl}	I_{data}	C_{diode}	C_s	R_s	C_p
25 V	0 \rightarrow 25 V	25 \rightarrow 0 V	0 \rightarrow 5 μ A	6.4 pF	6.61 pF	100 Ω	570 fF

itors (C_p) were set at 570 fF, about one order of magnitude higher than the values given above in order to achieve simulation convergence. Figure 7(c) shows the simulated output current (I_{out}) versus input current (I_{in}) characteristics for both pixel electrode circuits. In this simulation, the a-Si:H TFT density-of-state (DOS) model developed by our group was used.⁹⁾ Also, the experimental circuit parameters were used for this pixel circuit simulation. As expected, the simulation results indicate that the output currents for both pixel elec-

trode circuits are very close to the ideal case. The output current levels differ by only less than 0.5% from the ideal case at low currents, indicating excellent I_{out} - I_{in} linearity. Moreover, a pixel output current level higher than 5 μA can be achieved with these pixel electrode circuits. For an 11-inch VGA full-color AM-OLED with a pixel electrode size of $\sim 100 \times 200 \mu m^2$, this output current level is equivalent to a current density of 25 mA/cm². Assuming the OLEDs with an external quantum efficiency of 1%, the display brightness

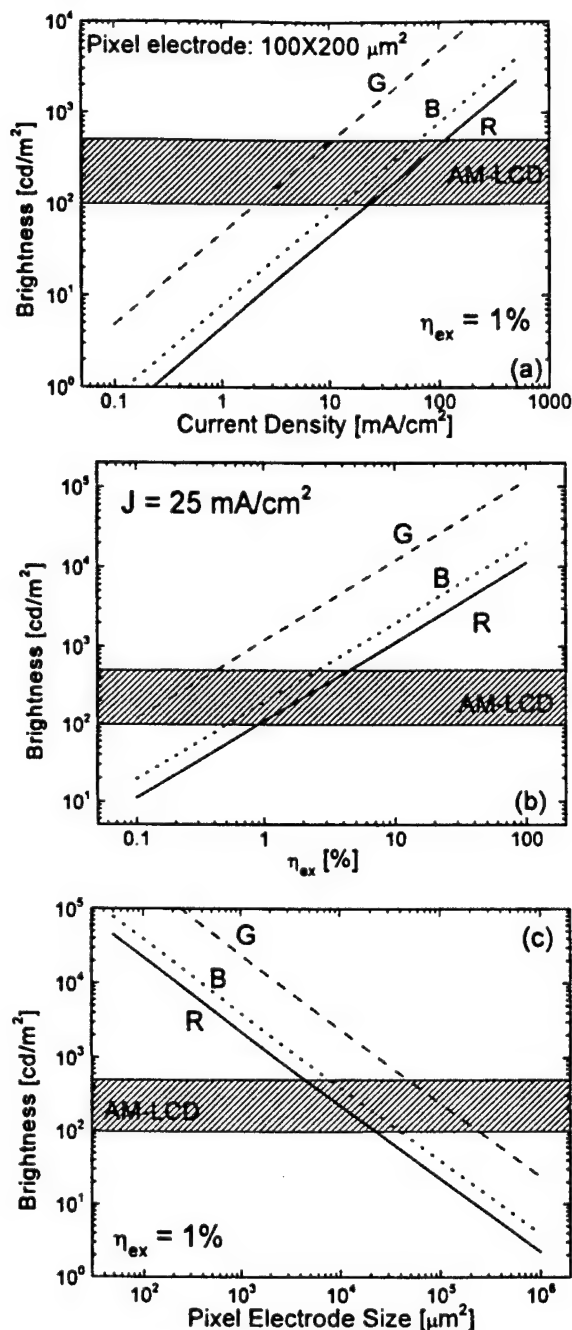


Fig. 8. OLED brightness as a function of (a) current density ($\eta_{\text{ex}} = 1\%$), (b) OLED external quantum efficiency ($J = 25 \text{ mA/cm}^2$), and (c) pixel electrode size ($\eta_{\text{ex}} = 1\%$ and $I = 5 \mu\text{A}$) for R, G, B emissions saturated at 650 nm, 540 nm, and 480 nm, respectively.

of ~ 110 , ~ 1200 , and $\sim 200 \text{ cd/m}^2$ for red (650 nm), green (540 nm), and blue (480 nm) light emission, respectively, can be achieved [Fig. 8(a)]. In Fig. 8(b), the display brightness as a function of OLED external quantum efficiency is shown for an applied pixel current density of 25 mA/cm^2 . In Fig. 8(c), the display brightness for different pixel electrode sizes is shown. These brightness values were calculated using the

following equation:

$$L = 683 E(\lambda) \eta_{\text{ex}} \frac{hc}{\pi \lambda e} J,$$

where L is brightness; $E(\lambda)$ is the luminous efficiency of light with wavelength of λ , with $E(650 \text{ nm}) = 0.107$, $E(540 \text{ nm}) = 0.954$, $E(480 \text{ nm}) = 0.139$ values used in this work; J is the applied current density; η_{ex} is the device external quantum efficiency, e is the electron charge, c is the velocity of light, and h is Planck's constant. It is clear from these figures that the calculated brightness values are more than sufficient for most portable AM-OLED applications.

6. Conclusions

We have designed, fabricated, and analyzed a constant-current four-TFT pixel electrode circuit based on a-Si:H TFT technology for active-matrix organic light-emitting displays. Experimental results indicate that continuous pixel electrode excitation can be achieved with different pixel electrode circuits discussed in this paper. The pixel electrode circuits showed excellent electrical reliability with virtually no output current variation even when a large TFT threshold voltage shift was observed. In addition, two improved pixel electrode circuits have been proposed to achieve high output current level and good output-input characteristic linearity. With a typical OLED external quantum efficiency of 1%, the output current level of this pixel electrode circuit can achieve a pixel electrode brightness that is more than sufficient for most portable AM-OLED applications.

Acknowledgements

The authors would like to thank Mr. T. Tsukamizu, R. Tsuchiya and Dr. S. Martin for their technical assistance. This work was partially supported by the Center for Display Technology and Manufacturing at the University of Michigan, the Grant-in-Aid for Science Research (No. 11694167) from the Ministry of Education, Science, Sports and Culture of Japan, and the DARPA-ONR grant (N0014-99-1-0958).

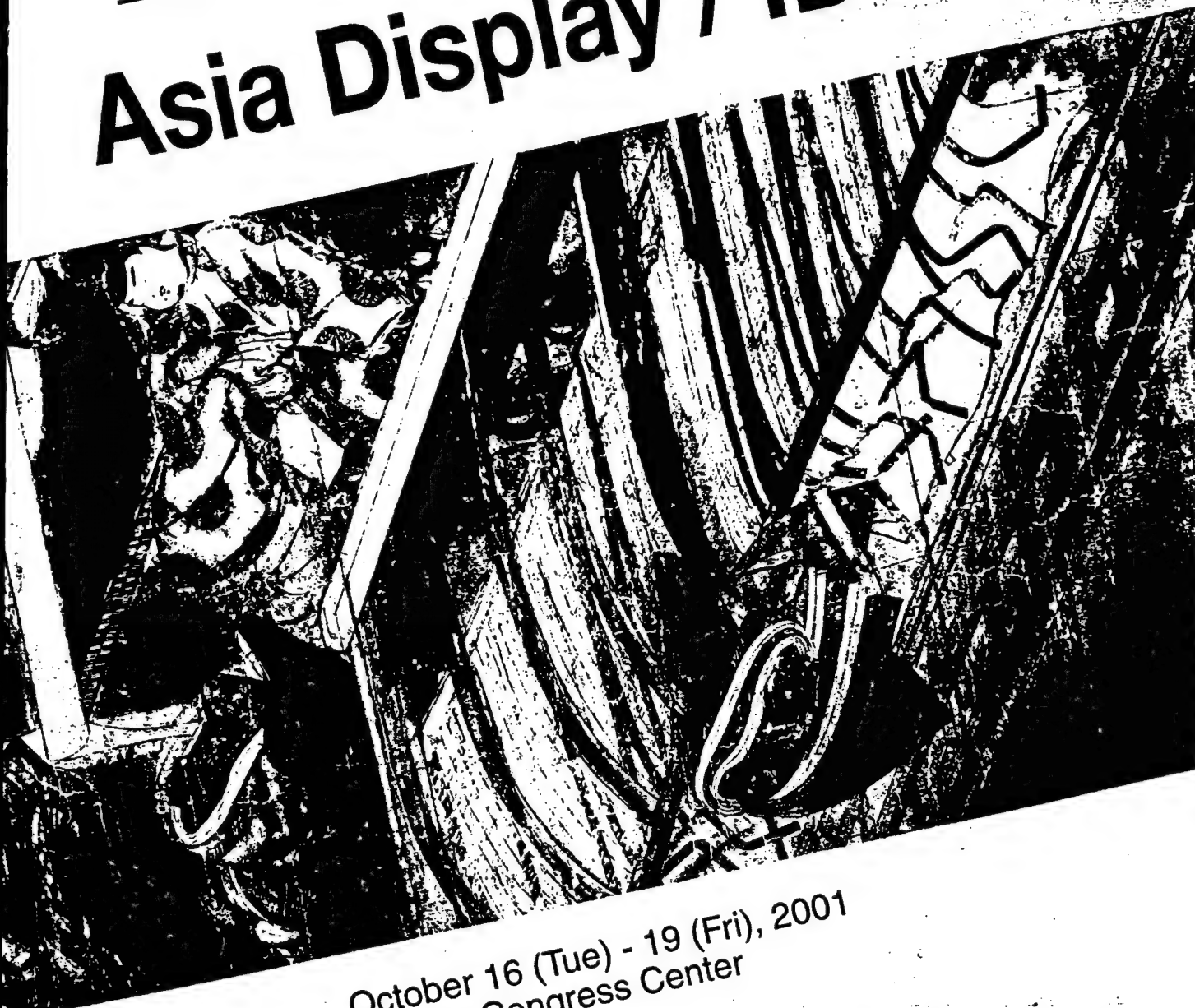
- 1) C. C. Wu, S. Theiss, M. H. Lu, J. C. Sturm and S. Wagner: Tech. Dig. IEDM, 1996, p. 957.
- 2) M. Stewart, R. S. Howell, L. Pires, M. K. Hatalis, W. Howard and O. Prache: Tech. Dig. IEDM, 1998, p. 871.
- 3) T. Shimoda, H. Ohshima, S. Miyashita, M. Kimura, T. Ozawa, I. Yudasaka, S. Kanbe, H. Kobayashi, R. H. Friend, J. H. Burroughes and C. R. Towns: Proc. Asia Display '98, 1998, p. 217.
- 4) R. M. A. Dawson, Z. Shen, D. A. Furst, S. Connor, J. Hsu, M. G. Kane, R. G. Stewart, A. Ipri, C. N. King, P. J. Green, R. T. Flegal, S. Pearson, W. A. Barrow, E. Dickley, K. Ping, C. W. Tang, S. Van Slyke, F. Chen, J. Shi, J. C. Sturm and M. H. Lu: Symp. Dig. 1998 SID, 1998, p. 11.
- 5) Y. He, S. Gong, R. Hattori and J. Kanicki: Appl. Phys. Lett. **74** (1999) 2265.
- 6) Y. He, R. Hattori and J. Kanicki: Proc. 20th Int. Display Research Conf., 2000, p. 354.
- 7) C. Y. Chen and J. Kanicki: IEEE Electron Device Lett. **17** (1996) 437.
- 8) R. J. Baker, H. W. Li and D. E. Boyce: CMOS Circuit Design, Layout, and Simulation, IEEE Press Series on Microelectronic Systems, 1998.
- 9) C. Y. Chen and J. Kanicki: Proc. 26th European Solid State Device Research Conf., 1996, p. 1023.

SID
SOCIETY FOR INFORMATION DISPLAY

ITE

The 21st International Display Research Conference in conjunction with
The 8th International Display Workshops

Asia Display / IDW '01



October 16 (Tue) - 19 (Fri), 2001
Nagoya Congress Center
Nagoya, Japan

Proceedings

Organic Polymer Light-Emitting Devices on Flexible Plastic Substrates for AM-OPLED

Yongtaek Hong and Jerzy Kanicki

Organic & Molecular Electronics Laboratory, Solid State Electronics Laboratory,
Dept. of Electrical Engineering and Computer Science, University of Michigan, Ann Arbor, MI 48109

Abstract

The opto-electronic properties of the organic polymer light-emitting devices (OPLEDs) fabricated on flexible plastic substrates have been studied for active-matrix organic polymer light-emitting display (AM-OPLED) applications. The characterization was done for both green and red light OPLEDs. The hole injection layer and hole transport layer were used in OPLEDs for optimum opto-electronic device performances. The effect of different cathode-metalization methods, such as thermal and electron-beam evaporations, on the device performances has also been investigated.

Introduction

Over last several years, there is a tremendous interest in the organic polymer light-emitting devices (OPLEDs) fabricated on flexible plastic substrates. Among different flat panel display (FPD) technologies, most likely OPLEDs are the most suitable for flexible plastic substrates. So far, only a few groups have reported small molecule-based OLEDs on flexible plastic substrates.¹ Our group has worked on OPLEDs on flexible plastic substrates over last several years.^{2,3}

In this paper, we report the opto-electronic performances of the red and green light-emitting devices fabricated on flexible substrates for active-matrix organic polymer light emitting display (AM-OPLED) applications.

Experimental

Figure 1 shows the schematic of the measurement system used in this study. The integrating sphere was used to collect all the light emission from the devices. The electrical and optical data acquisitions were controlled by a personal computer. The electroluminescence (EL) was measured with a calibrated CCD spectrum system.

The plastic substrates with patterned ITO electrodes, which have the sheet resistance of about 12.2 ohms/square and the transmission greater than 80 % over the visible range were used. The substrate size is 2"x2". The substrates were cleaned in the ultrasonic bath of isopropanol. Without any ITO surface treatment, hole injection layer (HIL), hole transport layer (HTL) and light emissive layer (LEL) were sequentially spin coated and cured in the vacuum oven. Then, aluminum cathode was

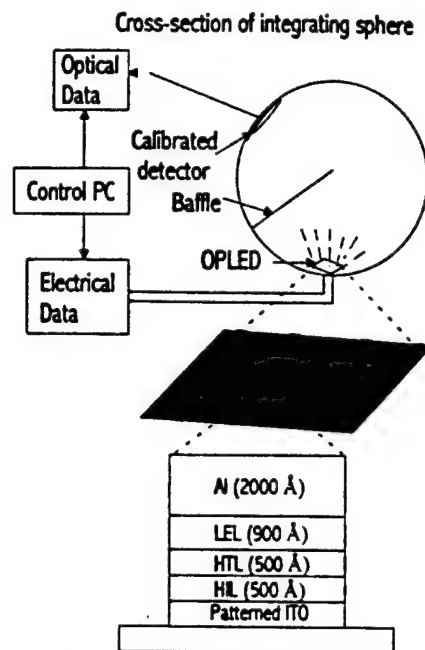
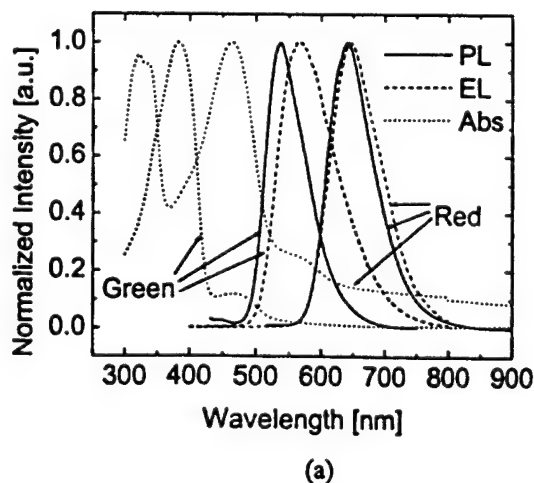


Figure 1 Device structure and measurement setup used in this work.

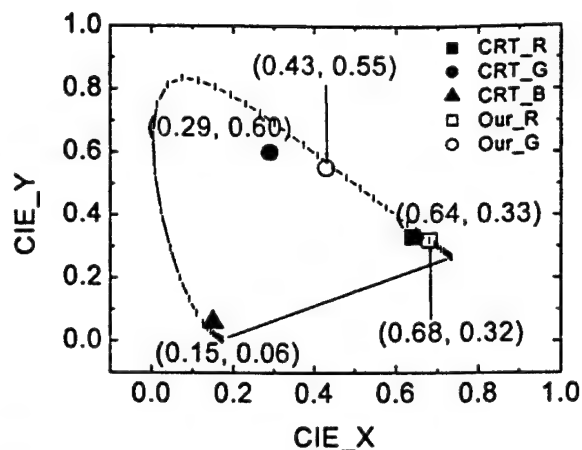
thermally or electron-beam evaporated through shadow masks under a high vacuum condition ($\sim 10^{-6}$ Torr). The device area defined by the cross-section of anode and cathode is 0.05"x0.05".

Results and Discussions

As shown in Fig. 1, multi-layer structures were used to improve OPLEDs opto-electronic performances. The PEDOT/PSS, PC6, and Dow red

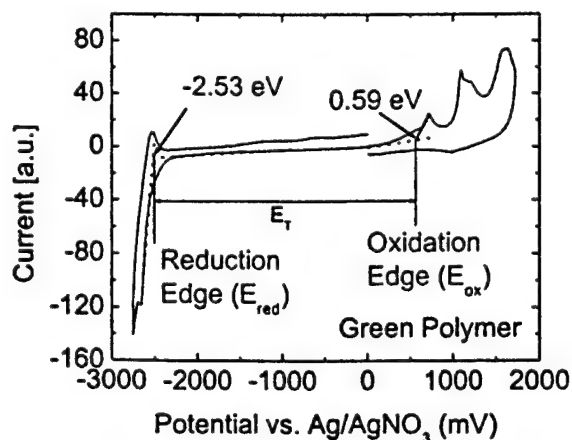
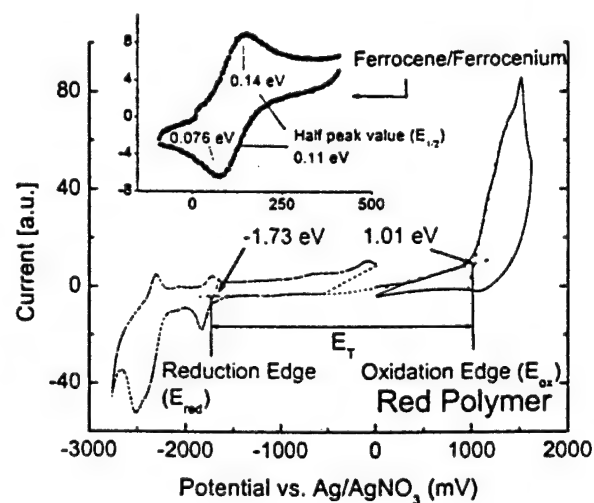


(a)

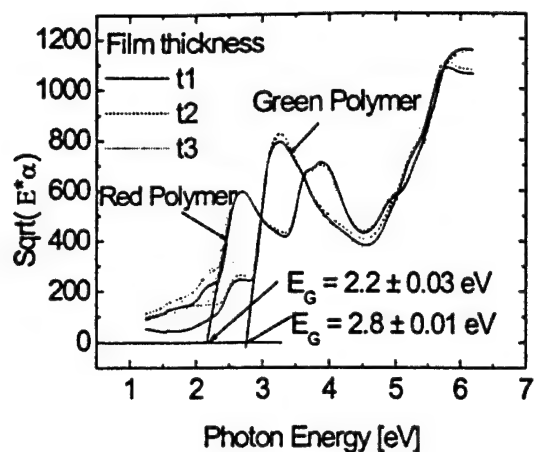


(b)

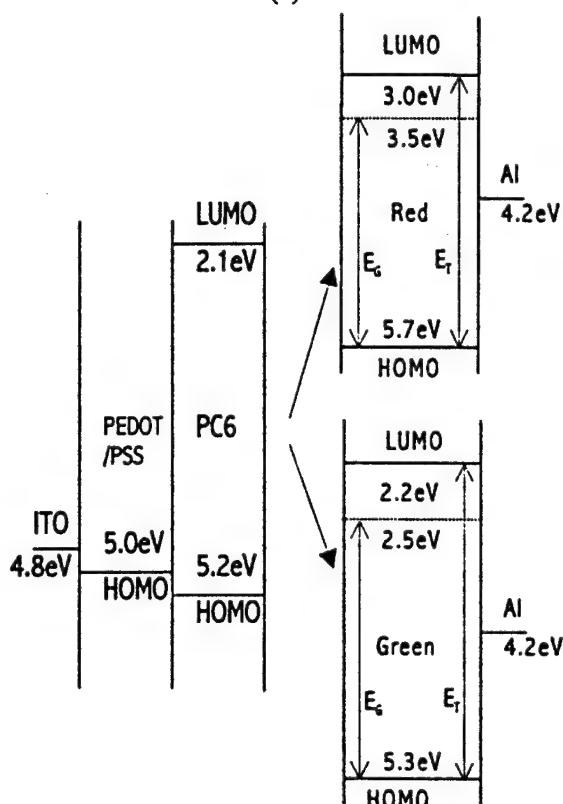
Figure 2. Photoluminescence, electroluminescence, and absorption spectra (a), and CIE data (b) of the green and red light emitting polymers are shown.



(a)



(b)



(c)

Figure 3 Cyclic voltammetry data (a) and Tauc plots (b) for light emissive polymers are shown; t1, t2, and t3 represent 1000/2000, 800/1000, 600/700 Å for red/green polymers, respectively. Energy band diagram (c) extracted from (a) and (b); E_T and E_G are transport and optical band gaps, respectively.

/green light-emitting polymers were used for HIL, HTL, LEL, respectively. The material characteristics of the PEDOT/PSS and PC6 have been reported elsewhere.^{4,5} Fig. 2(a) shows the photoluminescence (PL), electroluminescence (EL), and absorption (Abs) spectra of the Dow green and red light emitting polymers. The absorption and PL spectra were

obtained for several single layer thin films deposited on quartz substrates with different thickness. The EL spectra were measured for ITO/HIL/LEL/aluminum structure. The peak values of Abs/PL/EL for green and red LEL are 383/537/568-nm and 465/639/644-nm, respectively. The EL spectra of both the green and red light-emitting polymers are red-shifted with respect to PL. From EL spectra, Commission Internationale de l'Eclairage (CIE) data for our two light-emitting polymers have been obtained as shown in Fig. 2(b). The CIE values for cathode ray tube (CRT) red, green, and blue light emission are also given in this figure. We obtained (0.43, 0.55) and (0.68, 0.32) for Dow green and red light-emitting polymers, respectively. From the figure, it is found that our polymers can be used for full color AM-OLED applications once the blue light-emitting polymer is added.

To develop the energy band diagram of our devices, we used a combination of the cyclic voltammetry (CV) and Tauc plots of the absorption spectra. From the CV spectra shown in Fig. 3(a), the positions of the lowest unoccupied molecular orbital (LUMO) and highest occupied molecular orbital (HOMO) with respect to the vacuum energy level, and the transport band gap (E_T) have been obtained by using the following procedures. The onsets of oxidation (E_{ox}) and reduction (E_{red}) are obtained from the measured CV spectra. In our case, we observed two reduction and oxidation peaks for red and green LEL, respectively. However, since we believe that the first reduction and oxidation potentials represent the triggering point of reduction and oxidation processes, we used these values to define LUMO and HOMO levels for our light emissive polymers. By assuming a scale factor relating Ferrocene/Ferrocenium couple to vacuum of ~ 4.8 eV⁴, the HOMO and LUMO levels can be defined by measuring E_{ox} , E_{red} , and $E_{1/2}$.

$$\text{HOMO} = (E_{ox} - E_{1/2}) + 4.8 \text{ [eV]},$$

$$\text{LUMO} = (E_{red} - E_{1/2}) + 4.8 \text{ [eV]},$$

where, $E_{1/2}$ is the averaged half peak value of ferrocene level. In our case, HOMO and LUMO levels of red/green light-emitting polymers are 5.7/5.7 eV and 3.0/2.6 eV, respectively.

The polymer optical band gap energy (E_G) was obtained from the Tauc plot of absorption spectra shown in Fig 3(b). If we assume that our spin-coated polymers are amorphous 3-D system, in which the electron wave functions can spread in all directions, the following equation can be derived.⁶

$$\sqrt{\alpha h\nu} \propto (h\nu - E_G)$$

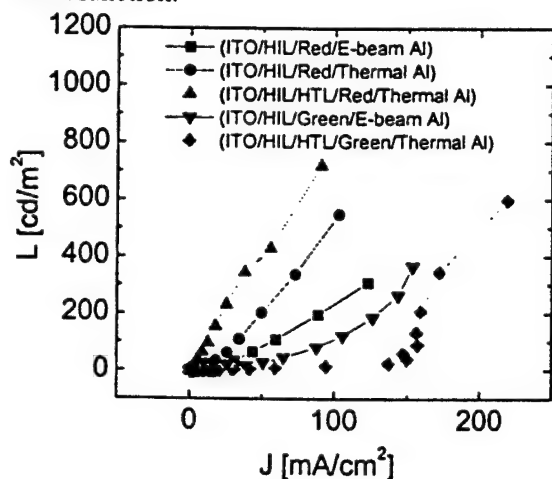
where α and $h\nu$ are absorption coefficient and photon energy, respectively. This equation shows that optical band gap can be extrapolated when the square

root of the product of absorption coefficient and photon energy is plotted versus photon energy. In Fig. 3(b), Tauc plots and linear fits for our emissive polymers with different thickness are shown. From this figure, we extracted $E_G = 2.2 \pm 0.03$ eV and 2.8 ± 0.01 eV for red and green polymers, respectively. Using the above extracted energy level values, the energy band diagram for our double layer OLEDs was constructed as shown in Fig. 3 (c). The HOMO level of PEDOT/PSS and work functions of Al and ITO are also included. By combining HIL and HTL in one OLED structure, the effective hole injection barrier is reduced from 0.9/0.5 eV to three steps of 0.2/0.2, 0.2/0.2, and 0.7/0.1 eV for red/green light-emitting polymers, respectively. For red devices, this staircase-like gradual increase of the HOMO levels between ITO and LEL enhances the device brightness and efficiencies measured at the same current densities as shown in Fig. 4, where emission (EE) and power (PE) efficiencies are defined by the ratio of brightness to current flow across the devices and the ratio of light output power to electrical input power, respectively. These improvements are due to reduction of effective barrier for hole injection into LEL.

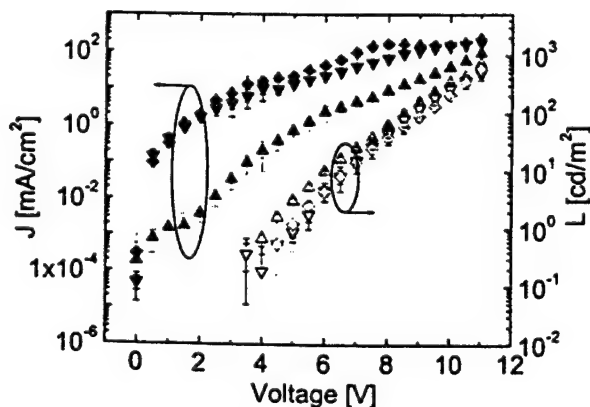
For green OLEDs, slightly poorer device performances have been obtained in comparison with the red OLEDs. The same device structures, e.g. ITO/HIL/LEL/e-beam Al and ITO/HIL/HTL/LEL/thermal Al were used in both cases. We speculate that this difference is due to larger electron injection barrier at the cathode of the green devices (about 0.8 – 1.0 eV larger than barrier of the red devices). From Fig. 4(a), the L-J characteristics of green devices do not show the linear relationship over the whole current levels in comparison with the red devices. This behavior is more apparent for the devices with the HIL (two linear segments). Also the total current flow increased for green OLED with HIL in comparison with the devices without HIL while the light output did not change that much for the same voltage levels as shown in Fig. 4(b). This observation can indicate that the holes contribution to the total current flow is larger when HIL is added in the device structure. This additional layer will reduce effective hole injection barrier between anode and LEL. At the same time in this structure, however, a higher electron injection barrier limits the optical device performances by reducing the electron density at the LEL/cathode interface. From our results, we can conclude that the electron injection barrier at the cathode is the limiting factor in the green OLED performance optimization. Therefore, green device opto-

electronic performances can only be improved if a low work function metal cathode, such as calcium or erbium is used, and/or an additional electron injection layer between LEL and cathode is introduced. These issues will be discussed in a separate publication.

We have also investigated the effect of different cathode-metalization methods, such as electron-beam and thermal evaporation, on the optical and electrical performances of the OLEDs. From our results, we have concluded that devices with thermally evaporated cathodes have better opto-electronic performances. We speculate that this difference is associated either with the damage of LEL or metal migration to the inside of polymer induced by electron beam evaporation method. Both can cause deep gap states (defects) formation in the polymer and subsequent decrease in device luminance. The defects will trap electrons and reduce carrier recombination efficiency. It should be noticed that metal deposited by both methods has the same work function.



(a)



(b)

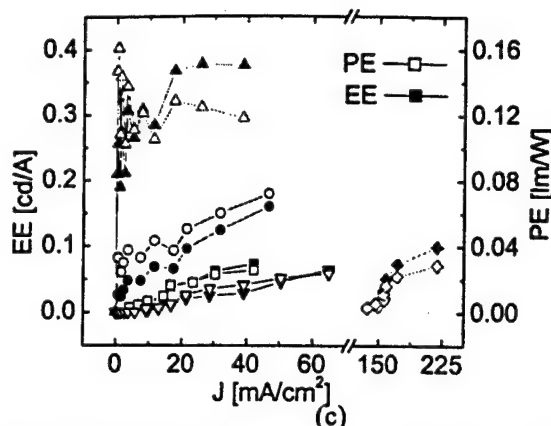


Figure 4 Optical and electrical performances of the red and green light-emitting devices fabricated on the flexible plastic substrates are shown, where PE and EE are power and emission efficiencies defined in the text, respectively.

Conclusions

We have fabricated the multi-layer red and green OLEDs based on poly-fluorenes using aluminum as a cathode metal. We found that device optical and electrical performances can be improved by introducing a combination of the HIL and HTL in the device structure and by using a thermal evaporation method for cathode metal deposition. The following opto-electrical properties have been obtained for our red/green OLEDs, respectively: turn-on voltage: $\sim 3.5/5.0$ V; voltage and current density at 100 cd/m^2 : $\sim 8/9.1$ V and $\sim 15/150 \text{ mA/cm}^2$; maximum light emission and power efficiencies at $\sim 20/220 \text{ mA/cm}^2$: $\sim 0.4/0.1 \text{ cd/A}$ and $\sim 0.13/0.03 \text{ lm/W}$.

Acknowledgement

This research was supported by ONR-DARPA and NIH grants. Authors also thank Shujen Lee for PL and CV measurements.

References

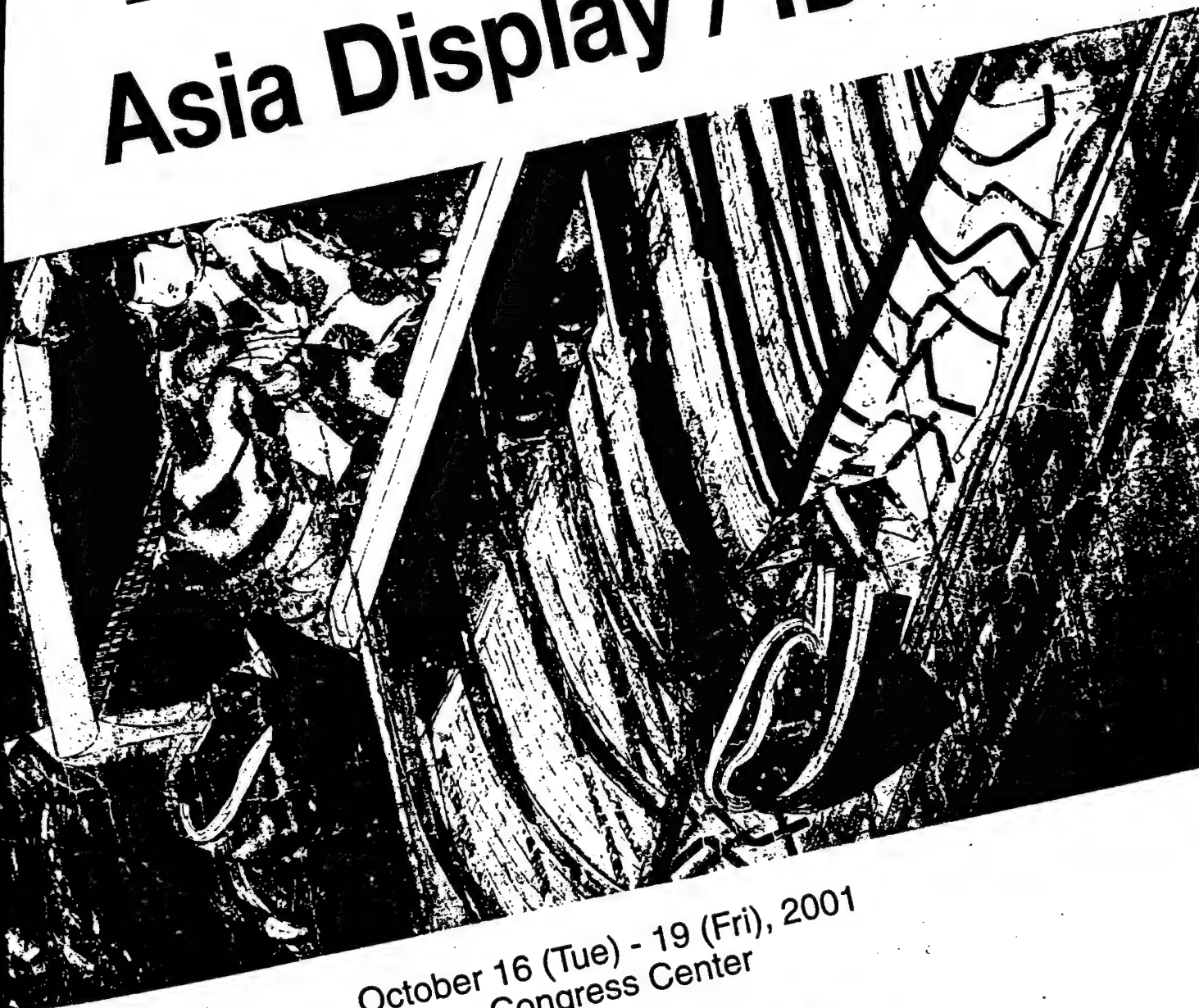
1. P.E. Burrows, G.L. Graff, M.E. Gross P.M. Martin, M. Hall, E. Mast, C. Bonham, W. Bennett, L. Michalski, M. Weaver, J.J. Brown, D. Fogarty, and L.S. Sapochak, *Proceedings of SPIE* 4105, 75 (2001).
2. Y. He and J. Kanicki, *Proceedings of SPIE* 4105, 143 (2001).
3. Y. Hong, Z. Hong, and J. Kanicki, *Proceedings of SPIE* 4105, 356 (2001).
4. Y. Hong, Z. Hong, M.D. Curtis, and J. Kanicki, *Conference Record of the IDRC 2000*, 183 (2000).
5. Y. Hong, Z. He, S. Lee, and J. Kanicki, *Proceedings of SPIE* (in press).
6. J. Tauc, R. Grigorovici, and A. Vancu, *Phys. Stat. Sol.* 15, 627 (1966).

ITE

SID
SOCIETY FOR INFORMATION DISPLAY

The 21st International Display Research Conference in conjunction with
The 8th International Display Workshops

Asia Display / IDW '01



October 16 (Tue) - 19 (Fri), 2001
Nagoya Congress Center
Nagoya, Japan

Proceedings

Amorphous Silicon Thin-Film Transistors Based Active-Matrix Organic Light-Emitting Displays

J. Kanicki, J.-H. Kim, J.Y. Nahm, Y. He, and R. Hattori*

Organic & Molecular Electronics Laboratory, Department of EECS,
The University of Michigan, Ann Arbor, MI 48109, USA.

*Department of Electronic Device Engineering, Kyushu University, Fukuoka, Japan

ABSTRACT

In our laboratory we have simulated, designed, and fabricated hydrogenated amorphous silicon (a-Si:H) thin-film transistors (TFTs) based pixel electrode circuits for active-matrix organic light-emitting displays (AM-OLEDs). These pixel circuits, having very small feed-through voltages, can supply a continuous output current at an adequate level for AM-OLEDs up to 500 dpi of resolution. Each pixel electrode has also compensation circuits that will allow to adjust the output current level for the OLED and a-Si:H TFTs threshold voltage variations. Therefore, we can control display brightness uniformity at an acceptable level.

INTRODUCTION

In the past several years different types of pixel electrode circuits have been proposed for the active-matrix (AM) organic light-emitting displays (OLEDs). For the micro-displays, crystalline silicon (c-Si) CMOS based pixel electrode circuits have been developed [1-3]. These c-Si based AM-OLEDs have limited size (< 2 inch) and use organic light-emitting devices with the top transparent cathode metal electrode. For large-area AM-OLED, the polycrystalline silicon (poly-Si) thin film transistor (TFT) pixel electrode circuits have been introduced [4-7]. The advantage of poly-Si TFT AM-OLEDs is that the display drivers can be integrated with the pixel electrode circuits. Another possible technology for AM-OLED is hydrogenated amorphous silicon (a-Si:H) TFT technology. This type of technology can be very cost effective over large-area.

Important issue that needs to be addressed in the AM-OLEDs is a poor uniformity of display brightness that can be caused by TFT and/or OLED electrical degradation. This problem cannot be easily addressed if a simple voltage driving method is used to produce display gray levels. A few different methods have been proposed to address this problem, such as current driving [7-10], time-ratio gray-scale [6], and area-ratio gray-scale methods [5].

In this paper, we will summarize circuit simulation and experimental results obtained for the a-Si:H three and four TFTs AM-OLEDs pixel electrode circuits developed in our group that can overcome the brightness uniformity problem.

A-Si:H TFT PIXEL ELECTRODE CIRCUITS

In AM-OLED, in order to turn on OLED continuously, a minimum of two a-Si:H or poly-Si TFTs are needed. It should be noticed that, in this type of pixel electrode circuit, any variation of TFTs and OLEDs electrical parameters will introduce different output current levels for each pixel even if driving TFT gate-source voltage and drain-source voltage are kept constant. This output current non-uniformity will result in OLED brightness non-uniformity since luminance of the OLED is usually proportional to applied current level.

To overcome this problem, we proposed two different pixel electrode circuits configurations: voltage driving 3-a-Si:H TFTs and current driving 4-a-Si:H TFTs circuits. Both configurations have their own strengths and shortcomings.

3-a-Si:H TFTs pixel electrode circuits

The 3 - a-Si:H TFT pixel electrode circuit is shown in Figure 1 [11]. In this schematic diagram, C_{ST} is storage capacitor, T1 is switching TFT, T2 is active resistor, and T3 is large-sized high-capacity constant current driving TFT.

The pixel electrode circuit operation of the AM-OLED can be explained as follows. During the gate scan voltage (V_{select}) pulses to a high level, an image data (V_{data}) is fed to the gate electrode of the constant current driving TFT controlling the amount of the drain current (driving current) of the driving TFT. The drain electrode of the driving TFT is connected to a high-voltage source through the active resistor. At the same time, V_{data} is stored in the storage capacitor. For a given frame time depending on the refresh rate of the AM-OLED design, the gate voltage of the constant current driving TFT remains at the same level even after V_{scan} drops low, since C_{ST} keeps the image data (V_{data}). In this case, the current compensation circuit is represented by an active resistor (T2) TFT, with gate and drain electrodes connected together, operating only in saturation mode. The operating current determines the voltage drop across the active resistor. For any reason, e.g., when the threshold voltage of the constant current driver increases or the turn-on voltage of the OLED increases, if the current flowing through the active resistor decreases, the voltage drop across the active resistor decreases. That will allow for a high current to flow back through the OLED pixel, compensating for

the parameter changes in both the constant current driver and the OLED.

The pixel electrode circuit performance of the AM-OLED was simulated using the Cadence circuit simulator, Spectre. The a-Si:H TFT model used in this simulation was previously developed within our group [12]. Using the OLED and a-Si:H TFT models, 100 x 100 active-matrix array for AM-OLED with 300 dpi resolution (127 μm x 127 μm pixel size) was designed and simulated for driving voltages (V_{drv}) ranging from 4 to 10 V. In each case, the data and the scan voltages were the same as the driving voltages. The transient pixel electrode circuit simulation results are shown for 30 msec. The ON- and OFF-states are shown for the driving voltage of 10 V, Figure 2. The storage capacitance was optimized during the AM-OLED simulation. The optimum value was chosen to be large enough for good image retention and to fit into the pixel area (e.g., pixel electrode aperture ratio was optimized in this design).

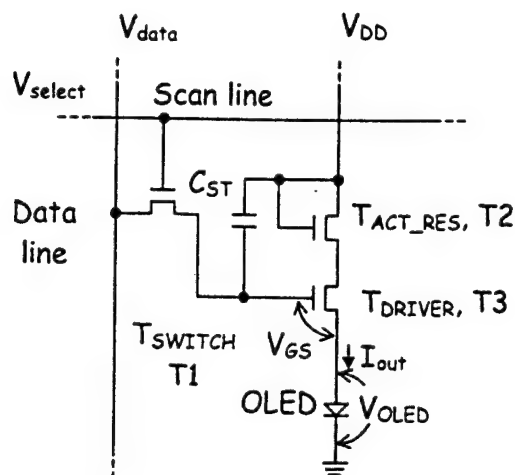


Figure 1. A schematic diagram of the AM-OLED pixel electrode circuit [11].

With a storage capacitance of 0.4 pF, the switching between the ON- and OFF-states was completed within the scan time. In addition, the image data stored in the storage capacitor was retained without any loss during the retention period for AM-OLED frame time (60 Hz).

During the AM-OLED pixels operation, the feed-through voltage drops occur while the V_{scan} signal drop. Feed-through voltage is an abrupt voltage change induced by a capacitive coupling of the gate signal through the gate-source capacitance. Typically, the AM-LCD pixel electrode circuit has a feed-through voltage of about 1 to 2 V at the source electrode of the switching TFT [11, 13]. On the other hand, the feed-through voltage of our AM-OLED pixel is only of a few tenths of mV. This was achieved by using the cascaded TFT connection of the switching TFT and the constant current driving TFT. This low feed-through voltage will enhance the gray level controllability of the AM-OLED.

Another advantage of the gray level control in AM-OLED over AM-LCD is the absence of the asymmetrical feed-through voltage effect associated with the dual data voltage levels ($V_{\text{d+}}$ and $V_{\text{d-}}$).

The extensive pixel electrode circuit simulation and analysis results indicate that a continuous pixel electrode excitation can be achieved with these circuits, and a pixel electrode driving output current level up to 1.4 μA can be reached with the a-Si:H TFT technology.

AM-OLEDs with the resolution up to 500 dpi have been designed with 3-a-Si:H TFTs configuration in our group. The AM-OLED described in this paper features 45 % aperture ratio, 300 dpi pixel, switching TFT (with W/L of 30 μm / 10 μm), active resistor TFT (with W/L of 15 μm / 10 μm), driving TFT (with W/L of 105 μm / 10 μm), and C_{ST} of 0.4 pF.

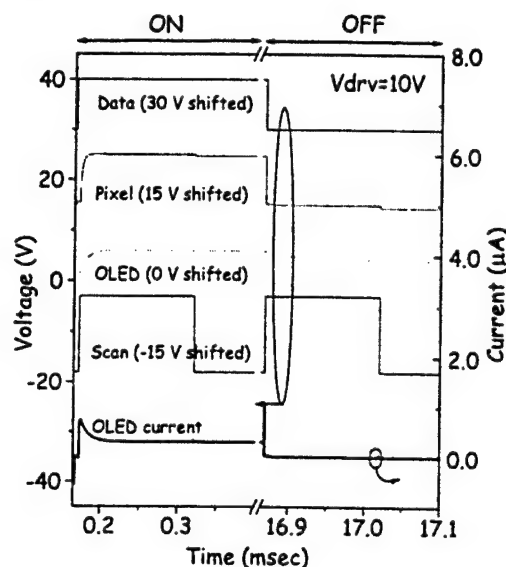


Figure 2. Simulation example of the AM-OLED operation for driving voltages of 10 V.

4-a-Si:H TFTs pixel electrode circuits

Four a-Si:H TFT current driving pixel electrode circuit [14-17] is shown in Figure 3. T1 and T2 serve as switches to adjust OLED output current (I_{out}) to input data current (I_{data}) level when a pixel electrode is selected (V_{select1} is high, V_{select2} is low). T4 is another switching TFT that is turned on only when the pixel electrode is deselected (V_{select1} is low, V_{select2} is high). A common source line (V_{dd}) is used to supply I_{out} current when the pixel electrode is deselected.

T3 operates as driving TFT connected to OLED. During pixel-selected period, I_{out} value is set to match I_{data} as I_{data} flows from input current source through data busline-to-T2-to-T3. During the same pixel electrode selected period, gate-source ($V_{\text{gs}}=V_{\text{Ca}}$) and drain-source (V_{ds}) voltage values are set to certain values to achieve $I_{\text{out}}=I_{\text{data}}$ with the help of charges stored in storage capacitance (C_{ST}) by T3. These V_{gs} and V_{ds} can vary from pixel-to-pixel to maintain $I_{\text{data}}=I_{\text{out}}$ independent of the OLED and TFTs operating parameters. Examples of

the device parameter variations are OLED and TFT threshold voltages, and TFT mobility, which could result from manufacturing and material variations, and pixel electrode circuitry aging.

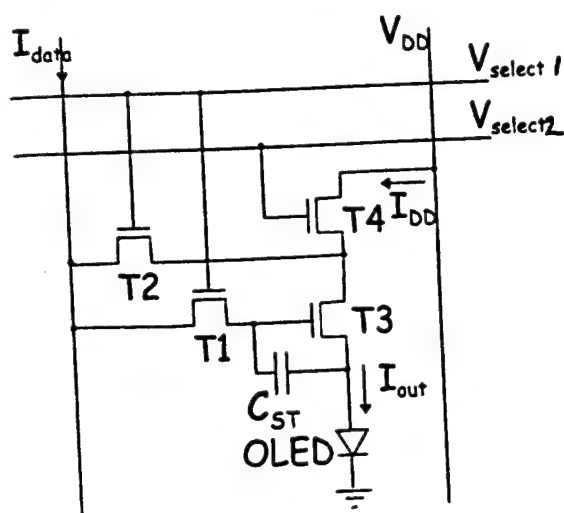


Figure 3. The a-Si:H four TFTs current driving pixel electrode circuit.

During pixel-deselected period, I_{out} flows through V_{dd} line-T4-T3, and should be maintained very closely to the value set during pixel-selected period. This is possible because the drain current of TFT does not change significantly for the same V_{gs} and different V_{ds} values in TFT saturation region. However, for a-Si:H TFTs with non-ideal saturation characteristics, as the V_{ds} of T3 increases during pixel-deselected period, I_{out} could be higher than initial I_{data} . Another effect that can change I_{out} during the transition from pixel-selected to pixel-deselected period is charge redistribution of C_{ST} due to TFT parasitic capacitances of T1, which results in V_{GS} and I_{out} reduction during pixel-deselected period.

Simulation and experimental results have confirmed that I_{out} can be auto-corrected for OLED and TFT characteristic variation when four TFTs pixel electrode circuit is used, Figure 4 [14-17]. This compensation cannot be achieved for two TFTs pixel electrode circuits. An example showing simulated I_{out} current dependence on driving TFT threshold voltage shifts for two- and four TFT pixel electrode circuits is shown in Figure 5. The output current is simulated for pixel-deselected period (one frame time).

For this simulation Cadence SPECTRE software was used, and OLED and a-Si:H TFT models were fitted to experimental data developed in our group [12]. In our simulation, the following parameters were used: TFT mobility (μ) = 0.49 cm²/Vs in linear region, TFT threshold voltage (V_{th}) = 2.55V, W/L(T1) = 50μm/6μm, W/L(T2) = 100μm/6μm, W/L(T3) = 172μm/6μm, W/L(T4) = 189μm/6μm, I_{data} = 5μA, $V_{select1}(\text{high})$ = $V_{select2}(\text{high})$ = 30V, $V_{select1}(\text{low})$ = $V_{select2}(\text{low})$ = 0V, V_{DD} = 30V, C_{ST} = 5pF, C_{oled} = 1.5pF, TFT parasitic

capacitance model parameter: C_{gs0} (gate-to-source) = C_{ds0} (gate-to-drain) = 50×10^{-10} F/m.

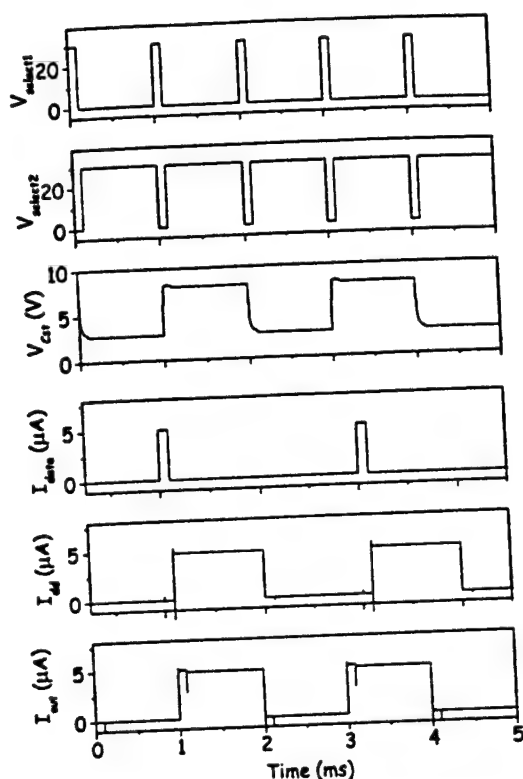


Figure 4. Simulation example of pulse diagram for 4-a-Si:H TFTs current driving pixel electrode circuit for I_{data} = 5μA.

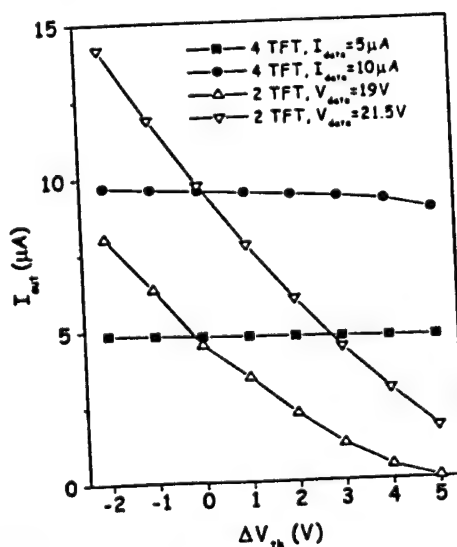


Figure 5. Simulation results of the OLED output current (I_{out}) dependence on TFT threshold voltage shifts for two TFTs voltage and four TFT current driving pixel electrode circuits.

For the two TFTs voltage driving pixel electrode circuit, $V_{gs} \approx 8.1V$ is needed to achieve $I_{out} = 5\mu A$ when $V_{th} = 2.6V$ and threshold voltage shift is zero ($\Delta V_{th} = 0V$). As expected, for the two TFTs pixel electrode circuit, I_{out} decreases as ΔV_{th} increases since TFT output current is proportional to $(V_{gs} - V_{th})^2$ in saturation region. It is obvious when $\Delta V_{th} = 5.5V$ and $V_{gs} - V_{th} = 0V$, I_{out} is close to zero. In the four TFT current driving pixel electrode circuit, V_{gs} is automatically set to a certain value to produce $I_{data} = 5\mu A$ regardless of V_{th} shifts and I_{out} does not decrease much even up to $\Delta V_{th} = 10V$. The reduction of I_{out} observed for the four TFTs pixel electrode circuit is due to reduction of V_{ds} of T3 since V_{ds} of T4 is high for higher V_{th} . Overall, this result clearly indicated that four TFT current driving pixel electrode circuit has much lower reduction of I_{out} over two TFTs pixel electrode circuit.

In the ideal case, I_{out} should be equal to the I_{data} . But in reality I_{out} is limited by a-Si:H TFT characteristics and driving voltage conditions. The simulated results shown in Figure 6 indicate that I_{out} is slightly lower than the ideal value when $I_{data} > 20\mu A$ and the deviation increases with increasing I_{data} . The discrepancy between I_{data} and I_{out} is due to shift of the T3 operation point from the saturation into the linear region. During the pixel-deselected period, if I_{data} is high, the V_{ds} shifts to lower value that is limited by V_{dd} value. Thus, T3 operates in the linear region instead of the desired saturation region and I_{out} cannot keep the same current level at pixel-selected period. However, according to our calculation, I_{out} current level over $20\mu A$ is not necessary for AM-OLED. Using simple calculations and pixel electrode circuit simulations, we have designed AM-OLED based on 4-a-Si:H TFTs pixel electrode circuit.

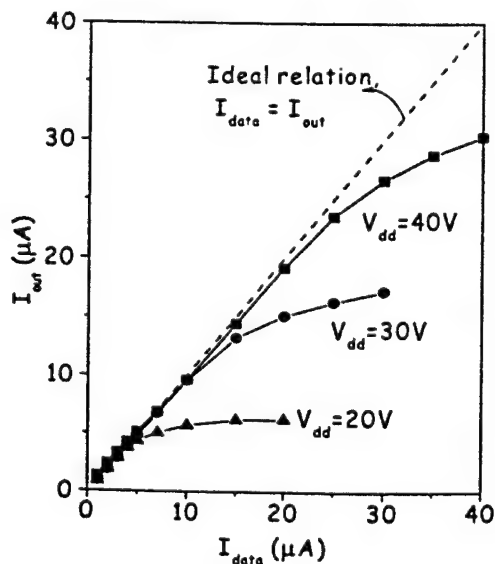


Figure 6. Relation between OLED output current (I_{out}) and input data current (I_{data}) when $V_{select1}$ (high) = $V_{select2}$ (high) = $V_{dd} = 20, 30$, and $40V$, respectively.

An example of such AM-OLED is shown in Figure 7. So far, the AM-OLEDs with 4-a-Si:H TFT pixel electrode circuits having the resolution up to 300 dpi have been developed in our group.

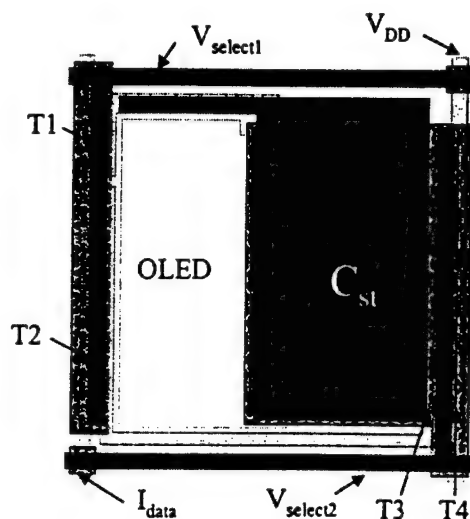


Figure 7. Top view and cross-section of the pixel electrode with pixel size = $254 \times 254 \mu m^2$, OLED size = $77 \times 185 \mu m^2$, aperture ratio = 22%, and $C_{ST} = 3.5pF$.

ACKNOWLEDGEMENT

This work was supported by ONR-DARPA and NIH grants.

REFERENCES

1. K. Pichler et al., *Proc. of SPIE*, 3797, 258 (1999).
2. T. Feng et al., *Proc. of SPIE*, 4105, 30 (2001).
3. H.E. Abraham et al., *Proc. of SPIE*, 4105, 37 (2001).
4. R.M.A. Dawson et al., *Proc. of SID Sym.*, p. 11 (1998).
5. M. Kimura et al., *IEEE Trans. on Elec. Dev.*, 46, 2282 (1999).
6. T. Shimoda et al., *Proc. of IEDM*, p. 107 (1999).
7. M. Mizukami et al., *Proc. of SID Sym.*, p. 912 (2000).
8. K. Inukai et al., *Proc. of SID Sym.*, p. 924 (2000).
9. G. Rajeswaran et al., *Proc. of SID Sym.*, p. 974 (2000).
10. S.J. Bae et al., *Proc. of IDRC Sym.*, p. 358 (2000).
11. J.-H. Kim et al., *Proc. SPIE Medical Imaging*, 4319, 306 (2001).
12. C.-Y. Chen et al., *Proc. of ESSDERC'96*, p. 1023 (1996).
13. M. Ohta, M. et al., *Japan Display*, 431 (1992).
14. R. Hattori et al., *IEICE Trans. Electron.*, E83-C, 779 (2000).
15. Yi He et al., *IEEE EDL*, 21, 590 (2000).
16. Yi He et al., *Jpn. J. Appl. Phys.*, 40, 1199 (2001).
17. Yi He et al., *IEEE Trans. on Elec. Dev.*, 48, 1322 (2001).

EXTENDED ABSTRACTS

THE FIRST
INTERNATIONAL CONFERENCE
on the SCIENCE and TECHNOLOGY
of EMISSIVE DISPLAYS and LIGHTING



SOCIETY FOR INFORMATION DISPLAY



Sponsored by
Phosphor Technology Center of Excellence (PTCOE)
Defense Advanced Research Projects Agency (DARPA)
Society for Information Display (SID)

November 12-14, 2001
San Diego, California

ORGANIC POLYMER LIGHT-EMITTING DEVICES (OPLEDs) ON PLASTIC SUBSTRATES FOR ACTIVE-MATRIX ORGANIC POLYMER LIGHT-EMITTING DISPLAYS (AM-OPLEDs)

Jerzy Kanicki^{a*}, Yongtaek Hong^a, Shujen Lee^b and Zhiqi. He^a

^aDept. of Electrical Engineering and Computer Science, University of Michigan, Ann Arbor, MI

^bDept. of Macromolecular Science and Engineering, University of Michigan, Ann Arbor, MI

Abstract

The opto-electronic properties of the organic polymer light-emitting devices (OPLEDs) fabricated on flexible plastic substrates are discussed. The optimized design and technological issues associated with these devices are also presented. More specifically the issues related to plastic substrates properties, optimization of the device structure including energy band diagram construction, and cathode metallization methods are addressed. The Monte Carlo simulation was used to optimize the device light emission output. The OPLED angular dependence of the light emission was also measured and compared with the simulation results. Finally the OPLEDs lifetime and pixel electrode design for active-matrix (AM) OPLEDs are addressed. All devices discussed during this presentation have been fabricated at the University of Michigan.

Simulation and measurement of angular dependence of light emission from OPLEDs

A Monte Carlo method for modeling the light transport phenomena was used to study the effect of the light transport process on the optical performance of the OPLEDs. In this simulation we assumed a point light source having photon emission spectra represented by photoluminescence (PL) spectra of the organic polymers. This simulation method describes the fate of photons through multiple scattering events determined by the wavelength-dependent material optical properties in a 3-D Cartesian geometry, thus considering the effects of refraction at different interfaces, back-reflection, and absorption within the polymer layers.¹

We applied this method to analyze the light wavelength distribution and extraction efficiency of the OPLEDs. The preliminary results showed that the simulated light emission spectra of green and red light-emitting devices were very similar to the measured PL spectra as shown in Fig. 1. We also established that the calculated extraction efficiency for the red ($\eta_{\text{ext}}=21.71\%$) and green ($\eta_{\text{ext}}=21.70\%$) OPLEDs were approximately the same. We further investigated the light emission angular distribution of the OPLEDs, and found that the angular distribution is a quasi-Lambertian with increased intensity in the forward direction for both red and green devices as shown in Fig. 2. It was found that the light refraction at different interfaces leads to this quasi-Lambertian angular distribution, while the absorption and the back-reflection have minor effects. To further qualify the applicability of this method in the emissive structure, we measured the angular distribution of the OPLEDs as shown in Fig. 2. The preliminary results showed that the experimental angular distribution of the OPLEDs was very close to a Lambertian distribution. Further investigation on qualifying this simulation method for optimizing the OPLEDs is underway.

Device opto-electronic characteristics

Plastic substrates

We used ITO-patterned plastic substrates from 3M in this work. As shown in Fig. 3, the plastic substrates have a multi-layered structure to reduce gas transmission through the substrates. To improve ITO electrical performance without loss of optical properties, a thin metal layer is placed under the ITO layer. The measured properties of the plastic substrates are summarized in Table 1. Since it is well known that the degradation of the OPLEDs is strongly related to water vapor and oxygen permeation, it is critical to further reduce the gas transmission through the substrates for commercial applications. Hence, we have investigated the effect of different coating layers on the plastic substrate properties. The detailed process and measurement setup for these coating layers have been reported elsewhere.² The best results have been obtained by using a combination of the hydrogenated amorphous silicon (a-SiN_x) and hydrogenated amorphous silicon dioxide (a-SiO_x) layers deposited by low temperature PECVD, Table 1. From our results, it can be concluded that a low temperature multi-layer

* E-mail: kanicki@eecs.umich.edu (fax) 734-936-0347

inorganic films deposited over the plastic substrates can reduce the gas transmission rates to the levels undetectable by the conventional MOCON method.

Organic polymers

In our work, multi-layer device structure, shown in Fig. 3, was used to improve OPLEDs opto-electronic performances. ITO and aluminum were used as anode and cathode, respectively. PEDOT/PSS, PC6, and Dow red/green light emissive polymers were used for hole injection layer (HIL), hole transport layer (HTL), and light emissive layer (LEL), respectively. The material characteristics of PEDOT/PSS and PC6 have been published elsewhere.³ Figure 4 shows the photoluminescence (PL), electroluminescence (EL), and absorption (Abs) spectra of the Dow green and red light emissive polymers. The chemical structures were reported elsewhere.⁴ We used the polymers cyclic voltammetry (CV) and Tauc spectra to construct the energy band diagram of the fabricated devices, Figure 5. Detailed results and procedures have been reported elsewhere.⁵

OPLEDs opto-electronic characteristics

The opto-electronic characteristics of the OPLEDs are affected by the device structure.⁶ We have employed multi-layer, HIL/HTL/LEL, structure between anode and cathode electrodes to obtain high performance OPLEDs on flexible plastic substrates. Good device performances were obtained for red OPLEDs as shown in Fig. 6. The staircase-like HOMO levels increase has reduced effective hole injection energy barrier between anode and LEL. This reduction enhanced the device efficiencies. However, for green devices, the HIL/HTL bi-layer increased the current flow through the devices without any enhancement of the optical properties. Therefore, it can be concluded from these data that for shorter-wavelength light emitting devices such as green OPLEDs, the opto-electronic performances can only be improved by introducing a low work function cathode such as calcium or erbium, and/or an additional electron injection layer between LEL and cathode. In addition to the device structure, the device performances are also affected by cathode metalization methods. We have demonstrated that thermal evaporation of aluminum gave less damage and metal migration between LEL and cathode in comparison with the electron-beam evaporation method. Thus devices made with thermally evaporated cathode showed better device performances.⁵

OPLEDs lifetime

We have studied OPLEDs operating lifetime related to the initial brightness levels and the type of device driving signals. It is well known that alternative current (ac) driving can improve the device operation stability in Alq based OLEDs since the negative bias component can remove the accumulated or trapped charge in the devices.⁷ We also found that by refreshing our OPLEDs with an appropriate negative bias during the continuous direct current (dc) operation, the device operation lifetime can be increased. Using this ac-like driving method, we also established the relationship between the device lifetime and the initial brightness for our unpackaged devices, which can be expressed as a first-order exponentially decaying function.

$$t_{50\% \text{ drop}} = A + B \times e^{\frac{-L_{\text{initial}}}{C}},$$

where A, B, and C are fitting constants and the operating lifetime ($t_{50\% \text{ drop}}$) is defined as the time corresponding to 50% loss of the initial device brightness (L_{initial}). Figure 7 shows an example of measured lifetime result for red OPLEDs on flexible plastic substrate without any packaging.

Active-matrix organic polymer light-emitting displays (AM-OPLEDs)

As organic polymer device technology has matured, there are tremendous interests in OPLEDs based plastic flat panel displays. Over last several years, our group has also focused our efforts on amorphous silicon thin-film transistor (a-Si:H TFT) based pixel electrode circuit design for AM-OPLEDs on plastic substrates. We have developed two types of pixel electrode circuits – three⁸ and four^{9,10,11} a-Si:H TFT configurations, where voltage and current signals are used as data signals, respectively. For both cases, appropriate control signals and circuit configurations are included, which automatically compensate for the long-term-operation threshold voltage shifts of the OPLEDs and a-Si:H TFTs. We think that a-Si:H TFT technology is fully compatible with large area plastic opto-electronics.

Acknowledgements

This work was supported by ONR-DARPA and NIH grants. Authors also thank Drs. A. Badano, J. Kim, and Y. He, and Prof. R. Hattori for their many contributions to this research over last several years.

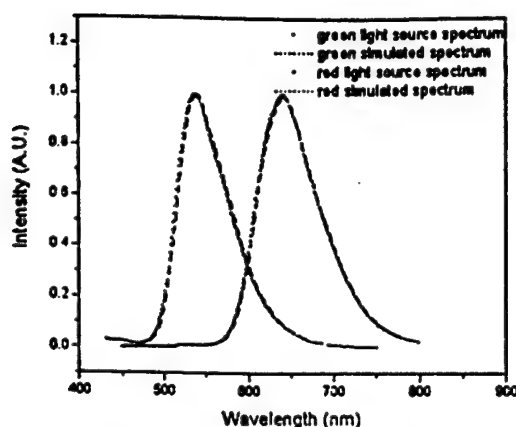


Figure 1: The measured PL and calculated EL spectra are shown.

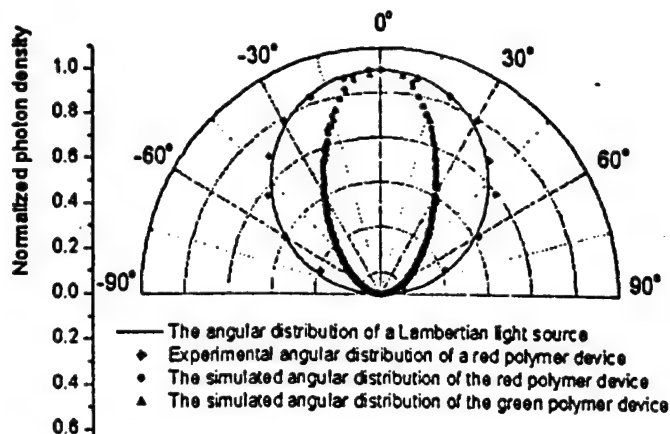


Figure 2: The simulated angular distribution of the red and green OLEDs is shown. The experimental angular distribution of red OLED is also included.

Table 1. Properties of plastic substrates with ITO
(*: Limit of the MOCON test)

Item	Description
Sheet Resistance	~ 12 Ω /
Transmission	> 80 % over visible range
ITO Roughness	1.7 nm (RMS) over 0.5 μm^2
O ₂ Transmission Rate	1.56 $\times 10^{-5}$ (cc/cm ² -day-atm) 2.53 $\times 10^{-7}$ (with a-SiN _x and a-SiO _x coating)
Water Vapor Transmission Rate	3.66 $\times 10^{-4}$ (g/cm ² -day-atm) <1.55 $\times 10^{-5}$ * (with a-SiN _x and a-SiO _x coating)

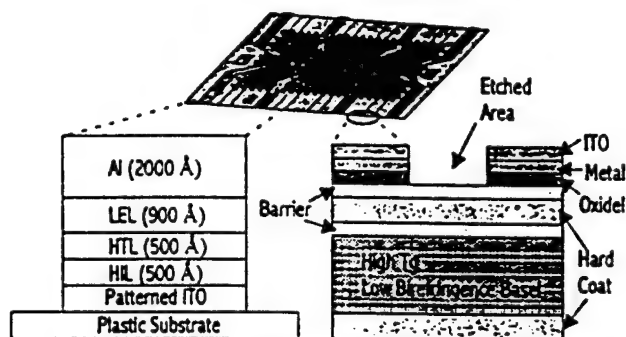


Figure 3. Structures of plastic substrates and fabricated OLEDs are shown.

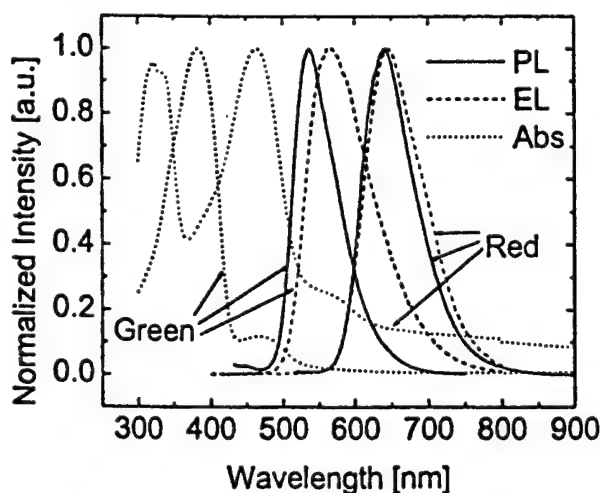


Figure 4. PL, EL, Abs of Dow green and red light emissive polymers are shown.

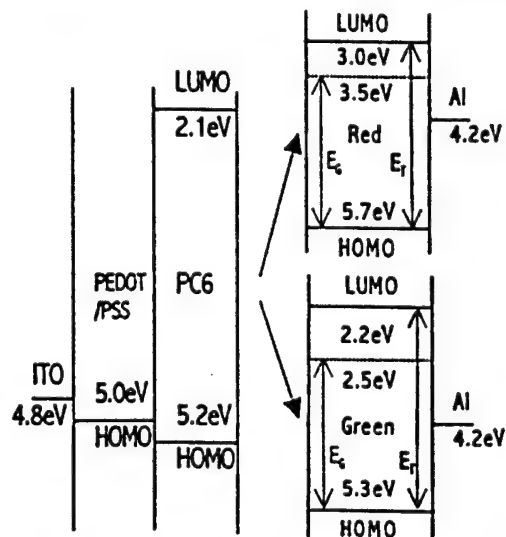


Figure 5 Energy band diagram for green and red OLEDs is shown.

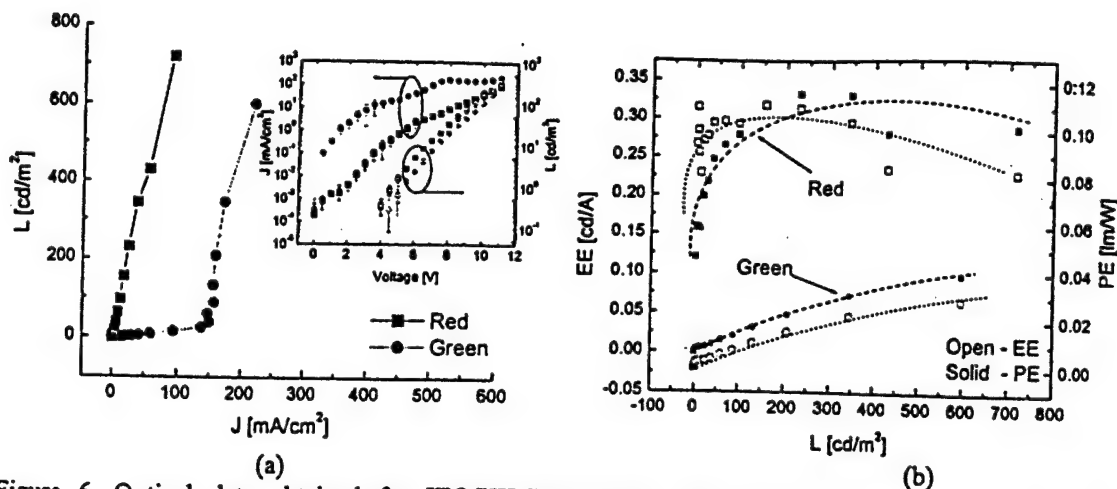


Figure 6. Optical data obtained for ITO/HIL/HTL/LEL/thermal Al devices are shown. (a) J-V-L characteristics (L-J characteristics are also included) and (b) Emission and power efficiencies versus luminance are also shown.

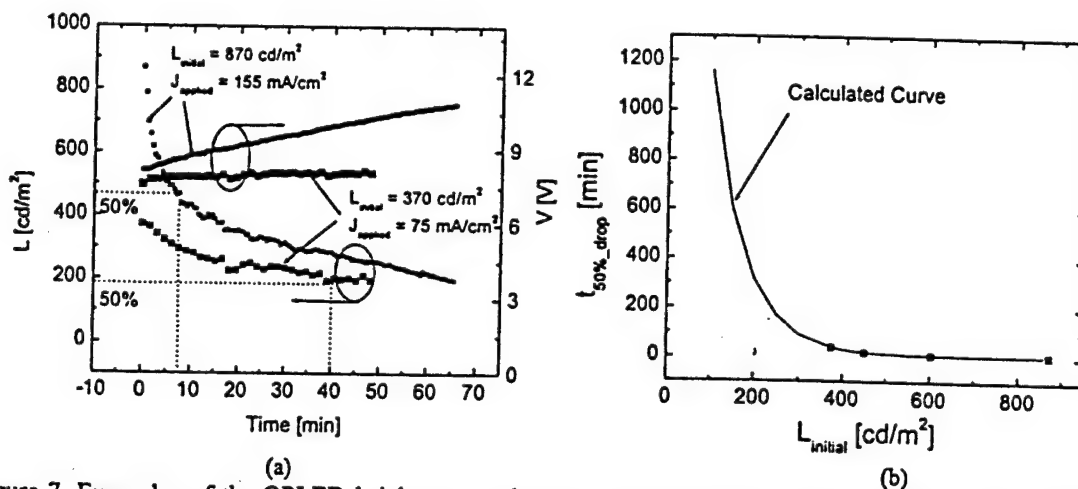


Figure 7. Examples of the OPLED brightness evaluation with the time for initial brightness level of 870 and 370 cd/m^2 are shown (a). The relationship between device lifetime ($t_{50\% \text{ drop}}$) and initial brightness (L_{initial}) of our unpackaged red OPLEDs is shown (b). The calculated curve is also included in this figure. All data were obtained at room temperature under the ambient conditions.

References

- ¹ A. Badano and J. Kanicki, *J. Appl. Phys.* **90**, 1827 (2001).
- ² Y. Hong, Z. He, S. Lee and J. Kanicki, *Proceedings of SPIE '01*, (in press).
- ³ Y. Hong, Z. Hong, M.D. Curtis and J. Kanicki, *Conference Record of the IDRC 2000*, 183 (2000).
- ⁴ M. Bernius, M. Inbasekaran, E. Woo, W. Wu and L. Wujkowski, *Proceedings of SPIE 3797*, 129 (1999).
- ⁵ Y. Hong and J. Kanicki, *Conference Record of the IDRC 2001* (in press).
- ⁶ Y. He and J. Kanicki, *Appl. Phys. Lett.* **76**, 661 (2000).
- ⁷ S.A. Van Slyke, C.H. Chen and C.W. Tang, *Appl. Phys. Lett.* **69**, 2160 (1996).
- ⁸ J. Kim and J. Kanicki, *Conference Record of ICCEL-3*, O-50 (2001).
- ⁹ Y. He, R. Hattori and J. Kanicki, *IEEE Elec. Dev. Lett.* **21**, 590 (2000).
- ¹⁰ Y. He, R. Hattori and J. Kanicki, *IEEE Trans. Elec. Dev.* **48**, 1322 (2001).
- ¹¹ Y. He, R. Hattori and J. Kanicki, *Jpn. J. Appl. Phys.* **40**, 1199 (2001).

PROCEEDINGS OF SPIE REPRINT



SPIE—The International Society for Optical Engineering

Reprinted from

Organic Light-Emitting Materials and Devices V

30 July–1 August 2001
San Diego, USA



Volume 4464

©2002 by the Society of Photo-Optical Instrumentation Engineers
P.O. Box 10, Bellingham, Washington 98227 USA. Telephone 360/676-3290.

Air-stable organic polymer red light-emitting devices on flexible plastic substrates

Yongtaek Hong^{a*}, Zhiqi He^a, Shujen Lee^{a,b}, and Jerzy Kanicki^a

Organic & Molecular Electronics Research Group, Department of Electrical Engineering and Computer Science, University of Michigan, Ann Arbor, MI 48109

^bDepartment of Macromolecular Science and Engineering, University of Michigan, Ann Arbor, MI 48109

ABSTRACT

Organic polymer red light-emitting devices (OPLEDs) with the double layer structure have been fabricated on flexible plastic substrates. Dow red emissive polymer and poly (3,4-ethylenedioxythiophene)/poly (styrene) (PEDOT/PSS) have been used as an emissive and a hole injection polymer, respectively. The spin coating technique was used to deposit different polymers. The absorption and the cyclic voltammetry spectra have been used to construct the band diagram of our OPLEDs. The following electrical and optical properties have been obtained for our OPLEDs: turn-on voltage, defined at 1 cd/m² = ~3.0 V; voltage and current density defined at 100 cd/m² = ~6.5 V and ~34 mA/cm²; maximum emission efficiency = ~0.25 cd/A; and maximum luminous efficiency = ~0.1 lm/W. The extrapolated lifetime of unpackaged OPLEDs on flexible plastic substrate of about 1160 min for initial brightness of 100 cd/m² has been obtained.

Keywords: Organic polymer light-emitting devices, red emissive polymer, flexible plastic substrate, lifetime

1. INTRODUCTION

Today, organic light-emitting devices (OLEDs) are considered as the next generation flat panel display technology for such applications as smart identification cards, screens of mobile units, and automotive displays. Since the first introduction of the OLEDs based on small molecules¹ and conjugated polymers², OLED based displays first appeared at market in 1999. So far, most displays have been built on rigid glass or silicon substrates, and only a few groups have reported devices fabricated on flexible plastic substrates,³ even though the low cost and low temperature processing of the OLEDs render them as most probable candidates for flexible flat panel display applications. Over last several years, we have focused our efforts on organic polymer-based devices and display implementation on the flexible plastic substrates.^{4,5} As a part of our efforts, in this paper the water vapor and oxygen permeation properties of our plastic substrates are reported. The multiple-layer coating of the plastic substrates used will allow to achieve an acceptable level of water vapor and oxygen permeation for commercial application.

Also today, the research on full color organic material-based display has gained considerable attention, and several groups have reported good device performances made of red, green, and blue emissive materials based on poly (fluorene).^{6,7,8} A few years ago our group reported a high performance poly (fluorene) based green light-emitting devices on flexible substrates.^{4,5} In this paper, the electrical and optical properties of the red light-emitting devices fabricated on flexible substrates are described.

2. EXPERIMENTAL

Flexible plastic substrates with patterned indium tin oxide (ITO) electrodes from 3M were used in this study. The electrical, optical, and surface properties of the plastic substrates have been reported elsewhere.⁴ Oxygen and water vapor permeations through our plastic substrates were investigated using the experimental setup shown in the Fig. 1(a) and American Society for Testing and Material (ASTM)^{9,10} methodology. The transmission rates of water vapor and oxygen

* Contact: yongtaek@engin.umich.edu; www.eecs.umich.edu/~fpdum; phone: 1-734-936-0972; fax: 1-734-615-2843; Organic & Molecular Electronics Research Group 1049 BIRB, 2360 Bonisteel Blvd. Ann Arbor, MI 48109

were obtained by detecting the amount of water vapor and oxygen molecules diffusing through the plastic films with an infrared sensor and a Coulometric sensor, respectively.

The plastic substrates were cleaned in the ultrasonic bath of isopropanol before polymer deposition. Then, a hole injection layer (HIL, 500-600 Å) and a light-emissive layer (LEL, 800-900 Å) were consecutively spin-coated. Xylene was used as a solvent for LEL polymer. Since the PEDOT is deposited from an aqueous solution, it was not dissolved by xylene during the device fabrication. Aluminum cathode (~2000 Å) was thermally evaporated through shadow masks under a high vacuum (~10⁻⁶ torr) with 5 Å/s rates. Before electrical and optical measurements were performed, the devices were thermally annealed in the nitrogen at 90 °C for one hour. All the device fabrication steps have been done in the cleanroom of class 100.

The absorption and photoluminescence (PL) spectra were measured with a CARY UV-Visible spectrophotometer and FluoroMax-2, respectively. Films of comparable thickness used in OLEDs were prepared on the quartz substrates for these measurements. The cyclic voltammetry (CV) spectra were recorded by a home made three-electrode electrochemical system controlled by a computer. The electroluminescence (EL) spectra were measured in the air using a CCD spectrum system calibrated by a Labsphere USS-600 Uniform Source System. The current and brightness versus voltage characteristics were measured in the air with a programmable voltage source (Keithley 230), an electrometer (Keithley 617) and IL1700 Research Radiometer from International Light. The fabricated devices were mounted on the edge of the integrating sphere (INS250) and then all the electrical and optical measurements were performed at the same time by using a personal computer to control different setups as shown in the Fig. 1(b).

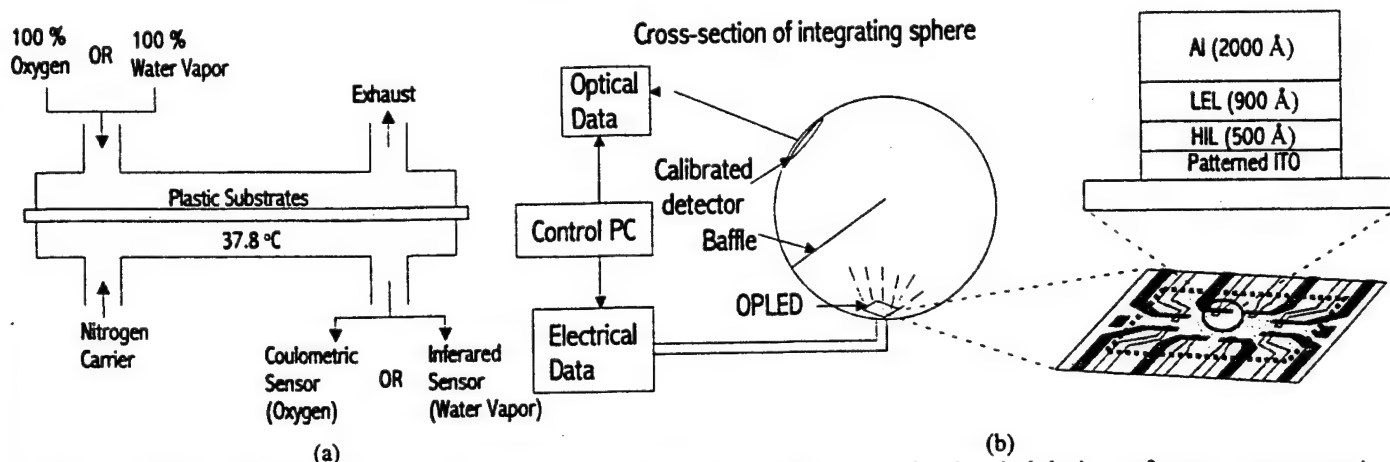


Figure 1. Schematic representation of (a) oxygen and water permeability and (b) electrical and optical device performance measurement setups (An integrating sphere was used to collect all the emitted light output. The structures of the OPLEDs used in this study are also shown.)

3. RESULTS AND DISCUSSION

3.1. Water vapor and oxygen permeability of our plastic substrates

It is well known that the degradation mechanism of the OPLEDs is strongly related to water vapor and/or oxygen permeation into the devices.¹¹ Since the water vapor and oxygen can trigger (or accelerate) the OPLED degradation, it is critical that plastic substrates have the lowest possible water vapor and oxygen permeability. To investigate the gas permeability, we measured the transmission rates of water vapor and oxygen of our plastic substrates. As shown in Fig. 2, the transmission rates are saturated as gas exposure time increases and these saturated values represent the maximum transmission rates (TR_{max}). Using TR_{max} , transmission rate (TR) and permeability (P) values can be calculated with the following equations.

$$TR = \frac{TR_{max}}{P_{gas}}, \quad (1)$$

$$P = TR \times L, \quad (2)$$

where, P_{gas} and L are the partial pressure of gas (water vapor or oxygen) and the plastic film thickness, respectively. To further reduce the water vapor and oxygen permeability through the plastic substrates, we have deposited several types of low temperature layers on the top of the plastic substrates. The hydrogenated amorphous silicon nitride and amorphous silicon oxide (a-SiN_x:H and a-SiO_x:H) were deposited by a low temperature (60°C) plasma-enhanced chemical vapor deposition (LT-PECVD) method, the polypropylene glycol (PPG) was spin-coated and cured at low temperature, and

chromium/aluminum bi-layer was deposited by sputtering method. Table 1 summarizes the transmission rates and permeability for different plastic film structures. From this table, it can be concluded that the combination of a-SiN_x:H and a-SiO_x:H layers shows the best results. And it is also clear from our data that a low temperature multi-layer inorganic films deposited over the plastic substrates can reduce the water vapor and oxygen transmission rates to the levels that are undetectable by the methods used in this study.

Table 1 The permeability of the water vapor and oxygen through plastic substrates, where TR and P are transmission rate and permeability, and pITO and bITO are patterned and blank ITO, respectively (*: measurement setup detection limit).

Samples	Water Vapor TR (g/cm ² -day-atm)	Water Vapor P (g-cm/cm ² -sec-atm)	Oxygen TR (cc/cm ² -day-atm)	Oxygen P (cc-cm/cm ² -sec-atm)
pITO/substrate/a-SiO _x :H (~2500 Å)	<1.55×10 ⁻⁵ *	<3.56×10 ⁻¹²	1.30×10 ⁻⁶	3.00×10 ⁻¹³
pITO/substrate/a-SiN _x :H (~2500 Å)	3.74×10 ⁻⁵	8.58×10 ⁻¹²	3.86×10 ⁻⁶	8.87×10 ⁻¹³
pITO/substrate/a-SiN _x :H/a-SiO _x :H (~1500 Å/~1500 Å)	<1.55×10 ⁻⁵ *	<3.56×10 ⁻¹²	2.53×10 ⁻⁷	5.76×10 ⁻¹⁴
bITO /substrate/Cr/Al (~400 Å~2000 Å)	<1.55×10 ⁻⁵ *	<3.56×10 ⁻¹²	3.94×10 ⁻⁶	9.09×10 ⁻¹³
pITO/substrate/PPG (~8.9 μm)	5.06×10 ⁻⁴	1.16×10 ⁻¹¹	2.13×10 ⁻⁵	4.92×10 ⁻¹²
substrate/blank ITO (bITO)	1.17×10 ⁻⁴	2.69×10 ⁻¹⁰	2.27×10 ⁻⁵	5.00×10 ⁻¹²
substrate/patterned ITO (pITO)	3.66×10 ⁻⁴	8.4×10 ⁻¹¹	1.56×10 ⁻⁵	3.58×10 ⁻¹²

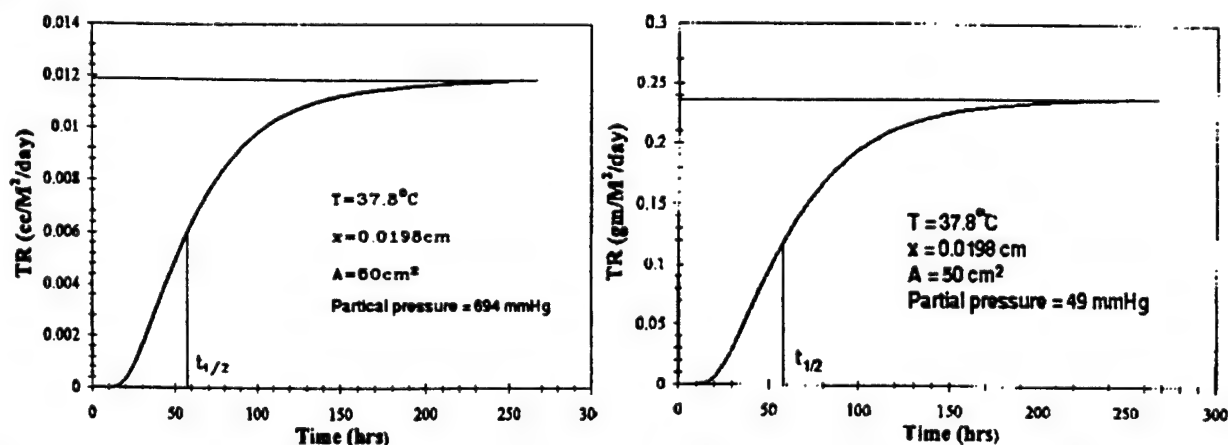


Figure 2. An example of the oxygen (a) and water vapor (b) transmission rates through pITO/substrate/a-SiO_x:H and pITO/substrate/a-SiN_x:H, where pITO is patterned ITO substrate.

3.2. Material Properties

Figure 3(a) shows the absorption, photo-luminescence (PL), and electroluminescence (EL) spectra of our emissive polymer. The absorption and PL spectra were obtained for several single layer thin films deposited on quartz substrates with different thickness. The EL spectra of single and double layer devices were measured for ITO/Red polymer/Al and ITO/PEDOT/Red polymer/Al structures, respectively. The absorption peak is located at 465 nm with a shoulder at 575 nm. The PL spectra Stokes-shifted in comparison with the absorption spectra has peak located at 640 nm. The EL peak and full-width-half-maximum (FWHM) values for single and double layer structures are 645/94 nm and 650/110 nm, respectively.

The EL peak of the double layer device structure is shifted to the larger wavelength by 5 nm and its EL shape broadens by 16 nm in comparison with the single layer device structure.

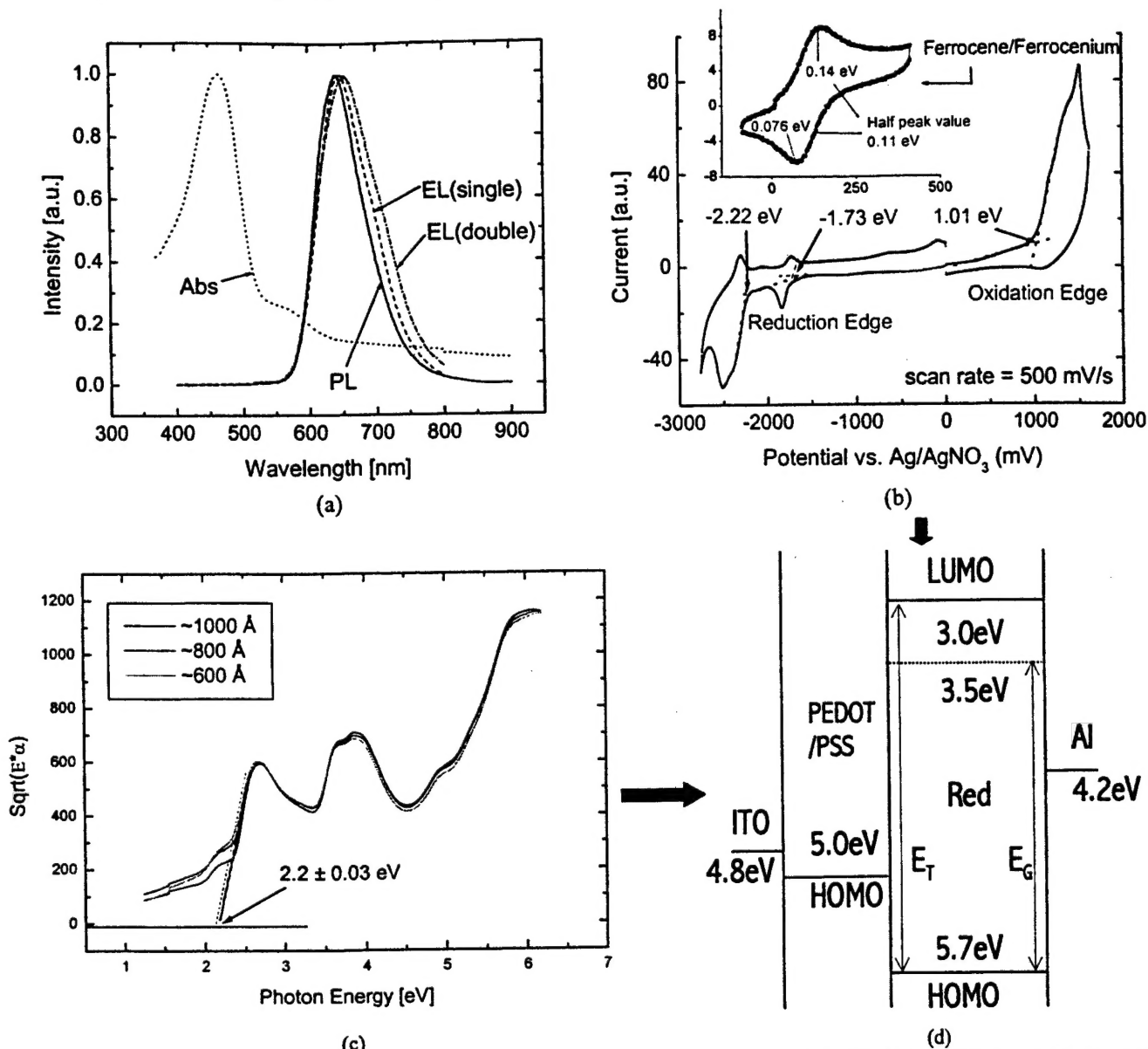


Figure 3. The absorption, photoluminescence, and electroluminescence spectra of our emissive polymer thin film are shown (a). EL spectra were obtained for both single and double layer device structures. In the cyclic voltammetry spectra, two separate reduction peaks were observed (b). We believe that the charge transport is triggered at the first peak edge and thus, we chose 2.7 eV as a transport band gap (E_T) for our emissive polymer. The Tauc plots (c) of absorption spectra for different film thickness are also shown. We averaged obtained three optical band gap values and chose 2.2 eV as the optical band gap (E_G) for our emissive polymer. From (b) and (c), the energy band diagram can be obtained for the fabricated OLEDs (d). The ITO and Al work functions and PEDOT/PSS HOMO levels^{1,2} are also included for reference. The details are explained in the text.

In Fig. 3(b), the cyclic voltammetry (CV) spectrum is shown, from which the positions of the lowest unoccupied molecular orbital (LUMO, ~3.0 eV) and highest occupied molecular orbital (HOMO, ~5.7 eV) with respect to the vacuum energy level have been obtained. First, the oxidation (E_{ox}) and reduction (E_{red}) potentials are obtained from the measured CV spectrum. In our case, we observed two reduction peaks and thus, two reduction potentials. However, since we believe that the first reduction potential (E_{red} , ~1.73 eV) represents the triggering point of reduction process, we used this value to define LUMO level of our emissive polymer. The oxidation potential (E_{ox} , ~1.01 eV) was used to calculate the HOMO level of the polymer. All E_{ox} and E_{red} potentials were chosen at the cross-section of two linear fit lines at the onset of oxidation/reduction since it is known that the onset potentials are associated more closely with the reduction/oxidation processes than the peak

potentials.¹³ By assuming a scale factor relating Ferrocene/Ferrocenium couple to vacuum of $\sim 4.8 \text{ eV}^{-1}$,⁴ the HOMO and LUMO levels can be defined by measuring E_{ox} , E_{red} , and $E_{1/2}$.

$$\text{HOMO} = (E_{ox} - E_{1/2}) + 4.8 [\text{eV}], \quad (3)$$

$$\text{LUMO} = (E_{red} - E_{1/2}) + 4.8 [\text{eV}], \quad (4)$$

where, $E_{1/2}$ is the averaged half peak value of ferrocene level. In our case, HOMO and LUMO levels are 5.7 and 3.0 eV, respectively. Knowledge of the HOMO and LUMO levels will allow to define the transport band gap (E_T) of the polymer as shown in Fig. 3(d).

The optical band gap (E_G) was obtained from the so-called Tauc plot of absorption spectra shown in Fig. 3(c). Assuming that spin-coated polymer layer is an amorphous 3-D system, in which the electron wave functions can spread in all directions, the following equation can be derived:¹⁵

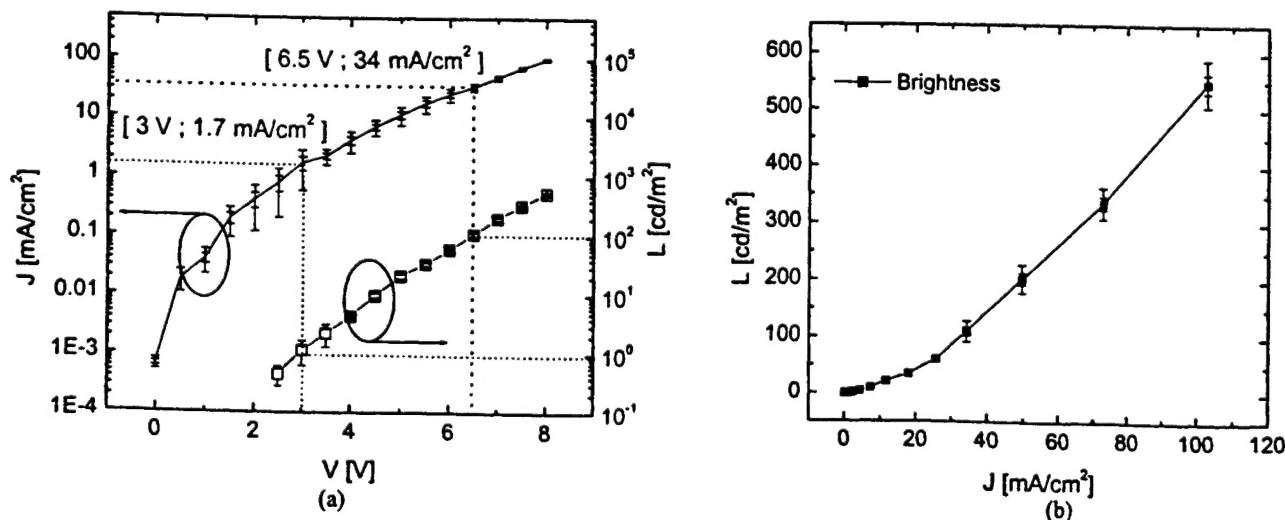
$$\sqrt{\alpha \hbar \omega} \propto (\hbar \omega - E_G), \quad (5)$$

This equation shows that optical band gap can be extracted when the square root of the product of absorption coefficient (α) and photon energy ($\hbar \omega$) is plotted versus photon energy. In Fig. 3(c), Tauc plot for thin film emissive polymer with different thickness is shown. From this plot we obtained $E_G = 2.2 \text{ eV} \pm 0.03 \text{ eV}$.

Knowing different energy levels, the energy band diagram of our double layer OLEDs was constructed as shown in Fig. 3(d). The HOMO level of PEDOT/PSS and work functions of Al and ITO are also included. By inserting PEDOT/PSS layer, the effective hole injection barrier is reduced from 0.9 eV to two-step of 0.2 and 0.7 eV. We found that this reduced effective barrier improves the electrical and optical performances of the OLEDs. The details are described in the following section.

3.3. OLEDs Electrical and Optical Characteristics

The current density and brightness versus applied voltage characteristics (J-L-V) for double layer OLEDs fabricated on flexible plastic substrates are shown in Figure 4(a). The turn-on voltage and the current density levels defined at 1 cd/m^2 are $\sim 3.0 \text{ V}$ and 1.7 mA/cm^2 , respectively. The initial light emission was observed at voltage of 2.5 V . The brightness of 100 cd/m^2 , which represents an acceptable value for certain flat panel display applications, has been achieved at relatively low voltage and current density levels (6.5 V , 34 mA/cm^2). We observed the substrate-melting phenomenon at the high current density levels (over 600 mA/cm^2). To avoid this phenomenon, only voltages up to certain levels can be applied. We found that the maximum brightness of about 600 cd/m^2 can be achieved at the voltage and current density levels of 8 V and 100 mA/cm^2 , respectively. The brightness versus current density characteristic is shown in Fig. 4(b). A quite linear relationship between brightness and current density has been observed for the fabricated devices. Figure 4(c) shows the emission (EE) and power (PE) efficiencies versus current densities for the same devices. The emission and power efficiencies are defined as the ratios of brightness to current density and luminous flux to consumed electrical power, respectively. The maximum emission and power efficiencies of 0.25 cd/A and of 0.1 lm/W were obtained at the current density of about 60 mA/cm^2 . The device efficiencies can be further improved by engineering the hole injection and transport properties, that is, adding an appropriate hole transport layer (HTL) between HIL and LEL, thus balancing the hole and electron carriers in the light-emitting region. The details of such device structure will be reported elsewhere.¹⁶



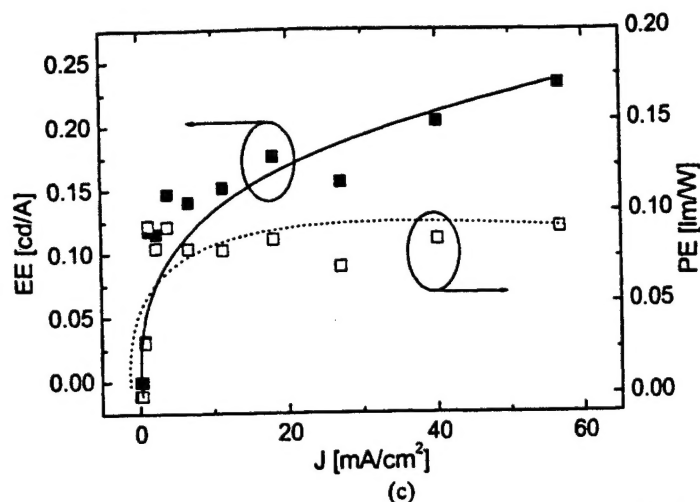


Figure 4. Current density and brightness versus applied voltage (a), brightness versus current density characteristics (b), and emission (EE) and power (PE) efficiencies versus current density (c) for double layer OLEDs fabricated on flexible plastic substrates are shown.

3.4. Lifetime test results

The lifetime test has been performed with our unpackaged OLEDs on flexible plastic substrates at room temperature under the ambient conditions ($T = \sim 25^\circ\text{C}$, $\text{RH} = \sim 30\%$). The change of brightness and voltage across the devices versus operation time was measured at several constant current levels corresponding to different initial brightness (L_{initial}) levels. We also applied appropriate negative current to OLEDs every 30 seconds during the lifetime measurement for about 10 seconds to remove accumulated or trapped charges in the devices. By refreshing the devices, it is found that the OLED operation lifetime can be increased, in comparison with the lifetime of the devices that are continuously biased without the negative bias refresh. This effect is also consistent with the improved stability of Alq based OLEDs induced by the reverse bias component in alternative current (ac) operation.¹⁷

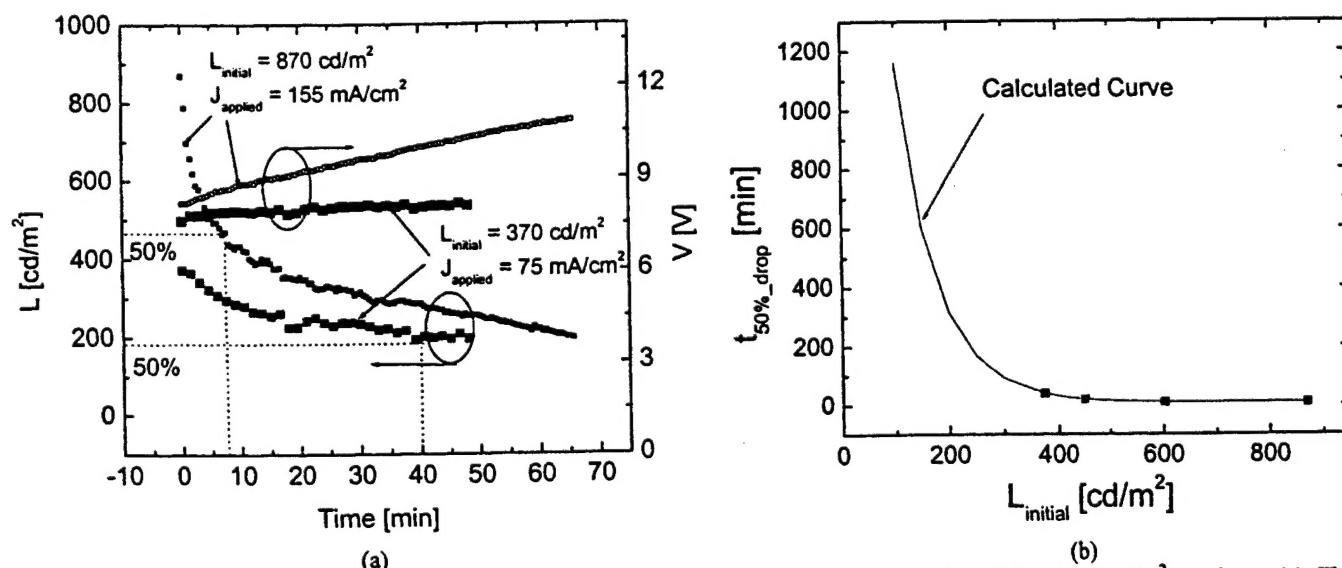


Figure 5. Examples of the OLED brightness evaluation with the time for initial brightness level of 870 and 370 cd/m^2 are shown (a). The relationship between device lifetime ($t_{50\% \text{ drop}}$) and initial brightness (L_{initial}) for our unpackaged double layer OLEDs is shown (b). The calculated curve is also included in this figure. All data were obtained at room temperature under the ambient conditions.

In Fig. 5(a), examples of the device brightness variation with the time are shown. In these specific cases, the device initial brightness levels were 870 and 370 cd/m^2 . We have defined the device lifetime as the time ($t_{50\% \text{ drop}}$) corresponding to 50% loss of the initial device brightness as shown in Fig. 5(a) (dotted lines). While the voltage across the devices increases without abrupt change, the brightness initially decreases rapidly and then, decreases at much slower rate. It should be noticed that the slope of these curves is initial brightness intensity dependent as shown in Fig. 5(a). The relationship between device

lifetime and L_{initial} for our OLEDs at room temperature under ambient conditions can be fitted by a first-order exponential decaying function:

$$t_{50\% \text{ drop}} = A + B \times e^{\frac{-L_{\text{initial}}}{C}} \text{ (min)}, \quad (6)$$

where $A = 8.45$, $B = 4288.42$, and $C = 75.9$, respectively. From this equation, the OLED lifetime of about 1160 min for $L_{\text{initial}} = 100 \text{ cd/m}^2$ can be estimated. The lifetime of our OLEDs will be much increased if the devices are fabricated and packaged under water vapor and oxygen free environment. This type of data will be reported in different publication. We can also conclude from Figure 5(b) that OLED lifetime is decreasing with the increasing device operating initial brightness.

4. CONCLUSIONS

The structural, optical, and electrical properties of the red light-emissive polymer have been studied. The following electrical properties have been obtained for our devices: turn-on voltage and current density levels (defined at 1 cd/m^2) = $\sim 3.0 \text{ V}$ and 1.7 mA/cm^2 ; maximum emission efficiency = $\sim 0.25 \text{ cd/A}$; and maximum luminous efficiency = $\sim 0.1 \text{ lm/W}$. The voltage and current density of $\sim 6.5 \text{ V}$ and $\sim 34 \text{ mA/cm}^2$ are needed to achieve $L = 100 \text{ cd/m}^2$. The extrapolated lifetime of unpackaged OLEDs on flexible plastic substrate of about 1160 min for $L_{\text{initial}} = 100 \text{ cd/m}^2$ has been obtained. This lifetime is decreasing function of the OLEDs initial brightness.

ACKNOWLEDGEMENT

This research was supported by ONR - DARPA and NIH grants.

REFERENCES

References

- ¹ C.W. Tang and S.A. Van Slyke, *Appl. Phys. Lett.* **51**, 913 (1987).
- ² J.H. Burroughes, D.D.C. Bradley, A.R. Brown, R.N. Marks, K. Mackay, R.H. Friend, P.L. Burn, and A.B. Holmes, *Nature* **347**, 539 (1990).
- ³ P.E. Burrows, G.L. Graff, M.E. Gross P.M. Martin, M. Hall, E. Mast, C. Bonham, W. Bennett, L. Michalski, M. Weaver, J.J. Brown, D. Fogarty, and L.S. Sapochak, *Proceedings of SPIE* **4105**, 75 (2001).
- ⁴ Y. He and J. Kanicki, *Proceedings of SPIE* **4105**, 143 (2001).
- ⁵ Y. Hong, Z. Hong, and J. Kanicki, *Proceedings of SPIE* **4105**, 356 (2001).
- ⁶ M. Bernius, M. Inbasekaran, E. Woo, W. Wu, and L. Wujkowski, *Proceedings of SPIE* **3797**, 129 (1999).
- ⁷ S.J.M. O'Connor, C.R. Towns, R. O'Dell, J.H. Burroughes, *Proceedings of SPIE* **4105**, 9 (2001).
- ⁸ S. Tokito, K. Weinfurter, H. Fujikawa, T. Tsutsui, and T. Taga, *Proceedings of SPIE* **4105**, 69 (2001).
- ⁹ ASTM Test for Oxygen Gas Transmission Rate Through Plastic Film and Sheeting (D-3985).
- ¹⁰ ASTM Standard Test Method for Water Vapor Transmission Rate Through Plastic Film and Sheeting Using a Modulated Infrared Sensor (F1249).
- ¹¹ A. Bernsten, Y. Crooner, C. Liedenbaum, H. Schoo, R.J. Visser, J. Vleggaar, and P. van de Weijer, *Optical Materials* **9**, 125 (1998).
- ¹² R. Friend, J. Burroughes, and T. Shimoda, *Physics World*, 35 (1999).
- ¹³ S. Janietz, D.D.C. Bradley, M. Grell, C. Giebeler, M. Inbasekaran, and E.P. Woo, *Appl. Phys. Lett.* **73**, 2453 (1998).
- ¹⁴ Y. Hong, Z. Hong, M.D. Curtis, and J. Kanicki, *Conference Record of the IDRC 2000*, 183 (2000).
- ¹⁵ J. Tauc, R. Grigorovici, and A. Vancu, *Phys. Stat. Sol.* **15**, 627 (1966).
- ¹⁶ Y. Hong, S. Lee, and J. Kanicki, *ICEL-3 Conference Record* (to be published).
- ¹⁷ S.A. Van Slyke, C.H. Chen, and C.W. Tang, *Appl. Phys. Lett.* **69**, 2160 (1996).